

**TRANSFORMATIONS IN CLAY-RICH FAULT ROCKS: CONSTRAINING FAULT  
ZONE PROCESSES AND THE KINEMATIC EVOLUTION OF REGIONS**

by

**Samuel Haines**

**A dissertation submitted in partial fulfillment  
of the requirements of the degree of  
Doctor of Philosophy  
(Geology)  
in The University of Michigan  
2008**

**Doctoral committee:**

**Professor Ben A. van der Pluijm, Chair  
Professor Roman D. Hryciw  
Associate Professor Udo Becker  
Associate Professor Todd A. Ehlers  
Research Scientist Chris Michael Hall**

Περι δε σεισμου και κινεσεωσ γησ μετα ταυτα λεκτεον, η γαρ αιτια του παθουσ εκομενη  
τουτου του γενουσ εστιν.

- Aristotle, *Meteorologia*, II, vii

*"We must go on to discuss earthquakes and movements of the earth next, for their  
cause of their occurrence is as our last subjects"*

© Samuel Haines

2008

To Monamie, with love, and Kaajal, with bellyrubs

## ACKNOWLEDGMENTS

It may or may not take a village to raise a child, but it does take a village to write a thesis. I am grateful to have had the opportunity to work with Ben van der Pluijm, who helped turn a “know-it-all” into someone who might actually know something. I am grateful to my committee members, Roman Hryciw, Udo Becker, Todd Ehlers and Chris Hall, who have taken the time to provide feedback and refining the thought of much of what is presented here. Todd’s informal seminars were one of the high points of my time here, and helped me figure out what a good scientific problem might actually look like. Chris’s assistance with the Ar-dating was invaluable and made 3 chapters in this thesis possible. My time in the Grand Duchy of Structure and Tectonics at Michigan has been greatly enriched by Rob van der Voo who teaches one of the best courses I have ever taken. I also owe a big debt of gratitude to Eric Essene, who’s curiosity about almost any rock, and openness to discuss almost any geological problem has been a joy to experience. Marin Clark, Nathen Niemi, Kasey Lohmann, Peter van Keken, Larry Ruff, Steve Kesler, Sam Mukasa, Jamie Gleason, Bruce Wilkinson and Shannon Peters have all challenged me scientifically and pushed me to think in new ways. Anja Schleicher’s fellow love of clays, and facility with the TEM, has been a real pleasure.

I am grateful to several co-workers for the opportunity to participate in so much interesting science. Chris Marone, Demian Saffer and Matt Ikari at Penn State, and Daniel Köhn, Till Sachau, at Mainz and Kevin Aanyu and Andreas Schuman at Makerere

University in Uganda, have all introduced me to new scientific problems, and the Mainz group let me make the trip of a lifetime, twice. I would especially like to thank Tom O'Rourke at Cornell for planting the seed of a PhD in my head at a restaurant in Queens back in 2001. Pete D'Onfro at ConocoPhillips has been both a mentor and a friend. Daryl Cowan and Nick Hayman introduced me to the fault rocks of the Death Valley area; I benefited greatly from their knowledge.

I have benefited enormously from the many students here, both graduate and undergraduate who have made my time here a pleasure. First, Monamie Bhadra, who gave me an (undeserved) second look and eventually decided to become my wife. Eric Kneller, J.P. Brandenburg, Elizabeth Anderson, Nico de Koker, John Solum, Jim Hnat, Cheryl Peyser, Sara Torscher, Zeb Page, Chris Stefano, Francek Hasiuk, Nadja Insel, Boris Avdeev, Alison Duvall, and Alex Janevski have all made this place into the pleasure that it has been. If you're looking, but not on the list, you should be.

Lastly, I would like to thank my parents, who tolerated a globe-trotting son for years with patience, and more than a little bemusement, for all their love and support.

## TABLE OF CONTENTS

|   |       |
|---|-------|
| DEDICATION .....  | ii    |
| ACKNOWLEDGMENTS.....  | iii   |
| LIST OF FIGURES.....  | xi    |
| LIST OF TABLES.....   | xvii  |
| LIST OF APPENDICIES .....   | xviii |
| ABSTRACT .....  | xix   |
| CHAPTER 1: INTRODUCTION .....   | 1     |
| Motivation for the dissertation research.....   | 1     |
| Fault zone weakness .....   | 1     |
| Previous study of clay gouges .....   | 3     |
| Objectives of the dissertation .....  | 4     |
| Outline of dissertation.....  | 5     |
| Summary of research goals .....   | 9     |
| References.....   | 10    |
| CHAPTER 2: THE MINERALOGY OF CLAY-RICH GOUGES IN LOW-ANGLE NORMAL<br>FAULTS: THE NATURE AND SIGNIFICANCE OF CLAY MINERAL<br>TRANSFORMATIONS ..... | 14    |
| Abstract .....  | 14    |
| Introduction.....   | 15    |
| Geological setting and sample locations .....   | 18    |
| Regional setting.....   | 24    |
| Ruby Mountains .....  | 24    |

|   |     |
|---|-----|
| Death Valley area detachments .....                                 | 24  |
| Colorado River extensional corridor .....                           | 28  |
| West Salton detachment fault .....                                  | 31  |
| Central Mojave metamorphic core complex .....                       | 31  |
| Metasomatic chloritic footwall alteration .....                     | 32  |
| Methods .....   | 33  |
| Sampling and clay separation .....                                  | 33  |
| X-ray diffraction .....   | 33  |
| WILDFIRE modeling .....   | 34  |
| Results .....   | 35  |
| Chloritic gouges .....  | 41  |
| Chlorite alteration gouges .....                                    | 46  |
| Illitic gouges .....  | 60  |
| Discussion .....  | 70  |
| Conclusions .....   | 76  |
| Acknowledgments .....   | 77  |
| References .....  | 78  |
| CHAPTER 3: CLAY FABRICS IN NATURAL AND ARTIFICIAL FAULT GOUGE ..... | 87  |
| Abstract: .....   | 87  |
| Introduction .....  | 88  |
| Clay Fabric .....   | 91  |
| Faults studied .....  | 92  |
| Methods for X-Ray texture goniometry .....                          | 97  |
| Low-angle normal faults .....                                       | 97  |
| Results .....   | 102 |
| Natural gouges .....  | 102 |



|   |     |
|---|-----|
| Experimental gouges .....   | 108 |
| Discussion and Conclusion .....   | 118 |
| Acknowledgments: .....  | 125 |
| References .....  | 126 |
| <br>CHAPTER 4: CLAY QUANTIFICATION AND AR-AR DATING OF SYNTHETIC AND<br>NATURAL GOUGE - APPLICATION TO THE MIOCENE SIERRA MAZATÁN<br>DETACHMENT FAULT, SONORA, MEXICO ..... |     |
| Abstract: .....   | 133 |
| Introduction .....  | 134 |
| Fault dating and illite polytypism.....   | 138 |
| Fault dating .....  | 138 |
| Illite Polytypism .....   | 139 |
| Geologic setting.....   | 142 |
| Methods.....  | 145 |
| Standard sample preparation.....  | 145 |
| Sierra Mazatán sample preparation.....  | 146 |
| WILDFIRE modeling .....   | 147 |
| Argon dating.....   | 149 |
| Results and quantification. ....  | 149 |
| Interpretation and discussion.....  | 159 |
| Conclusions .....   | 163 |
| Acknowledgments .....   | 164 |
| References .....  | 165 |
| <br>CHAPTER 5: FAULT AND PROVENANCE AGES IN THE PYRENEES –<br>CONSTRAINTS FROM FAULT GOUGE DATING.....  |     |
| Abstract .....  | 169 |
| Introduction.....   | 170 |

|   |     |
|---|-----|
| Fault dating .....  | 172 |
| Geological setting .....  | 173 |
| Methods .....   | 176 |
| Sample locations.....   | 176 |
| South-central transect.....   | 180 |
| Ter-Freser section.....   | 181 |
| Gouge sample preparation .....  | 183 |
| WILDFIRE modeling .....   | 184 |
| Ar-Ar dating.....   | 185 |
| Results.....  | 185 |
| South-central Pyrenees .....  | 187 |
| Ter-Freser section.....   | 193 |
| Discussion .....  | 197 |
| Fault ages .....  | 197 |
| Provenance Ages.....  | 201 |
| Summary and conclusions .....   | 203 |
| Acknowledgments .....   | 204 |
| References .....  | 205 |
| <br>  |     |
| CHAPTER 6: DATING THE DETACHMENT FAULT SYSTEM OF THE RUBY MOUNTAINS, NEVADA – SIGNIFICANCE FOR KINEMATICS OF LOW-ANGLE NORMAL FAULTs..... | 211 |
| Abstract .....  | 211 |
| Introduction.....   | 212 |
| Fault dating.....   | 215 |
| Field area.....   | 217 |
| Methods.....  | 220 |
| Sampling and clay separation.....   | 220 |

|   |     |
|---|-----|
| X-ray diffraction .....   | 220 |
| WILDFIRE modeling .....   | 221 |
| Ar-Ar dating .....  | 221 |
| Results .....   | 222 |
| Outcrop and gouge characterization - Secret Pass .....  | 222 |
| High-angle normal fault .....   | 225 |
| Upper detachment .....  | 228 |
| Main detachment .....   | 232 |
| Clover Hill .....   | 235 |
| Illite Ar-Ar ages .....   | 241 |
| Secret Pass .....   | 241 |
| Secret Pass muscovite and biotite ages .....  | 241 |
| Clover Hill ages .....  | 243 |
| Interpretation and discussion .....   | 246 |
| Conclusions .....   | 253 |
| Acknowledgments .....   | 254 |
| References .....  | 255 |
| Chapter 7: Conclusions .....  | 261 |
| References .....  | 271 |
| APPENDIX A: CLAY MINERAL ASSEMBLAGES IN FAULT GOUGES FROM THE<br>RWENZORI MOUNTAINS, UGANDA ..... | 274 |
| Regional introduction .....   | 274 |
| Methods .....   | 277 |
| Results .....   | 279 |
| Low-altitude surface gouges .....   | 281 |
| Smectite-dominated gouges .....   | 281 |

|  |     |
|--|-----|
| Detrital gouges and disaggregation bands ..... | 284 |
| Discussion and conclusions .....               | 290 |
| Acknowledgements .....                         | 292 |
| References .....                               | 293 |
| APPENDIX B – FIELD SAMPLE LOCATIONS .....      | 295 |

## LIST OF FIGURES

|   |    |
|---|----|
| <b>Figure 2-1:</b> Schematic map of the western US showing major tectonic features and the location of detachment faults sampled in this study (numbered) and other detachment faults mentioned in the text. .... | 19 |
| <b>Figure 2-2:</b> Sketch geologic map of the Death Valley area, CA showing sample locations for low-angle normal faults in the Black and Panamint mountains.....   | 25 |
| <b>Figure 2-3:</b> Sketch geologic map of the Colorado River extensional corridor, Ca and AZ, showing sample locations for low-angle normal faults sampled in this study.....                                     | 29 |
| <b>Figure 2-4:</b> Outcrop photographs and XRD patterns of oriented preparations of the clay fraction of gouge at Mormon-2.....   | 43 |
| <b>Figure 2-5:</b> Outcrop photographs of the Chemehuevi detachment at Lobeck Pass. Note regions of differing clay mineralogy highlighted in photo and Reidel shears visible in the tan palygorskite crust.....   | 44 |
| <b>Figure 2-6:</b> XRD patterns from regions of gouge identified in Figure 2.5.....   | 45 |
| <b>Figure 2-7</b> XRD patterns from random preparations of scaly gouge at Mormon-2 and Lobeck Pass separated into size fractions.....   | 47 |
| <b>Figure 2-8:</b> XRD patterns of random preparations of crushed scaly gouge and crushed footwall collected at Mormon Point (upper profiles) and Lobeck Pass (lower profiles)..                                  | 48 |
| <b>Figure 2-9:</b> Field photographs and XRD patterns of oriented preparations of the clay fraction of gouge from the Buckskin detachment at A-Bomb Canyon.....   | 49 |
| <b>Figure 2-10:</b> Field photographs and XRD patterns of oriented preparations of the clay fractions of chloritic and Mg-rich mineral layers in gouge at Mormon-3.....   | 50 |
| <b>Figure 2-11:</b> XRD patterns of oriented preparations of size fractions of the Mg-rich gouge at Mormon Point.....   | 52 |
| <b>Figure 2-12:</b> Outcrop photos and XRD patterns of oriented preparations of size fractions of gouge from Copper Canyon.....   | 54 |
| <b>Figure 2-13:</b> Field photographs and XRD patterns of oriented preparations of the clay size fraction of gouge from upper-plate normal faults linked to the Whipple detachment. ....                          | 55 |

|  |     |
|--|-----|
| <b>Figure 2-14:</b> XRD patterns of size fractions of green gouge at Whip-5. (pictured in Figure 2.13).....  | 56  |
| <b>Figure 2-15:</b> Photomicrograph of basalt dyke intruded along fault plane at Whip-5.....   | 57  |
| <b>Figure 2-16:</b> Graphs of chlorite composition in low-angle normal fault gouge and wallrock composition as estimated from XRD intensities of (00l) peaks of random preparations.....   | 59  |
| <b>Figure 2-17:</b> Outcrop photographs and XRD patterns of clay gouges from the Amargosa detachment at Ashford Klippe.....  | 62  |
| <b>Figure 2-18:</b> XRD patterns of random preparations of gouges from Ashford Klippe and Mosaic Canyon illustrating the transformation from 2M1 illite in the coarse and medium fractions to 1Md illite in the fine fraction..... | 63  |
| <b>Figure 2-19:</b> XRD patterns of gouge from Ashford Klippe (previous figure) modeled using WILDFIRE.....  | 64  |
| <b>Figure 2-20:</b> Outcrop photographs of the Badwater detachment at Badwater-1.....  | 65  |
| <b>Figure 2-21:</b> XRD patterns of the clay fraction of footwall, gouge and hangingwall at Badwater-1.....  | 67  |
| <b>Figure 2-22:</b> XRD patterns of random preparations of gouge from Badwater-1. (previous figure) and the Waterman Hills illustrating the transformation of K-feldspar to 1M <sub>d</sub> illite.....                            | 68  |
| <b>Figure 3-1:</b> Schematic illustration of clay fabric orientation in fault zones.....   | 90  |
| <b>Figure 3-2:</b> Location map for samples used in this study.....  | 93  |
| <b>Figure 3-3:</b> Illustration of X-ray goniometry data acquisition and reduction.....  | 99  |
| <b>Figure 3-4:</b> Sketch figure of biaxial double direct shear apparatus geometry. (after Saffer & Marone, 2003).....   | 101 |
| <b>Figure 3-5:</b> Plot of representative sliding friction test with stepped normal stress.....  | 103 |
| <b>Figure 3-6:</b> Natural clay fabric intensity data.....   | 105 |
| <b>Figure 3-7:</b> Experimental clay fabric intensity data.....  | 110 |
| <b>Figure 3-8:</b> Effect of compression versus shear on clay fabric orientation.....  | 111 |
| <b>Figure 3-9:</b> Effect of increasing shear strain on clay fabric orientation and strength....   | 112 |
| <b>Figure 3-10:</b> Scanning electron images of experimental samples used in this study...   | 114 |
| <b>Figure 3-11:</b> Experimental clay fabric intensity data.....   | 116 |

|   |     |
|---|-----|
| <b>Figure 3-12:</b> Graph showing the relationship of clay mineral content with fabric strength for samples with similar normal stress conditions and at similar shear strains..  | 117 |
| <b>Figure 3-13:</b> Comparison of published fabric intensity from sedimentary sequences with observed clay fabric intensities in clay gouges.   | 122 |
| <b>Figure 3-14:</b> Schematic figure showing relative roles of compaction and authigenic mineral growth in diagenetic sequences as inferred from fabric intensity measurements.   | 124 |
| <b>Figure 4-1:</b> Mineral transformations observed in clay gouges that are suitable for dating by illite age analysis..  | 135 |
| <b>Figure 4-2:</b> Cartoon illustrating fault gouge sample preparation and Illite Age Analysis process.   | 137 |
| <b>Figure 4-3:</b> Stacked XRD tracings for 2M1 muscovite (Owl Creek pegmatite, Wind River Mts, WY, USA) and 1Md illite (IMt-1, Silver Hill, MT, USA).  | 140 |
| <b>Figure 4-4:</b> Location map of northwest Mexico and surrounding areas showing location of study area and selected geographic and tectonic features.   | 143 |
| <b>Figure 4-5:</b> Stacked XRD tracings for six artificial mixtures of Owl Creek muscovite (2M1) and IMt-1 illite (1Md).  | 150 |
| <b>Figure 4-6:</b> Best matches of WILDFIRE patterns using WILDFIRE and a lowest-variance approach.   | 151 |
| <b>Figure 4-7:</b> XRD tracings for six artificial mixtures of Owl Creek muscovite (2M1) and IMt-1 illite (1Md) and best matches calculated using WILDFIRE and our approach.  | 152 |
| <b>Figure 4-8:</b> Best matches of WILDFIRE patterns to XRD tracings of Owl Creek muscovite (2M1 - black) calculated using WILDFIRE (grey) using two different approaches.  | 154 |
| <b>Figure 4-9:</b> Predicted vs. actual comparison of polytype quantification using a strict lowest-variance approach and our approach. which uses the entire pattern between 21 and 36 degrees 2 $\theta$ for 1Md-rich mixtures, while for the 2M1-rich mixtures, our approach focuses on matching the 2M1-specific peaks. | 155 |
| <b>Figure 4-10:</b> XRD patterns (black) and best matches (grey) for size fractions of gouge from Sierra Mazatan.   | 156 |
| <b>Figure 4-11:</b> Ar-Ar spectra for the five size fractions of gouge from Sierra Mazatán.   | 158 |
| <b>Figure 4-12:</b> Illite age analysis plot for gouge from Sierra Mazatán detachment fault.  | 160 |
| <b>Figure 4-13:</b> Summary plot of age data from the Sierra Mazatán detachment.  | 162 |
| <b>Figure 5-1:</b> Location map of faults studied (red circles) and approximate projection onto ECORS seismic profile.  | 174 |

|  |     |
|--|-----|
| <b>Figure 5-2:</b> Geologic map with sample locations, cross-section and stratigraphic column for the Ter-Freser river section shown. ....   | 177 |
| <b>Figure 5-3:</b> Outcrop photographs of some thrusts sampled for this study.....   | 178 |
| <b>Figure 5-4:</b> Typical quantification of the relative abundance of the 2M <sub>1</sub> and 1M <sub>d</sub> polytypes of illite in the coarse, medium and fine fractions size fractions of a fault gouge, and associated Ar-Ar spectra..... | 186 |
| <b>Figure 5-5:</b> Illite age analyses plots of the nine gouges sampled in this study.....   | 188 |
| <b>Figure 5-6:</b> Map showing distribution of fault gouge ages for the 9 faults sampled.....  | 189 |
| <b>Figure 5-7:</b> Map showing the age of the detrital component of fault gouge.....   | 202 |
| <b>Figure 6-1:</b> Generalized geologic map of the Ruby Mountains-East Humboldt Range in northeastern Nevada.....  | 218 |
| <b>Figure 6-2:</b> Simplified geologic map of the Secret Creek Gorge area and cross section showing the locations of the three detachment faults described in this paper. along with a simplified cross section along A – A'.....              | 223 |
| <b>Figure 6-3:</b> Field photos showing outcrops of faults at Secret Pass sampled in this study.....   | 224 |
| <b>Figure 6-4:</b> Field photograph and XRD patterns of <2µm fraction from upper-plate normal fault rocks (Secret-1).....  | 226 |
| <b>Figure 6-5:</b> XRD patterns of gouge and wall rocks of upper-plate normal fault, separated into size fractions.. ....  | 227 |
| <b>Figure 6-6:</b> XRD patterns from Secret 1-1 with polytype quantifications determined using WILDFIRE-generated patterns.....  | 229 |
| <b>Figure 6-7:</b> XRD patterns and NEWMOD matches of fine fractions from gouge and wallrocks of hanging-wall high-angle normal fault (Secret-1).....  | 230 |
| <b>Figure 6-8:</b> Outcrop photograph and XRD patterns of the <2 µm fraction of the gouge of the upper low-angle detachment (Secret 2-1).....  | 231 |
| <b>Figure 6-9:</b> Upper figure: patterns from oriented preparations.. ....  | 233 |
| <b>Figure 6-10:</b> Outcrop photo and XRD patterns of the <2 µm fraction of each region visible in photo.. ....  | 234 |
| <b>Figure 6-11:</b> XRD patterns from size fractions of the gouge of the main low-angle detachment (Secret 4-2).. ....   | 236 |
| <b>Figure 6-12:</b> HD-TEM lattice fringe images of clays from the main detachment (Secret 4-2).....   | 237 |



|  |     |
|--|-----|
| <b>Figure 6-13:</b> Outcrop photo and XRD patterns from the gouge zone at Clover Hill. of the <2 $\mu\text{m}$ fraction of each region visible in the photo.....   | 239 |
| <b>Figure 6-14:</b> XRD patterns from random preparations of size fractions of Clover-2 and illite polytype quantifications done using WILDFIRE.....   | 240 |
| <b>Figure 6-15:</b> Illite polytypism quantifications and $^{40}\text{Ar}$ - $^{39}\text{Ar}$ illite step-heating spectra from fine-grained sized fractions of the three gouges (<0.05 m) from the three detachment faults exposed at Secret Pass..... | 242 |
| <b>Figure 6-16:</b> $^{40}\text{Ar}$ - $^{39}\text{Ar}$ illite step-heating spectra for coexisting muscovite and biotite from quartzite mylonites at Secret Pass (locality SP-1, Figure 6.2) and at Clover Hill (sample Clov-Q1).....                  | 244 |
| <b>Figure 6-17:</b> $^{40}\text{Ar}$ - $^{39}\text{Ar}$ illite step-heating spectra for size fractions of illitic gouge at Clover Hill (Clover-2) and illite age analysis plot..   | 245 |
| <b>Figure 6-18:</b> Sketch showing constraints on the amount of post-faulting footwall rotation on dips of Secret Pass faults active at 12 Ma, and thus the dips at which the detachment fault system was active..                                     | 250 |
| <b>Figure 6-19:</b> Exhumation histories for Secret Pass and Clover Hill as inferred from data from this study and published sources.....  | 252 |
| <b>Figure 7-1:</b> Schematic figure showing the six mineral transformations found in low-angle normal faults as in this study.....   | 269 |
| <b>Figure A 1:</b> Shaded relief 90 DEM of the Rwenzori Mountains with borders and major rift-flank faults.....  | 276 |
| <b>Figure A-2:</b> Small-scale maps of sample locations.....   | 278 |
| <b>Figure A-3:</b> Outcrop photos of fault exposures along the Fort Portal – Bundibugyo road north of Kichwamba.....   | 282 |
| <b>Figure A-4:</b> XRD patterns of oriented preparations of four samples (<2.0 $\mu\text{m}$ size fraction) from low elevations in the eastern Rwenzoris.....  | 283 |
| <b>Figure A-5:</b> Field photos of brittle fault exposed on the northwest flank of Mt Baker, east of Scott Elliot Pass, elevation 4065 m.....  | 285 |
| <b>Figure A-6:</b> XRD patterns for gouges sampled at high altitudes at Scott Elliot Pass and at Freshfield Pass.....  | 286 |
| <b>Figure A-7:</b> Field photographs and XRD pattern of brittle fault exposed on the southeast side of Mt Stanley.....   | 287 |
| <b>Figure A-8:</b> Field photographs of normal fault at Katwen Crater.....   | 288 |

**Figure A-9:** Summary sketch of Rwenzori massif indicating distribution of various types of fault rocks observed. Relief is not to scale.....291

## LIST OF TABLES

|  |     |
|--|-----|
| <b>Table 2-1:</b> Sample locations and sample names used in this study. ....   | 20  |
| <b>Table 2-2:</b> Geologic and sample collection information for each of the outcrops sampled in this study. ....                        | 21  |
| <b>Table 2-3:</b> Table showing mineralogy as determined by XRD of all samples in this study.....  | 36  |
| <b>Table 2-4:</b> XRD analysis of the fine fraction (< 0.05 $\mu\text{m}$ ) of the 29 gouge samples separated into size fractions.. .... | 42  |
| <b>Table 2-5:</b> List of some metamorphic core complexes and low-angle normal faults that lack clay-rich fault rocks. ....              | 76  |
| <b>Table 3-1:</b> Fabric intensity measurements for natural faults sampled in this study. ....   | 104 |
| <b>Table 3-2:</b> Results of XTG measurements on experimental samples.....   | 109 |
| <b>Table 5-1:</b> Locations of faults sampled in this study.....   | 179 |
| <b>Table A-1:</b> Mineralogy of fault gouge samples in the Rwenzoris as determined by XRD.. ....   | 280 |

## LIST OF APPENDICIES

|  |            |
|--|------------|
| <b>APPENDIX A: CLAY MINERAL ASSEMBLAGES IN FAULT GOUGES FROM THE RWENZORI MOUNTAINS, UGANDA.....</b> | <b>274</b> |
| <b>APPENDIX B: FIELD SAMPLE LOCATIONS.....</b>   | <b>295</b> |

## ABSTRACT

### TRANSFORMATIONS IN CLAY-RICH FAULT ROCKS: CONSTRAINING FAULT ZONE PROCESSES AND THE KINEMATIC EVOLUTION OF REGIONS

by

Samuel Haines

Chair: Ben A. van der Pluijm

The apparent mechanical weakness of faults in the brittle regime (<300 °C) conflicts with theoretical and laboratory predictions that active faults should be strong and not slip at the low angles observed in the field. Clay-rich fault rocks have been suggested as a reason for this weak behavior, and clay mineralogy of brittle faults in a variety of tectonic environments is the central theme of this thesis. A systematic study of the mineralogy of fault rocks in the western US distinguishes three sets of mineral transformations: 1.) Detrital chlorite → chlorite-smectite and smectite; 2.) Detrital chlorite → Mg-rich assemblage of sepiolite, talc lizardite or palygorskite. 3.) Detrital muscovite → authigenic 1M<sub>d</sub> illite, or detrital feldspar → authigenic 1M<sub>d</sub> illite. Fabric intensity measurements of these fault rocks demonstrate that clay fabrics are uniformly weak in comparison with other phyllosilicate-rich rocks. Fabric studies of experimentally-produced gouges indicate

that fabric intensity is sensitive to shear strain and normal stress, yet is largely independent of total clay mineral content. The observation that  $1M_d$  illite growth in gouges is common motivated the development of a robust fault gouge dating technique for these rocks. Study of the Sierra Mazatàn metamorphic core complex demonstrates the reliability of the clay dating method that quantifies the relative abundances of illite polytypes and dating by the Ar-Ar method. The ages of both authigenic and detrital components are shown to be fully consistent with geologic constraints. Application of  $1M_d$  illite dating in gouges from the Spanish Pyrenees demonstrates 'pulses' of deformation during the Paleogene and lateral variation in the timing and style of deformation. Gouge ages from the Ruby Mountains, Nevada, show that low- and high-angle normal faults were active coevally, requiring that this detachment system was active at dips  $<30^\circ$ . Gouges from the Rwenzori Mountains of Uganda formed in the top 2 km of the crust, where significant mineral transformations did not occur. The results of these studies address the controversial issues of fault strength and orientation, produce a new method to date brittle gouge with potentially wide application, and constrain the spatial-temporal window of clay transformations in fault gouge.

## CHAPTER 1: INTRODUCTION

### Motivation for the dissertation research

#### Fault zone weakness

Brittle fault rocks have been of interest to the structural geology and geophysics communities for over a century (e.g. Lyell, 1851; Lapworth, 1885; Waters & Campbell; 1935, Reed; 1964; Wu et al., 1975; Sibson, 1977) and speculation as to the nature and causes of faulting processes has occurred since ancient times (see Frontispiece). Since the 1960's, field evidence indicates that many seismically active faults are weaker than would be expected from laboratory properties of rocks (e.g., Brune et al, 1969; Kanamori & Anderson, 1975; Lachenbruch & Sass, 1980; Rice, 1992; Williams et al., 2004). Rock friction experiments indicate that most rock types, regardless of composition, have a relatively uniform coefficient of friction of 0.6 to 0.85 (Byerlee, 1978), and this recognition is often referred to as 'Byerlee's Law'.

Four lines of evidence have been presented to argue that brittle faults are significantly weaker than would be predicted from Byerlee's Law. The first argument for fault weakness is the relatively small post-seismic stress drops recorded after earthquakes. Static stress drops after major earthquakes range from 0.1 to 10 MPa, whereas the theoretical stress drops would be on the order of 100's of MPa (Kanamori & Anderson, 1975; Kanamori, 1994). The second argument for fault weakness is the lack of

significant frictional heating as measured by heat anomalies. Conductive heat flow measurements in the vicinity of the San Andreas Fault suggest that the fault is not generating any significant heat, whereas significant frictional heating would be predicted for the coefficients of friction from Byerlee's Law ( $\mu = 0.6 - 0.85$ ) (Brune et al., 1969; Lachenbruch & Sass, 1982). Note that convective cooling by fluids has been advanced as an alternative explanation for this heat flow paradox (e.g., Scholz, 2002). The third line of evidence for anomalous fault weakness is the discovery that the direction of the maximum principle horizontal stress in the vicinity of active faults, such as the San Andreas Fault, is nearly perpendicular to the fault (Zoback, 1987; Mount & Suppe, 1987; Zoback et al., 2007). A maximum principle stress at high angles to the fault requires that the coefficient of friction on the fault for slip to occur is very low ( $\mu = \sim 0.1$ ). The fourth argument for fault weakness is the existence of normal faults that slip at dips  $< 30^\circ$  (Longwell, 1945, Armstrong, 1972, Wernicke, 1981; John & Foster, 1993; Wernicke, 1995; Campbell-Stone et al., 2007). Coulomb's empirical law for shear fracture argues that normal faults should not form at dips below  $50^\circ$ , and the Amonton-Coulomb friction law for sliding along faults predicts that the crust should fracture along new higher-angle faults instead of slipping along existing low-angle faults. Many normal faults in the Basin and Range and elsewhere, however, show compelling field evidence for slip at dips below  $30^\circ$  (e.g. John & Foster, 1993; Campbell-Stone et al., 2007). It thus seems that major brittle faults do not behave as predicted by rock mechanics experiments and theory. This motivated the research focus on the properties of brittle fault rocks, particularly clay-rich fault rocks, as they may offer an explanation for the abundant field observations of fault weakness.



## Previous study of clay gouges

The properties of rocks within major fault zones have received increasing attention as a possible explanation for anomalously weak faults (e.g. Wu et al., 1975; Wu, 1978; Rutter et al., 1986; Chester & Logan, 1987; Chester et al., 1993; Evans and Chester, 1995; Chester & Chester, 1998, Vrolijk & van der Pluijm, 1999; Cladouhos, 1999; Cowan, 1999, Schulz & Evans, 2000; Cowan et al., 2003; Solum et al., 2003, 2005, Hayman et al., 2004; Numelin et al., 2005; Hayman, 2006; Schleicher et al., 2006). However, most studies have focused only on the physical description, properties and bulk geochemistry of brittle fault rocks. Relatively few studies have focused on the clay minerals and, especially, clay mineral transformations in fault gouges (e.g. Vrolijk & van der Pluijm, 1999, van der Pluijm et al., 2001; Solum et al., 2003, 2005, Casciello et al., 2004; Hayman, 2006, Schleicher, 2006). The recognition that the growth of authigenic clay may be an important process in the evolution of faults in the brittle regime ( $<<300\text{ }^{\circ}\text{C}$ ), and not just a product of local alteration, is relatively recent (Vrolijk & van der Pluijm, 1999), and has opened up new avenues for understanding fault zone processes and new insights in the ongoing debate concerning the frictional strength of brittle faults (e.g., Rice, 1992, Scholz, 2000). Reaction-softening of faults as a mechanism for reducing the coefficient of friction of faults has been proposed previously (Wintsch et al., 1995), but studies that document specific clay mineral transformations in gouges are surprisingly few (Vrolijk & van der Pluijm, 1999, van der Pluijm et al., 2001; Solum et al., 2003, 2005, Casciello et al., 2004, Schleicher, 2006; Haines & van der Pluijm, 2008, Appendix A). Identifying the various clay mineral transformations that are common to fault gouges in differing tectonic environments is, therefore, a key first step to understanding the role of clay mineralogy in the mechanics of brittle faults, particularly in faults that apparently slip at mechanically unfavorable orientations, and is a central goal of this thesis.

## **Objectives of the dissertation**

The dissertation has four overlapping objectives: 1.) mineralogical, to provide an overview of the spectrum of clay mineral transformations in natural faults, 2.) kinematic, to constrain fabrics in clay gouges, 3.) methodological, to further develop the techniques of dating authigenic mineralization in clay gouge, and 4.) evolutionary, to use the age of clay gouges to test hypotheses of the evolution of regions.

The mineralogic objective of the research is examined in Chapters 2, 4, 5, 6, and Appendix A. While studies increasingly identify mineral transformations in brittle faults (e.g. Vrolijk & van der Pluijm, 1999; Warr & Cox, 2001; Solum et al., 2003, 2005; Casciello et al, 2004; Solum & van der Pluijm, 2004; Schleicher et al., 2006), most all have characterized fault rocks from an individual fault, and as such, our understanding of the spectrum of mineral transformations in brittle fault rocks is fragmentary and disconnected. Chapter 2 is a mineralogical survey of gouges from a class of faults, low-angle normal faults, while Chapters 4, 5, and 6 build on this characterization by dating neoformed illite in fault gouges. A summary discussion of the spectrum of clay transformations in brittle fault rocks is found in the Conclusions. The kinematic aspects of fabric development in clay gouge are described in Chapter 3. The methodological aspects of the thesis, particularly improvements in polytype quantification, are addressed in Chapter 4, while a new approach to gouge dating applicable to illite-rich gouges where the detrital precursor mineral is not obvious, is explained in Chapter 6. The evolutionary aspects of the thesis work are addressed in Chapters 5 and 6, where regional histories of the Ruby Mountains in Nevada and the Spanish Pyrenees are tested.

## Outline of dissertation

Chapter 2 which will be submitted to the *American Journal of Science*, provides the rationale for the study. The chapter is a detailed XRD study of the clay mineralogy of low-angle normal faults, examining the fault rocks of low-angle normal faults as a class. Gouge samples from 30 outcrops of 17 different low-angle normal faults from the southwestern US and northern Mexico were examined by XRD and several key mineral transformations are found to occur in clay gouges separated both in space and time. Gouges dominated by detrital minerals derived from the wallrock and gouges dominated by authigenic mineralization are both identified. Three major series of transformations are observed: 1.) An early detrital chlorite-rich assemblage being transformed to a chlorite-smectite and discrete smectite assemblage in a process analogous to retrograde diagenesis. 2.) Alteration of the detrital chlorite-rich assemblage to a very Mg-rich low-temperature (<150 °C) assemblage of palygorskite, or sepiolite, lizardite and talc. 3.) Growth of authigenic illite, either from dissolution of detrital mica, or from dissolution of detrital K-feldspar. As detrital gouges are preserved in many low-angle normal faults, but some low-angle normal faults lack clay gouges entirely, clay mineral transformations can be important in facilitating slip at low dips, but cannot alone be invoked to explain low-angle normal fault slip.

Chapter 3, which will be submitted to the *Journal of Geophysical Research* (Haines, van der Pluijm, Ikari, Saffer & Marone), examines the intensity of clay fabric orientation in fault zones as determined by X-ray texture goniometry (XTG), including many samples characterized mineralogically in Chapter 2. The anisotropy of clay fabrics in brittle fault zones has been posited as a mechanism for localized fault zone weakening. The

chapter examines the intensity of clay fabrics from several natural brittle fault zones and in experimentally produced samples that were subject to compression and shear. Samples from low-angle normal faults were combined with previously published data from thrust faults and strike-slip faults to build a picture of fabric intensity from faults in a variety of tectonic settings and with varied mineralogical compositions. Experimental gouges were also measured, after being sheared at a variety of normal stresses, shear strains, and clay contents. Clay gouges in natural fault zones from a variety of geologic environments are found to have uniformly weak fabrics, regardless of tectonic environment or of clay mineralogy. Clay fabric intensities in artificially-sheared clay-quartz mixtures are found to be similar to those found in natural gouges, but to increase systematically with increasing normal stress and shear strain. Total clay content does not significantly affect fabric strength. The chapter demonstrates that weak fabrics in clay-rich gouges are ubiquitous and that, if anisotropic fault zone permeability causes fault weakening, this anisotropy must be a transient feature that is not preserved. The chapter also argues from the experimental natural datasets that very intense clay fabrics can only be generated by clay mineral growth and cannot be generated solely by mechanical means.

Chapter 4, published as Haines & van der Pluijm (2008) in the *Journal of Structural Geology*, uses the widespread growth of the low-temperature  $1M_d$  polytype of illite in gouge documented in Chapter 2 to develop a robust technique for dating  $1M_d$  illite in gouge. The approach has yielded promising earlier results (Ylagan, 2002, Solum et al, 2005, Solum & van der Pluijm, 2007), but had not been systematically developed. The chapter presents a description of the polytype quantification methodology of dating authigenic illite and its application to gouge formation in a Miocene metamorphic core complex detachment fault in northwest Mexico. The chapter demonstrates that the

relative abundance of the two common polytypes of illite in artificially-prepared mixtures can be successfully quantified using synthetic XRD patterns calculated using WILDFIRE©, a computer program that calculates 3-dimensional XRD patterns for clay minerals. The quantification approach is then applied to gouge from the Sierra Mazatàn detachment fault in Sonora, Mexico. The ages of both authigenic illite and detrital illite are determined, and the age of the detrital component of the gouge is shown to be the same as that of the footwall granite, as established by published Ar-Ar ages from K-feldspar in the vicinity of the detachment (Wong & Gans, 2003). Besides direct dating of deformation, the work is also significant as the age of the detrital component had not yet been shown to be geologically meaningful. The chapter conclusively demonstrates that both the age of illite in gouge and in wall rock can be reliably determined.

Chapter 5, which will be submitted in shortened form to *Geology*, applies the gouge-dating technique to authigenic illite in a series of thrust faults in the south-central Pyrenees in Spain. The ages of fault gouges are used to evaluate the 'critical wedge hypothesis' for thrust belt evolution. Two transects of faults were sampled, a set across the south-central Pyrenees and a set of closely-spaced faults in the southeastern Pyrenees. Evidence for both in-sequence thrusting and out-of-sequence thrusting are found. The fault gouge ages indicate that thrusting in parts of the Pyrenees occurred in 'pulses', with a late Cretaceous, latest Paleocene, to earliest Eocene event and a major mid-to-late Eocene thrusting event. It also shows that forward progression of faulting occurs elsewhere in the orogenic foreland. Building on work presented in Chapter 4, the age of the detrital component of the gouges is directly related to the provenance of the detrital micas in the wallrock sediments, which indicates a Hercynian provenance for much of the sediment in the southern Pyrenean foreland basin.

Chapter 6, which will be submitted to *Tectonics*, characterizes and dates authigenic illite in the detachment fault system of the Ruby Mountains metamorphic core complex in Nevada. The ages of fault gouges from a suite of kinematically-linked normal faults with contrasting dips place constraints on the evolution of the detachment fault and in particular in evaluating the controversial rolling hinge hypothesis for low-angle normal fault evolution. The Ruby Mountains are unusual among metamorphic core complexes in that both the main detachment fault and high-angle faults that sole into the detachment are exposed, all contain gouges that are amenable to dating. The observed overlap of ages leads to the conclusion that all faults were active coevally as part of a kinematically-linked detachment fault system. The ages also indicate that the fault system could not have rotated significantly, as the high-angle fault (current dip 52°) could not have formed as a normal fault at dips much above 70°. Post-faulting rotation of the low-angle detachment (current dip ~10°), therefore, implies a fault dip of  $\leq 30^\circ$  at the time of slip. The overlap of all three gouge ages indicates slip at a low dip on the main detachment that is not consistent with the passage of a 'rolling hinge'. The chapter also outlines a new approach to dating authigenic illite/smectite in gouges where a clear change in the percentage of illite in illite-smectite between various size fractions is not apparent. The authigenic illite-rich I/S phase is isolated by centrifugation and the XRD patterns are modeled using WILDFIRE<sup>®</sup> to demonstrate that the isolated I/S is monomineralic and entirely of one polytype. The I/S is then dated by Ar-Ar methods.

Appendix A is an overview of the mineralogy of a suite of gouges collected during two field seasons from the Rwenzori Mountains of Uganda in the East African Rift Valley. This represents a significant field effort, but ultimately unsuccessful project toward dating the timing of rift-flank uplift in this area. The Appendix documents brittle fault rocks that primarily formed in the upper 2-3 km of the crust, which is too shallow to contain many of

the transformations in fault rocks that are exhumed from greater depth. Field data associated with the collection of these samples and a 2-dimensional numerical model for rift propagation will be published as Koehn, Saccau, Haines, & Aanyu, (2008) in *Tectonophysics*.

#### Summary of research goals

- The thesis describes the mineralogy of clay-rich fault gouges from a variety of geological environments, both extensional and compressional, and in particular describes the prevalence of clay mineral transformations in fault gouge.
- The thesis quantifies the intensity of clay fabrics and compares them to fabric intensities of other phyllosilicate-rich rocks.
- The thesis documents the growth of the low-temperature  $1M_d$  polytype of illite in gouges from several geologic environments and develops a robust fault-dating method. A solution toward dating illite-rich gouges where the detrital phase is not obvious is also outlined.
- The thesis applies direct dating of fault gouge to two regional problems: 1.) The kinematic evolution of the foreland fold-and-thrust belt of the Spanish Pyrenees and 2.) The dip of a low-angle normal fault system in the Ruby Mountains, Nevada, at the time of slip and evolutionary models for this setting, as constrained by the relative ages of various faults in that system.

## References

- Armstrong, R., (1972). Low-angle (denudation) fault, hinterland of the Sevier orogenic belt, eastern Nevada and western Utah. *Geological Society of America Bulletin* 83, p. 1729-1754
- Brune, J., Henyey, T., & Roy, R., (1969). Heat flow, and rate of slip along the San Andreas Fault, California. *J. Geophysical Research* 14, pp. 3,821-3,827.
- Buck, W. (1988) Flexural rotation of normal faults, *Tectonics* 7, pp. 959-973.
- Byerlee, J. (1978). Friction of rocks. *Pure and Applied Geophysics* 116, 615-626.
- Campbell-Stone, E., John, B., Foster, D., Geissman, J. & Livaccari, R., (2000). Mechanisms for accommodation of Miocene extension: Low-angle normal faulting, magmatism, and secondary breakaway faulting in the southern Sacramento Mountains, southeastern California. *Tectonics*, 19, pp. 566-587
- Casciello, E., Ceserano, M., & Cosgrove, J., (2004). Shear deformation of pelitic rocks in a large-scale natural fault. *In: Flow processes in faults and shear zones, eds: Alsop, G., Holdsworth, R., McAffery, K. & Hand, M. Geological Society, London Special Publications 224*, pp. 113-125.
- Chester, F., & Chester, J., (1998). Ultracataclastic structure and friction processes of the Punchbowl fault, San Andreas system, California. *Tectonophysics* 295, pp. 199-221.
- Chester, F., Evans, J., & Biegel, R., (1993). Internal structure and weakening mechanisms of the San Andreas Fault. *J. Geophysical Research B* 98, pp. 771-786.
- Chester, F. & Logan, J., (1987). Composite planar fabric of gouge from the Punchbowl Fault, California. *J. Structural Geology* 9, pp. 621-634.
- Cladouhos, T., (1999), Shape preferred orientations of survivor grains in fault gouge. *J. Structural Geology* 21, p. 419-436.
- Cowan, D., Cladouhos, T., and Morgan, J., (2003), Structural geology and kinematic history of rocks formed along low-angle normal faults, Death Valley, California. *Geological Society of America Bulletin* 115, p. 1230-1248.
- Cowan, Darrel S., (1999), Do faults preserve a record of seismic slip? - a field geologist's opinion. *J. Structural Geology* 21, p. 2703-2719.
- Cowan, D., and Miller, M., (1999), Distributed flow vs. localized slip in late Cenozoic low-angle fault zones, Death Valley, California. *Seismological Research Letters* 70, p. 247.



- Evans, J., & Chester, F., (1995). Fluid-rock interaction in faults of the San Andreas system: Inferences from San Gabriel fault rock geochemistry and microstructures. *J. Geophysical Research B* 100, pp. 13,007-13,020.
- Haines, S., & van der Pluijm, B., (2008). Clay quantification and Ar-Ar dating of synthetic and natural gouge. *J. Structural Geology* 30, pp. 525-538.
- Hayman, N., Housen, B., Cladouhos, T. & Livi, K., (2003a). Magnetic and clast fabrics as measurements of grain-scale processes within the Death Valley shallow crustal detachment faults. *J. Geophysical Research B* 109, doi:10.1029/2003JB002902.
- Hayman, N., (2006) Shallow crustal fault rocks from the Black Mountain detachments, Death Valley, CA. *J. Structural Geology*, 28, pp. 1767-1784.
- John, B. & Foster, D., (1993). Structural and thermal constraints on the initiation angle of detachment faulting in the southern Basin and Range: The Chemehuevi Mountains case study. *Geological Society of America Bulletin* 105, pp. 1091-1108.
- Kanamori, H. and Anderson, D. (1975). Theoretical basis of some empirical relations in seismology. *Bulletin of the Seismological Society of America* 65, 1073-1095.
- Kanamori, H. (1994). Mechanics of earthquakes. *Annual Reviews of Earth and Planetary Science* 22, 207-237.
- Lachenbruch, A. & Sass, J., (1980). Heat flow and energetics of the San Andreas fault zone. *Journal of Geophysical Research B*, 85, pp. 6,185-6,222.
- Longwell, C., (1945). Low-angle normal faults in the Basin and Range province. *American Geophysical Union Transactions* 26, pp. 1087-1118.
- Lyell, C., (1851). A manual of elementary geology. John Murray, London.
- Mount, V. and Suppe, J. (1987). State of stress near the San Andreas fault: Implications for wrench tectonics. *Geology* 15, 1143-1146.
- Numelin, T., Marone, C. & Kirby, E., (2005) Frictional properties of natural fault gouge from a low-angle normal fault, Panamint Valley, CA. *Tectonics* 26, doi:10.1029/2005TC001916
- Reed, J., (1964). Mylonites, cataclasites and associated rocks along the Alpine Fault, South Island, New Zealand. *New Zealand Journal of Geology and Geophysics* 7, pp. 645-684.
- Rice, J. (1992). Fault stress states, pore pressure distributions, and the weakness of the San Andreas Fault. *In: Fault Mechanics and Transport Properties of Rocks; a Festschrift in Honor of W. F. Brace* (edited by Evans, B. and Wong, T.-F.). Academic Press, San Diego, CA, pp. 475-503.

- Rutter, E., Maddock, R., Hall, S., & White, S., (1986). Comparative microstructures of natural and experimentally produced clay-bearing fault gouges. *Tectonophysics* 124, pp. 3-29.
- Schleicher, A., van der Pluijm, B., Solum, J., & Warr, L., (2006). Origin and significance of clay-coated fractures in mudrock fragments of the SAFOD borehole (Parkfield California). *Geophysical Research Letters* 33, L16313, doi:10.1029/2006GL026505, 2006
- Scholz, C. (2000). Evidence for a strong San Andreas fault. *Geology* 28, 163-166.
- Schulz, S., & Evans, J., (2000). Mesoscopic structure of the Punchbowl Fault, southern California and the geologic and geophysical structure of active strike-slip faults. *J. Structural Geology* 22, pp. 913-930.
- Sibson, R., (1977). Fault rocks and fault mechanisms. *J. Geological Society of London* 133, pp. 191-213.
- Solum, J., van der Pluijm, B. & Peacor, D. (2003) Influence of phyllosilicate mineral assemblages, fabrics and fluids on the behavior of the Punchbowl Fault, southern California. *J. Geophysical Research B* 108, doi: 10.1029/2002JBG001858.
- Solum, J., van der Pluijm, B. & Peacor, D. (2005) Neocrystallization, fabrics and age of clay minerals from an exposure of the Moab Fault, Utah. *J. Structural Geology* 27, pp. 1563-1576.
- Solum, J., van der Pluijm, B., (2007). Reconstructing the Snake River/Hoback Canyon segment of the Wyoming thrust Belt through direct dating of fault rocks. In *Whence the Mountains? Inquiries into the Evolution of Orogenic Systems: A volume in honor of Ray Price. Geological Society of America Memoir* 433, pp. 183-196.
- van der Pluijm, B., Hall, C., Vrolijk, P., Pevear, D., Covey, M., (2001). The dating of shallow faults in the Earth's crust. *Nature* 412, pp. 172-175.
- Vrolijk, P. and van der Pluijm, B. (1999) Clay gouge. *J. Structural Geology* 21, 1039-1048.
- Waters, A., & Campbell, C., (1935). Mylonites from the San Andreas Fault Zone. *American Journal of Science* 29, pp. 473-503.
- Warr, L., & Cox, S., (2001). Clay mineral transformations and weakening mechanisms along the Alpine Fault, New Zealand. In: *The nature and significance of fault zone weakening. Geological Society, London, Special Publications* 186, pp. 85-103.
- Wernicke, B., (1981). Low-angle normal faults in the Basin and Range province: Nappe tectonics in an extensional orogen. *Nature* 291, pp. 645-648.

- Wernicke, B. (1995) Low-angle normal faults and seismicity: A review. *J. Geophysical Research B* 100, pp. 20,159 – 20,174
- Wernicke, B. & Axen, G. (1988) On the role of isostasy in the evolution of low-angle normal fault systems. *Geology* 16, pp. 848-851.
- Williams, C., Grubb, F., and Galanis, S., (2004). Heat flow in the SAFOD pilot hole and implications for the strength of the San Andreas Fault. *Geophysical Research Letters* 31, L15S14, doi:10.1029/2003GL019352.
- Wintsch, R., Christofferson, R., & Kronenberg, A., (1995). Fluid-rock weakening of fault zones. *J. Geophysical Research B* 100, pp. 13,021-13,032.
- Wu, F., (1978). Mineralogy and physical nature of clay gouge. *Pure and Applied Geophysics* 116, pp. 655-689.
- Wu, T., Blatter, L., & Roberson, H., (1975). Clay gouges in the San Andreas Fault System and their possible implications. *Pure and Applied Geophysics* 113, pp. 87-95.
- Ylagan, R. Kim, C., Pevear, D., Vrolijk, P., 2002. Illite polytype quantification for accurate K-Ar determination. *American Mineralogist* 87, 1536-1545
- Zoback, M.D., Zoback, M. L., Mount, V., Suppe, J., Eaton, J., Healy, J., Oppenheimer, D., Reasenberg, P., Jones, L., Raleigh, C., Wong, I., Scotti, O., & Wentworth, C. (1987). New evidence on the state of stress of the San Andreas fault system. *Science* 238, 1105-1111.
- Zoback, M., Hickman, S., Boness, N., Weiserberg, T., Erzinger, J., (2007). Stress and pore pressure within and near the San Andreas Fault in Central California: observations from SAFOD and the surrounding crust related to the mechanics of faulting. *Geological Society of America abstracts with programs* 39, no. 6, pp.421.

## CHAPTER 2: THE MINERALOGY OF CLAY-RICH GOUGES IN LOW-ANGLE NORMAL FAULTS: THE NATURE AND SIGNIFICANCE OF CLAY MINERAL TRANSFORMATIONS

### Abstract

The existence of low-angle normal faults (LANFs) is among the most perplexing problems in structural geology, as slip on low-dipping normal faults violates widely-held assumptions about fracture mechanics, rock friction, and the strength of faults. Although mylonitic faults rocks and breccias found in LANFs have been extensively described, the mineralogy of clay-rich gouges and any mineral transformations in gouge remain relatively unknown. We therefore present a systematic XRD study of clay gouges from 30 outcrops of 17 detachment faults ranging from the Ruby Mountains in northeastern Nevada to the Sierra Mazatán metamorphic core complex in northwestern Mexico, with an emphasis on faults in the Death Valley area of California and the Colorado River extensional corridor in SE California and Arizona. Low-angle faults that evolved from a plastic mid-crustal shear zone and detachments that formed in the brittle regime were both sampled. Extensive clay mineral transformations were observed in one or more clay horizons in 29 of the 30 faults sampled; only one outcrop preserved a detrital gouge that was formed by cataclasis only. Transformations observed are of three general categories: 1.) 'Retrograde diagenesis' transformations of an early, detrital chlorite-rich gouge derived from chloritic breccias in the footwalls of many detachments that formed from a mid-crustal shear zone to authigenic chlorite-smectite and saponite (Mg-rich tri-

octahedral smectite). 2.) Reaction of detrital chlorite-rich gouges with Mg-rich fluids at low temperatures (50-150 °C) that occurred late in the deformation history to produce localized lenses of one of two assemblages: sepiolite + saponite + talc + lizardite or palygorskite +/- chlorite +/- quartz. 3.) Growth of authigenic 1Md illite, either by transformation of detrital 2M<sub>1</sub> illite or muscovite, growth of authigenic illite from the dissolution of K-feldspar. Illitization of detrital illite-smectite is also observed, but is uncommon. We conclude that clay gouges from LANFs contain evidence for widespread formation of low-friction materials in fault zones that would promote reaction-weakening and slip of pre-existing detachment surfaces; however, gouge formation cannot explain slip on low-angle normal faults that lack clay-rich gouges entirely, as reported elsewhere.

## **Introduction**

The existence of normal faults with low dips (<30°) has been recognized in the field since the first years of the last century (Ransome et al, 1910, Longwell, 1945), but the low dips observed in the field are in apparent contradiction with widely accepted ideas about rock mechanics. Experimental data and rock mechanics theory predict that normal faults in the brittle regime should not form at dips <45°, and rock friction data indicate that frictional slip of most geological materials is not possible at dips <30° (Byerlee, 1978, Sibson, 1985, Collitini & Sibson, 2001). Continental low-angle normal faults (LANFs or detachment faults) are a class of faults that were first recognized in the Basin and Range of the western US in conjunction with Tertiary metamorphic tectonites (e.g. Anderson, 1971; Armstrong, 1972, Davis & Coney, 1979; Crittenden et al, 1980; Wernicke, 1981; Wernicke et al, 1988) and have since been recognized world-wide (e.g.

Froitzenheim & Eberli, 1990, Lister et al., 1991, Manatschal, et al., 1999, Martinez et al., 2001). Typically, low-angle normal faults juxtapose a mid-crustal footwall and an unmetamorphosed, usually sedimentary hangingwall. The faults usually have displacements of 10-30 km and expose a footwall of foliated and lineated mylonites that are overprinted by a distinctive ductile to brittle structural history. This history is recorded by the successive overprinting of the mylonites (if present) by a bottom-to-top series of distinctive brittle fault rock types, 1.) a chlorite-epidote rich breccia that formed at greenschist-facies conditions in a cataclastic flow regime that can be tens of meters thick, 2.) a fine-grained lithified cataclasite, frequently referred to as 'microbreccia', and 3.) clay-rich fault gouge, recording deformation at progressively higher structural levels as the footwall is exhumed. Some low-angle normal faults clearly evolved from mid-crustal shear zones (e.g. the Ruby Mts, NV, Death Valley turtlebacks, CA, Central Mojave metamorphic core complex, CA, Whipple Mts, CA, Buckskin-Rawhide Mts, AZ, Harcuvar and Harquahalla Mts, AZ, and Sierra Mazatán, Mexico – Snoke, 1980; Davis et al., 1980; Dokka & Glazner, 1982; Reynolds & Spencer, 1985; Vega Granillo & Calmus, 2003) while others lack mylonitic footwalls and evolved almost entirely in the brittle upper crust (e.g. the Chemehuevi Mts, CA, West Salton detachment, CA, Panamint Mts, CA, Dante's View low-angle normal fault, CA, Amargosa detachment, CA - John, 1987, Hodges et al, 1990; Topping, 1993, Axen & Fletcher, 1998, Chichinski, 2000).

While a voluminous literature debates the formation and mechanics of low-angle normal faults (LANFs) and their potential for seismicity (e.g. Miller et al., 1983; Spencer, 1984; Buck, 1988; Wernicke & Axen, 1988; Spencer & Chase, 1989; Yin, 1989; Liavaccari et al, 1993; Lister & Baldwin, 1993; Wernicke, 1995; Axen & Bartley, 1997; Collettini & Simpson, 2001; Axen, 2004; Walker et al, 2006; Christe-Blick et al, 2007), surprisingly

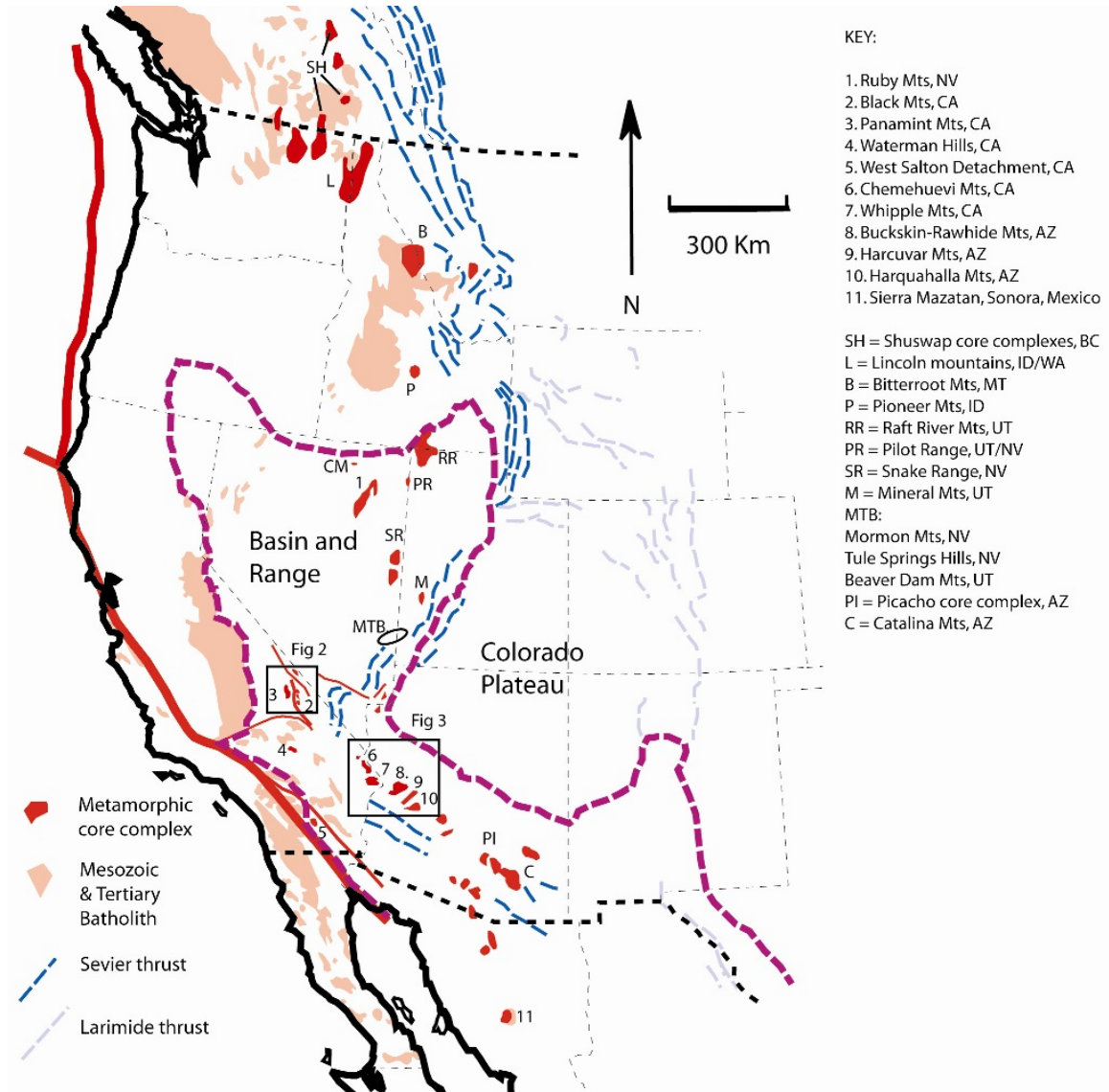
little attention has been paid to the mineralogy of the brittle fault rocks found within these structures. Many gouge zones in low-angle normal faults are clay-rich, and clays are an important component in the physical behaviour of brittle fault systems (e.g. Vrolijk, 1990; Saffer et al., 2001; Brown et al., 2003; Saffer & Marone, 2003; Schleicher et al., in press). The structural geometries of clay-rich fault rocks from a suite of faults in the Death Valley area have been extensively described (e.g. Cladahou, 1999; Cowan, 1999; Cowan et al., 1999, Hayman et al., 2003a) and other work has focused on the geochemistry and particle size distribution of low-angle normal fault gouges (Hayman, 2006), along with mineralogical data, but the clay mineral assemblages of low-angle normal faults and, in particular, any patterns of authigenic mineral growth remain unclear. The clay mineralogy of low-angle normal faults can have important implications for the frictional properties of fault zones. Chlorite and illite both have frictional strengths of  $\mu = 0.25 - 0.55$ , significantly lower than the  $0.6 - 0.8$  assumed from Byerlee's law, and pure smectite has reported frictional strengths as low as  $\mu = 0.14$  (Scholz, 2002, Brown, 2003). Frictional experiments on clay-rich low-angle normal fault gouges indicate frictional strengths of  $\mu = 0.41 - 0.52$  (Numelin et al., 2005). If low-friction clay minerals can be shown to be growing in the fault zone at the time of slip, they can thus change the frictional properties of the fault zone and allow lower dips during slip. This study examines the clay mineralogy of a suite of low-angle normal faults in the western and southwestern US, collected from 32 exposures of a total of 17 detachments ranging from the Ruby Mountains metamorphic core complex in NE Nevada to the Sierra Mazatàn metamorphic core complex in Sonora, Mexico. We show the presence of both detrital and authigenic minerals in clay gouges and demonstrate patterns of clay mineral transformations in gouges that are common to low-angle normal faults and metamorphic core complex detachments throughout the US southwest of widely varying ages and wall

rock compositions. These mineral transformations give novel insights into the conditions in the fault zone during gouge formation.

### **Geological setting and sample locations**

Low-angle normal faults and metamorphic complexes are found in a discontinuous band extending from southeastern British Columbia in the north through the Cordillera and into the eastern Basin and Range to northwestern Mexico in the south. Exhumation occurred during the Eocene in the northern metamorphic core complexes (north of the Idaho border) and during the Oligocene and Miocene in the central and southern portions of the belt (Axen et al., 1993). The youngest exhumation is in the Death Valley area where low-angle faults as young as Pleistocene are preserved (Axen et al, 1993). As reconnaissance work for this study and previous work indicates that many of the northern core complexes north of the Ruby Mountains in Nevada have brittle fault rocks that are dominated by lithified cataclasites, this work focused on the southern metamorphic core complexes where clay gouges are frequently exposed. A total of 17 detachment faults were sampled in this study at 30 outcrops, collecting and characterizing a total of 57 gouge samples, 29 hangingwall samples and 39 footwall samples (see Figure 2.1 and Tables 2.1 & 2.2 for locations and descriptions of the lithologies).





**Figure 2-1:** Schematic map of the western US showing major tectonic features and the location of detachment faults sampled in this study (numbered) and other detachment faults mentioned in the text. Redrawn and modified from Davis & Coney, (1979).

| <b>Detachment fault</b>     | <b>Range</b>                   | <b>Sample locality</b>              | <b>Sample</b>    | <b>Latitude</b> | <b>Longitude</b> |
|-----------------------------|--------------------------------|-------------------------------------|------------------|-----------------|------------------|
| Amargosa detachment         | Black Mts, CA                  | Klippe north of Ashford Canyon      | Ashford Klippe   | 34° 10' 8"      | 113° 40' 46"     |
| "                           | "                              | Exclamation Rock                    | Exclamation Rock | 35° 55' 11"     | 116° 32' 39"     |
| "                           | "                              | Virgin Springs Wash                 | Virgin Springs W | 35° 56' 3"      | 116° 34' 56"     |
| Badwater turtleback         | Black Mts, CA                  | Unnamed wash                        | Badwater-1       | 36° 15' 25"     | 116° 46' 29"     |
| "                           | "                              | Natural Bridge Wash                 | Badwater-2       | 36° 17' 11"     | 116° 45' 47"     |
| Buckskin-Rawhide detachment | Buckskin Mts, AZ               | "A-bomb canyon"                     | A-bomb-1         | 34° 10' 8"      | 113° 40' 46"     |
| Buckskin-Rawhide detachment | Plomosa Mts, AZ                | Plomosa Drive roadcut               | Plomosa          | 33° 48' 24"     | 114° 5' 4"       |
| Buckskin-Rawhide detachment | Rawhide Mts, AZ                | Near Swansea town site              | Swansea          | 34° 10' 8"      | 113° 50' 38"     |
| Bullard detachment          | Harcuvar Mts, AZ               | South side of Bullard Peak          | Bullard          | 34° 3' 33"      | 113° 17' 19"     |
| Bullard detachment          | Harquahalla Mts, AZ            | Ojo de Aguiilla peak                | Aguiilla         | 33° 53' 16"     | 113° 10' 41"     |
| Central Mojave core complex | Waterman Hills, CA             | Below radio towers                  | Waterman Hills   | 34° 58' 16"     | 117° 2' 31"      |
| Chemehuevi detachment       | Chemehuevi Mts, CA             | Lobeck Pass                         | Lobeck           | 34° 41' 28"     | 114° 37' 4"      |
| Copper Canyon turtleback    | Black Mts, CA                  | Unnamed wash south of Copper Canyon | Copper           | 36° 7' 28"      | 116° 44' 34"     |
| Dante's View Fault          | Black Mts, CA                  | Dante's View road, mile 11.3        | Dante            | 36° 13' 27"     | 116° 42' 39"     |
| Emigrant Fault              | Panamint Mts, CA               | Unnamed wash on west side Tucki Mt. | Tucki            | 36° 31' 12"     | 117° 11' 12"     |
| "                           | "                              | off Wildrose Canyon road            | Wildrose         | 36° 34' 12"     | 117° 13' 34"     |
| Gregory Peak detachment     | Black Mts, CA                  | "Size 36 canyon"                    | Size 36          | 35° 57' 50"     | 116° 40' 34"     |
| Mormon Point turtleback     | Black Mts, CA                  | W side Mormon Point                 | Mormon-1         | 36° 2' 45"      | 116° 45' 39"     |
| "                           | "                              | E side Mormon Point                 | Mormon-2         | 36° 2' 37"      | 116° 44' 12"     |
| "                           | "                              | E side Mormon Point                 | Mormon-3         | 36° 2' 31"      | 116° 44' 20"     |
| Mosaic Canyon Fault         | Panamint Mts, CA               | Mosaic Canyon                       | Mosaic           | 36° 34' 12"     | 117° 8' 18"      |
| Panamint range front LANF   | Panamint Mts, CA               | South Park Canyon                   | South Park       | 36° 0' 5"       | 117° 12' 1"      |
| Ruby Mts core complex       | Ruby Mts, NV                   | Rt 231 roadcut                      | Clover-1         | 41° 3' 48"      | 115° 1' 21"      |
| "                           | "                              | Rt 229 roadcut                      | Secret-1         | 40° 52' 12"     | 115° 15' 36"     |
| "                           | "                              | Rt 229 roadcut                      | Secret-2         | 40° 52' 6"      | 115° 15' 22"     |
| "                           | "                              | Rt 229 roadcut                      | Secret-3         | 40° 51' 54"     | 115° 15' 16"     |
| "                           | "                              | Rt 229 roadcut                      | Secret-4         | 40° 51' 54"     | 115° 15' 17"     |
| Salton Sea detachment       | Santa Rosa Mts, CA             | Wonderstone Wash                    | 571              | 33° 20' 44"     | 116° 8' 12"      |
| Sierra Mazatan core complex | Sierra Mazatan, Sonora, Mexico | Near Rancho La Feliciana            | Maz-1            | 29° 9' 58"      | 110° 13' 58"     |
| Whipple detachment          | Whipple Mts, CA                | E end Whipple Wash                  | Whip-3           | 34° 21' 55"     | 114° 16' 44"     |
| "                           | "                              | E end Whipple Wash                  | Whip-4           | 34° 22' 2"      | 114° 16' 47"     |
| "                           | "                              | E end Whipple Wash                  | Whip-5           | 34° 22' 8"      | 114° 17' 11"     |

**Table 2-1:** Sample locations and sample names used in this study.

| Detachment fault                     | Outcrop          | Footwall   | Hangingwall   | Gouge   | Strike/dip | Reference                  |
|--------------------------------------|------------------|--|---|---|------------|----------------------------|
| Amargosa detachment                  | Ashford Klippe   | Yournalized coarse-grained quartzofeldspathic granite  | Indurated Pliocene polymict conglomerates   | 1-2 m of varigated reddish and greenish clayey gouge with clear P, R, and Y surfaces. Gouge was separated into size fractions. Footwall immediately below is greenish and highly altered granite which was sampled separately.                                  | 330/16W    | Wright & Troxel, (1984)    |
| Amargosa detachment                  | Exclamation Rock | Brecciated biot + musc + qtz +feldspar schistose gneiss  | Neoproterozoic Crystal Spring quartzite   | 1 m of reddish-brown clayey gouge at base of Crystal Springs. Gouge is separated from the footwall by 0.5 m of clay-rich breccia with angular clasts of footwall gneisses to 4 cm. Lense of lower clayey breccia is incorporated into upper clayey gouge. Sampl | 090/15S    | Wright & Troxel, (1984)    |
| Amargosa detachment                  | Virgin Springs W | Chloritized and brecciated granitic gneiss with abundant Fe-oxide veins  | Neoproterozoic Crystal Spring quartzite   | 0.5 m of varigated reddish and greenish clayey gouge with P foliation and clear R and Y surfaces. Sampled brownish, reddish and greenish gouges separately. Separated brownish gouge into size fractions.   | 290/40S    | Wright & Troxel, (1984)    |
| Badwater turtleback                  | Badwater-1       | Intensively chloritized friable and rubbley granitic gneiss  | Weakly indurated Pleistocene gravels with 1.5 m of fluviially re-worked ash, possibly Bishop Tuff | 0.2 m of reddish brown clayey gouge. Separated gouge into size fractions.   | 345/36W    | Hayman et al, (2003b)      |
| Badwater turtleback                  | Badwater-2       | Mylonitic brecciated chlor + qtz schist. Brecciated for 2 m below contact  | Weakly indurated Pleistocene gravels  | 0.2 m of reddish brown clayey gouge. Seperated gouge into size fractions.   | 010/26W    | Hayman et al, (2003b)      |
| Buckskin-Rawhide A-bomb-1 detachment |                  | Chlor + epi + calc tectonic breccia with angular clasts of granite and Fe-stained quartzofeldspathic mylonite to boulder size. Extensive epid + qtz + hematite veining. Breccia is 1-5 meters thick. | Fractured quartzofeldspathic granite  | Fault zone architecture is complex. The footwall contact is sharp, and overlain by 0.3 m of clayey gouge with a lower greenish layer and an upper reddish layer; each layer was sampled separately. The gouge layer is overlain by a 1-2 m thick hangingwall br | 340/15W    | Spencer & Reynolds, (1986) |
| Buckskin-Rawhide Pin-3 detachment    |                  | Chlor + epi + calc altered quartzofeldspathic gneiss   | Mezozoic limestone and dolomite   | Very poor exposure of gouge zone. Sample was collected in friable altered gneiss 3' below base of limestone and 1' above competent chloritized gneiss.  | -          | Spencer & Reynolds, (1986) |
| Buckskin-Rawhide Swansea detachment  |                  | Chlor + epi +cal + hematite schist   | Tertiary limestone  | No gouge is present at contact between limestone and schist. Intensive hydrothermal alteration and veining along contact. All three samples were collected from schist < 0.3 m below the contact with the limestone.  | -          | Spencer & Reynolds, (1986) |
| Bullard detachment                   | Bullard          | Fractured and chloritized granite  | Fractured and chloritized granite   | No outcrop of main detachment, but a shear zone sub-parallel to, and 5 m below the trace of the main detachment with 0. 3m of reddish clayey gouge does outcrop. Upper reddish layer in gouge and lower greenish unit in gouge were sampled, and red layer was  | 045/40S    | Reynolds & Spencer, (1985) |
| Bullard detachment                   | Aguilla          | Chlor + epi + calc + qtz schist  | Slicified monomict breccia with quartzite clasts  | 1.0 m complex gouge zone. Upper 0.3 m is reddish-brown and clast-rich relative to lower units. Central reddish unit is 0.2 m thick and clay-rich. Lower greenish-black unit is 0.3 m thick and clay-rich at top and transitional to fractured chlorite schist a | 330/25E    | Reynolds & Spencer, (1985) |

**Table 2-2:** Geologic and sample collection information for each of the outcrops sampled in this study.

| Detachment fault            | Outcrop        | Footwall  | Hangingwall   | Gouge   | Strike/dip | Reference                               |
|-----------------------------|----------------|---|---|---|------------|---|
| Central Mojave core complex | Waterman Hills | Miocene granodiorite  | Tertiary rhyolite   | Gouge zone is 0.5 m thick and complex. Transitions from both the footwall and hangingwall into the gouge zone are gradational. Lowest sample is from altered footwall at base of gouge zone and was separated into size fractions. The footwall is overlain by  | 020/20E    | Anderson, (2007)                        |
| Chemehuevi detachment       | Lobeck         | Proterozoic granite - chlor + epi + calc alteration for 5m below fault plane  | Massive Tertiary breccia composed of granitic clasts          | 0.5 m thick complex gouge zone. Lowest unit is 0.3 m thick and greenish. Upper unit is 0.2 m thick, reddish, clayey and is bisected by a very hard tan layer with striated surfaces. Green, red and tan layer were all sampled separately. Green layer was sepa | 310/10N    | Miller & John, (1999)                   |
| Copper Canyon turtleback    | Copper         | Chloritized dioritic gneiss and dolomite  | Indurated Pliocene polymict conglomerates                     | 2.4 m of greenish scaly gouge. Gouge was separated into size fractions.   | 345/35W    | Miller & Pavlis, (2005)                 |
| Dante's View fault          | Dante          | Miocene tuff  | Miocene rhyolite  | 1.0 m thick fault breccia zone with sharp contacts and 0.1 m thick clayey gouge near base of breccia. Gouge and breccia were sampled separately and each separated into size fractions. Breccia has striated clasts --> boulder size. Upper 5 cm of breccia zon | 090/25N    | Drews, (1963)                           |
| Emigrant Fault              | Tucki          | Neoproterozoic metapelite, thoroughly altered and sheared for 10 m below base of gouge. Top of footwall has thoroughly kaolinized pegmatitic intrusions in 10-15 m below base of gouge. Upper contact of gouge is sharp and planar. | Pliocene middle Nova formation weakly indurated conglomerates | 1.5 m thick varigated red and blackish clayey gouge with clear R & Y surfaces, P foliation, and local flow folds. Upper 10 cm and middle of gouge zone were sampled separately, and middle of gouge was separated into size fractions. Gouge and footwall are c | 355/20W    | Snyder & Hodges, (2000)                 |
| Emigrant Fault              | Wildrose       | Greenish friable chlorite schist with dolomitic marble intercallations.   | Pliocene upper Nova formation weakly indurated conglomerates  | Gouge zone is 0.5 m thick. Lower 30 cm are light yellowish brown gouge, overlain by 20 cm of dark grey clayey gouge. Dark clayey gouge was separated into size fractions  | 020/20W    | Hodges et al, (1989)                    |
| Gregory Peak fault          | Size 36        | Miocene porphyritic granodiorite, fractured and fractures cemented with Fe-oxides, but unaltered more than 5 m below contact. Top 5 m is a clayey breccia that becomes progressively clayey towards the gouge zone.                 | Pliocene weakly indurated conglomerates                       | 0.5 - 1.0 m thick clayey gouge, distinguishable into upper and lower units which were sampled separately. Outcrop pictured in Fig 3A of Hayman (2006). Upper layer is relatively clast-rich compared to lower layer and contains discrete blocks of hangingall  | 340/20W    | Wright & Troxel, (1984), Hayman, (2006) |
| Mormon Point turtleback     | Mormon-1       | Proterozoic dolomite and quartzofeldspathic gneiss.   | Pleistocene weakly indurated conglomerates                    | 20 cm clayey gouge with rounded and abraded clasts to pebble size. Gouge was separated into size fractions.   | 355/26W    | Knott, (1999), Hayman, (2006)           |
| Mormon Point turtleback     | Mormon-2       | Chlor + epi + calc altered Miocene Willow Springs diorite. Alteration extends 20m+ into footwall.   | Indurated Pleistocene - Recent conglomerates                  | 1.0 m of clayey gouge. Upper half is reddish brown and lower half is greenish. Sampled separately, and greenish gouge separated into size fractions.  | 030/28W    | Knott, (1999), Hayman, (2006)           |

**Table 2.2 (Continued)**

| Detachment fault            | Outcrop    | Footwall  | Hangingwall  | Gouge  | Strike/dip | Reference                     |
|-----------------------------|------------|---|--|--|------------|-------------------------------|
| Mormon Point turtleback     | Mormon-3   | Fractured quartzofeldspathic gneiss and dolomite. Fractured and altered 1-2 m below contact with gouge. | Indurated Pleistocene - Recent conglomerates                               | Gouge zone is 1.0 - 1.5 m thick. Lower unit is yellowish and 0.75 m thick, while upper unit is variegated dark green and dark red and scaly. Lower unit clearly truncates upper unit. Upper unit shows clear flow folding in recesses in hangingwall.            | 010/28W    | Knott, (1999), Hayman, (2006) |
| Mosaic Canyon fault         | Mosaic     | Neoproterozoic Noonday dolomite   | Neoproterozoic Stirling quartzite  | Gouge zone is 20+ meters thick. Gouge is black and shaley and was sampled near top and near base. Upper 20 meters of the footwall is sheared greenish chlorite schist with blocks of dolomite up to 3 m in size above relatively sharp contact with unaltered N  | 290/45N    | Hodges et al, (1990)          |
| Panamint range front LANF   | South Park | Altered muscovite schist  | Pleistocene-Recent fanglomerates   | 0.5 - 1.0 m thick clayey reddish and brownish gouge with abundant folds in main gouge and in recesses in the hangingwall.  | 350/20W    | Cichanski (2000)              |
| Ruby Mts core complex       | Clover-1   | Cambrian (?) amphibolite-facies marble. Stylolyzed 1-2 m below contact with gouge zone.                 | Miocene conglomerates, clasts predominantly pebble-sized carbonate clasts. | Good photo in Mueller & Snoke, (1993) and in Chapter x. Gouge zone is 1.0 m thick, upper 2/3 is dark reddish brown clayey gouge which was sampled and separated into size fractions. The lower 1/3 is yellowish-white and was sampled in two places, along the c | 020/15W    | Mueller & Snoke, (1993)       |
| Ruby Mts core complex       | Secret-1   | Mississippian Diamond Peak shale  | Miocene Humboldt Formation siltstones                                      | 0.2 m of clayey gouge. Upper greenish layer and lower brownish layer were sampled separately. Greenish layer was separated into size fractions.  | 050/45N    | Snoke & Lush (1984)           |
| Ruby Mts core complex       | Secret-2   | Mississippian Diamond Peak shale  | Miocene Humboldt Formation siltstones                                      | 0.5 m clayey gouge. Three sub-regions were sampled, an upper reddish layer, a middle greenish layer and a lower yellowish layer. Yellowish layer was separated into size fractions.  | 036/20W    | Snoke & Lush (1984)           |
| Ruby Mts core complex       | Secret-4   | Neoproterozoic or lower Paleozoic sicified carbonate mylonite   | Miocene Humboldt Formation zeolitized tuff                                 | 1.0 m clayey gouge. Three sub-regions were sampled, an upper brownish layer, a bright greenish clayey layer and a hard blackish clayey layer. The black layer was separated into size fractions.   | 030/15W    | Snoke & Lush (1984)           |
| Salton Sea detachment       | 571        | Paleozoic metasediments   | Paleozoic metasediments  | 0.2 - 0.5 m blackish clayey gouge  |            | S. Janecke, pers. comm.       |
| Sierra Mazatan core complex | Maz-1      | Fractured and sheared Eocene granite  | Cretaceous metavolcanics   | 0.5 m yellowish-brown clayey gouge. Gouge was separated into size fractions.   | 045/20W    | Wong & Gans, (2003)           |
| Whipple detachment          | Whip-3     | Miocene War Eagle megabreccia deposits.   | Miocene War Eagle megabreccia deposits.                                    | 0.5 m hard clayey gouge. Upper reddish layer and lower greenish layer were sampled separately.   | 350/36E    | Davis, (1988)                 |
| Whipple detachment          | Whip-5     | Miocene War Eagle megabreccia deposits.   | Miocene War Eagle megabreccia deposits.                                    | 1.0 m hard clayey gouge. Greenish layer was separated into size fractions  | 015/40E    | Davis, (1988)                 |

**Table 2.2 (Continued)**

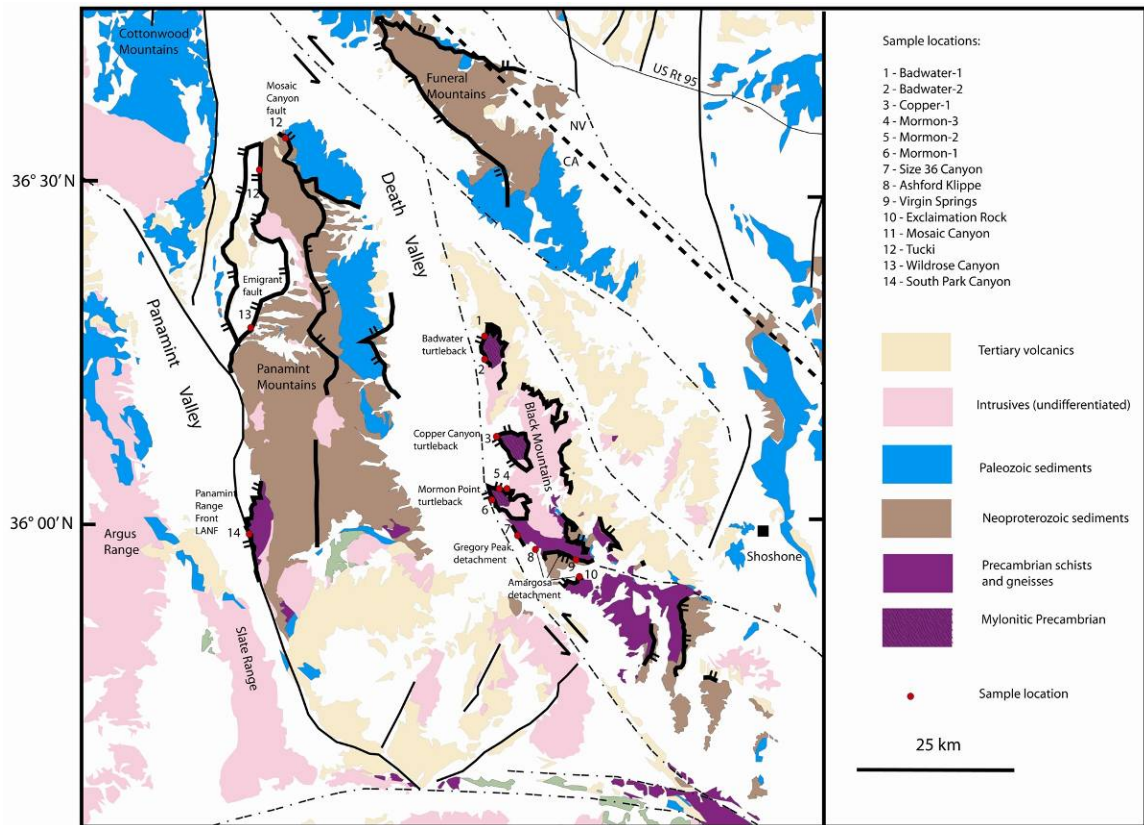
## **Regional setting**

### Ruby Mountains

The Ruby Mountains are a well-exposed core complex in northeastern Nevada (Howard, 1980, Snoke, 1980) extending ~150 km along strike from SW to NE (See Figure 2.1). The complex was exhumed by a large WNW-dipping, 1-2 km thick shear zone that strikes along the NW side of the range. The detachment was active from the late Cretaceous to the Miocene (Mueller & Snoke, 1993, McGrew & Snee, 1994, Colgan & Metcalf, 2006). The detachment fault evolved from a well-defined mid-crustal mylonite zone found in the footwall of the brittle detachment. The main detachment, an overlying brittle detachment in the hangingwall and a high-angle normal fault that soles into the main detachment are all exposed along Nevada Rt 229 (see Chapter 6 for a further discussion of the outcrops). The upper detachment and high-angle normal fault that soles into the main detachment both juxtapose siltstones against footwall shales, while the main detachment juxtaposes zeolitized tuffs against silicified carbonate mylonites in the footwall.

### Death Valley area detachments

The Black Mountains on the east side of Death Valley and the western flank of Panamint Mountains on the west side of Death Valley have a suite of spectacularly exposed low-angle normal faults that have been the source of considerable interest and controversy (see Figure 2.2). The faults record considerable extension in the Death Valley area from the Miocene to Recent, although the exact timing and magnitude of extension remain the subject of controversy (see Miller & Pavlis, 2005, for discussion). Three low-angle normal faults known as ‘turtlebacks’ are exposed along the east side of Death Valley



**Figure 2-2:** Sketch geologic map of the Death Valley area, CA showing sample locations for low-angle normal faults in the Black and Panamint mountains. Redrawn after USGS Misc. Field Studies map MF-2370.

(Curry, 1938, Wright et al., 1974, Miller & Pavlis, 2005). The Badwater, Copper Canyon, and Mormon Point turtlebacks are exposed along the east side of Death Valley, while the Gregory Peak detachment and the Amargosa Detachment (also known as the Amargosa Chaos; Noble, 1941) are exposed further to the south (Figure 2.2). Each turtleback has a distinctive turtleshell-like form with an anticlinal carapace of mylonitic mid-crustal rocks separated from a hangingwall of unmetamorphosed Miocene to Recent sediments by a ductile to brittle normal fault. The Badwater detachment was sampled at an unnamed wash near the southern edge of the detachment and at Natural Bridge. At both localities the fault juxtaposes mylonitic granite and schist in the footwall against Pleistocene gravels and fanglomerates. The Copper Canyon turtleback was sampled at the base of the turtleback, where the turtleback fault descends into Quaternary alluvium. The fault juxtaposes Pliocene conglomerates in the hangingwall against Proterozoic gneisses and marbles in the footwall. The Gregory Peak and Amargosa detachments both lack mylonites in the footwalls and apparently were active entirely in the brittle regime. The Gregory Peak detachment fault sampled at "Size 36 canyon" separates a brecciated but unmylonized granite in the footwall and Pliocene gravels in the hangingwall. The Amargosa detachment, the basal fault in the Amargosa Chaos suite of low-angle normal faults in the southern Black Mountains was sampled both in Virgin Springs Wash and at Exclamation Rock. At both outcrops the fault juxtaposes Middle Proterozoic schistose gneisses in the footwall and quartzites of the Crystal Springs formation.

Two contrasting models have been proposed for the evolution of the Black Mountains detachments. The 'rolling hinge' model interprets the turtlebacks, the Gregory Peak detachment, and the Amargosa Detachment as gigantic mullions of a single normal fault surface, or a series of kinematically linked low-angle fault surfaces that accommodated



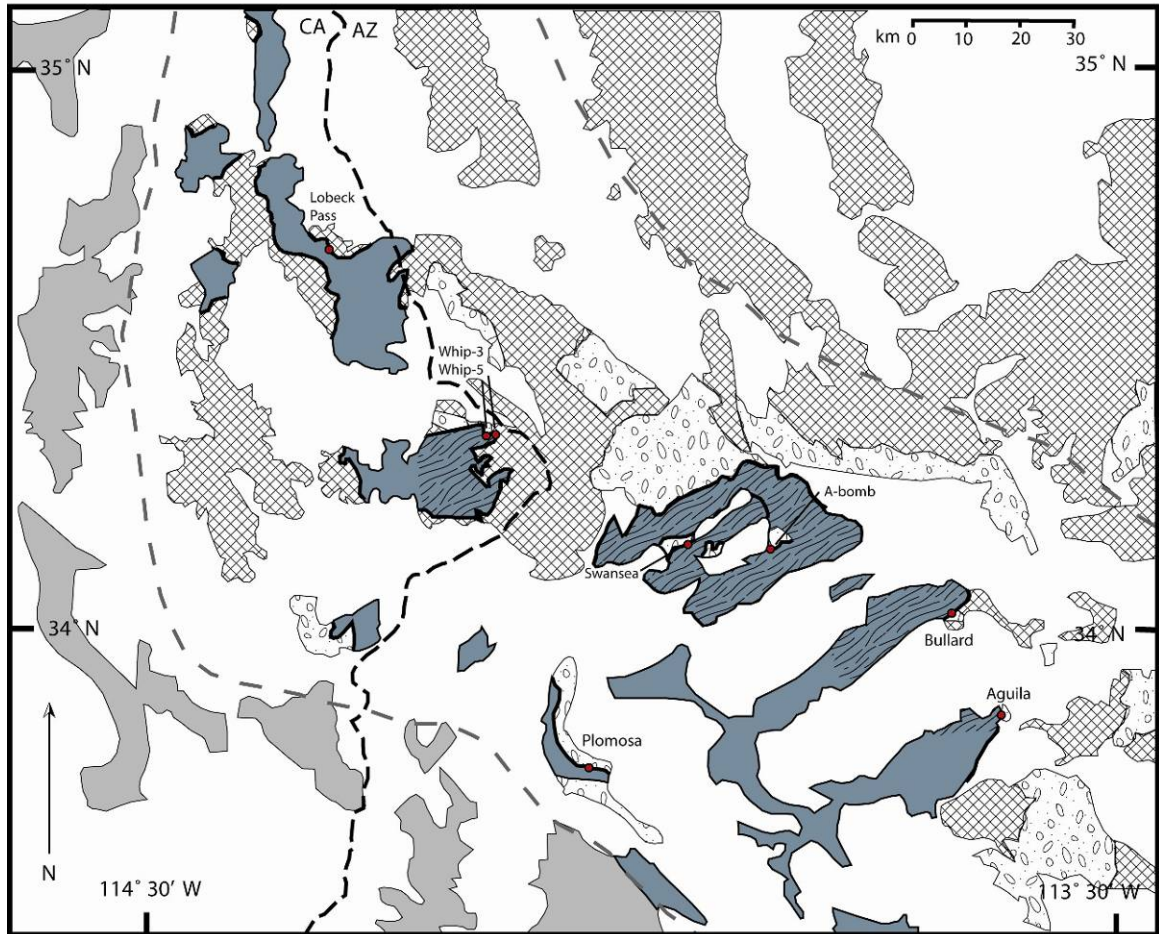
the large NW-directed displacements, transporting the Panamint Mountains off of the Black Mountains during the Miocene to their present position to the northwest (e.g., Stewart, 1983, Snow & Wernicke, 2000), and transporting the Cottonwood Mountains northwestward off the Panamint Mountains from ~12 Ma to <3.35 Ma (Hodges, et al, 1990, Snyder & Hodges, 2000). An alternate model, the 'distributed faulting model' or 'pull-apart model', views the observed large-magnitude NW-SE offset of Mesozoic and Cenozoic units accommodated by a series of distinct, deeply rooted normal faults, each with only a few km of displacement aided by an en-echelon array of similarly deeply rooted strike-slip faults (Burchfiel & Stewart, 1966, Wright et al, 1991, Serpa & Pavlis, 1996, Wright et al, 1999, Miller & Prave, 2001, Miller & Pavlis, 2005). It has recently been proposed that the Black Mountains turtlebacks mylonitic fault rocks are Cretaceous thrusts that have been reactivated as mylonite zones during the mid-Miocene, and were then reactivated in the brittle regime during the Late Miocene and Pliocene. Thus the turtleback normal faults may not be the products of continuous exhumation from plastic to brittle conditions, but rather the consequence of episodic reactivation of pre-existing discontinuities at progressively higher structural levels (Miller & Pavlis, 2005).

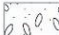

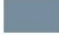


The Panamint Mountains are bounded on their west flank partially by a series of west-dipping low-angle normal faults on the eastern side of Panamint Valley that formed during the latter stages of the exhumation of the Panamint Mountains (Hodges et al., 1989, 1990). The Mosaic Canyon fault (also known as the Harrisburg Fault, Hodges et al., 1990), which dips moderately to the east and bisects the northern portion of the Panamint Mountains, has been argued to be an overturned west-dipping normal fault that may be contiguous with the Emigrant fault on the west side of the range. The Mosaic Canyon fault was sampled at Mosaic Canyon, where the fault juxtaposes Neoproterozoic metasediments (Johnnie Quartzite in the hangingwall and Noonday

Dolomite in the footwall). The Emigrant Fault was sampled in two localities, in an unnamed wash of the west side of the Panamint Mountains south of Black Point, and in the Wildrose Canyon area, south of the point where the Emigrant Fault and another low-angle detachment, the Towne Pass Fault, merge. At both outcrops, the fault juxtaposes Pliocene conglomerates of the middle Pliocene Nova Formation against Neoproterozoic metasediments in the footwall. Both the Mosaic Canyon fault and Emigrant Fault typically lack mylonitic footwalls and evolved entirely in the brittle upper crust at low dips from 11.4 Ma to < 3.3 Ma, coeval with the deposition of the supra-detachment Nova Basin (Hodges et al., 1990; Snyder & Hodges, 2000). A separate low-angle fault outcrops further south along the east side of Panamint Valley, the Panamint Valley low-angle fault (Cichanski, 2000). The Panamint Valley low-angle normal fault was sampled in South Park Canyon, where the fault dips 20° west and juxtaposes Pliocene and older Pleistocene conglomerates against a footwall of Proterozoic schists. The Panamint Valley low-angle normal fault lacks a mylonitic footwall and was apparently active entirely in the brittle regime.

#### Colorado River extensional corridor

The Colorado River extensional corridor is a 100 km x 300 km region of considerable Oligocene-Miocene extension in southeastern California and west-central Arizona straddling the Colorado River (Howard & John, 1987) (see Figure 2.3). Approximately 50 km of NE-directed extension was accommodated by a single master detachment fault or suite of faults that dips 10-20° northeast, with the footwall rocks drawn from underneath upper crustal rocks located to the northeast (Spencer & Reynolds, 1991). The region exposes five major low-angle detachment faults, two in California (Chemehuevi detachment and the Whipple detachment) and three along strike in west-central Arizona



-  = Hangingwall (sedimentary)
-  = Hangingwall (volcanic & plutonic)
-  = Footwall (undivided)
-  = Mylonitic footwall
-  = Sample location

**Figure 2-3:** Sketch geologic map of the Colorado River extensional corridor, Ca and AZ, showing sample locations for low-angle normal faults sampled in this study. Redrawn and modified after Carter et al, (2006).

(the Buckskin-Rawhide detachment, the Harcuvar detachment and the Harquahala detachment). Smaller subparallel detachments are frequently found both above and below the main detachment at each core complex. All the detachment faults share a dip  $<30^\circ$ , a top-to-the-northeast sense of shear and common timing of exhumation from 23-12 Ma (e.g. John & Foster, 1993, Carter et al, 2006), and it has been proposed that all the major exhumed footwalls are range-scale “mega-mullions” of a single detachment system (Spencer & Reynolds, 1991). The footwalls of the detachments are typically Proterozoic gneisses and schists, and Cretaceous and Miocene plutonic rocks. Footwall rocks are mylonitic in the Whipple, Buckskin-rawhide, Harcuvar and Harquahala Mountains, and unmylonized in the Chemehuevi and Sacramento Mountains and smaller ranges to the north, indicating that the central and southern portions of the Colorado River extensional corridor evolved from mid-crustal shear zones, while the northern reach was active entirely under brittle conditions and may have initiated at or near current dips  $<20^\circ$  (John & Foster, 1993, Miller & John, 1999). The Chemehuevi detachment was sampled on the north-west side of Lobeck Pass where the fault juxtaposes a post 18.5 Ma monomict megabreccia (Miller & John, 1999) against a chloritized but unmylonized 19.1 Ma granite (Foster et al, 1996). Faults kinematically linked to the Whipple detachment were sampled at the northeast corner of the core complex near where Whipple Wash reenters the hangingwall of the core complex. The main detachment is not exposed, but high-angle normal faults that sole into the main fault are well-exposed and contain clay gouge. The faults both juxtapose Miocene silicified monolithic breccias of the War Eagle mega-landslide against chloritized, but unmylonized upper-plate granites of probable Cretaceous age (Davis et al., 1980). The Buckskin-Rawhide detachment was sampled at three sites, at two poor outcrops near the ghost town of Swansea and in the Plomosa Range, respectively, and at “A-Bomb Canyon” (Spencer & Reynolds, 1986) where the fault juxtaposes a granite in the upper

plate over a chlorite tectonic breccia in the footwall. The Harcuvar detachment (the Bullard detachment *cf.* Reynolds & Spencer, 1985) was sampled north of Bullard Peak, where the detachment places Miocene conglomerates over upper Cretaceous to lower Tertiary variably mylonitic granitic rocks (Spenser & Reynolds, 1985). The Harquahala detachment was sampled on the west slope of Eagle Eye Peak where the fault places a monomict silicified breccia over chloritized and variably mylonitized schists.

#### West Salton detachment fault

The West Salton Detachment Fault is one of a suite of east-dipping Pliocene and Pleistocene low-angle normal faults on the western side of the Miocene-to-Recent Salton Trough, which forms the northern end of the Gulf of California (Axen & Fletcher, 1998). The detachment was sampled in Wonderstone Wash where the fault juxtaposes Paleozoic greenschist- and amphibolite-facies metasediments in both the hangingwall and footwall.

#### Central Mojave metamorphic core complex

The Central Mojave metamorphic core complex is exposed in the Waterman Hills, Mitchell Range and Newberry Mountains of southeastern California. The detachment accommodated 40-50 km of NE-directed extension during the early Miocene (Walker et al., 1990). The detachment fault trace trends roughly northwest-southeast and dips gently to the east. The northern and central reaches of the fault expose greenschist-facies mylonites, while the southern portion of the fault in the Newberry Mountains lacks a mylonitic footwall and probably evolved entirely in the brittle regime (Fletcher et al,

1995). The detachment fault was sampled in the northern Waterman Hills where it juxtaposes Tertiary rhyolites in the hangingwall and mylonitic granodiorite in the footwall. The temporal and kinematic relationship of the brittle fault to the mylonitic detachment is complex in that kinematic indicators associated with the brittle fault records north-south extension as opposed to the northeast-southwest extension recorded by the mylonites (Anderson, 2007).

The low-angle faults sampled for this study are of three varieties with respect to their evolution from an older mid-crustal detachment: 1.) Faults that demonstrably evolved from mid-crustal mylonitic detachments (the Ruby Mountains detachment, Whipple Mountains detachment, Buckskin-Rawhide Mountains detachment, Bullard Detachment in the Harquahala and Harcuvar Mountains), 2.) Faults that clearly evolved entirely in the brittle regime (the Mosaic Canyon Fault, Emigrant Fault, Panamint Valley low-angle normal fault, the Gregory Peak and Amargosa detachments in the Black Mountains, the Chemehuevi detachment, and the West Salton detachment), and 3.) Faults where the relationship of the brittle detachment to underlying mylonites may be ambiguous (Black Mountains turtlebacks and the Waterman Hill exposure of the central Mojave metamorphic core complex detachment).

#### Metasomatic chloritic footwall alteration

Chlorite metasomatic alteration and brecciation of the footwall extending for meters to tens to hundreds of meters below the detachment fault surface is a common feature of metamorphic core complex detachment faults (Crittenden, 1980, Kerrich, 1988). Chlorite alteration is found at all of the detachments sampled in this study that are thought to have evolved from mid-crustal shear zones (Badwater, Copper Canyon, and Mormon Point

turtlebacks, Whipple detachment, Buckskin-Rawhide detachment, Harcuvar detachment, Harquahala detachment), as well as at the Chemehuevi detachment, which mostly lacks mylonites in the footwall, although some local mylonites are described (Campbell-Stone, 2000). The chlorite metasomatic alteration is nearly always developed in footwall rocks that are dioritic or granitic in composition. Mylonitic marbles that are locally present in the footwalls of the Black Mountains and that are intercalated with extensively chloritized gneisses are unaltered. The breccias contain a distinctive assemblage of chlorite + epidote + calcite that overprints mylonitic fabrics and imparts a distinctive greenish color to the rocks. Isotopic and fluid inclusion studies indicate the alteration forms at greenschist-facies metamorphic conditions (300-350 °C, Kerrich, 1988, and 350-520 °C, Morrison & Anderson, 1998) by an influx of Fe-, Mg- and Mn-rich meteoric or igneous fluids (Smith et al., 1991, Morrison, 1998).

## **Methods**

### Sampling and clay separation

About 0.5 kg of clay gouge material was collected at each fault exposure, sampling visibly distinct regions at outcrop separately. Samples were disaggregated by soaking in water and suspended repeatedly until the sample was free of salts. The clay-sized material (<2 µm ) was separated using Stoke's law techniques. The accumulated clay fraction was centrifuged into three different size fractions, (2 µm – 0.4 µm, 0.4 µm–0.05 µm and <0.05µm) spanning roughly two orders of magnitude in grain size.

### X-ray diffraction

To characterize the main clay minerals present in each sub-region of a fault exposure, oriented clay slurry mounts of the <2 µm fraction were used. Samples were scanned

from 2-35° 2 $\theta$  (Cu-K $\alpha$ ) at a scan rate of 1°/minute, both air dried and after ethylene glycol solvation for 24 hours. The nature of illite-smectite (I/S) and the effect of any ordering (R0, R1, etc) were determined using NEWMOD (Reynolds & Reynolds, 1996). NEWMOD calculates one-dimensional XRD patterns for (00l) reflections of illite and illite-smectite (I/S) and allows the user to vary the crystallite size, the composition of the clay phase, the percentage of illite in illite-smectite (I in I/S) and the hydration state of that smectite, as well as any ordering in I/S. Once the principal clay minerals were identified, material was separated into size fractions as described above, and illitic and chloritic material was selected for polytypism analysis. As the polytype-specific peaks used to establish the polytypism of illite and chlorite are non-00l peaks and are suppressed by the oriented mounts used to identify the main clay minerals present, random sample preparations of the same material using a side-loaded sample packer (Moore & Reynolds, 1997) were used to accentuate the non-00l peaks. Illitic samples were step-scanned from 16-44° 2 $\theta$  with a step size of 0.05° and a count time of 40 seconds per step. Polytypism of chlorite was established using similar random powder sample preparations as for illitic samples, but, as the polytype-specific peaks are much stronger than those for illite, samples were scanned from 4-40° 2 $\theta$  at a scan rate of 1°/minute, following the procedures of Brindley and Brown (1980). The composition of chlorite was estimated from peak intensities from the same patterns using the technique of Brindley & Brown, (1980).

#### WILDFIRE modeling

To determine the relative abundance of the various polytypes of illite (2M<sub>1</sub> and 1M<sub>d</sub>) in each size fraction of illitic gouge identified by XRD scans of the oriented mounts, diffraction patterns from random XRD patterns of the same material were modeled using



WILDFIRE<sup>®</sup> (Reynolds, 1993). WILDFIRE<sup>®</sup> calculates three-dimensional X-ray diffraction patterns for randomly oriented grains and allows the user to experiment with many mineralogic variables to fully capture the variability of structure ordering in illites, along with allowing the user to vary the thickness of the diffracting crystallites, the randomness of the sample (also known as the Dollase factor), the percentage of interlayered smectite, its hydration state and any ordering of the illite/smectite (Reichweite) (Reynolds, 1993). This multitude of options allows for better matching of real powder patterns than early approaches that used empirical ratios of peak areas derived from a single set of standards (see summary in Dalla Torre et al., 1994).

## **Results**

30 separate fault outcrops were sampled, giving a total of 59 gouge samples as many outcrops had two or three different gouge horizons visible at outcrop. Results from XRD identification of the clay minerals present in both the various horizons of the gouge and the wall rocks of the various detachment faults are presented in Table 3. All except one of the outcrops sampled contained significant clay minerals in at least one horizon. An outcrop of the Buckskin-Rawhide detachment near Swansea, AZ had granular material that superficially resembled gouge in the field, but XRD indicated the material between the footwall and hangingwall to be a mixture of gypsum and Fe oxides. An outcrop of the Buckskin-Rawhide Mountains detachment contained clays, but it could not be definitively established in the field that the clays were from fault gouge and not soil. 29 of the gouge samples from a total of 23 outcrops were then selected for separation into size fractions. Of the 29 gouge samples separated into size fractions, 25 gouges had a different clay mineral or polytype dominating the <0.05  $\mu\text{m}$  fraction than the 2.0 – 0.4  $\mu\text{m}$  fraction (see

| Detachment fault            | Outcrop             | Sample            | Size fraction      | Clay minerals |     |            |              |                                  |                                  |     |     |   |   |   | Non-clay minerals |    |    |   |    |   |   |
|-----------------------------|---------------------|-------------------|--------------------|---------------|-----|------------|--------------|----------------------------------|----------------------------------|-----|-----|---|---|---|-------------------|----|----|---|----|---|---|
|                             |                     |                   |                    | C             | C/S | Ordering I | Polytype I/S | (R)                              | Sm                               | Sep | Pal | T | L | K | Q                 | KF | Pl | A | Ca | D | G |
| Amargosa detachment         | Ashford Klippe      | Hangingwall       | <2.0 µm            |               |     |            | x            |                                  |                                  |     |     |   | x | X | x                 | x  |    | x |    |   |   |
|                             |                     | Gouge             | 2.0 - 0.4 µm       |               |     |            | x            | 2M <sub>1</sub> /1M <sub>0</sub> |                                  |     |     |   | x | X | x                 | x  |    | x | x  |   |   |
|                             |                     | Gouge             | 0.4 - 0.05 µm      |               |     |            | X            | 2M <sub>1</sub> /1M <sub>0</sub> |                                  |     |     |   |   |   | x                 |    | x  |   | x  | x |   |
|                             |                     | Gouge             | <0.05 µm           |               |     |            | X            | 1M <sub>d</sub>                  |                                  |     |     |   |   |   |                   |    |    |   |    |   |   |
|                             |                     | Altered footwall  | <2.0 µm            |               |     |            | X            |                                  |                                  |     |     |   | x |   |                   |    |    |   |    |   |   |
|                             | Exclamation Rock    | Hangingwall       | Crushed whole rock |               |     |            |              |                                  |                                  |     |     |   |   |   |                   |    |    |   |    |   | X |
|                             |                     |                   | Gouge              | 2.0 - 0.4 µm  |     |            |              | x                                | 2M <sub>1</sub> /1M <sub>0</sub> |     |     |   |   |   |                   | X  | x  |   |    |   |   |
|                             |                     |                   | Gouge              | 0.4 - 0.05 µm |     |            |              | X                                | 2M <sub>1</sub> /1M <sub>0</sub> |     |     |   |   |   |                   | x  |    |   |    |   |   |
|                             |                     |                   | Gouge              | <0.05 µm      |     |            |              | X                                | 2M <sub>1</sub> /1M <sub>0</sub> |     |     |   |   |   |                   |    |    |   |    |   |   |
|                             |                     | Clayey breccia    | <2.0 µm            |               |     |            | X            |                                  |                                  |     |     |   | x |   |                   |    |    |   |    |   | x |
|                             | Virgin Springs W    | Footwall          | Crushed whole rock |               | x   |            | x            | 2M <sub>1</sub>                  |                                  |     |     |   |   |   | X                 | x  | x  |   |    |   |   |
|                             |                     |                   | Crushed whole rock |               |     |            |              |                                  |                                  |     |     |   |   |   |                   | X  |    |   |    |   |   |
|                             |                     | Hangingwall       | Crushed whole rock |               |     |            |              |                                  |                                  |     |     |   |   |   |                   | X  |    |   |    |   |   |
|                             |                     |                   | Greenish gouge     | <2.0 µm       |     |            |              | X                                |                                  |     |     |   |   |   |                   | x  |    |   |    |   |   |
|                             |                     |                   | gouge              | <2.0 µm       |     |            |              | X                                |                                  |     |     |   |   |   |                   | x  |    |   |    |   |   |
|                             | Badwater turtleback | Badwater-1        | Hangingwall        | <2.0 µm       |     |            |              |                                  |                                  |     |     |   |   | x |                   |    |    |   |    |   | X |
|                             |                     |                   | Gouge              | 2.0 - 0.4 µm  | x   |            |              | x                                | 1M <sub>d</sub>                  |     |     |   |   |   |                   |    | X  |   |    |   | x |
|                             |                     |                   | Gouge              | 0.4 - 0.05 µm | x   |            |              | x                                | 1M <sub>d</sub>                  |     |     |   |   |   |                   |    | X  |   |    |   | x |
|                             |                     |                   | Gouge              | <0.05 µm      |     |            |              | X                                | 1M <sub>d</sub>                  |     |     |   |   |   |                   |    |    |   |    |   |   |
| Footwall                    |                     |                   | <2.0 µm            | X             |     |            | x            |                                  |                                  |     |     |   |   |   |                   |    |    |   |    |   |   |
| Badwater-2                  | Badwater-2          | Hangingwall       | <2.0 µm            | x             |     |            | x            | 2M <sub>1</sub>                  |                                  |     | X   |   | x | x | x                 |    |    |   |    |   |   |
|                             |                     | Gouge             | 2.0 - 0.4 µm       |               |     |            | x            | 2M <sub>1</sub> /1M <sub>0</sub> |                                  |     |     |   |   |   | X                 | x  |    |   | x  |   |   |
|                             |                     | Gouge             | 0.4 - 0.05 µm      |               |     |            | x            | 2M <sub>1</sub> /1M <sub>0</sub> |                                  |     |     |   |   |   | X                 |    |    |   |    |   |   |
|                             |                     | Gouge             | <0.05 µm           |               |     |            | x            | 2M <sub>1</sub> /1M <sub>0</sub> |                                  |     | x   |   |   |   |                   |    |    |   |    |   |   |
|                             |                     | Footwall          | <2.0 µm            |               |     |            | X            | 2M <sub>1</sub>                  |                                  |     |     |   |   |   |                   |    |    |   |    | x | x |
|                             |                     | Footwall mylonite | Crushed whole rock | x             |     |            |              |                                  |                                  |     |     |   |   |   | X                 |    |    |   |    | x |   |
|                             |                     | Footwall diabase  | Crushed whole rock | x             |     |            |              |                                  |                                  |     |     |   |   |   | x                 | X  |    |   |    | x |   |
|                             |                     | Footwall diabase  | Crushed whole rock | x             |     |            |              |                                  |                                  |     |     |   |   |   |                   |    |    |   |    |   |   |
| Rawhide detachment          | A-bomb-1            | Breccia           | 2.0 - 0.4 µm       | x             |     |            | x            | 2M <sub>1</sub>                  |                                  |     |     |   |   |   | X                 | x  |    |   |    | x |   |
|                             |                     | Breccia           | 0.4 - 0.05 µm      | X             |     |            |              |                                  |                                  |     |     |   |   |   |                   |    |    |   |    |   |   |
|                             |                     | Breccia           | <0.05 µm           | X             |     |            |              |                                  |                                  |     |     |   |   |   |                   |    |    |   |    |   |   |
|                             |                     | Upper red gouge   | <2.0 µm            |               | x   | R0         |              |                                  |                                  |     | X   |   |   |   |                   |    |    |   |    |   |   |
|                             |                     | Lower green gouge | <2.0 µm            |               | x   | R0         |              |                                  |                                  |     | X   |   |   |   |                   |    |    |   |    |   |   |
|                             |                     | Footwall          | Crushed whole rock | x             |     |            |              |                                  |                                  |     |     |   |   |   |                   | X  | x  |   |    |   |   |
| Buckskin-Rawhide detachment | Plomosa             | Altered footwall  | <2.0 µm            |               |     |            | x            | 2M <sub>1</sub>                  |                                  | X   |     |   |   | x |                   |    |    |   | x  |   |   |
| Buckskin-Rawhide detachment | Swansea             | Veins             | <2.0 µm            |               |     |            |              |                                  |                                  |     |     |   |   |   |                   |    |    |   | x  | X |   |
| "                           | "                   | Footwall          | <2.0 µm            | X             |     |            |              |                                  |                                  | x   |     |   | x |   |                   |    |    |   |    |   |   |
| "                           | "                   | Footwall          | <2.0 µm            | X             |     |            | x            |                                  |                                  | x   |     |   |   |   |                   |    |    |   | x  |   |   |

**Table 2-3:** Table showing mineralogy as determined by XRD of all samples in this study. (continued on following pages). C = chlorite, C/S = chlorite/smectite, R0 = disordered, R1 = ordered, I = illite, I/S = illite/smectite, R = Reichweit (R0, R1, etc), Sm = smectite, Sep = sepiolite, Pal = palygorskite, T = talc, L = lizardite, K = kaolinite, Q = quartz, KF = K-feldspar, P = plagioclase, A = analcime, Ca = calcite, D = dolomite, G = gypsum, H/C = heulandite/clinoptilite.

| Detachment fault            | Outcrop        | Sample              | Size fraction      | Clay minerals |     |          |    |        |                                  |                 |    |     |     |   |   |   |   | Non-clay minerals |    |   |    |   |   |     |   |   |   |
|-----------------------------|----------------|---------------------|--------------------|---------------|-----|----------|----|--------|----------------------------------|-----------------|----|-----|-----|---|---|---|---|-------------------|----|---|----|---|---|-----|---|---|---|
|                             |                |                     |                    | C             | C/S | Ordering | I  | p-type | I/S                              | (R)             | Sm | Sep | Pal | T | L | K | Q | KF                | PI | A | Ca | D | G | H/C |   |   |   |
| Bullard detachment          | Bullard        | Hangingwell         | <20µm              |               | x   | R0       |    | x      | 2M <sub>1</sub>                  |                 |    |     |     |   |   | x |   |                   |    |   |    |   | x |     |   |   |   |
| "                           | "              | Upper gouge         | <20µm              |               | x   | R0       |    | X      |                                  |                 |    |     | x   |   |   |   |   |                   |    |   |    |   | x |     |   |   |   |
| "                           | "              | Upper gouge         | 20-04µm            |               | x   | R0       |    | X      | 2M <sub>1</sub> /1M <sub>1</sub> |                 |    |     | x   |   |   |   |   |                   |    |   |    |   | x |     |   |   |   |
| "                           | "              | Upper gouge         | 0.4-0.05µm         |               |     |          |    | X      | 2M <sub>1</sub> /1M <sub>1</sub> |                 |    |     |     |   |   |   |   |                   |    |   |    |   |   | x   |   |   |   |
| "                           | "              | Upper gouge         | <0.05µm            |               | x   | R0       |    | X      | 2M <sub>1</sub> /1M <sub>1</sub> |                 |    |     | x   |   |   |   |   |                   |    |   |    |   |   |     | x |   |   |
| "                           | "              | Footwall            | <20µm              |               | X   | R0       |    | x      | 2M <sub>1</sub>                  |                 |    |     | x   |   |   |   |   | x                 | x  | x |    | x |   |     |   |   |   |
| Bullard detachment          | Aquila         | Hangingwell         | <20µm              |               |     |          |    |        |                                  |                 |    |     |     |   |   |   |   |                   |    |   |    |   |   |     |   |   |   |
| "                           | "              | Upper gouge         | <20µm              |               | X   |          |    |        |                                  |                 |    |     |     |   |   |   |   |                   |    |   |    |   |   | x   |   |   |   |
| "                           | "              | Gouge               | <20µm              |               | x   |          |    | x      |                                  |                 |    |     | X   |   |   |   |   |                   |    |   |    |   |   |     | x |   |   |
| "                           | "              | Lower gouge         | <20µm              |               | x   |          |    | x      |                                  |                 |    |     | X   |   |   |   |   |                   |    |   |    |   |   |     |   |   |   |
| "                           | "              | Footwall breccia    | Crushed whole rock |               | x   |          |    |        |                                  |                 |    |     |     |   |   |   |   |                   |    |   |    |   | X |     | x |   | x |
| "                           | "              | Footwall            | Crushed whole rock |               | x   |          |    |        | x                                | 2M <sub>1</sub> |    |     |     |   |   |   |   |                   |    |   |    |   | X |     |   |   |   |
| Central Mojave core complex | Waterman Hills | Hangingwell breccia | <20µm              |               |     |          |    | x      |                                  |                 |    |     | x   |   |   |   |   |                   |    |   |    |   | X | x   |   |   |   |
| "                           | "              | Hangingwell breccia | <20µm              |               |     |          |    | x      |                                  |                 |    |     | x   |   |   |   |   |                   |    |   |    |   | X |     |   |   |   |
| "                           | "              | Grey gouge          | 20-04µm            |               |     |          |    | x      | 1M <sub>1</sub>                  |                 |    |     |     |   |   |   |   |                   |    |   |    |   | X | x   |   |   |   |
| "                           | "              | Grey gouge          | 0.4-0.05µm         |               |     |          |    | X      | 1M <sub>1</sub>                  |                 |    |     |     |   |   |   |   |                   |    |   |    |   |   | x   |   |   |   |
| "                           | "              | Grey gouge          | <0.05µm            |               |     |          |    | X      | 1M <sub>1</sub>                  |                 |    |     |     |   |   |   |   |                   |    |   |    |   |   |     |   |   |   |
| "                           | "              | Brownish gouge      | <20µm              |               |     |          |    | x      |                                  |                 |    |     | X   |   |   |   |   |                   |    |   |    |   |   |     |   |   |   |
| "                           | "              | Altered footwall    | 20-04µm            |               |     |          |    | x      |                                  |                 |    |     | X   |   |   |   |   |                   |    |   |    |   |   |     |   | x | X |
| "                           | "              | Altered footwall    | <0.4µm             |               |     |          |    | x      |                                  |                 |    |     | X   |   |   |   |   |                   |    |   |    |   |   |     |   | x |   |
| Chemehuevi detachment       | Lobeck         | Hangingwell         | Crushed whole rock |               |     |          |    |        |                                  |                 |    |     |     |   |   |   |   |                   |    |   |    |   | X | x   | x |   |   |
| "                           | "              | Gouge               | <20µm              |               | x   |          |    |        |                                  |                 |    |     |     |   |   |   |   |                   |    |   |    |   |   |     |   |   |   |
| "                           | "              | Gouge               | Crushed whole rock |               | x   |          |    |        |                                  |                 |    |     |     |   |   |   |   |                   |    |   |    |   |   | x   |   | x |   |
| "                           | "              | Gouge               | 20-04µm            |               | X   |          |    |        |                                  |                 |    |     |     |   |   |   |   |                   |    |   |    |   |   |     | x | x |   |
| "                           | "              | Gouge               | 0.4-0.05µm         |               | X   |          |    |        |                                  |                 |    |     |     |   |   |   |   |                   |    |   |    |   |   |     | x | x |   |
| "                           | "              | Gouge               | <0.05µm            |               | X   |          |    |        |                                  |                 |    |     |     |   |   |   |   |                   |    |   |    |   |   |     |   |   |   |
| "                           | "              | Footwall            | Crushed whole rock |               | x   |          |    |        |                                  |                 |    |     |     |   |   |   |   |                   |    |   |    |   |   | X   | x | x | x |
| Copper Canyon turtleback    | Copper         | Hangingwell         | 20-04µm            |               | x   |          |    |        | X                                | 2M <sub>1</sub> |    |     |     |   |   |   |   |                   |    |   |    |   |   |     | x |   |   |
| "                           | "              | Gouge               | 20-04µm            |               | x   | X        | R1 |        |                                  |                 |    |     |     |   |   |   |   |                   |    |   |    |   |   |     | x |   |   |
| "                           | "              | Gouge               | 0.4-0.05µm         |               | x   | X        | R1 |        |                                  |                 |    |     |     |   |   |   |   |                   |    |   |    |   |   |     |   |   |   |
| "                           | "              | Gouge               | <0.05µm            |               | X   | R0       |    |        |                                  |                 |    |     |     |   |   |   |   |                   |    |   |    |   |   |     |   |   |   |
| "                           | "              | Footwall            | Crushed whole rock |               | x   |          |    |        |                                  |                 |    |     |     |   |   |   |   |                   |    |   |    |   |   | X   |   | x |   |
| Dante's View Fault          | Dante          | Hangingwell         | Crushed whole rock |               |     |          |    |        |                                  |                 |    |     | x   |   |   |   |   |                   |    |   |    |   |   | x   | X |   |   |
| "                           | "              | Tan horizon         | Crushed whole rock |               |     |          |    |        |                                  |                 |    |     | x   |   |   |   |   |                   |    |   |    |   |   | x   |   |   |   |
| "                           | "              | Breccia             | 20-04µm            |               |     |          |    |        |                                  |                 |    |     | X   |   | x |   |   |                   |    |   |    |   |   |     |   |   | x |
| "                           | "              | Breccia             | 0.4-0.05µm         |               |     |          |    |        |                                  |                 |    |     | X   |   | x |   |   |                   |    |   |    |   |   |     |   |   | x |
| "                           | "              | Breccia             | <0.05µm            |               |     |          |    |        |                                  |                 |    |     | X   |   | x |   |   |                   |    |   |    |   |   |     |   |   | x |
| "                           | "              | Gouge               | 20-04µm            |               |     |          |    |        |                                  |                 |    |     | X   |   | x |   |   |                   |    |   |    |   |   |     | x |   |   |
| "                           | "              | Gouge               | 0.4-0.05µm         |               |     |          |    |        |                                  |                 |    |     | X   |   | x |   |   |                   |    |   |    |   |   |     | x |   |   |
| "                           | "              | Gouge               | <0.05µm            |               |     |          |    |        |                                  |                 |    |     | X   |   | x |   |   |                   |    |   |    |   |   |     |   | x |   |
| "                           | "              | Footwall            | Crushed whole rock |               |     |          |    |        |                                  |                 |    |     | X   |   |   |   |   |                   |    |   |    |   |   |     | x | x |   |

Table 2-3 (Continued)

| Detachment fault        | Outcrop  | Sample           | Size fraction      | Clay minerals |     |          |   |                                  |                 |     |    |     |     |   | Non-clay minerals |    |   |    |    |   |    |    |   |     |   |   |
|-------------------------|----------|------------------|--------------------|---------------|-----|----------|---|----------------------------------|-----------------|-----|----|-----|-----|---|-------------------|----|---|----|----|---|----|----|---|-----|---|---|
|                         |          |                  |                    | C             | C/S | Ordering | I | p-type                           | I/S             | (R) | Sm | Sep | Pal | T | L                 | K  | Q | KF | Pl | A | Ca | D  | G | H/C |   |   |
| Erigrant Fault          | Tucki    | Hangrwell        | <20µm              | x             |     |          | X | 2M <sub>1</sub>                  |                 |     |    | x   |     |   |                   |    |   |    |    |   |    |    |   | x   |   |   |
|                         |          | Upper gouge      | <20µm              |               |     |          | X |                                  |                 |     |    |     |     |   |                   |    |   |    |    |   |    |    |   |     | x |   |
|                         |          | Lower gouge      | 20-0.4µm           |               |     |          | X | 2M <sub>1</sub> /1M <sub>2</sub> |                 |     |    |     |     |   |                   |    |   |    |    |   |    |    |   |     |   | x |
|                         |          | Lower gouge      | 0.4-0.05µm         |               |     |          | X | 2M <sub>1</sub> /1M <sub>2</sub> |                 |     |    |     |     |   |                   |    |   |    |    |   |    |    |   |     |   | x |
|                         |          | Lower gouge      | <0.05µm            |               |     |          | X | 2M <sub>1</sub> /1M <sub>2</sub> |                 |     |    |     |     |   |                   |    |   |    |    |   |    |    |   |     |   | x |
|                         |          | Altered footwell | <20µm              |               |     |          |   | x                                |                 |     |    |     |     |   |                   |    |   |    |    |   |    |    |   | x   | X |   |
|                         |          | Footwell         | <20µm              |               |     |          |   | X                                | 2M <sub>1</sub> |     |    |     |     |   |                   |    |   |    |    |   |    |    |   |     |   | x |
| Erigrant Fault          | Wildrose | Hangrwell        | <20µm              | x             |     |          | X | 2M <sub>1</sub>                  |                 |     |    | x   |     |   |                   |    |   |    |    | X |    |    |   | x   | x |   |
|                         |          | Upper gouge      | 20-0.4µm           | x             |     |          |   |                                  |                 |     | x  | R3  |     |   |                   |    |   |    |    | X |    |    |   | x   | x |   |
|                         |          | Upper gouge      | 0.4-0.05µm         |               |     |          |   |                                  |                 | X   | R3 |     |     |   |                   |    |   |    |    |   |    |    | x |     |   |   |
|                         |          | Upper gouge      | <0.05µm            |               |     |          |   |                                  |                 | X   | R3 |     |     |   |                   | tr |   | x  |    |   |    |    |   |     |   |   |
|                         |          | Lower gouge      | <20µm              |               |     |          |   |                                  |                 | X   | R3 |     |     |   |                   |    |   |    |    |   |    |    |   |     |   |   |
|                         |          | Footwell schist  | Crushed whole rock |               | X   |          |   |                                  |                 |     |    |     |     |   |                   |    |   |    |    |   |    |    | x |     | x |   |
| Gregory Peak fault      | Size 36  | Hangrwell        | <20µm              |               |     |          | x |                                  |                 |     |    | X   |     |   |                   |    | x |    |    | x |    | x  |   |     |   |   |
|                         |          | Hangrwell        | <20µm              |               |     |          | x |                                  |                 |     |    | X   |     |   |                   |    |   | x  |    |   | x  |    | x |     |   |   |
|                         |          | Upper gouge      | <20µm              |               |     |          | X | 1M <sub>2</sub>                  |                 |     |    |     |     |   |                   |    |   |    |    |   | x  |    |   |     |   |   |
|                         |          | Lower gouge      | 20-0.4µm           | x             |     |          | x | 2M <sub>1</sub> /1M <sub>2</sub> |                 |     |    |     |     |   |                   |    |   |    |    |   | X  | x  | x |     |   |   |
|                         |          | Lower gouge      | 0.4-0.05µm         |               |     |          | x | 2M <sub>1</sub> /1M <sub>2</sub> |                 |     |    |     |     |   |                   |    |   |    |    |   | X  | x  | x |     |   |   |
|                         |          | Lower gouge      | <0.05µm            |               |     |          | X | 1M <sub>2</sub>                  |                 |     |    |     |     |   |                   |    |   |    |    |   |    |    |   |     |   |   |
|                         |          | Footwell breccia | 20-0.4µm           | x             |     |          | x | 1M <sub>2</sub>                  |                 |     |    |     |     |   |                   |    |   |    |    |   |    | x  | x | X   |   |   |
|                         |          | Footwell breccia | 0.4-0.05µm         | x             |     |          | x | 1M <sub>2</sub>                  |                 |     |    |     |     |   |                   |    |   |    |    |   |    | x  | X |     |   |   |
|                         |          | Footwell breccia | <0.05µm            |               |     |          | X | 1M <sub>2</sub>                  |                 |     |    |     |     |   |                   |    |   |    |    |   |    |    |   |     |   |   |
|                         |          | Footwell         | Crushed whole rock | x             |     |          |   |                                  |                 |     |    |     |     |   |                   |    |   |    |    |   |    | X  | x | x   |   |   |
| Mormon Point turtleback | Mormon-1 | Hangrwell        | <20µm              |               |     |          | x |                                  |                 |     |    | X   |     |   |                   |    |   |    |    |   |    |    |   |     |   |   |
|                         |          | Gouge            | 20-0.4µm           |               |     |          | x |                                  |                 |     |    | x   |     |   |                   |    |   |    |    |   | x  |    | x | X   | x |   |
|                         |          | Gouge            | 0.4-0.05µm         |               |     |          | x |                                  |                 |     |    | x   |     |   |                   |    |   |    |    |   |    | x  | X | x   | x |   |
|                         |          | Gouge            | <0.05µm            |               |     |          |   |                                  |                 | X   | R0 |     |     |   |                   |    |   |    |    |   |    | tr |   |     |   |   |
|                         |          | Footwell         | Crushed whole rock | x             |     |          |   |                                  |                 |     |    |     |     |   |                   |    |   |    |    |   |    | X  | x | x   |   |   |
| Mormon Point turtleback | Mormon-2 | Hangrwell        | Crushed whole rock |               |     |          | x | 2M <sub>1</sub>                  |                 |     |    |     |     |   |                   |    |   |    |    |   | X  | x  | x |     |   |   |
|                         |          | Green gouge      | Crushed whole rock | x             |     |          |   |                                  |                 |     |    |     |     |   |                   |    |   |    |    |   |    | X  | x | x   |   |   |
|                         |          | Reddish gouge    | <20µm              | X             |     |          |   |                                  |                 |     |    |     |     |   |                   |    |   |    |    |   |    |    |   | x   |   |   |
|                         |          | Green gouge      | 20-0.4µm           | X             |     |          |   |                                  |                 |     |    |     |     |   |                   |    |   |    |    |   |    |    |   |     |   |   |
|                         |          | Green gouge      | 0.4-0.05µm         | X             |     |          |   |                                  |                 |     |    |     |     |   |                   |    |   |    |    |   |    |    |   |     |   |   |
|                         |          | Green gouge      | <0.05µm            | X             |     |          |   |                                  |                 |     |    |     |     |   |                   |    |   |    |    |   |    |    |   |     |   |   |
|                         |          | Footwell         | Crushed whole rock | x             |     |          |   |                                  |                 |     |    |     |     |   |                   |    |   |    |    |   |    | X  | x | x   |   |   |
|                         |          | Footwell         | Crushed whole rock | x             |     |          |   |                                  |                 |     |    |     |     |   |                   |    |   |    |    |   |    | X  | x | x   |   |   |
|                         |          | Footwell         | Crushed whole rock | x             |     |          |   |                                  |                 |     |    |     |     |   |                   |    |   |    |    |   |    | X  | x | x   |   |   |
|                         |          | Footwell         | Crushed whole rock | X             |     |          |   |                                  |                 |     |    |     |     |   |                   |    |   |    |    |   |    |    |   | x   |   |   |
|                         |          | Footwell         | Crushed whole rock | x             |     |          |   |                                  |                 |     |    |     |     |   |                   |    |   |    |    |   |    |    | X | x   | x |   |
|                         |          | Footwell         | Crushed whole rock | x             |     |          |   |                                  |                 |     |    |     |     |   |                   |    |   |    |    |   |    |    | X | x   | x |   |
|                         |          | Footwell         | Crushed whole rock | x             |     |          |   |                                  |                 |     |    |     |     |   |                   |    |   |    |    |   |    |    | X | x   | x |   |
| Mormon Point turtleback | Mormon-3 | Hangrwell        | Crushed whole rock |               |     |          | x | 2M <sub>1</sub>                  |                 |     |    |     |     |   |                   |    |   |    |    |   | X  | x  | x |     |   |   |
|                         |          | Upper gouge      | 20-0.4µm           | X             |     |          |   |                                  |                 |     |    |     |     |   |                   |    |   |    |    |   |    |    |   |     |   |   |
|                         |          | Upper gouge      | 0.4-0.05µm         | X             |     |          |   |                                  |                 |     |    |     |     |   |                   |    |   |    |    |   |    |    |   |     |   |   |
|                         |          | Upper gouge      | <0.05µm            | X             |     |          |   |                                  |                 |     |    |     |     |   |                   |    |   |    |    |   |    |    |   |     |   |   |
|                         |          | Lower gouge      | 20-0.4µm           | x             |     |          |   |                                  |                 |     |    | X   | x   |   |                   |    |   |    |    |   |    |    |   |     |   |   |
|                         |          | Lower gouge      | 0.4-0.05µm         |               |     |          |   |                                  |                 |     | X  | x   |     |   |                   |    |   |    |    |   |    |    |   |     |   |   |
|                         |          | Lower gouge      | <0.05µm            |               |     |          |   |                                  |                 |     | X  | x   |     |   |                   |    |   |    |    |   |    |    |   |     |   |   |
|                         |          | Footwell         | Crushed whole rock | x             |     |          | x | 2M <sub>1</sub>                  |                 |     |    |     |     |   |                   |    |   |    |    |   |    | X  | x | x   |   |   |

Table 2-3 (Continued)

| Detachment fault          | Outcrop    | Sample                     | Size fraction      | Clay minerals |     |          |    |                                  |     |     |         |     |     |    |    |   |   | Non-clay minerals |    |   |    |   |   |     |   |  |
|---------------------------|------------|----------------------------|--------------------|---------------|-----|----------|----|----------------------------------|-----|-----|---------|-----|-----|----|----|---|---|-------------------|----|---|----|---|---|-----|---|--|
|                           |            |                            |                    | C             | C/S | Ordering | I  | p-type                           | I/S | (R) | Sm      | Sep | Pal | T  | L  | K | Q | Kf                | Pl | A | Ca | D | G | H/C |   |  |
| Mosaic Canyon fault       |            |                            |                    |               |     |          |    |                                  |     |     |         |     |     |    |    |   |   |                   |    |   |    |   |   |     |   |  |
| "                         | Mosaic     | Hangingwell                | Crushed whole rock |               |     |          |    |                                  |     |     |         |     |     |    |    |   |   |                   | X  |   |    |   |   |     |   |  |
| "                         | "          | Gouge                      | <20µm              | x             |     |          | X  |                                  |     |     |         |     |     | tr |    |   |   |                   |    |   |    |   |   | x   |   |  |
| "                         | "          | Gouge                      | 20-0.4µm           |               |     |          | X  | 2M <sub>1</sub> /1M <sub>2</sub> |     |     |         |     |     | tr |    |   |   |                   | tr |   |    |   |   |     |   |  |
| "                         | "          | Gouge                      | 0.4-0.05µm         |               |     |          | X  | 2M <sub>1</sub> /1M <sub>2</sub> |     |     |         |     |     | tr |    |   |   |                   |    |   |    |   |   |     |   |  |
| "                         | "          | Gouge                      | <0.05µm            |               |     |          | X  | 2M <sub>1</sub> /1M <sub>2</sub> |     |     |         |     |     | tr |    |   |   |                   |    |   |    |   |   |     |   |  |
| "                         | "          | Gouge                      | <20µm              | x             |     |          | X  |                                  |     |     |         |     |     | tr |    |   |   |                   |    |   |    |   |   | x   |   |  |
| "                         | "          | Footwall                   | Crushed whole rock |               |     |          |    |                                  |     |     |         |     |     |    |    |   |   |                   |    |   |    |   |   | X   |   |  |
| Paramint range front LANF |            |                            |                    |               |     |          |    |                                  |     |     |         |     |     |    |    |   |   |                   |    |   |    |   |   |     |   |  |
| "                         | South Park | Hangingwell                | Crushed whole rock |               |     |          | x  | 2M <sub>1</sub>                  |     |     |         |     |     |    |    |   |   |                   | X  | x | x  |   |   |     |   |  |
| "                         | "          | Gouge                      | 20-0.4µm           |               |     |          | x  | 1M <sub>2</sub>                  |     |     |         |     |     | x  |    |   |   |                   | X  | x |    |   | x |     |   |  |
| "                         | "          | Gouge                      | 0.4-0.05µm         |               |     |          | X  | 1M <sub>2</sub>                  |     |     |         |     |     |    |    |   |   |                   | x  | x |    |   |   | x   |   |  |
| "                         | "          | Gouge                      | <0.05µm            |               |     |          | X  | 1M <sub>2</sub>                  |     |     |         |     |     |    |    |   |   |                   |    |   |    |   |   |     |   |  |
| "                         | "          | Gouge                      | <20µm              |               |     |          | X  | 1M <sub>2</sub>                  |     |     |         |     |     | x  |    |   |   |                   | x  |   |    |   |   |     |   |  |
| "                         | "          | Gouge                      | <20µm              |               |     |          | X  | 1M <sub>2</sub>                  |     |     |         |     |     | x  |    |   |   |                   | x  |   |    |   |   |     |   |  |
| "                         | "          | Footwall                   | Crushed whole rock |               |     |          | X  | 2M <sub>1</sub>                  |     |     |         |     |     |    |    |   |   |                   | x  |   |    |   |   |     |   |  |
| Ruby/Mts core complex     |            |                            |                    |               |     |          |    |                                  |     |     |         |     |     |    |    |   |   |                   |    |   |    |   |   |     |   |  |
| "                         | Clover-1   | Hangingwell                | Crushed whole rock |               |     |          | x  | 2M <sub>1</sub> /1M <sub>2</sub> |     |     |         |     |     |    |    |   |   |                   |    |   |    |   | x | X   |   |  |
| "                         | "          | Brownish gouge             | 20-0.4µm           |               |     |          | x  | 2M <sub>1</sub> /1M <sub>2</sub> |     |     |         |     |     |    |    |   |   |                   |    |   |    |   |   |     |   |  |
| "                         | "          | Brownish gouge             | 0.4-0.05µm         |               |     |          | x  | 2M <sub>1</sub> /1M <sub>2</sub> |     |     |         |     |     |    |    |   |   |                   |    |   |    |   |   |     |   |  |
| "                         | "          | Brownish gouge             | <0.05µm            |               |     |          | X  | 1M <sub>2</sub>                  |     |     |         |     |     |    |    |   |   |                   |    |   |    |   |   |     |   |  |
| "                         | "          | Brown/yellow gouge contact | <20µm              |               |     |          | tr |                                  |     |     |         |     |     |    |    |   |   | X                 | x  |   |    | x |   |     |   |  |
| "                         | "          | Yellowish gouge            | <20µm              |               |     |          |    |                                  |     |     |         |     |     |    |    |   |   | X                 | x  |   |    | x |   |     |   |  |
| "                         | "          | Footwall                   | Crushed whole rock |               |     |          |    |                                  |     |     |         |     |     |    |    |   |   |                   |    |   |    |   | X |     |   |  |
| Ruby/Mts core complex     |            |                            |                    |               |     |          |    |                                  |     |     |         |     |     |    |    |   |   |                   |    |   |    |   |   |     |   |  |
| "                         | Secret-1   | Hangingwell                | 20-0.4µm           |               |     |          |    |                                  |     | x   | R3      | x   |     |    | x  |   |   | X                 |    |   |    |   |   |     |   |  |
| "                         | "          | Hangingwell                | 0.4-0.05µm         |               |     |          |    |                                  |     | X   | R3      | x   |     |    | tr |   |   | x                 |    |   |    |   |   |     |   |  |
| "                         | "          | Hangingwell                | <0.05µm            |               |     |          |    |                                  |     | X   | R0      | tr  |     |    |    |   |   |                   |    |   |    |   |   |     |   |  |
| "                         | "          | Greenish gouge             | 20-0.4µm           |               |     |          |    |                                  |     | X   | R1R3    |     |     |    | x  |   |   | x                 |    |   |    |   |   |     |   |  |
| "                         | "          | Greenish gouge             | 0.4-0.05µm         |               |     |          |    |                                  |     | X   | R1R3    |     |     |    | tr |   |   |                   |    |   |    |   |   |     |   |  |
| "                         | "          | Greenish gouge             | <0.05µm            |               |     |          |    |                                  |     | X   | R0      |     |     |    |    |   |   |                   |    |   |    |   |   |     |   |  |
| "                         | "          | Brownish gouge             | <20µm              |               |     |          | x  |                                  |     | X   | R1 & R3 |     |     |    | x  |   |   | x                 |    |   |    | x |   |     |   |  |
| "                         | "          | Footwall                   | 20-0.4µm           |               |     |          | X  | 2M <sub>1</sub> /1M <sub>2</sub> |     |     |         |     |     |    | x  |   |   | x                 |    |   |    |   |   | x   |   |  |
| "                         | "          | Footwall                   | 0.4-0.05µm         |               |     |          | X  | 2M <sub>1</sub> /1M <sub>2</sub> |     |     |         |     |     |    |    |   |   | x                 |    |   |    |   |   |     |   |  |
| "                         | "          | Footwall                   | <0.05µm            |               |     |          | X  | 1M <sub>2</sub>                  |     |     |         |     |     |    |    |   |   |                   |    |   |    |   |   |     |   |  |
| "                         | Secret-2   | Hangingwell                | <20µm              |               |     |          |    |                                  |     | x   | R3      | x   |     |    | x  |   |   | X                 |    |   |    |   |   |     |   |  |
| "                         | "          | Gouge                      | <20µm              |               |     |          |    |                                  |     | X   | R1      | x   |     |    | x  |   |   | x                 |    |   |    | x |   |     |   |  |
| "                         | "          | Gouge                      | <20µm              |               |     |          |    |                                  |     | X   | R1      | x   |     |    | x  |   |   | x                 |    |   |    |   |   | x   |   |  |
| "                         | "          | Gouge                      | 20-0.4µm           |               |     |          |    |                                  |     | x   | R1R3    |     |     |    | x  |   |   | X                 |    |   |    | x |   |     |   |  |
| "                         | "          | Gouge                      | 0.4-0.05µm         |               |     |          |    |                                  |     | X   | R1      |     |     |    | x  |   |   | x                 |    |   |    | x |   |     |   |  |
| "                         | "          | Gouge                      | <0.05µm            |               |     |          |    |                                  |     | X   | R0      |     |     |    |    |   |   |                   |    |   |    |   |   |     |   |  |
| "                         | "          | Footwall                   | <20µm              |               |     |          | X  | 2M <sub>1</sub> /1M <sub>2</sub> |     |     |         |     |     |    | x  |   |   | x                 |    |   |    |   |   | x   |   |  |
| Ruby/Mts core complex     |            |                            |                    |               |     |          |    |                                  |     |     |         |     |     |    |    |   |   |                   |    |   |    |   |   |     |   |  |
| "                         | Secret-4   | Hangingwell                | Crushed whole rock |               |     |          |    |                                  |     |     |         |     |     |    |    |   |   |                   |    |   |    |   |   |     | X |  |
| "                         | "          | Gouge                      | <20µm              |               |     |          |    |                                  |     |     |         |     |     |    | X  |   |   | x                 | x  |   |    | x |   |     |   |  |
| "                         | "          | Gouge                      | <20µm              |               |     |          |    |                                  |     |     |         |     |     |    | X  |   |   |                   |    |   |    |   |   |     |   |  |
| "                         | "          | Gouge                      | 20-0.4µm           |               |     |          |    |                                  |     | x   | R3      |     |     |    | x  |   |   | X                 |    |   |    | x |   |     |   |  |
| "                         | "          | Gouge                      | 0.4-0.05µm         |               |     |          |    |                                  |     | X   | R1      |     |     |    | x  |   |   |                   |    |   |    |   |   |     |   |  |
| "                         | "          | Gouge                      | <0.05µm            |               |     |          |    |                                  |     | X   | R0      |     |     |    |    |   |   |                   |    |   |    |   |   |     |   |  |
| "                         | "          | Footwall                   | Crushed whole rock |               |     |          |    |                                  |     |     |         |     |     |    |    |   |   |                   | X  |   |    |   | x | x   |   |  |

Table 2-3 (continued)

| Detachment fault            | Outcrop          | Sample         | Size fraction      | Clay minerals |     |            |        |                                  |     |    |     |     |   |   | Non-clay minerals |    |    |    |   |    |   |   |     |    |  |  |
|-----------------------------|------------------|----------------|--------------------|---------------|-----|------------|--------|----------------------------------|-----|----|-----|-----|---|---|-------------------|----|----|----|---|----|---|---|-----|----|--|--|
|                             |                  |                |                    | C             | C/S | Ordering I | p-type | I/S                              | (R) | Sm | Sep | Pal | T | L | K                 | Q  | KF | Pl | A | Ca | D | G | H/C |    |  |  |
| Salton Sea detachment       | Wonderstone Wash | Gouge          | <2.0 µm            | x             |     |            | x      |                                  |     |    |     | X   |   |   | tr                | x  |    |    |   |    |   | x |     |    |  |  |
| Sierra Mazatan core complex | Maz-1            | Gouge          | 2.0 - 1.0 µm       |               |     |            | x      | 2M <sub>1</sub> /1M <sub>d</sub> |     |    |     |     |   |   |                   |    | X  |    |   |    |   |   | x   |    |  |  |
| "                           | "                | Gouge          | 1.0 - 0.5 µm       |               |     |            | x      | 2M <sub>1</sub> /1M <sub>d</sub> |     |    |     |     |   |   |                   |    | X  |    |   |    |   |   | x   |    |  |  |
| "                           | "                | Gouge          | 0.5 - 0.1 µm       |               |     |            | X      | 2M <sub>1</sub> /1M <sub>d</sub> |     |    |     |     |   |   |                   |    |    |    |   |    |   |   |     | tr |  |  |
| "                           | "                | Gouge          | 0.1 - 0.05 µm      |               |     |            | X      | 2M <sub>1</sub> /1M <sub>d</sub> |     |    |     |     |   |   |                   |    |    |    |   |    |   |   |     |    |  |  |
| "                           | "                | Gouge          | <0.05 µm           |               |     |            | X      | 2M <sub>1</sub> /1M <sub>d</sub> |     |    |     |     |   |   |                   |    |    |    |   |    |   |   |     |    |  |  |
| Whipple detachment          | Whip-3           | Hangingwall    | Crushed whole rock |               |     |            |        |                                  |     |    |     |     |   |   |                   |    | X  | x  |   |    |   |   |     |    |  |  |
| "                           | "                | Reddish gouge  | <2.0 µm            | X             |     |            | x      |                                  |     |    |     |     |   |   |                   |    | x  | x  | x |    |   |   |     |    |  |  |
| "                           | "                | Cataclasite    | Crushed whole rock |               |     |            |        |                                  |     |    |     |     |   |   |                   |    | x  | x  | X |    |   |   |     |    |  |  |
| "                           | "                | Greenish gouge | <2.0 µm            | X             |     |            | x      |                                  |     |    |     |     |   |   |                   |    | x  | x  |   |    |   |   |     |    |  |  |
| "                           | "                | Footwall       | Crushed whole rock | x             |     |            |        |                                  |     |    |     |     |   |   |                   |    | x  | X  | x |    |   |   |     |    |  |  |
| "                           | Whip-5           | Hangingwall    | Crushed whole rock | x             |     |            | x      |                                  |     |    |     |     |   |   |                   |    | X  | x  |   |    |   |   |     |    |  |  |
| "                           | "                | Reddish gouge  | <2.0 µm            | X             |     |            | x      |                                  |     |    |     |     |   |   |                   |    |    |    |   |    |   |   | x   |    |  |  |
| "                           | "                | Greenish gouge | 2.0 - 0.4 µm       | X             |     |            | x      | 1M <sub>d</sub>                  |     |    |     |     |   |   |                   | tr |    |    |   |    |   |   |     | tr |  |  |
| "                           | "                | Greenish gouge | 0.4 - 0.05 µm      | X             |     |            | x      | 1M <sub>d</sub>                  |     |    |     |     |   |   |                   |    |    |    |   |    |   |   |     |    |  |  |
| "                           | "                | Greenish gouge | <0.05 µm           | x             |     |            | X      | 1M <sub>d</sub>                  |     |    |     |     |   |   |                   |    |    |    |   |    |   |   |     |    |  |  |
| "                           | "                | Footwall       | Crushed whole rock | x             |     |            |        |                                  |     |    |     |     |   |   |                   |    | X  | x  | x |    |   |   |     |    |  |  |

Table 2-3 (continued)

Table 4). Of the 23 outcrops from which at least one layer was separated into size fractions, 22 outcrops had evidence for significant growth of authigenic clay minerals. Only one detachment outcrop (Mormon-2) showed no evidence for significant clay mineral transformation in any region of the gouge. All of the  $<0.05 \mu\text{m}$  fractions contained one of four clay minerals: the  $1M_d$  polytype of illite, illite-rich illite-smectite, chlorite or smectite, and nearly all were dominated by only one of these four clays. (see Table 4). 15 of the 29 fine size fractions sampled were dominated by authigenic  $1M_d$  illite, with illite-rich I/S, chlorite and smectite dominating the remainder in roughly equal numbers, five illite-rich I/S, four chlorite and four smectite. The pervasive change in clay mineralogy from the relatively coarse, detrital-dominated  $2.0 - 0.4 \mu\text{m}$  fraction to the fine, authigenic-dominated  $<0.05 \mu\text{m}$  fraction of at least one gouge horizon indicates that clay minerals in the gouges had undergone transformations in nearly all the fault gouges sampled.

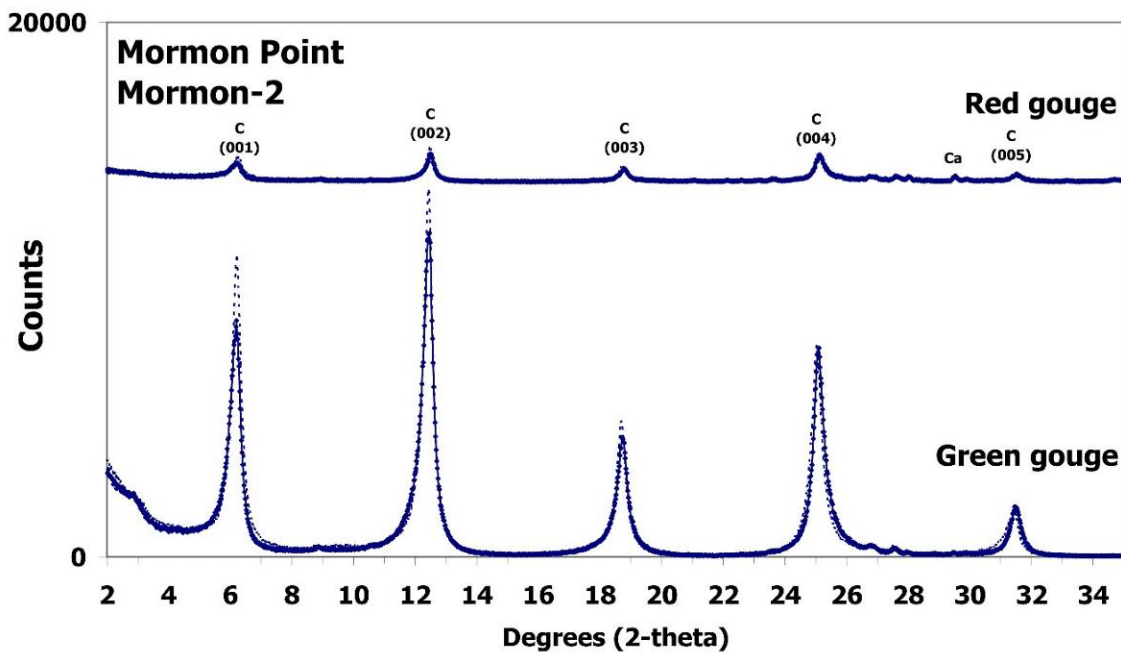
#### Chloritic gouges

Six outcrops sampled (Mormon Point turtleback (Mormon-2, Mormon-3), Copper Canyon turtleback, Chemehuevi detachment (Lobeck Pass), the Buckskin-Rawhide detachment (A-Bomb Canyon), and the Whipple detachment (Whip-5)) have a chlorite-dominated gouge layer in at least part of the fault zone that has a distinctive 'scaly' texture and that is frequently greenish in color. The 'scaly' gouge is usually in contact with chloritically-altered and brecciated footwall (see Figures 2.4, 2.5 and 2.6 for field photos and XRD patterns of the clay fraction of gouge at Mormon Point and Lobeck Pass). The Mormon-2 outcrop preserves a pristine detrital gouge, while the other five fault outcrops that have a green scaly gouge layer also evidence clay mineral transformations either within the another layer of the gouge zone (A-Bomb Canyon,

| Outcrop          | Sample           | Clay minerals |     |          |     |                                      |     |     |    |     |     |    | Non-clay minerals |   |   |    |    |   |    |   |   |     |  |
|------------------|------------------|---------------|-----|----------|-----|--------------------------------------|-----|-----|----|-----|-----|----|-------------------|---|---|----|----|---|----|---|---|-----|--|
|                  |                  | Chl           | C/S | Ordering | ill | <b>p-type</b>                        | I/S | (R) | Sm | Sep | Pal | T  | L                 | K | Q | KF | Pl | A | Ca | D | G | H/C |  |
| Ashford Klippe   | Gouge            |               |     |          | X   | <b>1M<sub>d</sub></b>                |     |     |    |     |     |    |                   |   |   |    |    |   |    |   |   |     |  |
| Exclamation Rock | Gouge            |               |     |          | X   | <b>2M<sub>1</sub>/1M<sub>d</sub></b> |     |     |    |     |     |    |                   |   |   |    |    |   |    |   |   |     |  |
| Virgin Springs W | Brownish gouge   |               |     |          | X   | <b>2M<sub>1</sub>/1M<sub>d</sub></b> |     |     |    |     |     |    |                   |   |   |    |    |   |    |   |   |     |  |
| Badwater-1       | Gouge            |               |     |          | X   | <b>1M<sub>d</sub></b>                |     |     |    |     |     |    |                   |   |   |    |    |   |    |   |   |     |  |
| Badwater-2       | Gouge            |               |     |          | X   | <b>2M<sub>1</sub>/1M<sub>d</sub></b> |     |     | x  |     |     |    |                   |   |   |    |    |   |    |   |   |     |  |
| A-bomb           | Breccia          | X             |     |          |     |                                      |     |     |    |     |     |    |                   |   |   |    |    |   |    |   |   |     |  |
| Bullard          | Upper gouge      |               | x   | R0       | X   | <b>2M<sub>1</sub>/1M<sub>d</sub></b> |     |     | x  |     |     |    |                   |   |   |    |    | x |    |   |   |     |  |
| WH68             | Grey gouge       |               |     |          | X   | <b>1M<sub>d</sub></b>                |     |     |    |     |     |    |                   |   |   |    |    |   |    |   |   |     |  |
| WH68             | Altered footwall |               |     |          |     |                                      |     |     |    | X   |     |    |                   |   |   |    |    |   |    |   |   | x   |  |
| Lobeck           | Gouge            | X             |     |          |     |                                      |     |     |    |     |     |    |                   |   |   |    |    |   |    |   |   |     |  |
| Copper           | Gouge            |               | X   | R0       |     |                                      |     |     |    |     |     |    |                   |   |   |    |    |   |    |   |   |     |  |
| Dante            | Breccia          |               |     |          |     |                                      |     |     | X  |     | x   |    |                   |   |   |    |    |   |    |   |   | x   |  |
| Dante            | Gouge            |               |     |          |     |                                      |     |     | X  |     | x   |    |                   |   |   |    |    |   |    |   |   | x   |  |
| Tucki            | Lower gouge      |               |     |          | X   | <b>2M<sub>1</sub>/1M<sub>d</sub></b> |     |     |    |     |     |    |                   |   |   |    |    |   |    |   |   | x   |  |
| Wildrose         | Upper gouge      |               |     |          |     |                                      | X   | R3  |    |     |     | tr | x                 |   |   |    |    |   |    |   |   |     |  |
| Size 36          | Lower gouge      |               |     |          | X   | <b>1M<sub>d</sub></b>                |     |     |    |     |     |    |                   |   |   |    |    |   |    |   |   |     |  |
| Size 36          | Footwall breccia |               |     |          | X   | <b>1M<sub>d</sub></b>                |     |     |    |     |     |    |                   |   |   |    |    |   |    |   |   |     |  |
| Mormon-1         | Gouge            |               |     |          |     |                                      |     | X   | R0 |     |     | tr |                   |   |   |    |    |   |    |   |   |     |  |
| Mormon-2         | Green gouge      | X             |     |          |     |                                      |     |     |    |     |     |    |                   |   |   |    |    |   |    |   |   |     |  |
| Mormon-3         | Upper gouge      | X             |     |          |     |                                      |     |     |    |     |     |    |                   |   |   |    |    |   |    |   |   |     |  |
| Mormon-3         | Lower gouge      |               |     |          |     |                                      |     |     | X  | x   |     | x  | x                 |   |   |    |    |   |    |   |   |     |  |
| Mosaic           | Gouge            |               |     |          | X   | <b>2M<sub>1</sub>/1M<sub>d</sub></b> |     |     |    |     |     | tr |                   |   |   |    |    |   |    |   |   |     |  |
| South Park       | Gouge            |               |     |          | X   | <b>1M<sub>d</sub></b>                |     |     |    |     |     |    |                   |   |   |    |    |   |    |   |   |     |  |
| Clover-1         | Brownish gouge   |               |     |          | X   | <b>1M<sub>d</sub></b>                |     |     |    |     |     |    |                   |   |   |    |    |   |    |   |   |     |  |
| Secret-1         | Greenish gouge   |               |     |          |     |                                      |     | X   | R0 |     |     |    |                   |   |   |    |    |   |    |   |   |     |  |
| Secret-2         | Gouge            |               |     |          |     |                                      |     | X   | R0 |     |     |    |                   |   |   |    |    |   |    |   |   |     |  |
| Secret-4         | Gouge            |               |     |          |     |                                      |     | X   | R0 |     |     |    |                   |   |   |    |    |   |    |   |   |     |  |
| Maz-1            | Gouge            |               |     |          | X   | <b>2M<sub>1</sub>/1M<sub>d</sub></b> |     |     |    |     |     |    |                   |   |   |    |    |   |    |   |   |     |  |
| Whip-5           | Greenish gouge   | x             |     |          | X   | <b>1M<sub>d</sub></b>                |     |     |    |     |     |    |                   |   |   |    |    |   |    |   |   |     |  |

**Table 2-4:** XRD analysis of the fine fraction (< 0.05 μm) of the 29 gouge samples separated into size fractions. Note that all samples consist predominantly (shown in **bold**) of chlorite-smectite, illite, illite-smectite or smectite in the finest size fraction which concentrates authigenic minerals. Chlorite in finest fraction is indistinguishable from coarser chlorites in gouge and footwall (see text for discussion) C = chlorite, C/S = chlorite/smectite, R0 = disordered, R1 = ordered, I = illite, I/S = illite/smectite, R = Reichweit (R0, R1, etc), Sm = smectite, Sep = sepiolite, Pal = palygorskite, T = talc, L = lizardite, K = kaolinite, Q = quartz, KF = K-feldspar, P = plagioclase, A = analcime, Ca = calcite, D = dolomite, G = gypsum, H/C = heulandite/clinoptilite.

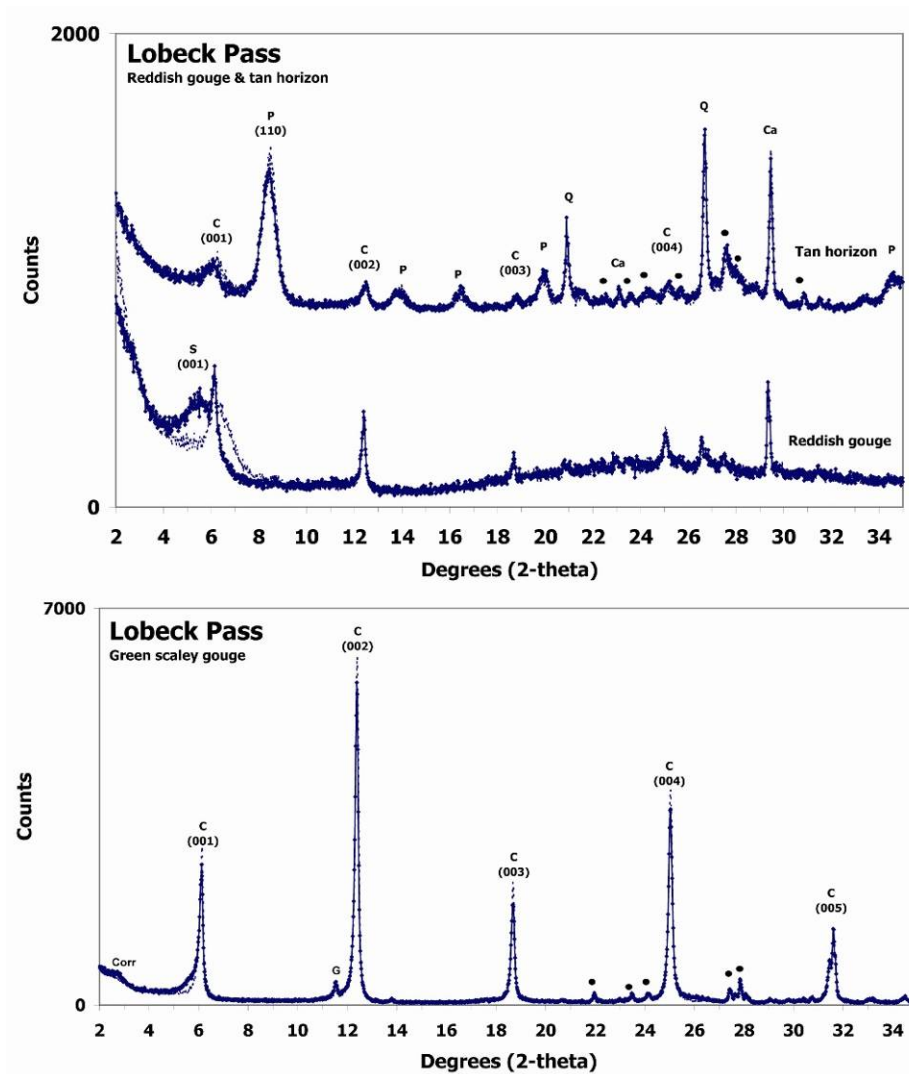




**Figure 2-4:** Outcrop photographs and XRD patterns of oriented preparations of the clay fraction of gouge at Mormon-2. Note the reddish and greenish regions of the gouge and the similar mineralogy as indicated by the XRD patterns of the red and green regions of the gouge. The difference in peak height between the two samples is a function of a larger diffracting domain size (coarser-grained) in the green material.



**Figure 2-5:** Outcrop photographs of the Chemehuevi detachment at Lobeck Pass. Note regions of differing clay mineralogy highlighted in photo and Reidel shears visible in the tan palygorskite crust. See discussion in text.

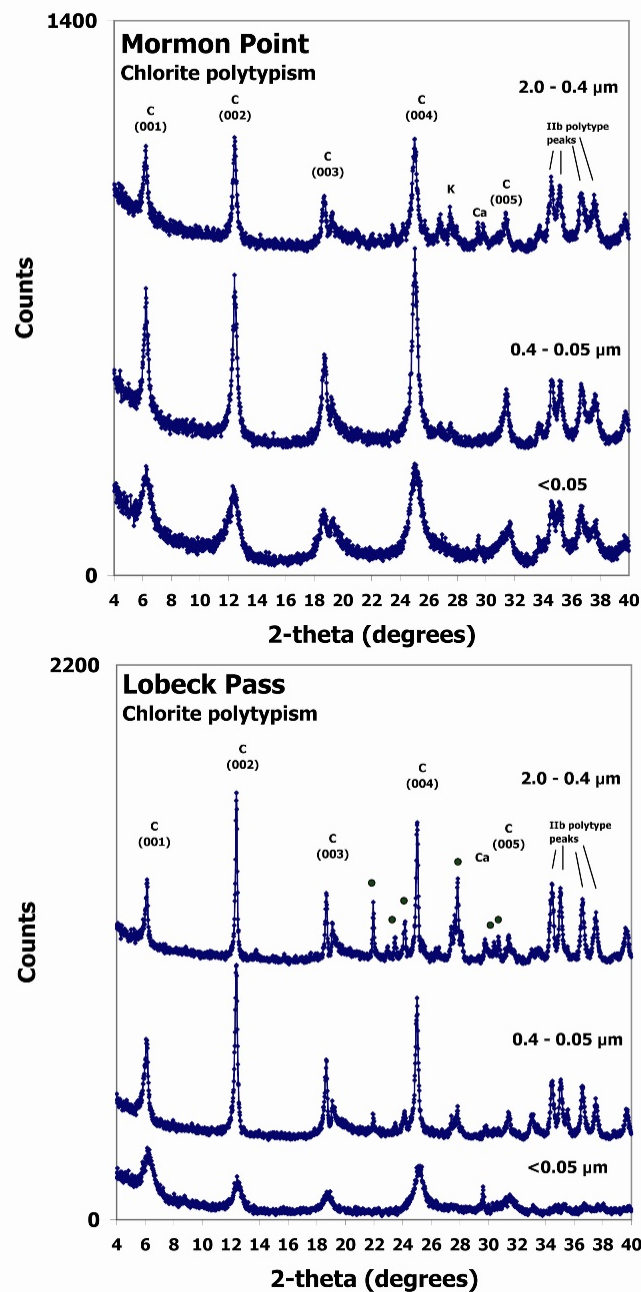


**Figure 2-6:** XRD patterns from regions of gouge identified in Figure 2.5. Bottom profile is from basal chlorite-dominated scaly gouge, upper two profiles are from reddish smectitic gouge and palygorskite horizon respectively. C = chlorite, P = palygorskite, Q = quartz, Ca = calcite, filled circles are K-feldspar peaks.

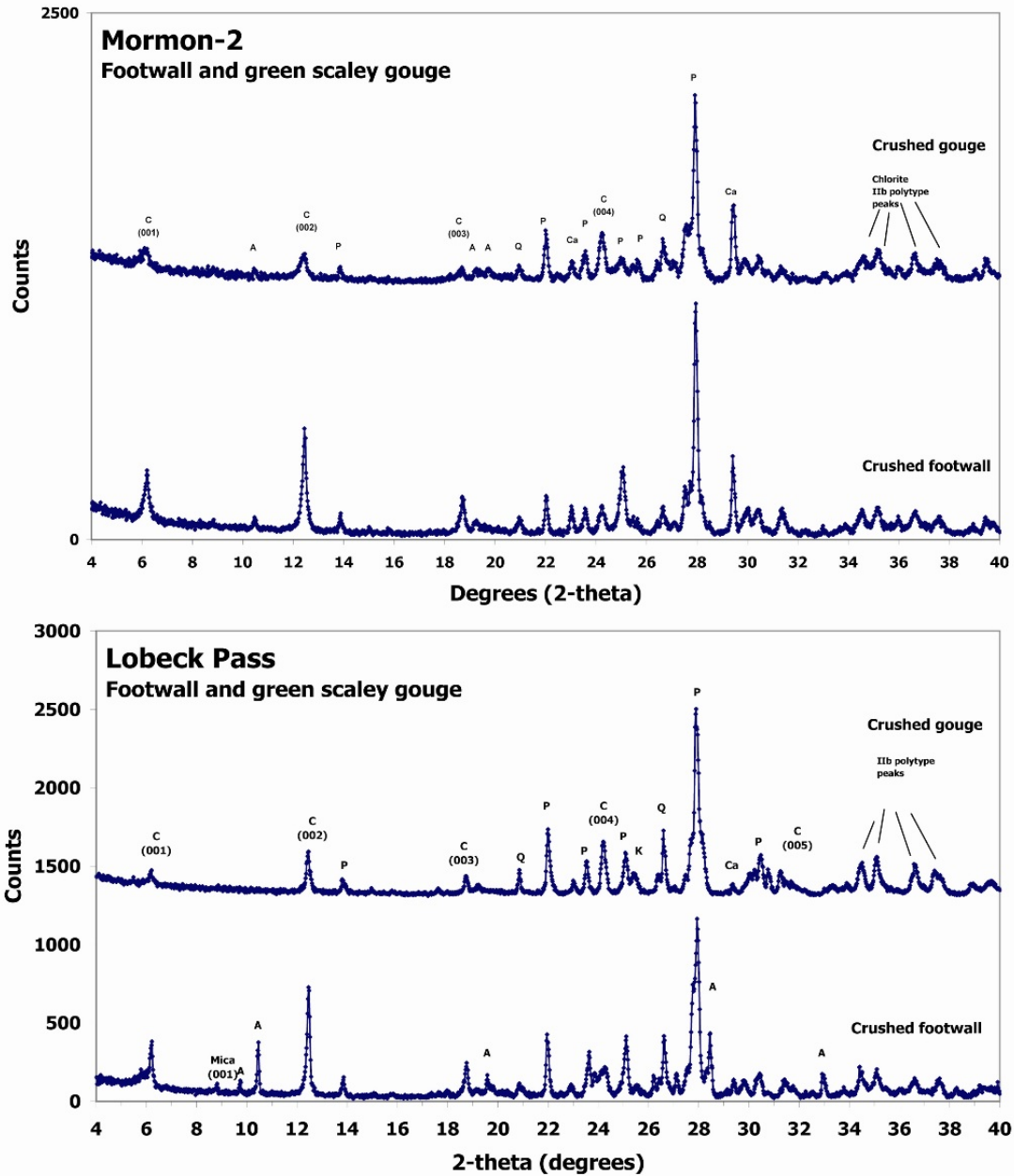
Mormon-3, Lobeck Pass) or within the green scaly gouge layer itself (Copper Canyon, Whip-5). At Mormon-2, a 1.0 m thick gouge zone has visibly distinct reddish and greenish layers at outcrop (see Figure 2.4). XRD analysis indicates that the reddish and greenish layers have almost identical chlorite compositions; the differences in color is attributed to differing oxidation states of Fe oxy-hydroxides on grain surfaces. At Lobeck Pass, the clay fraction of the green scaly gouge consists entirely of chlorite (Figures 2.5 and 2.6). Separation of the green scaly gouge at both localities into size fractions indicates that the scaly gouge at both Mormon-2 and Lobeck Pass consists exclusively of chlorite in all size fractions (see Figure 2.7). XRD powder patterns of crushed scaly gouge at Mormon-2 and at Lobeck Pass indicate that both scaly gouges are dominated by an assemblage of 11b-polytype chlorite, quartz, feldspar, and minor amphibole (see Figure 2.8). When the diffraction patterns of crushed scaly gouge and chloritically-altered footwall at both Lobeck Pass and Mormon-2 are compared, they are remarkably similar (see Figure 2.8), indicating that the scaly gouge is derived from cataclasis of the chloritically-altered footwall without a significant mineralogical transformation. This hypothesis is further tested below.

#### Chlorite alteration gouges

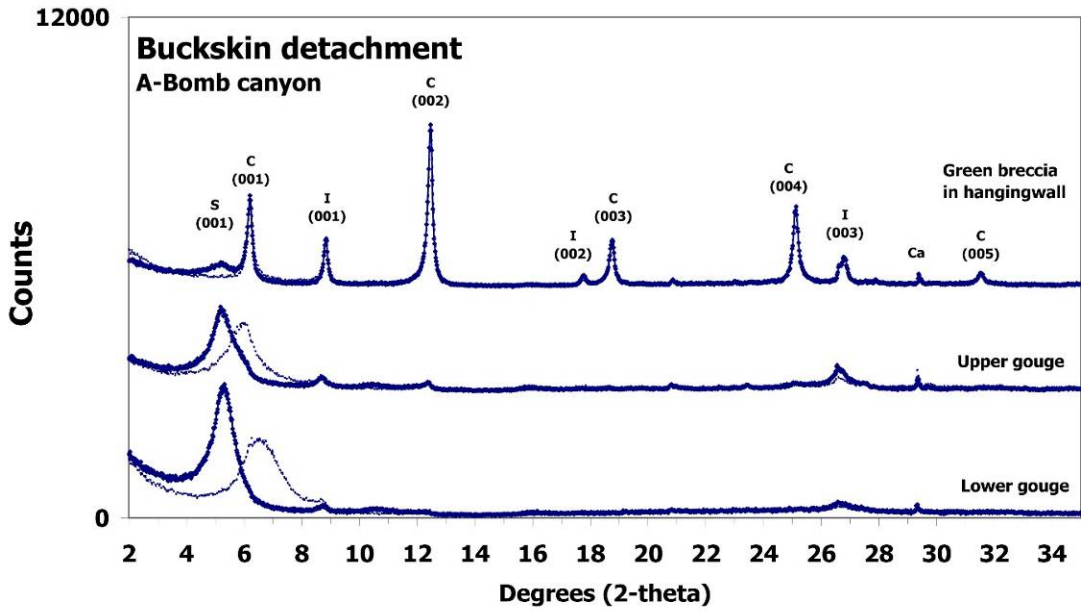
Outcrops at 3 of the 6 detachment faults with a scaly chloritic gouge layer (A-Bomb Canyon, Lobeck Pass and Mormon-3) all evidence at least one other gouge layer which is compositionally distinct and contains clay minerals derived from the detrital chlorite preserved in the scaly layer (see Figures 2.9 & 2.10, also Figure 2.5). At the A-Bomb Canyon exposure of the Buckskin-Rawhide detachment (see Figure 2.9) a 50 cm thick scaly chloritic breccia layer is preserved at the contact with the hangingwall granite, while a 20 cm-thick lower layer of the gouge outcrop consists predominantly of smectite;



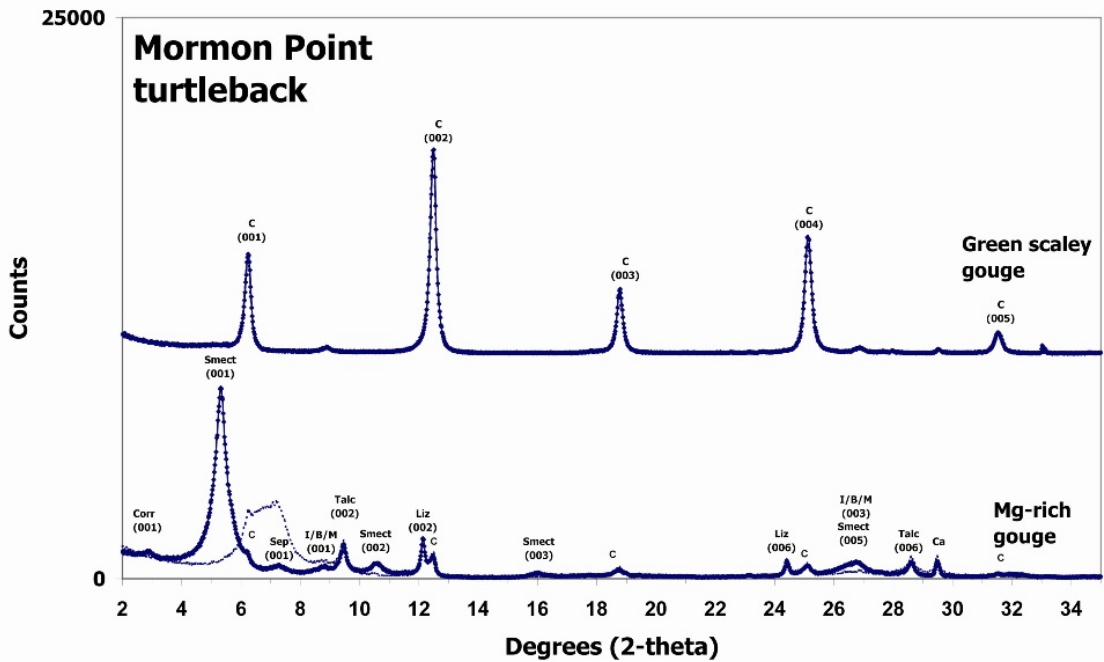
**Figure 2-7** XRD patterns from random preparations of scaly gouge at Mormon-2 and Lobeck Pass separated into size fractions. (see Figures 2.4 & 2.5). Note the decreasing abundance of non-clay minerals in the medium and fine fractions, and the lack of change in the clay mineralogy between the coarse and fine fractions at each locality. C = chlorite, K = K-feldspar, Ca = calcite, filled circles on lower profile are plagioclase peaks.



**Figure 2-8:** XRD patterns of random preparations of crushed scaly gouge and crushed footwall collected at Mormon Point (upper profiles) and Lobeck Pass (lower profiles). Note the similarity of XRD profiles of the crushed whole scaly gouge and crushed footwall at each locality, indicating a very similar bulk mineralogy of the gouge and footwall, and the IIB-specific polytype peaks common to all 4 profiles. C = chlorite, P = plagioclase, A = amphibole, Q = quartz, Ca = calcite.



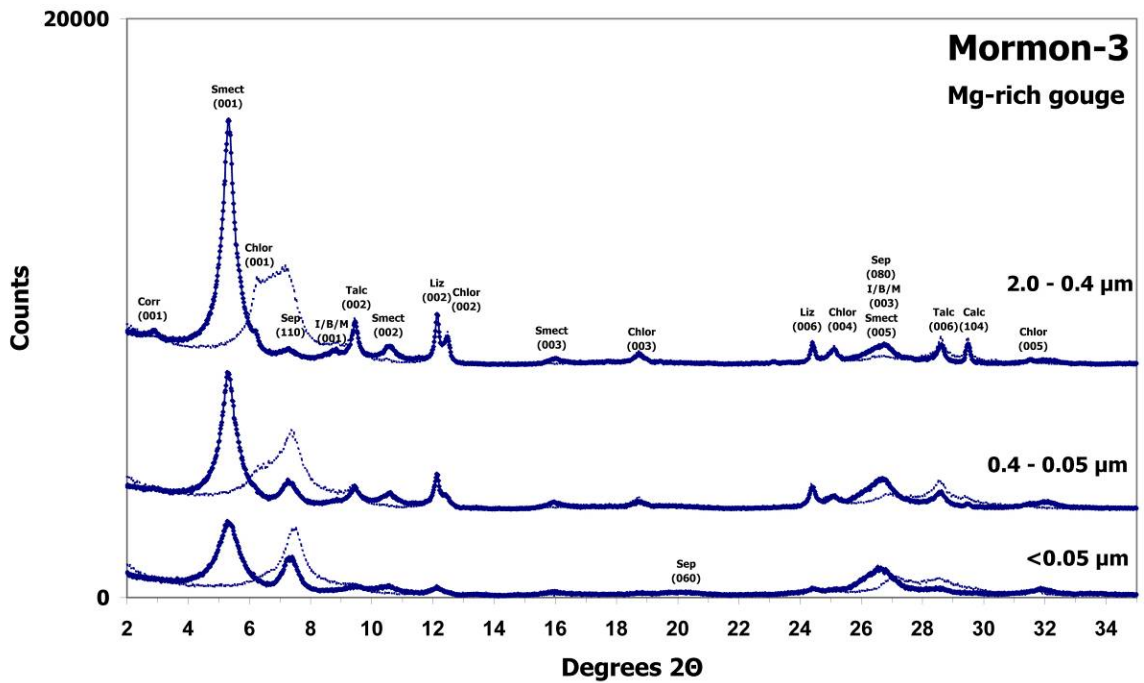
**Figure 2-9:** Field photographs and XRD patterns of oriented preparations of the clay fraction of gouge from the Buckskin detachment at A-Bomb Canyon. Note the prominent chlorite microbreccia ledge in the footwall in the left-hand photo. Outcrop pictured at right is at left-center of left-hand photo looking towards the camera. Note the chloritic breccia in the hangingwall and the smectitic gouge overlying the microbreccia ledge. S = smectite, C = chlorite, I = 10 Å mica (illite, muscovite, biotite), Ca = calcite.



**Figure 2-10:** Field photographs and XRD patterns of oriented preparations of the clay fractions of chloritic and Mg-rich mineral layers in gouge at Mormon-3. Note clear fabric in Mg-rich gouge indicating formation prior to end of slip on fault. C = chlorite, Smec = smectite, Sep = sepiolite, Corr = corrensite, I/B/M = 10 Å mica (illite, biotite, muscovite), Liz = lizardite, Ca = calcite.



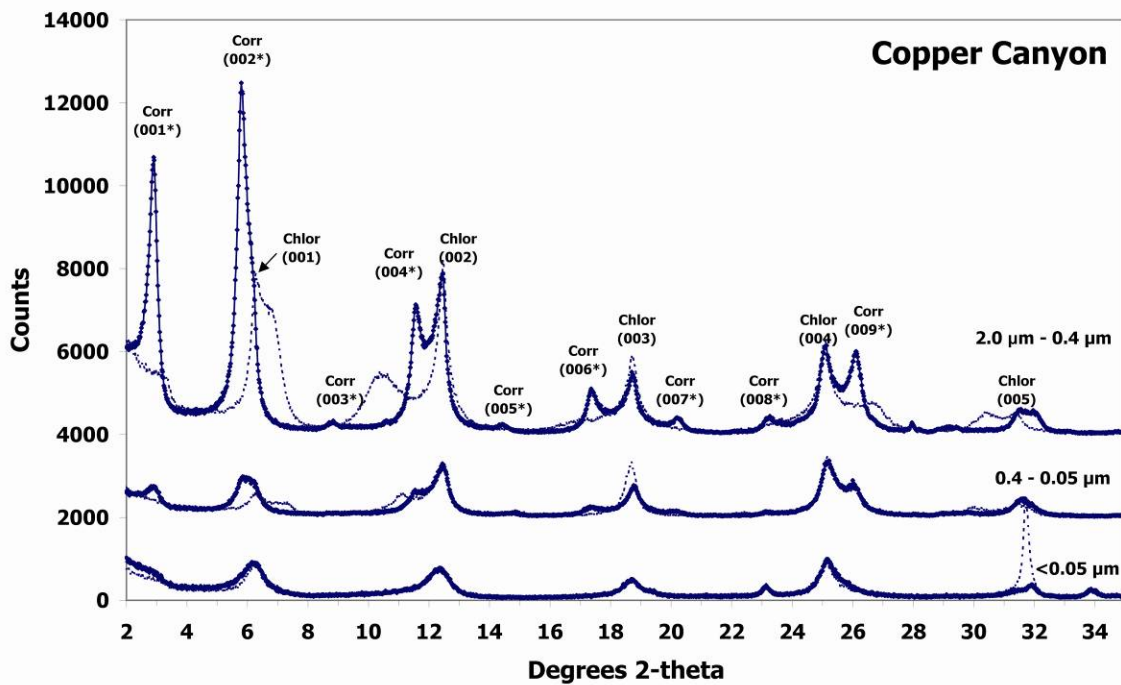
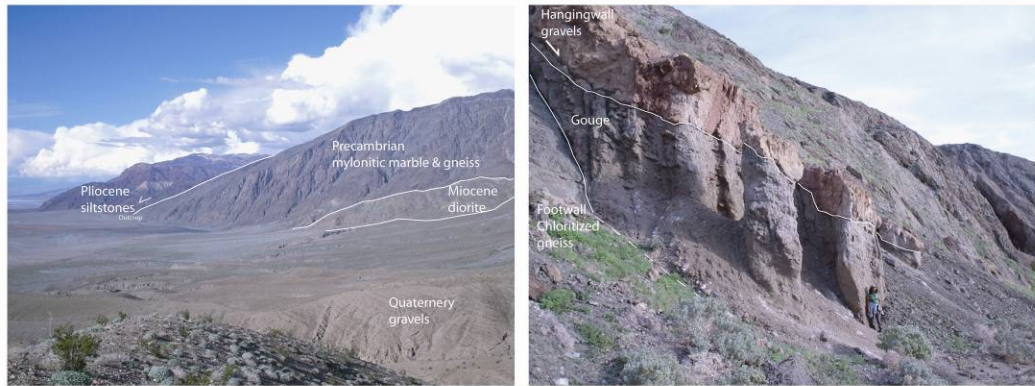
chlorite is present in small amounts in the coarse size fraction of the lower layers, but is absent in the  $<0.4 \mu\text{m}$  size fraction. The smectitic gouge has shear indicators consistent with dextral shear, indicating the smectite formed prior to the end of slip on the detachment. A (060) reflection at  $1.53 \text{ \AA}$  indicates that the smectite is tri-octahedral and is most likely saponite. At Lobeck Pass, a 20 cm thick reddish layer is found directly above the scaly chloritic layer (see Figure 2.5). The reddish layer contains chlorite and tri-octahedral smectite (saponite). The (001) reflection of the chlorite in the clay fraction is stronger than the (002) reflection, indicating some alteration of the chlorite towards a vermiculite-like composition (Moore & Reynolds, 1997), and the chlorite peaks are narrow ( $\text{FWHM} = 0.17 - 0.26^\circ$ ) indicating a large diffracting domain size, the gouge is most probably a mixture of variably altered detrital chlorite and authigenic saponite. The reddish layer is bisected by 5-10 cm thick hard tan horizon. XRD indicates the tan layer to be predominantly palygorskite with minor chlorite, quartz, and calcite. As the palygorskite-rich layer is cut by striated Riedel surfaces consistent with normal slip, the palygorskite clearly grew before the end of fault slip. Palygorskite is an Mg- and Al-rich phyllosilicate with a fibrous morphology that has been reported in brittle faults only once previously (García-Romero et al., 2006). At Mormon-3, a 10 cm to 1.0 m thick scaly chloritic gouge layer with clear folding structures is preserved along the contact with the hangingwall, and a 20 to 50 cm thick hard waxy yellowish layer is found along the contact with the footwall (see Figure 2.10). The yellowish layer consists of an Mg-rich clay mineral assemblage of saponite (Mg-rich smectite) and sepiolite with minor amounts of lizardite, talc and chlorite. Chlorite is only present in the coarse size fraction of the Mg-rich layer whereas the other Mg-rich minerals are all present in the medium and fine size fractions (see Figure 2.11), indicating that the chlorite is detrital and derived from the green scaly gouge, while the sepiolite, saponite, lizardite and talc are all authigenic. As the nearest ultramafic body that could be a source for detrital lizardite is



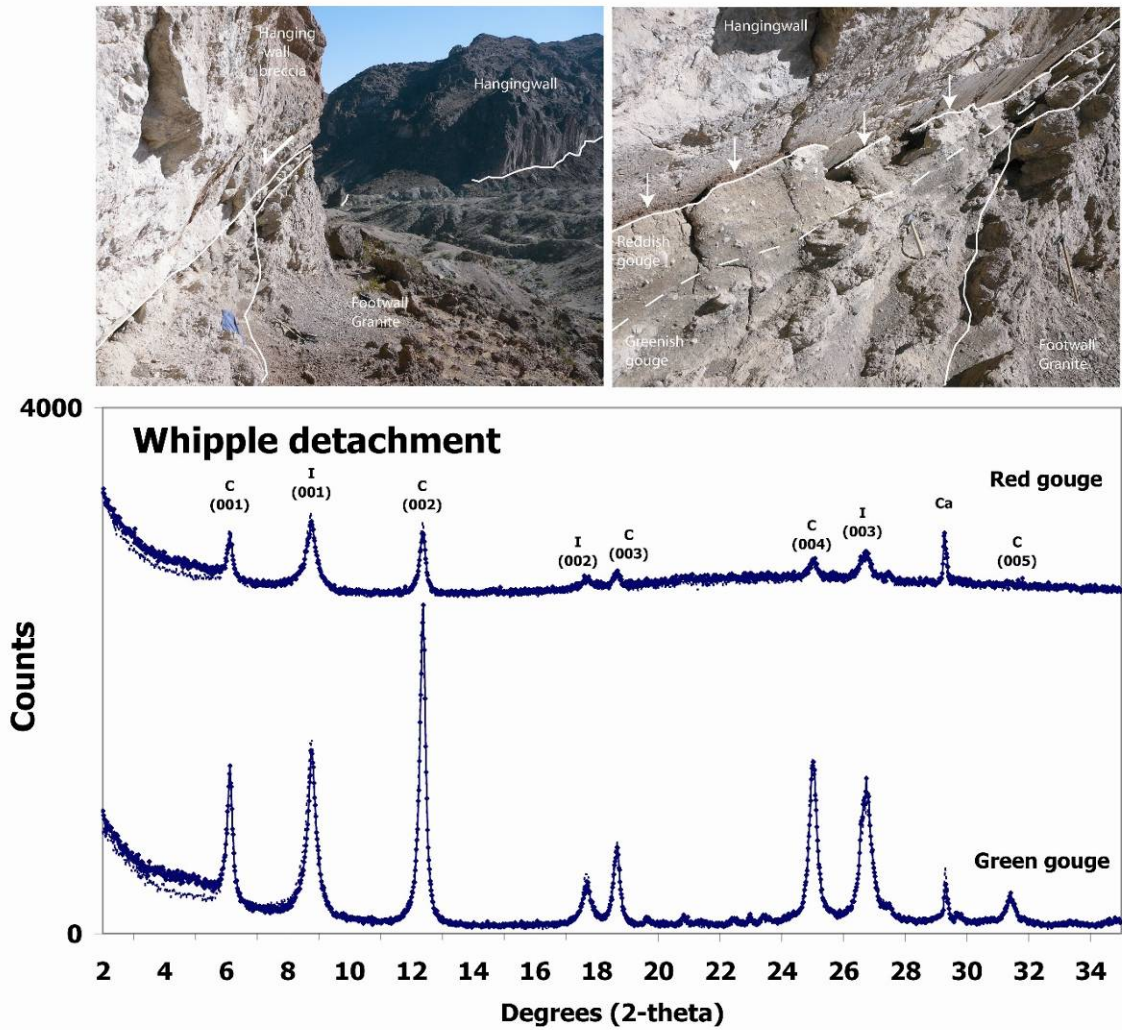
**Figure 2-11:** XRD patterns of oriented preparations of size fractions of the Mg-rich gouge at Mormon Point. Dashed line = air-dried, Solid line = after glycol salvation. Note presence of chlorite and corrensite in the coarse fraction only, and the presence of smectite (saponite), sepiolite, talc and lizardite in the fine (<0.05 μm) fraction.

in the foothills of the western Sierra Nevada, >150 km from the Mormon Point turtleback, a detrital origin for the lizardite is exceedingly unlikely. The nearest known outcrop of talc-rich rocks to Mormon Point are found in the contact aureole of the Kingston Peak pluton, 73 km to the southeast (Calzia et al., 1988), and a detrital origin for the talc is thus equally improbable.

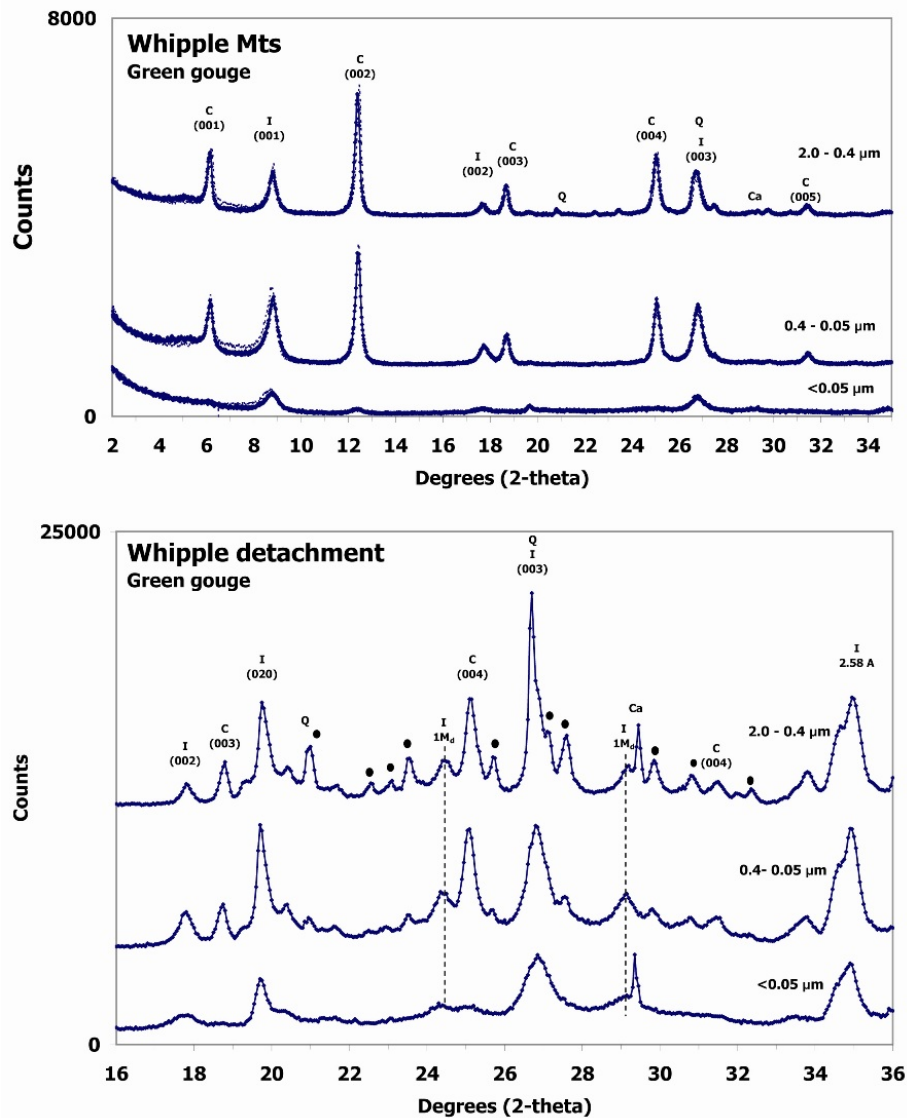
The other 2 outcrops have greenish gouges with scaly textures identical in the field to those described above, but more complex clay mineral assemblages. At Copper Canyon, a 2 - 5 m thick gouge layer consists of chlorite, corrensite (ordered chlorite-smectite) in the coarse and medium size fractions and an Mg-rich chlorite with smectite interlayers in the fine size fraction (see Figure 2.12). The XRD patterns indicate extensive transformation of detrital chlorite derived from the footwall to corrensite and transformation of both detrital chlorite and corrensite to a disordered Mg-rich chlorite-rich chlorite-smectite that is the only clay phase in the <0.05  $\mu\text{m}$  size fraction. At the Whipple detachment outcrop the gouge horizon ranges from 0.3 to 1.2 m in thickness below a sharp striated upper surface. The upper half of the gouge is reddish in color, and the lower half is greenish and scaly (see Figure 2.13). Both the reddish and greenish gouge contain chlorite and illite in the clay fraction, with the red gouge containing more illite than the green gouge. Upon separation into size fractions, the red gouge consists primarily of detrital chlorite in the coarse size fraction and authigenic  $1M_d$  illite in the fine fraction (see Figure 2.14), indicating authigenic illite growth, which will be discussed further below. A 1-5 cm basalt dyke intrudes the fault plane immediately below the striated hangingwall. The dyke consists of relict phenocrysts of zoned plagioclase set in a groundmass of fine-grained plagioclase laths and a matrix that heavily altered to opaque Fe oxides (see Figure 2.15). The dyke is not heavily sheared and was intruded after the gouge formed. No contact alteration is evident at the contact between the dyke



**Figure 2-12:** Outcrop photos and XRD patterns of oriented preparations of size fractions of gouge from Copper Canyon. Dashed line = air-dried, Solid line = after glycol saturation. Note presence of corrensite and chlorite in the coarse and medium size fractions, and fine fraction that consists of chlorite. The low-angle side of the chlorite (001) peak shifts on glycolation, which together with a small peak at  $2.8^\circ 2\theta$  (31Å) that the chlorite is actually a chlorite-rich chlorite-smectite with both R1 and R0 ordering. Corr = corrensite, Chlor = chlorite



**Figure 2-13:** Field photographs and XRD patterns of oriented preparations of the clay size fraction of gouge from upper-plate normal faults linked to the Whipple detachment. Dashed line = air-dried Solid line = after glycol salvation,. Note visually distinct layers have nearly identical clay mineralogies. Arrows in upper right-hand image show thin basalt dyke intruded along hangingwall fault surface. C = chlorite, I = illite, Ca = calcite



**Figure 2-14:** XRD patterns of size fractions of green gouge at Whip-5. (pictured in Figure 2.13). Upper figure is of oriented preparations (dashed = air-dried, solid = after glycol salvation), and lower figure is of random patterns of the same material. Note the transition from chlorite and feldspar-rich material in the coarse and medium size fractions to  $1M_d$  illite in the fine size fraction apparent from both the oriented and random preparations. Note also that the  $1M_d$  peaks are present in all size fractions and that  $2M_1$  polytype-specific peaks are absent from all size fractions. This transition is discussed further below. The relative abundance of chlorite in the oriented sample preparation compared to the random sample preparation is not a function of intra-sample heterogeneity, but of sample preparation, as the oriented slurry preparations concentrate clay-rich material at the top of the sample exposed to the X-ray beam. C = chlorite, I = illite, Q = quartz, Ca = calcite. Filled circles are K-feldspar peaks.

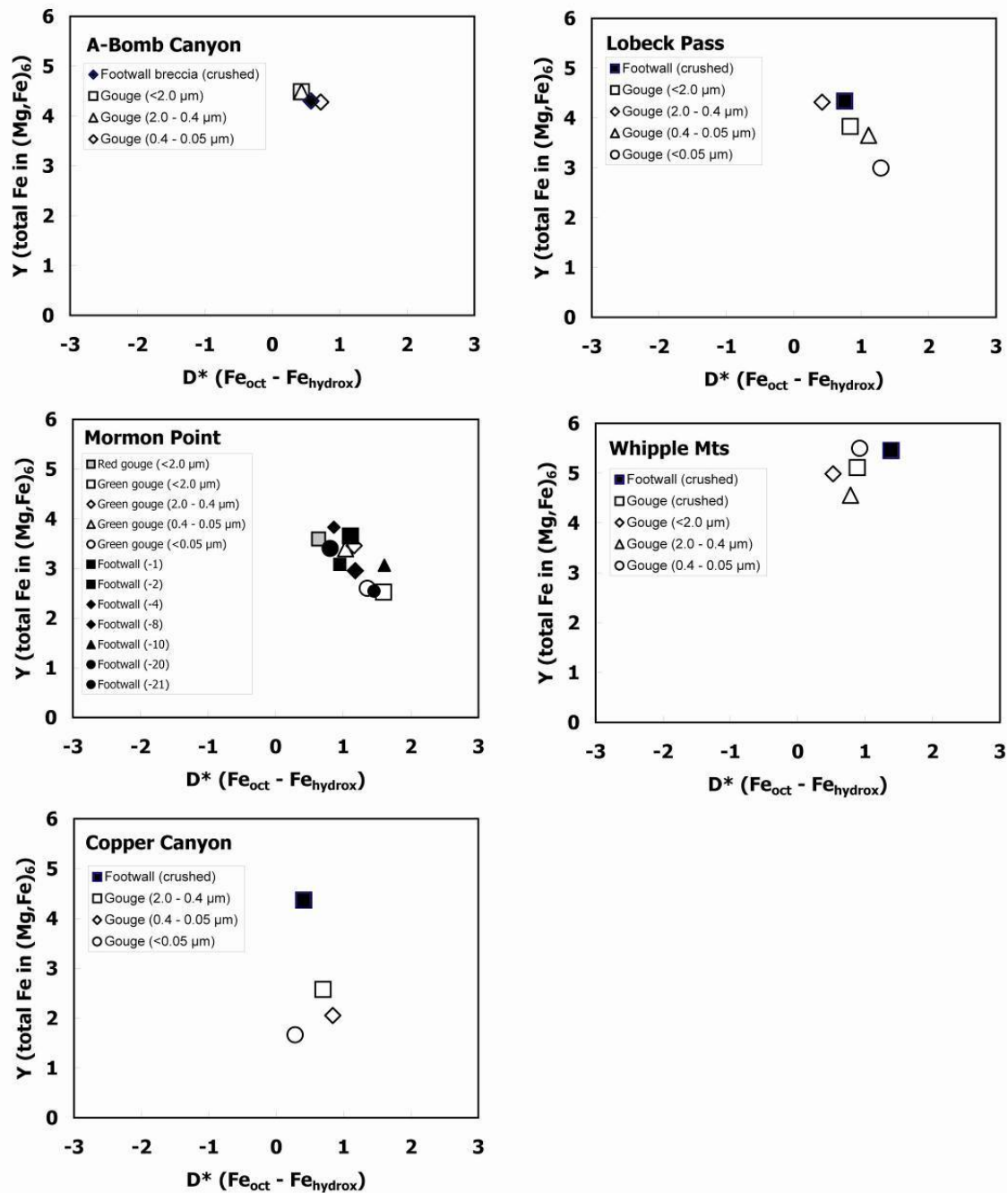


**Figure 2-15:** Photomicrograph of basalt dyke intruded along fault plane at Whip-5. Plane-polarized light. Note relict zoned plagioclase phenocryst in undeformed matrix of altered plagioclase laths and extensive Fe-oxide alteration. Field of view is 3 mm wide.

and the gouge.

To further demonstrate the common origin of the chlorite in the green scaly gouges and footwall, the compositions of chlorite in the footwall and in chloritic gouge at A-Bomb Canyon, Copper Canyon, Lobeck Pass, Mormon Point and the Whipple detachment are estimated from (00l) intensities using the technique of Brown & Brindley (1980). Chlorites in the footwall are somewhat Fe-rich  $((\text{Mg}_{1-1.5}, \text{Fe}_{4.5-5})_6[\text{Si,Al}]_8\text{O}_{20})(\text{OH})_{16}$  and chlorite from chloritic gouge at A-Bomb Canyon, Mormon-2 and the Whipple outcrop is essentially identical in composition to that in the footwall in all size fractions (see Figure 2.16). Chlorite in the finest size fractions at the Chemehuevi detachment expands slightly on glycolation and is slightly more Mg-rich consistent with some alteration of detrital chlorite to a Mg-rich, chloritic chlorite-smectite in the finer size fractions. At Copper Canyon, the chlorite in gouge is significantly more Mg-rich than that in the footwall, and will be discussed further below. The similarity of bulk mineralogy, chlorite composition and polytypism between chlorite in the footwall and chloritic gouge indicates that scaly chloritic gouge horizons are almost entirely detrital in origin and are not the result of chlorite growth in the fault zone during brittle deformation. A Mg-rich clay mineral gouge assemblage is also found at the Dante's View exposure where the wall rocks are not chloritized, and a hangwall rhyolite is juxtaposed against a smectitic tuff by a 50 cm – 1 m thick gouge zone with a distinct 5-10 cm thick tan hard horizon with striated surfaces. The gouge clay mineral assemblage consists predominantly of dioctahedral smectite (montmorillonite) and palygorskite with minor illite and zeolites (heulandite or clinoptillite). Smectite and palygorskite are present in the finest size fraction in roughly equal proportions to those found in the coarse fraction, indicating that both are authigenic. The hard tan layer along the hangingwall contact consists of palygorskite and quartz. The palygorskite is clearly authigenic as it forms a thin vein in





**Figure 2-16:** Graphs of chlorite composition in low-angle normal fault gouge and wallrock composition as estimated from XRD intensities of (00l) peaks of random preparations. (Brown & Brindley, 1980). Data are shown from A-Bomb Canyon, Lobeck Pass, Mormon-2, Whip-5 and Copper Canyon. Plotted are D (anisotropy of Fe distribution between octahedral sheet and hydroxide sheet) on the X axis against Y, total Fe per (Mg,Fe)<sub>6</sub> on the Y axis. Note general Fe-rich compositions and strong similarity of gouge chlorite composition to wall-rock chlorite composition at A-Bomb Canyon, Mormon-2 and Whip-5. Note also minor shift towards Mg-rich compositions in progressively fine size fractions at Lobeck Pass, and strong shift at Copper Canyon, consistent with transformation of chlorite to chlorite-rich chlorite-smectite.

the gouge zone and is not found in wall rock, and the smectite is most likely mechanically incorporated montmorillonite from the footwall tuff, although some smectite could have formed by alteration of clasts of hangingwall rhyolite found in the gouge zone.

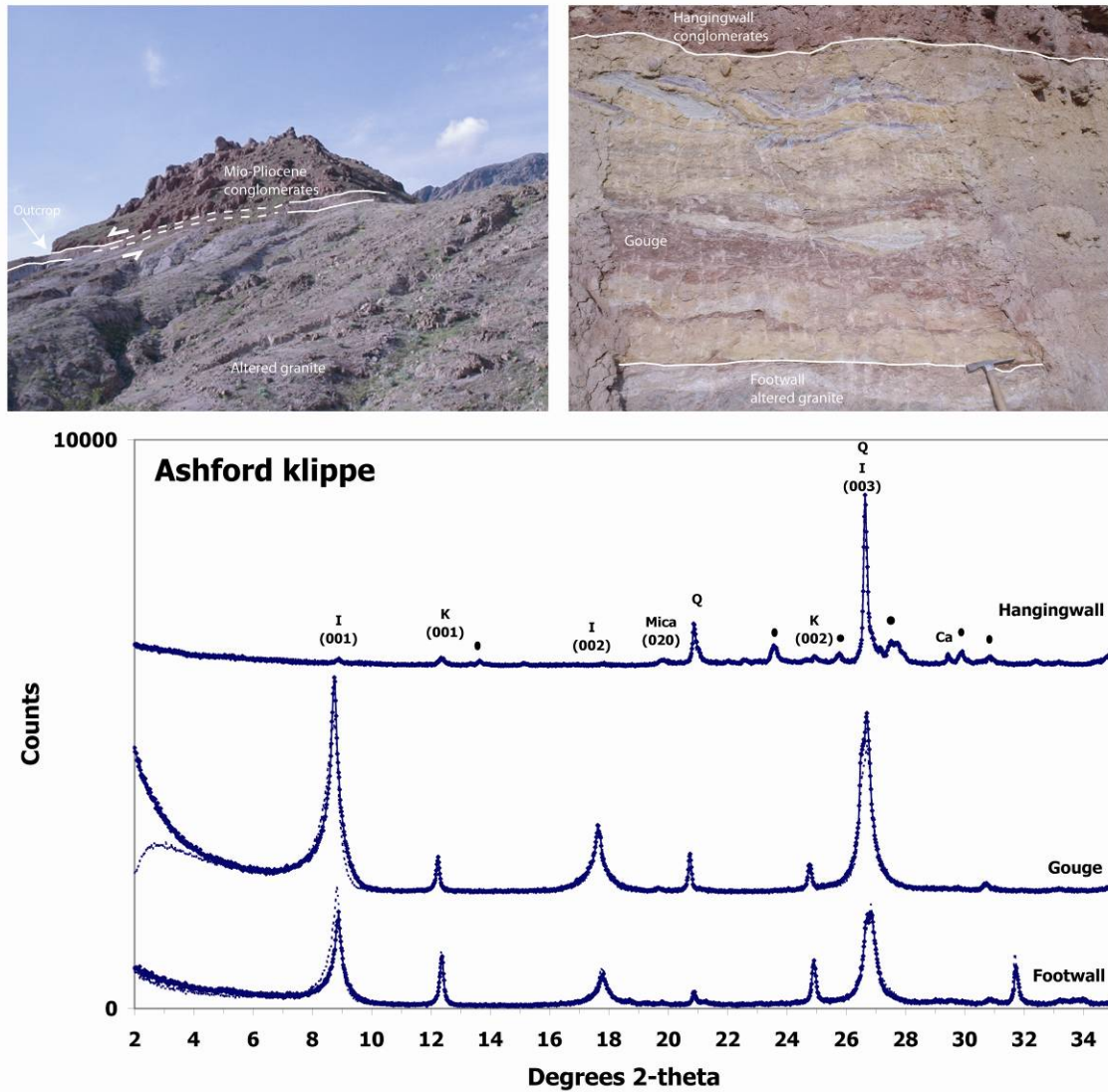
Three detachment fault outcrops with chloritic footwalls do not preserve a distinct scaly chloritic gouge layer, but do have gouges that contain significant chlorite in the coarse and medium fractions and chlorite-smectite minerals in the fine fractions. At the Bullard detachment (Aguila outcrop), the footwall is a chloritized variably mylonitic schist and the hangingwall is a silicified breccia. The gouge layer is 1 m thick and consists of three layers visible at outcrop, one dominated by chlorite with subsidiary tri-octahedral smectite, and two very similar layers with predominantly tri-octahedral smectite and subsidiary altered chlorite. At the Wonderstone Wash outcrop of the Salton Sea detachment, the gouge is 20-50 cm thick and consists predominantly of a tri-octahedral smectite and kaolinite with minor chlorite and a 10 Å mica, either illite or muscovite. The smectite is most likely derived from extensive alteration of chloritic footwall schists.

#### Illitic gouges

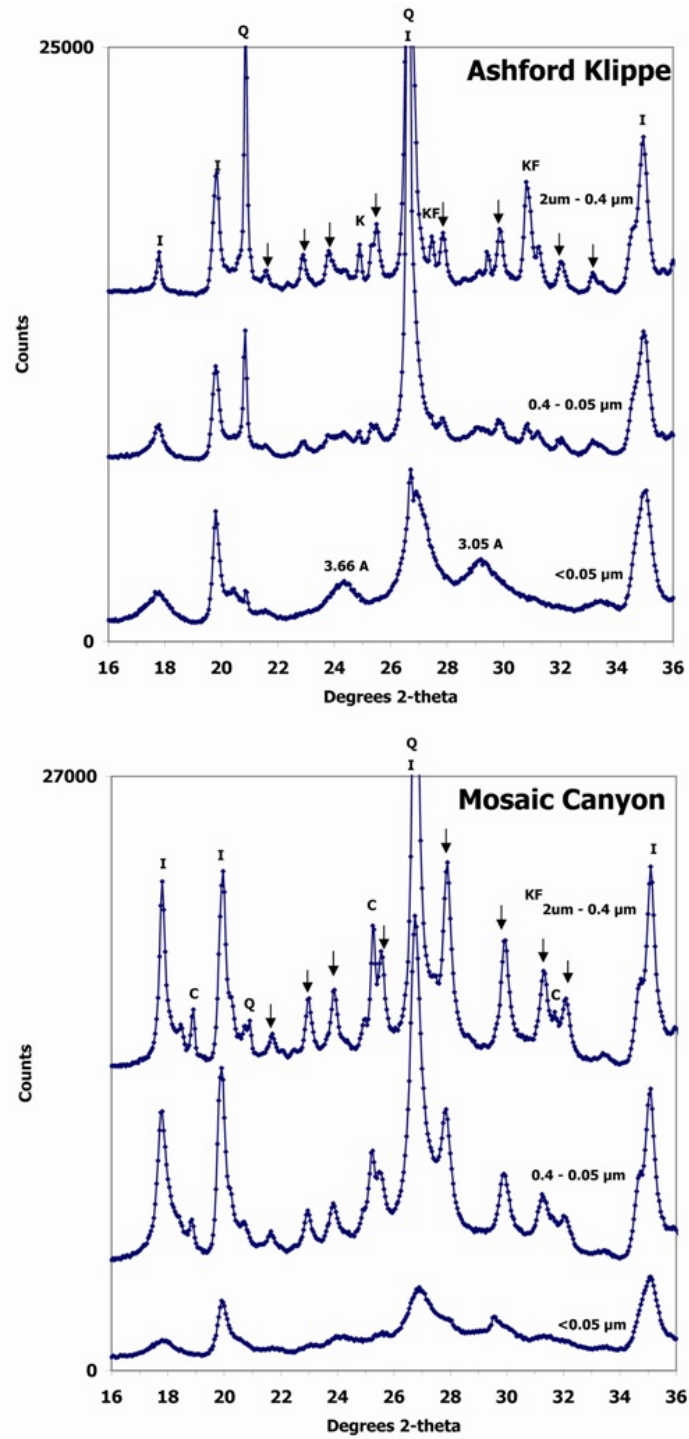
The remaining 19 detachment exposures have gouges that are dominated by authigenic illite or illite-rich illite-smectite. Of these, 6 detachment exposures have chloritized footwalls and gouges that are predominantly illitic (Badwater-1, Badwater-2, Bullard (Bullard outcrop), Wildrose Canyon, Mosaic Canyon, Whipple Detachment (Whip-5 – also discussed above)). The other 13 exposures have widely varying footwall compositions: granite (Ashford Klippe, Central Mojave core complex, Sierra Mazatàn, Size 36 Canyon), quartzofeldspathic schist or gneiss (Exclamation Rock, Mormon-1,

Virgin Springs, Wildrose Canyon), greenschist-facies metapelites (Tucki, South Park Canyon) shales (Secret-1, Secret-2) and variably silicified marbles (Clover-1, Secret-4). Two main classes of illitic gouges are distinguished, those with a transformation from the high-temperature  $2M_1$  polytype of illite (or muscovite) to the low-temperature  $1M_d$  polytype of illite, and gouges where a transformation from K-feldspar to the  $1M_d$  polytype of illite occurs. Both transformations occur in faults with and without chloritic footwalls. Seven detachment fault exposures have gouges where a transition from  $2M_1$  illite to  $1M_d$  illite occurs. At Ashford Klippe (see Figure 2.17) a hangingwall of Pliocene conglomerates is separated from a footwall of altered granite by a 1 m thick zone of variegated reddish, yellowish and greenish gouge. The gouge consists predominantly of illite and minor kaolinite. When separated into size fractions the gouge shows a clear transition from predominantly the  $2M_1$  polytype in the coarse and medium size fractions to an almost pure  $1M_d$  polytype in the finest size fraction (see Figures 2.18 and 2.19). Similar transitions from a coarse-grained detrital illite or muscovite are observed at Mosaic Canyon (see Figure 2.18), Sierra Mazatan (see Chapter 4, the Emigrant Fault (Tucki outcrop – see table 3), Ruby Mountains detachment (Clover Hill outcrop – see Chapter 6), and the Amargosa detachment (Exclamation Rock and Virgin Springs outcrops – see Table 3).

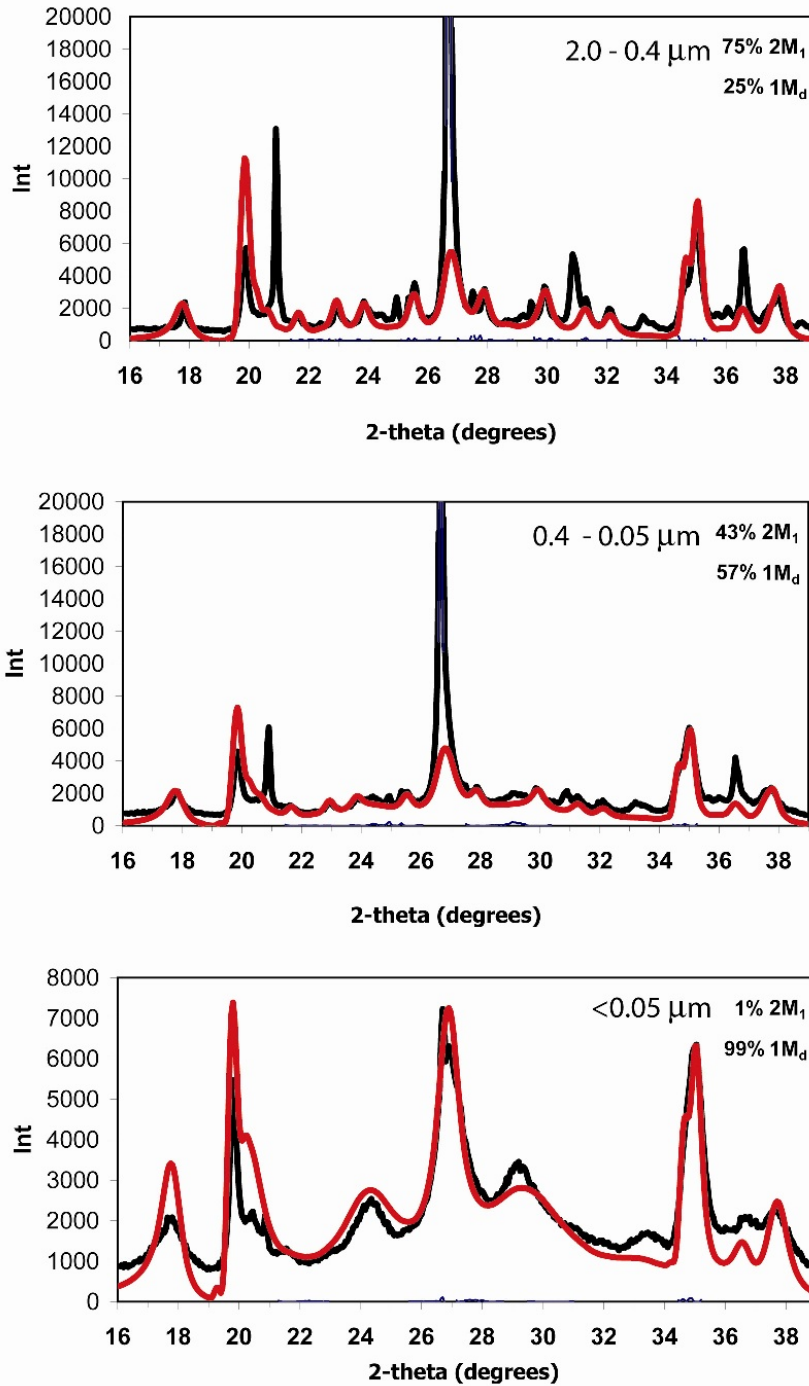
Eight detachment fault exposures have gouges where a transformation can be observed from detrital feldspar-dominated material to the authigenic  $1M_d$  polytype of illite. These gouges conspicuously lack the  $2M_1$  polytype of illite in any size fraction. At Badwater-1, a chloritic metasomatized quartzofeldspathic gneiss is separated from a hangingwall of weakly consolidated gravels and fluviually-reworked tuffs by a 20 cm thick clayey gouge (see Figure 2.20). The gouge consists predominantly of feldspar and illite, with chlorite



**Figure 2-17:** Outcrop photographs and XRD patterns of clay gouges from the Amargosa detachment at Ashford Klippe. XRD patterns are of oriented preparations of clay fraction (<2.0  $\mu\text{m}$ ), dashed line = air-dried, solid = glycol solvated. Note illitic nature of gouge and footwall altered granite. I = illite, K = kaolinite, Q = quartz, Ca = calcite, filled circles = K-feldspar



**Figure 2-18:** XRD patterns of random preparations of gouges from Ashford Klippe and Mosaic Canyon illustrating the transformation from 2M1 illite in the coarse and medium fractions to 1Md illite in the fine fraction.



**Figure 2-19:** XRD patterns of gouge from Ashford Klippe (previous figure) modeled using WILDFIRE. Note large shift in relative abundance of  $2M_1$  and  $1M_d$  polytypes between the coarse and fine size fractions. K = kaolinite, KF = K-feldspar, Q = quartz, I = illite, arrows are  $2M_1$  illite-specific polytype peaks

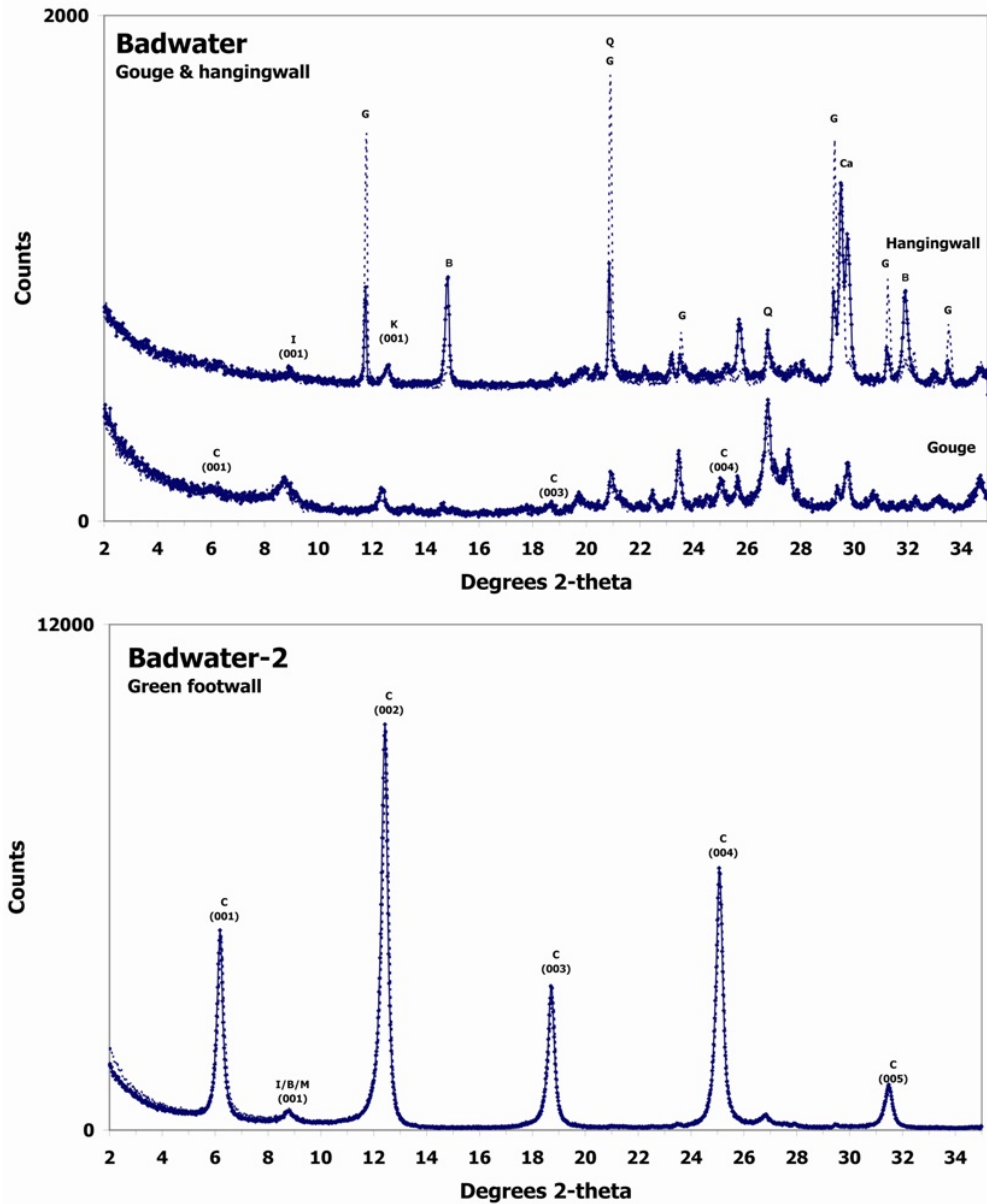


**Figure 2-20:** Outcrop photographs of the Badwater detachment at Badwater-1. Lower figure is taken at outcrop 50 m S of view in upper image. Note strong color change between illitic gouge and chloritic footwall. Note also sub-horizontal ashes in hangingwall displaced by steep normal faults. The sub-horizontal nature of the hangingwall ashes indicate slip at the current dip of  $36^\circ$ .

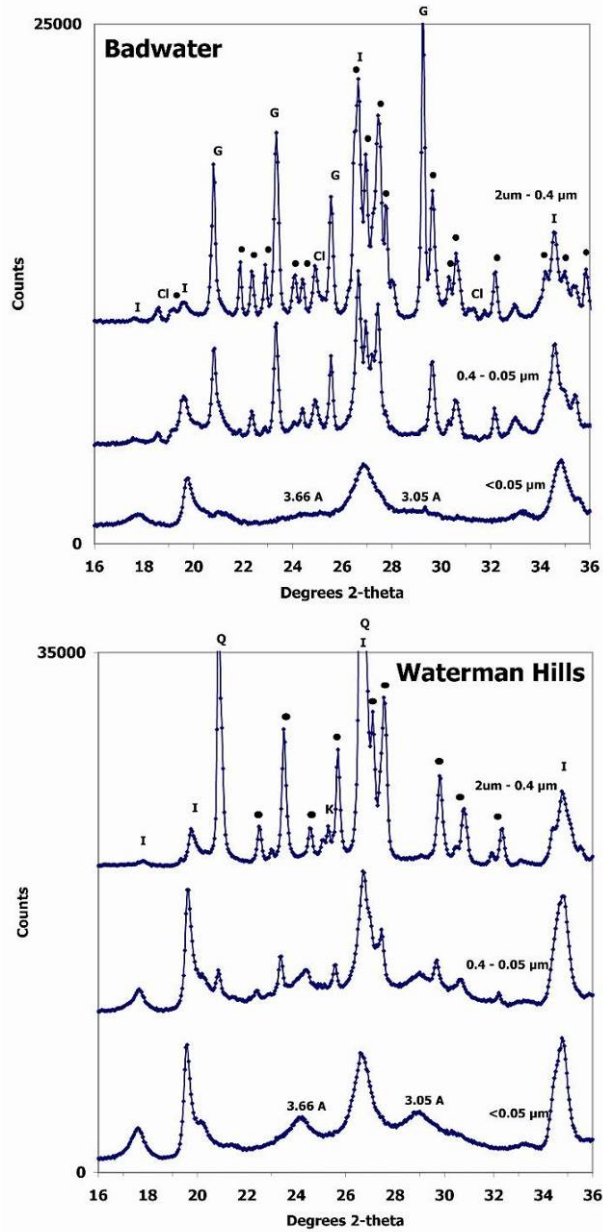
present in amounts only slightly above the limits of XRD detection (see Figure 2.21). Separation of the gouge into size fractions indicates that the coarse and medium size fractions of the gouge are dominated by microcline with subsidiary illite, and the fine size fraction consists entirely of a  $1M_d$  illite (see Figure 2.22). Although the strong feldspar peaks interfere with the area where the polytype-specific peaks for the  $2M_1$  polytype of illite are found, no  $2M_1$ -specific peaks are identifiable. The relative absence of chlorite in the gouge at Badwater indicates that the majority of detrital material in the gouge is being contributed by the hangingwall. The same reaction is observed in gouge at the Waterman Hills outcrop of the Central Mojave core complex detachment fault (see Figure 2.21), where no  $2M_1$  peaks are observed, but the polytype-specific peaks at  $24.3^\circ$  and  $29.1^\circ$  can be observed in all size fractions, although the peaks are much less intense in the coarse and medium size fractions owing to the presence of detrital feldspar in those size fractions. The same K-feldspar  $\rightarrow$   $1M_d$  illite reaction is observed in gouges at Badwater-2, Bullard, Mormon-1, Size 36, Canyon, South Park Canyon and Whip-5 – see Figure 2.14). The absence of the  $2M_1$  polytype in any size fraction and the presence of the  $1M_d$  polytype in all size fractions indicates that the authigenic  $1M_d$  illite is growing directly from the breakdown of detrital feldspar and not from the replacement of a detrital  $2M_1$  polytype by an authigenic  $1M_d$  polytype as has been reported from fault gouges elsewhere (van der Pluijm et al, 2001, 2006; Solum et al., 2005; Haines & van der Pluijm, 2008).

Four detachment fault exposures contain gouge where the dominant clay mineral is authigenic illite-rich illite-smectite (the three exposures of the Ruby Mountain detachment fault at Secret Pass (Secret-1, Secret-2 & Secret-4), and at Wildrose Canyon). At Secret Pass, three faults associated with the detachment are exposed (see





**Figure 2-21:** XRD patterns of the clay fraction of footwall, gouge and hangingwall at Badwater-1. Oriented preparations, dashed line = air-dried, solid = glycol solvated. C = chlorite, I = illite, K = kaolinite, Ca = calcite, G = gypsum, B = bassanite. I/B/M = 10 Å mica (illite, biotite, muscovite). Note lack of chlorite in gouge despite extensive chloritization of the footwall.



**Figure 2-22:** XRD patterns of random preparations of gouge from Badwater-1. (previous figure) and the Waterman Hills illustrating the transformation of K-feldspar to  $1M_d$  illite. Note the absence of  $2M_1$ -specific peaks and the presence of  $1M_d$  peaks in all size fractions of the Waterman Hills gouge. I = illite, Cl = chlorite, G = gypsum, Q = quartz, filled circles = feldspar peaks (undifferentiated).

Chapter 6 for a comprehensive treatment of the outcrops and clay mineralogy), the authigenic illite-smectite is a 1-water layer disordered illite smectite (85% I in I/S, R0) and forms by the illitization of hangingwall illite-smectite at Secret -1 and Secret-2, while at Secret-4 the detachment juxtaposes zeolitized tuffs in the hangingwall against silicified carbonate mylonites in the footwall. The tuffs are altered to pure montmorillonite in the upper layer of gouge at the outcrop and the lower layer consists almost exclusively of illite-rich illite-smectite. The source of the illite is <50 m along strike, where the hangingwall lithology changes from the Miocene zeolitized tuff to Mississippian shales, which were smeared along the fault plane and transformed to the authigenic I/S phase while the fault was active, evidenced by an Ar-Ar age of 12.4 Ma that is consistent with regional constraints on the time of fault movement (see Chapter 6. At Wildrose Canyon, a hangingwall of Pliocene conglomerates is separated from a footwall of chloritized amphibolite schist intercalated with mylonitic marble. The gouge zone is 30 cm thick and contains predominantly quartz, feldspar (both plagioclase and microcline) with lesser amounts of R3 illite-smectite and chlorite. Upon separation into size fractions, the abundance of the R3 I/S increases from the coarse to the fine size fraction, and the abundance of chlorite decreases (see Table 3). Trace amounts of talc are also present in the medium and fine size fractions. The gouge contains minerals clearly derived from both walls of the fault. The microcline is derived from the hangingwall as the footwall lacks potassic minerals, and is the most reasonable source of  $K^+$  for the illite-smectite, while the chlorite in the gouge is derived from the footwall.  $Mg^{++}$  required for talc growth is most likely derived from the footwall dolomitic marbles. No age relationship between the authigenic illite and authigenic talc can be determined from outcrop or the XRD patterns.

## Discussion

The clay mineral assemblages found in low-angle normal fault gouges indicate that mineral transformations in LANF clay gouges are widespread and ubiquitous. Only one exposure, Mormon-2 lacked evidence for any clay mineral transformation in the fault gouge. Numerous different transformations occur in fault gouge, but can be broadly grouped into three mineralogical reaction series :

- 1.) Chlorite → chlorite/smectite and tri-octahedral smectite
- 2.) Mg-rich fluid + silicates → Mg-rich phyllosilicate assemblage  
(palygorskite or sepiolite, talc, lizardite, smectite)
- 3.)  $1M_d$  illite growth reactions.

The chlorite-corrensite-smectite transformations can be thought of as 'retrograde diagenesis', while the Mg-rich assemblages and the K-rich illitic and I/S assemblages are both responses to external fluid fluxes.

### Chlorite and chlorite-breakdown gouges

Whereas the chloritic gouge preserved in some low-angle normal faults could be considered authigenic as it formed while the detachment was active at greenschist-facies conditions, it is clearly detrital material derived from the wall rock with respect to the subsequent brittle deformation. This chlorite-dominated detrital gouge is frequently transformed to mixed-layer chlorite-smectite phases and discrete tri-octahedral smectite (saponite). The initial chlorite in the metasomatic breccias and detrital gouge is relatively

Fe-rich, and the reaction sequence of chlorite to mixed-layer chlorite smectite phases to smectite results in a gradual removal of Fe and enrichment of Mg from the original detrital chlorite. This process of Mg enrichment of fault gouges of the Black Mountains is also apparent from geochemical data (Hayman, 2006). The reaction series can be thought of as 'retrograde diagenesis' of tri-octahedral phyllosilicates. The prograde diagenetic transformation of saponite to chlorite in mafic rocks has been extensively documented (e.g., Shau & Peacor, 1992) and the saponitic and corrensite gouges seen at many detachment outcrops can be considered a diagenetic reaction series in reverse, as the detrital chloritic gouge is transformed into a lower-temperature assemblage when the gouge is brought to progressively higher structural levels during detachment slip. Similar retrograde transformations of chlorite to corrensite and smectite have been observed in several sedimentary basins (e.g., Nieto et al., 2005).

Two distinct Mg-rich assemblages can be recognized in fault gouges, an authigenic sepiolite + sepiolite + talc + lizardite assemblage, and authigenic palygorskite growing in association with chlorite or quartz. Both formed from circulation of Mg-rich fluids along the fault plane at temperatures  $\ll 200$  °C late in the active slip history of the fault. Sepiolite and palygorskite are both fibrous Mg-rich phyllosilicates that form at very low temperatures (25 – 150 °C) and are rarely reported in fault rocks. Both minerals are principally found in association with evaporative carbonate and phosphatic environments in continental settings and as authigenic minerals in shallow and deep marine sediments, although vein occurrences of both minerals are known (Jones & Galan, 1988). Sepiolite is more common in continental settings (e.g. Hay et al., 1986), especially evaporative lacustrine environments, while palygorskite is more often reported as an authigenic mineral in marine sediments (e.g., Coutoure, 1977). In both settings, sepiolite and palygorskite form as a result of the interaction of Si- and Mg-rich alkali (pH

7-9) oxidized fluids with detrital minerals such as chlorite and illite at temperatures <<200 °C (Jones & Galan, 1988). The lowest possible temperature limit of the sepiolite + smectite + talc + lizardite assemblage is indicated by the synthesis of sepiolite and talc at 25 °C from fluids of pH > 8.5 (Siffert & Wey, 1962). The lower temperature limit for the growth of lizardite is uncertain, but certainly below 200 °C (O'Hanley et al., 1989). A temperature limit for the formation of the sepiolite + smectite + talc + lizardite assemblage is thus unclear, but is probably in the range of 50-150 °C. The source of the Mg-rich fluid is also uncertain, although dolomitic marbles found in the footwall at Mormon Point are a likely source of Mg in the Black Mountains turtlebacks (Hayman, 2006). A meteoric or basinal origin for the fluids seems far more likely than an igneous or metamorphic source owing to the low temperatures and alkali-rich oxidizing nature of the conditions required for the growth of either assemblage. As palygorskite contains significantly more Al than sepiolite, and the palygorskite assemblage is never found in conjunction with the sepiolite + smectite + talc + lizardite assemblage, the two assemblages may be the result of a common Mg-rich fluid interacting with relatively Al-poor chloritic gouge and wall rocks at Mormon Point to form sepiolite + smectite + talc + lizardite, and interacting with gouge partially derived from more Al-rich wall rocks (granites and rhyolites) at Lobeck Pass and Dante's View to form palygorskite. Both Mg-rich assemblages probably formed quite late in the history of the fault, although prior to the end of fault slip, as meteoric or basinal fluids descended the detachment locally scavenging Mg from dolomitic wall rock and reacted with older fault gouge.

#### Illite growth gouges

The growth of the authigenic 1M<sub>d</sub> polytype of illite in fault gouge is increasingly documented (van der Pluijm et al., 2001, 2006; Solum et al., 2005; Haines & van der

Pluijm, 2008, chapters 4, 5 & 6). All previous demonstrations of the growth of illite in fault gouge have documented a transformation from the high-temperature  $2M_1$  polytype to the low-temperature  $1M_d$  polytype or the illitization of illite-smectite (Vrolijk & van der Pluijm, 1999; Solum et al., 2005). Both transformations are observed in outcrops sampled in this study. The growth of authigenic  $1M_d$  illite by the breakdown of K-feldspar has been posited, but not demonstrated to occur in brittle fault rocks (Wintsch et al., 1995). The systematic change in gouges where the coarse fraction is dominated by K-feldspar and the fine fraction is dominated by  $1M_d$  illite and the absence of the  $2M_1$  polytype of illite in any size fraction indicates that K-feldspar is being broken down in the presence of water to form illite in some natural gouges. Large-scale K-feldspar metasomatism locally associated with economic (Au, Ag, Cu) deposits and extensive precipitation of hematite and Fe oxyhydroxides, has been documented in the hangingwalls of three detachment faults sampled in this study (Whipple detachment, Bullard detachment and the Buckskin-Rawhide detachment) and at several other metamorphic core complexes (e.g., the Picacho and Santa Catalina metamorphic core complexes AZ, Brooks, 1986). Oxygen isotope data from secondary K-feldspar indicate that the fluids responsible for upper-plate metasomatism were sedimentary brines that were neutral to alkalic and oxidizing (Roddy et al., 1988, Beretan, 1999). The same fluids may be responsible for the growth of authigenic illite in fault gouge in low-angle normal faults region-wide as meteoric or sedimentary fluids descended the fault plane, forming illite by the breakdown of K-feldspar and the precipitation of Fe oxyhydroxides responsible for the characteristic reddish color of many of the illitic gouges. However, geochemical data from the Black Mountains gouges demonstrate an enrichment of illite in fault gouge relative to the footwall, but only a minor change in the  $K_2O$  content of the gouge relative to the footwall, indicating that mineral transformations are occurring, but the fluids responsible for growth of hydrous phases are not 'flooding' the gouges with externally-sourced  $K^+$ , as

might be expected from K-feldspar metasomatism (Hayman, 2006). As illitic gouges are not confined to detachments with intense upper-plate K-feldspar metasomatism, authigenic illite growth in gouge and K-metasomatism of upper-plate rocks must be different processes. It has been demonstrated that descending meteoric or basinal fluids use upper-plate extensional faults as conduits (Roddy, 1988, Beretan, 1998), and it is possible that only in some detachment fault systems do they have enough exposure to potassic rocks to enrich sufficiently with K<sup>+</sup> to cause the upper-plate metasomatism seen in the Arizona core complexes that is rare elsewhere.

The relative proximity of the three Mormon Point outcrops and yet their highly variable clay mineral compositions, illustrate the importance of local wall rock composition and the variability of fluid circulation in gouge mineralogy and mineral transformations. The sepiolite + smectite + talc + lizardite assemblage at Mormon-3 is only 300 m along strike from Mormon-2, the only outcrop where a 'detrital' mechanically-derived chloritic gouge is preserved, indicating that Mg-rich fluid fluxes, and indeed fluid fluxes in general, may be localized phenomena and perhaps controlled by local wall-rock chemistry and not a detachment-scale fluid circulation system. Similarly, Mormon-1 is within 2 km of both of the other outcrops and yet has a gouge dominated by authigenic 1M<sub>d</sub> illite and lacks a detrital chloritic component of the gouge entirely. As footwall chemistry differs strongly between the three outcrops, while the hangingwall rocks are all Pliocene fanglomerates with a presumed common source area, it is likely that footwall chemistry drives clay gouge composition at Mormon Point. Footwall rocks have been observed to contribute much more material to the gouge of low-angle normal faults than hangingwall rocks in the Black Mountains and at Sierra Mazatán (Hayman, 2006, Haines & van der Pluijm, 2008) and this observation can also be applied to almost all the detachments sampled in



this study, except Badwater-1 and Size 36 Canyon, where incorporation of hangingwall material in gouge is documented (Hayman, 2006).

Although mineral transformations in the clay gouges found in low-angle normal faults are almost universal, clay-rich gouges are not universal in low-angle normal faults. Both published results and reconnaissance work for this study indicate that many detachment faults have fault rocks that are lithified cataclasites, consisting solely of silicate or carbonate fragments and lacking evidence of authigenic clay growth. Detachment fault exposures where the brittle fault rocks consist solely of well-indurated cataclasites can be found in many core complexes and low-angle normal faults (see Table 5 for a list). While the core complexes north of the Ruby Mountains in Nevada are mostly Eocene in age and may have been eroded to below the relatively shallow structural depths at which clay-rich gouges might have formed, the lack of clay-rich gouges at some southern core complexes, which are mostly Miocene in age and preserve the shallow structural levels at which clay-rich gouges would form, suggests that clay gouge formation is not a universal process in low-angle normal fault evolution and cannot alone be invoked to solve the mechanical paradox of low-angle normal faults. Where clay gouge formation does occur, however, it may significantly reduce friction on pre-existing detachment surfaces and facilitate slip at significantly lower angles such as the Ruby Mountains (see Chapter 6) and the Black Mountains turtlebacks, where fault slip is thought to have occurred as sliding of an extensional wedge (Hayman et al, 2003b).

| <b>Metamorphic core complex or low-angle normal fault with indurated cataclasite brittle fault rocks</b> | <b>Source</b>                        |
|--|--------------------------------------|
| Shushwap core complex, BC  | Vanderhaeghe et al., (1999)          |
| Lincon metamorphic core complex, WA  | Busch, (1991), Harms & Price, (1992) |
| Pioneer Mountains metamorphic core complex, ID   | O'Neill & Pavlis, (1988)             |
| Copper Mountains detachment, NV  | This study, Rahl et al., (2002)      |
| Raft River metamorphic core complex  | This study, Malavielle, (1987)       |
| Pilot Range detachment, UT/NV  | This study                           |
| Snake Range, NV  | This study, Miller et al., (1983)    |
| Mineral Mountains, UT  | This study, Barnett et al., (1996)   |
| Beaver Dam - Tule Springs - Mormon Mountains detachments   | Axen (2004), Anders et al., (2006)   |
| Newport detachment, NV   | This study                           |
| Whipple Mountains, CA  | Morrison & Anderson, (1998)          |
| Picacho metamorphic core complex, AZ   | Kerrich & Rehrig, W., (1987)         |

**Table 2-5:** List of some metamorphic core complexes and low-angle normal faults that lack clay-rich fault rocks.

## Conclusions

This study identifies and categorizes repeating patterns of clay mineral transformations in clay gouges from low-angle normal faults that are varied both in space and time. In detachment faults where the brittle detachment evolved from a mid-crustal shear zone with chloritically metasomatized footwall rocks, a pattern of an early chlorite-rich gouge that is detrital in origin being transformed to a 'retrograde diagenetic' assemblage of chlorite-smectite or discrete tri-octahedral smectite (saponite) is identified. The early detrital gouge is preserved in gouge zones at several core complexes and is mineralogically indistinguishable from the footwall chlorite breccias. This detrital chlorite is then frequently transformed into either chlorite-smectite (both random chlorite-smectite and corrensite are observed) or discrete smectite. The detrital chloritic gouge can also be locally transformed to one of two Mg-rich assemblages, a sepiolite + smectite + talc + lizardite assemblage, or palygorskite +/- chlorite +/- quartz. The Mg-rich assemblages

form at low temperatures (50-150 °C) by interaction of locally Mg-rich fluids with detrital chloritic gouge. It is noted that talc and lizardite are present only as minor constituents in the Mg-rich assemblages and are thus not a major factor in fault frictional properties (cf. Moore & Rymer, 2007). Authigenic  $1M_d$  illite and illite-rich illite-smectite are found in many fault gouges, both in detachments that evolved from mid-crustal shear zones and in detachments that formed and slipped entirely in the brittle regime. Authigenic illite and illite-smectite are observed to form by three processes. 1.) Transformation of detrital  $2M_1$  illite or muscovite to authigenic  $1M_d$  illite. 2.) Breakdown of K-feldspar to form authigenic  $1M_d$  illite. 3.) Illitization of detrital illite-smectite to form authigenic illite-rich illite-smectite. Transformations in clay gouges produce clay-rich fault rocks with lower coefficients of friction than is common for silicate rocks, and thus have the potential to significantly weaken the surfaces of pre-existing detachments. However, as clay-rich gouges are not ubiquitous in low-angle normal faults, they cannot alone be invoked to explain slip at anomalously low dips on these structures.

**Acknowledgments:** This study was funded by NSF grant EAR-047707, the Scott Turner Fund at the University of Michigan and an AAPG Grant-in-Aid to Haines. We are grateful to Daryl Cowan who introduced us to the fault rocks of the Black Mountains. We are also grateful to Carl Henderson for maintenance of the EMAL facility at the University of Michigan.

## References

- Anders, M., Christie-Blick, N. & Walker, C., (2006). Distinguishing between rooted and rootless detachment faults: A case study from the Mormon Mountains of southeastern Nevada. *J. Geology* 114, pp. 645-664.
- Anderson, E. (1942) The mechanics of faulting and dyke formation with respect to Britain: Edinburgh, Oliver and Boyd, 191 pp.
- Anderson, R., (1971). Thin skin distension in Tertiary rocks of southeastern Nevada. *Geological Society of America Bulletin* 82, p. 43-58.
- Anderson, R., (2007). A blister hypothesis for the Central Mojave metamorphic core complex near Barstow, California. *Geological Society of America Abstracts with Programs*, vol 39, pp. 227.
- Armstrong, R., (1972). Low-angle (denudation) fault, hinterland of the Sevier orogenic belt, eastern Nevada and western Utah. *Geological Society of America Bulletin* 83, p. 1729-1754
- Axen, G. (2004) Mechanics of low-angle normal faults. *In* Rheology and deformation of the lithosphere at continental margins, Karner, et al, eds. Columbia, pp. 45-91.
- Axen, G., Bartley, J., (1997). Field tests of rolling hinges: Existence, mechanical types, and implications for extensional tectonics. *J. Geophysical Research B* 102, pp. 20,515 - 20,537.
- Axen, G., & Fletcher, J., (1998). Late Miocene-Pleistocene extensional faulting, northern Gulf of California, Mexico and Salton Trough, California *International Geology Review*, 40, pp. 217 -244
- Axen, G., Taylor, W., & Bartley, J., (1993). Space-time patterns and tectonic controls of Tertiary extension and magmatism in the Great Basin of the western United States. *Geological Society of America Bulletin* 105, pp. 56-76.
- Barnett, D., Bowman, J., Bromley, C. & Cady, C., (1996). Kinematically limited isotope exchange in a shallow level normal fault, Mineral Mountains, Utah. *J. Geophysical Research B* 101, pp. 673-685.
- Beretan, K., (1999). Miocene potassium metasomatism, Whipple Mountains, southeastern California: A dateable tracer of extension-related fluid transport. *Geology* 27, pp. 259-262.
- Brooks, W., (1986). Distribution of anomalously high K<sub>2</sub>O volcanic rocks in Arizona: Metasomatism at the Picacho Peak detachment fault. *Geology* 14, pp. 339-342.
- Brown, G. & Brindley, G., (1980). X-ray diffraction procedures for clay mineral identification: *in* Brindley, G. & Brown, G., eds., Crystal structures of clay

minerals and their X-ray identification, *Monograph 5*, Mineralogical Society, London, p. 305-359.

- Brown, K., Kopf, A., Underwood, M. & Weinberger, J., (2003). Compositional and fluid pressure controls on the state of stress on the Nankai subduction thrust: a weak plate boundary. *Earth and Planetary Science Letters* 214, pp. 589-603.
- Buck, W. (1988) Flexural rotation of normal faults, *Tectonics* 7 pp. 959-973.
- Busch, J., (1991). Structural geology and development of the Lincon metamorphic core complex, northeast Washington. Unpublished M. Sc. Thesis, Washington State University, 126 pp.
- Byerlee, J., (1978). Friction of rocks. *Pure and Applied Geophysics* 116, pp. 615-626.
- Calzia, J., Frisken, J., Jachens, R., McMahan, A., & Runsey, C., (1986). Mineral resources of the Kingston Range Wilderness Study Area, San Bernardino County California: *U.S. Geological Survey Bulletin* 1709-C, 21 p.
- Campbell-Stone, E., John, B., Foster, D., Geissman, J. & Livaccari, R., (2000). Mechanisms for accommodation of Miocene extension: Low-angle normal faulting, magmatism, and secondary breakaway faulting in the southern Sacramento Mountains, southeastern California. *Tectonics*, 19, pp. 566-587.
- Carter, T., Kohn, B., Foster, D., Gleadow, A., & Woodhead, J., (2006). Late stage evolution of the Chemehuevi and Sacramento detachment faults from apatite (U/Th)/He thermochronometry – Evidence for mid-Miocene accelerated slip. *Geological Society of America Bulletin* 118, 689-709.
- Cichanski, M., (2000). Low-angle range-flank faults in the Panamint, Inyo and Slate ranges, California: Implications for recent tectonics of the Death Valley region. *Geological Society of America Bulletin* 112, p. 871-883.
- Christie-Blick, C., Anders, M., Willis, S., Walker, C. & Renik, B., (2007). Observations from the Basin and Range province (western United States) pertinent to the interpretation of regional detachment faults. *In: Imaging, mapping and modeling continental lithospheric extension and breakup*, Karner, G. et al., eds.. *Geological Society of London Special Publication* 282, pp. 421-441.
- Cladouhos, T., (1999), Shape preferred orientations of survivor grains in fault gouge. *J. Structural Geology* 21, p. 419-436.
- Colgan, J., & Metcalf, J, (2006) Rapid middle Miocene unroofing of the southern Ruby Mountains, Nevada: *Geological Society of America Abstracts with Programs*, v. 38, no. 7, p. 417.
- Collettini, C. & Sibson, R. (2001) Normal faults, normal friction? *Geology* 29, pp. 927-930.

- Couture, R., (1977). Composition and origin of palygorskite-rich and montmorillonite-rich zeolite-containing sediments from the Pacific Ocean. *Chemical Geology* 19, pp. 113-130.
- Cowan, D., Cladouhos, T., & Morgan, J., (2003), Structural geology and kinematic history of rocks formed along low-angle normal faults, Death Valley, California. *Geological Society of America Bulletin* 115, p. 1230-1248.
- Cowan, Darrel S., (1999), Do faults preserve a record of seismic slip? - a field geologist's opinion. *J. Structural Geology* 21, p. 2703-2719.
- Cowan, D., & Miller, M., (1999), Distributed flow vs. localized slip in late Cenozoic low-angle fault zones, Death Valley, California. *Seismological Research Letters* 70, p. 247.
- Crittenden, M. et al, (1980) eds. Cordilleran metamorphic core complexes *Geological Society of America Memoir* 153, 400 pp.
- Curry, H. (1938) "Turtleback" fault surfaces in Death Valley, California. *Geological Society of America Bulletin* 49, p. 1875.
- Davis, G., (1988). Rapid upward transport of mid-crustal mylonitic gneisses in the footwall of a Miocene detachment fault, Whipple Mountains, southeastern California. *Geologische Rundschau* 77, pp. 191-209.
- Davis, G. & Coney, P., (1979). Geologic development of the Cordilleran metamorphic core complexes. *Geology* 7, pp. 120-124.
- Davis, G., Anderson, E., Frost, E. & Shackelford, T., (1980). Mylonization and detachment faulting in the Whipple-Buckskin-Rawhide Mountains terrane, southeastern California and western Arizona. *in: Crittenden, M. et al., (1980) eds. Cordilleran metamorphic core complexes Geological Society of America Memoir* 153, pp. 79-130.
- Davis, G., & Lister, G., (1988), Detachment faulting in continental extension: Perspectives from the southwestern U.S. Cordillera, *in: Clark, S., Burchfiel, B., and Suppe, J., eds., Processes in continental lithospheric deformation: Geological Society of America Special Paper* 218, p. 133–159.
- Dokka, R., & Glazner, A., (1982). Aspects of early Miocene extension in the central Mojave desert, Geological excursions in the California desert, *Geological Society of America Cordillerian section guidebook*, pp. 31-45.
- Fletcher, J., Bartley, J., Martin, M., Glazner, A., & Walker, J., (1995). Large-magnitude continental extension: An example from the central Mojave metamorphic core complex. *Geological Society of America Bulletin* 107, pp. 1468-1483.
- Foster, D., Gleadow, A., Reynolds, S., & Fitzgerald, P., (1993). Denudation of metamorphic core complexes and the reconstruction of the transition zone, west central Arizona—Constraints from apatite fission-track thermochronology: *Journal of Geophysical Research B*, 98, p. 2167–2185.

- Foster, D., John, B., Campbell, E., & Fanning, C., (1996). The timing and role of syntectonic plutonism in development of the Colorado River Extensional Corridor: Sacramento Mountains example, *Geol. Soc. Am. Abstr. Programs*, 28(7), 450, 1996a.
- Foster, D. & John, B., (1999). Quantifying tectonic exhumation in an extensional orogen with the thermochronology: Examples from the southern Basin and Range Province, *in: Exhumation Processes: Normal Faulting, Ductile Flow, and Erosion*, eds. Ring, U et al. *Geological Society Special Publication* 154, pp. 356-378.
- Froitzenheim, N. & Eberli, G., (1990). Extensional detachment faulting in the evolution of a Tethys passive margin, Eastern Alps, Switzerland. *Geological Society of America Bulletin* 102, p. 1297-1308.
- García-Romero, E., Suárez, M., Oyarzun, R., López-García, J. & Regueiro, M., (2006). Fault-hosted palygorskite from the Serata de Níjar deformation zone (SE Spain). *Clays and Clay Minerals* 54, pp. 324-332.
- Haines, S. & van der Pluijm, B., (2008). Clay quantification and Ar-Ar dating of synthetic and natural gouge: Application to the Miocene Sierra Mazatán detachment fault, Sonora, Mexico. *J. Structural Geology* 30, pp. 525-538.
- Harms, T. & Price, R., (1992). The Newport Fault: Eocene listric normal faulting, mylonization and crustal extension in northeast Washington and northwest Idaho. *Geological Society of America Bulletin* 104, pp. 745-761.
- Hay, R., Pexton, R., Teague, T., & Kyser, T., (1986). Spring-related carbonate rocks, Mg clays and associated minerals in Pliocene deposits of the Amargosa Desert, Nevada and California. *Geological Society of America Bulletin* 97, pp. 1488-1503.
- Hayman, N., Housen, B., Cladouhos, T. & Livi, K., (2003a). Magnetic and clast fabrics as measurements of grain-scale processes within the Death Valley shallow crustal detachment faults. *J. Geophysical Research B* 109, doi:10.1029/2003JB002902
- Hayman, N., Knott, J., Cowan, D., Nemser, E., & Sarna-Wojcicki, A., (2003b), Quaternary low-angle slip on detachment faults in Death Valley, California. *Geology* 31, p. 343-346.
- Hayman, N., (2006) Shallow crustal fault rocks from the Black Mountain detachments, Death Valley, CA. *J. Structural Geology*, 28, pp. 1767-1784.
- Hodges, K., McKenna, L., Stock, J., Knapp, J., Page, L., Sternlof, K., Silverberg, D., Wust, G. & Walker, J., (1989). Evolution of extensional basins and Basin and Range topography west of Death Valley, California. *Tectonics* 8, pp. 453-467.
- Hodges, K., McKenna, L., & Harding, M., (1990). Structural unroofing of the central Panamint Mountains, Death Valley region, southeastern California. In: Basin and Range extensional tectonics near the latitude of Las Vegas, Wernicke, B., ed. *Geological Society of America Memoir* 176, pp. 377-390.

- Holm, D. & Dokka, R. (1993) Interpretation of cooling histories: An example from the Death Valley extended terrane, California. *Earth and Planetary Sciences Letters* 116, pp. 63-80.
- Howard, K. (1980) Metamorphic infrastructure in the northern Ruby Mountains, Nevada, *in: Cordilleran metamorphic core complexes*. Crittenden, M. et al. eds., *Geological Society of America Memoir* 153, pp. 335-347.
- Howard, K., & John, B., (1987). Crustal extension along a rooted system of imbricate low-angle faults: Colorado River extensional corridor, Californian and Arizona. *In: Continental Extensional Tectonics*, Coward, M et al., eds. *Geological Society of America Special Publication* 28, pp. 299-311.
- Jackson, J. (1987). Active normal faulting and crustal extension, *in Continental extensional tectonics*, ed. Coward, M, Dewey, J., & Hancock, P. pp. 3-18.
- Jackson, J. & White, N. (1989) Normal faulting in the upper continental crust: observations in regions of active extension. *J. Structural Geology* 11, pp. 15-36.
- John, B., (1987). Geometry and evolution of a mid-crustal extensional fault system: Chemehuevi Mts, southeastern California. *In: Continental extensional tectonics*, Coward, M., et al, eds., *Geological Society Special Publication* 28, pp. 315-335.
- John, B. & Foster, D., (1993). Structural and thermal constraints on the initiation angle of detachment faulting in the southern Basin and Range: The Chemehuevi Mountains case study. *Geological Society of America Bulletin* 105, pp. 1091-1108.
- Jones, B. & Galan, E., (1988). Sepiolite and palygorskite. *In: Hydrous phyllosilicates (exclusive of micas)*, Bailey, S., ed. *Reviews in Mineralogy* 19, pp. 631-674.
- Kerrich, R. (1988). Detachment zones of Cordilleran metamorphic core complexes: thermal, fluid and metasomatic regimes. *Geologische Rundschau*. 77, pp. 157-182.
- Kerrich, R. & Rehrig, W. (1987). Fluid motion associated with Tertiary mylonization and detachment faulting:  $^{18}\text{O}/^{16}\text{O}$  evidence from the Picacho metamorphic core complex, Arizona. *Geology* 15, pp. 58-62.
- Knott, J., Sarna-Wojcicki, A., Meyer, C., Tinsley III, J., Wells, S., & Wan, E., (1999). Late Cenozoic stratigraphy and tephrochronology of the western Black Mountains piedmont, Death Valley, California: implications for the tectonic development of Death Valley. *In: Wright, L.A., Troxel, B.W. (Eds.), Cenozoic Basins of the Death Valley Region*. *Geological Society of America Special Paper* 333, pp. 345-366.
- Liavaccari, R., Geissman, J. & Reynolds, S., (1993). Paleomagnetic evidence for large-magnitude low-angle normal faulting in a metamorphic core complex. *Nature* 351, pp. 56-59.
- Lister, G., Ethelridge, M. & Symonds, P. (1991). Detachment models for the formation of passive continental margins. *Tectonics* 10, pp. 1038-1064.



- Lister, G. & Baldwin, S., (1993). Plutonism and the origin of metamorphic core complexes. *Geology* 21, pp. 607-610.
- Longwell, C., (1945). Low-angle normal faults in the Basin and Range province. *American Geophysical Union Transactions* 26, pp. 1087-1118.
- Malavielle, J., (1987). Kinematics of compressional and extensional ductile shearing deformation in a metamorphic core complex of the northeastern Basin and Range. *J. Structural Geology* 9, pp. 541-554.
- Manatschal, G., (1999). Fluid- and reaction-assisted low-angle normal faulting: evidence from rift-related brittle fault rocks in the Alps (Err nappe, eastern Switzerland). *J. Structural Geology* 21, pp. 777-793.
- Martinez, F., Goodliffe, A. & Taylor, B., (2001). Metamorphic core complex formation by density inversion and lower-crust extrusion. *Nature* 411, pp. 930-934.
- McGrew, A. & Snee, L. (1994)  $^{40}\text{Ar}/^{39}\text{Ar}$  thermochronologic constraints on the tectonothermal evolution of the northern East Humboldt Range metamorphic core complex, Nevada. *Tectonophysics* 238, pp. 425-450.
- Miller, E., Gans, P. & Garing, J., (1983). The Snake Range décollement: an exhumed mid-Tertiary brittle-ductile transition. *Tectonics* 2, pp. 239-263.
- Miller, J., & John, B., (1999). Sedimentation patterns support seismogenic low-angle normal faulting, southeastern California and western Arizona. *Geological Society of America Bulletin* 111, pp. 1350-1370.
- Miller, M., & Pavlis, T., (2005). The Black Mountains turtlebacks: Rosetta stones of Death Valley tectonics. *Earth Science Reviews* 73, pp. 115-138.
- Moore, D., & Rymer, M., (2007). Talc-bearing serpentinite and the creeping section of the San Andreas Fault. *Nature* 448, pp. 795-797.
- Morrison, J. & Anderson, J. (1998). Footwall refrigeration along a detachment fault: Implications for the thermal evolution of core complexes. *Science* 279, pp. 63-66.
- Mueller, K., & Snoke, A. (1993) Progressive overprinting of normal fault systems and their role in Tertiary exhumation of the East Humboldt-Woods Hills metamorphic complex, northeast Nevada. *Tectonics* 12, pp. 361-371.
- Nieto, F., Pilar Mata, M., Baulex, B., Giorgetti, G., Árkai, P. & Peacor, D., (2005). Retrograde diagenesis, a widespread process on a regional scale. *Clay Minerals* 40, pp. 93-104.
- Noble, L. (1941) Structural features of the Virgin Spring area, Death Valley, California. *Geological Society of America Bulletin* 52, pp. 941-1000.
- O'Hanley, D., Chernosky, J. & Wicks, F., (1989). The stability of lizardite and chrysotile. *Canadian Mineralogist* 27, pp. 483-493.

- O'Neill, R. & Pavlis, T., (1988). Superposition of Cenozoic extension on Mesozoic compressional structures in the Pioneer Mountains metamorphic core complex. *Geological Society of America Bulletin* 100, pp. 1833-1845.
- Rahl, J., McGrew, A. & Foland, K., (2002). Transition from contraction to extension in the northeastern Basin and Range: New evidence from the Copper Mountains, Nevada. *J. Geology* 110, pp. 179-194.
- Ransom, F., Emmons, W. & Garrey, G. (1910). Geology and ore deposits of the Bullfrog district, Nevada, *U.S. Geological Survey Bulletin*, v 407, p. 1-130.
- Rehrig, W., & Reynolds, S., (1980), Geologic and geochronologic reconnaissance of a northwest-trending zone of metamorphic core complexes in southern and western Arizona, in Crittenden, M.D., et al., eds., Cordilleran metamorphic core complexes: *Geological Society of America Memoir* 153, p. 131-157.
- Reynolds, R. C., Jr. (1993). WILDFIRE - A computer program for the calculation of three-dimensional powder X-ray diffraction patterns for mica polytypes and their disordered variations, Hanover, New Hampshire
- Reynolds, S. & Spencer, J., (1985). Evidence for large-scale transport on the Bullard detachment fault, west-central Arizona. *Geology* 13, pp. 353-356.
- Rice, J., (1992). Fault stress states, pore pressure distributions and the weakening of the San Andreas fault. In: Evans, J. & Wong, T., eds, Fault mechanics and the transport properties of rocks.: A festschrift in honor of W. F. Brace. New York Academic Press, p. 475-504.
- Roddy, M., Reynolds, S., Smith, B. & Ruiz, J., (1988). K-metasomatism and detachment-related mineralization, Harcuvar Mountains, Arizona. *Geological Society of America Bulletin* 100, pp. 1627-1639.
- Saffer, D., Frye, K., Marone, C. & Mair, K., (2001). Laboratory results indicating complex and potentially unstable frictional behavior of smectite clay, *Geophysical Research Letters* 28 pp. 2297-2300.
- Saffer, D. & Marone, C., (2003) Comparison of smectite- and illite-rich gouge frictional properties: application to the updip limit of the seismogenic zone along subduction megathrusts. *Earth and Planetary Science Letters* 215, pp. 219-235.
- Scholz, C., (2002). The mechanics of earthquakes and faulting. Cambridge University Press. 471 pp.
- Shau, Y. & Peacor, D., (1992). Phyllosilicates in hydrothermally altered basalts from DSDP Hole 504B, Leg 83 – a TEM and AEM study. *Contributions to Mineralogy and Petrology* 112, pp. 119-133.
- Sibson, R., (1985). A note on fault reactivation. *J. Structural Geology* 7, pp. 751-754.

- Siffert, B. & Wey, R., (1962). Synthèse d'une sepiolite a temperature ordinaire. *C. R. Acad. Sci. Paris* 254, pp. 1460–1463.
- Smith, B., Reynolds, S., Day, H., & Bodnar, R., (1991). Deep-seated fluid involvement in ductile-brittle deformation and mineralization, South Mountains metamorphic core complex. *Geological Society of America Bulletin* 103, pp. 559-569.
- Snoke, A. (1980) Transition from infrastructure to superstructure in the Northern Ruby Mountains, Nevada. in: Crittenden, M. et al., (1980) eds. Cordilleran metamorphic core complexes *Geological Society of America Memoir* 153, pp. 287-333.
- Snoke, A. & Lush, A. (1984) Polyphase deformation Mesozoic-Cenozoic deformational history of the northern Ruby Mountains-East Humboldt Range, Nevada. *In: Western geological excursions*, Lintz, J. ed., *Geological Society of America Annual Meeting Guidebook* volume 4, Reno Nevada, Mackay School of Mines, pp. 232-260.
- Snow, J. & Wernicke, B. (2000) Cenozoic tectonism in the central Basin and Range: Magnitude, rate and distribution of upper crustal strain. *American Journal of Science* 300, pp. 659-719
- Spencer, J. (1984) The role of tectonic denudation in the warping and uplift of low-angle normal faults. *Geology* 12, pp. 95-98.
- Spencer, J., & Chase, C. (1989) Role of crustal flexure in initiation of low-angle normal faults and implications for evolution of the Great Basin. *J. Geophysical Research* B 94, pp. 1765-1775.
- Spencer, J. & Reynolds, S., (1986). Field trip guide to selected parts of the Harquahala, Granite Wash and Buckskin mountains, west-central Arizona. *Arizona Geological Society Digest*, volume XVI, pp. 382-388.
- Spencer, J., & Reynolds, S., (1991). Tectonics of mid-Tertiary extension along a transect through west central Arizona. *Tectonics* 10, pp. 1204-1221.
- Stewart, J. (1983) Extensional tectonics in the Death Valley area, California: Transport of the Panamint Range structural block 80 km northwestward. *Geology* 11, pp. 153-157.
- Snyder, N. & Hodges, K. (2000). Deposition and tectonic evolution of a supradetachment basin:  $^{40}\text{Ar}/^{39}\text{Ar}$  geochronology of the Nova formation, Panamint Range, California. *Basin Research* 12, pp. 19-30.
- Topping, D., (1993). Paleogeographic reconstruction of the Death Valley extended region: Evidence from Miocene large rock-avalanch deposits in the Amargosa Chaos Basin, California. *Geological Society of America Bulletin* 105, p. 1190-1213.
- Vanderhaeghe, O., Teyssier, C., & Wysoczanski, R., (1999). Structural and geochronological constraints on the role of partial melting during the formation of

- the Shuswap metamorphic core complex at the latitude of the Thor-Odin dome, British Columbia. *Canadian Journal of Earth Science* 36, pp. 917-943.
- Vega Granillo R. & Calums, T., (2003). Mazatan metamorphic core complex (Sonora, Mexico): structures along the detachment fault and its exhumation evolution. *J. South. American Earth Sciences* 16, 193-204.
- Vrolijk, P., (1990). On the mechanical role of smectite in subduction zones. *Geology* 18, pp. 703-707.
- Vrolijk, P. & van der Pluijm, B. (1999) Clay gouge. *J. Structural Geology* 21, 1039-1048.
- Walker, C., Anders, M., & Christie-Blick, N., (2006). Kinematic evidence for down-dip movement on the Mormon Peak detachment. *Geology* 35, pp. 259-262.
- Walker, J., Bartley, B. & Glazner, A., (1990). Large-magnitude Miocene extension in the central Mojave desert: Implications for Paleozoic to Tertiary paleogeography and tectonics. *J. Geophysical Research B* 95, pp. 557-569.
- Wernicke, B., (1981). Low-angle normal faults in the Basin and Range province: Nappe tectonics in an extensional orogen. *Nature* 291, pp. 645-648.
- Wernicke, B. (1995) Low-angle normal faults and seismicity: A review. *J. Geophysical Research B* 100, pp. 20,159–20,174.
- Wernicke, B. & Axen, G. (1988) On the role of isostasy in the evolution of low-angle normal fault systems *Geology*, 16 pp. 848-51.
- Wintsch, R., Christofferson, R., & Kronenberg, A., (1995). Fluid-rock reaction weakening of fault zones. *J. Geophysical Research B* 100, pp. 13,201–13,032.
- Wong, M. & Gans, P., (2003). Tectonic implications of early Miocene extensional unroofing of the Sierra Mazatán metamorphic core complex, Sonora, Mexico. *Geology* 31, 953-956
- Wright, L., Otton, J., & Troxel, B., (1974). Turtleback surfaces of Death Valley viewed as phenomena of extensional tectonics. *Geology* 2, pp. 53-54.
- Wright, L., & Troxel, B., (1984). Geology of the north ½ Confidence Hills 15' quadrangle, Inyo County, California. *Map sheet 34*, California Department of Conservation, Division of Mines and Geology.
- Yin, A. (1989) Origin of regional rooted low-angle normal faults: A mechanical model and its tectonic implications, *Tectonics* 8, pp. 469-482.

## CHAPTER 3: CLAY FABRICS IN NATURAL AND ARTIFICIAL FAULT GOUGE

### **Abstract:**

The role of phyllosilicate fabrics in fault gouge are a poorly understood component of the mechanical and hydrologic behavior of brittle fault zones. We report on fabric intensity measurements using X-ray texture goniometry on natural clay-rich fault gouges from low-angle detachment faults (Death Valley, California; Ruby Mountains, Nevada; West Salton Detachment Fault, California, and the Peramola thrust in NE Spain). We compare our results with previously published data to better understand phyllosilicate fabric intensities of clay gouges in a variety of tectonic environments and with various clay mineral assemblages. Phyllosilicate fabric intensity is quantified in terms of multiples of random distribution (MRD). Natural fault gouges have uniformly weak clay fabrics (MRD = 1.7 to 4.5, average MRD = 2.6) when compared to phyllosilicate-rich rocks found in other geologic settings, such as the mud-to-shale transition in compaction environments (MRD = 2 to ~7), the transition from shale to slate during low-grade metamorphism (MRD = 2 to ~20) and in mylonites and schists (MRD = 4 to ~24). Clay fabric intensities in natural gouges do not vary significantly either as a function of tectonic environment or of dominant clay mineral in the gouge. We compare these natural results with phyllosilicate fabric intensities measured in laboratory experiments on clay-quartz mixtures, in which normal stress (10 to 150 MPa), shear strain (0 to 25), and clay mineral content (montmorillonite) vary systematically. Fabric strengths from laboratory

samples are similar to those found in natural gouges (MRD = 1.7 to 4.6) and increase systematically with increasing shear strain and normal stress. Shear strain is important for developing stronger fabrics: samples subjected solely to compression have uniformly very weak fabrics (MRD = 1.6 – 1.8) even when compressed at high normal stresses (150 MPa). Total phyllosilicate content does not significantly affect clay fabric strength. Experimental gouges with low normal stresses and high shear strains produce fabric intensities similar to those found in natural gouges, whereas fabric intensities in experimental gouges at high normal stresses and high shear strains produce fabric intensities somewhat higher than those typically observed in natural gouges. The uniformly weak fabrics found in natural fault gouge indicate that, if anisotropic fault zone permeability causes fault weakening, this anisotropy must be a transient feature that is not preserved. Our results also show that tectonic conditions and slip rate cannot readily be deduced from fault fabrics alone.

## **Introduction**

Clay-rich fault gouges play a significant role in the frictional and hydrologic properties of seismic and aseismic faults (e.g. Sibson, 1977, Byerlee, 1978, Vrolijk & van der Pluijm, 1999). Although a large body of experimental data has quantified the frictional properties of clay-rich gouges (e.g. Lupini et al., 1981, Morrow et al., 1982, 2000, Logan et al., 1987, Moore et al., 1989, Saffer et al., 2001, Brown et al., 2003, Saffer & Marone, 2003, Numelin et al., 2005, Ikari et al., 2007), the relationship between fault strength, frictional stability, clay fabric, and clay mineralogy is not well understood. Quantifying such links is particularly important because there is clear evidence for a role of fabric and preferred orientation of phyllosilicates in natural faults, in interpreting slip rate and other in-situ

faulting conditions, from surface exposures of preserved faults and scientific fault drilling (e.g. Chester and Logan, 1987; Cladouhos, 1999a, 1999; Cowan, 2003; Storti et al., 2003; Di Toro et al., 2005).

Quantifying the intensity of fabrics that evolve during shear of clay gouges and assessing what that fabric preserves about fault zone properties and mechanical behavior is complex because clay fabrics are affected by many factors (Figure 3.1). Limited quantitative studies of clay fabric intensity in natural fault zones have shown that clay gouges generally have weak fabrics (Yan et al., 2001, Solum et al., 2003, 2005). The purpose of this paper is to examine phyllosilicate fabric intensities from clay-rich fault gouges in a variety of geologic environments and with varying clay mineral content. We investigate the role of tectonic environment and clay mineralogy on the intensity of natural clay gouge fabric by quantifying fabrics using X-ray texture goniometry (XTG). We present a synthesis of clay gouge fabric measurements and compare our new work with results for gouges from thrust faults, low-angle normal faults and strike slip faults. We examine natural gouges that contain predominantly illite, chlorite, smectite, kaolinite, palygorskite or sepiolite and assess the differences in fabric intensity of clay-rich gouges as a function of mineralogy.

To better understand the geologic processes that control clay fabrics (Figure 3.1), we also made measurements of fabric intensity for experimentally deformed clay gouges. The laboratory work focuses on clay and clay-quartz mixtures to assess the relative roles of normal stress, clay content, and shear strain. We demonstrate that clay gouge fabric develops primarily as a function of shear strain and normal stress during deformation and that fabric intensity is only weakly affected by the total clay mineral content.

## Phyllosilicate preferred orientation in clay-rich fault gouges

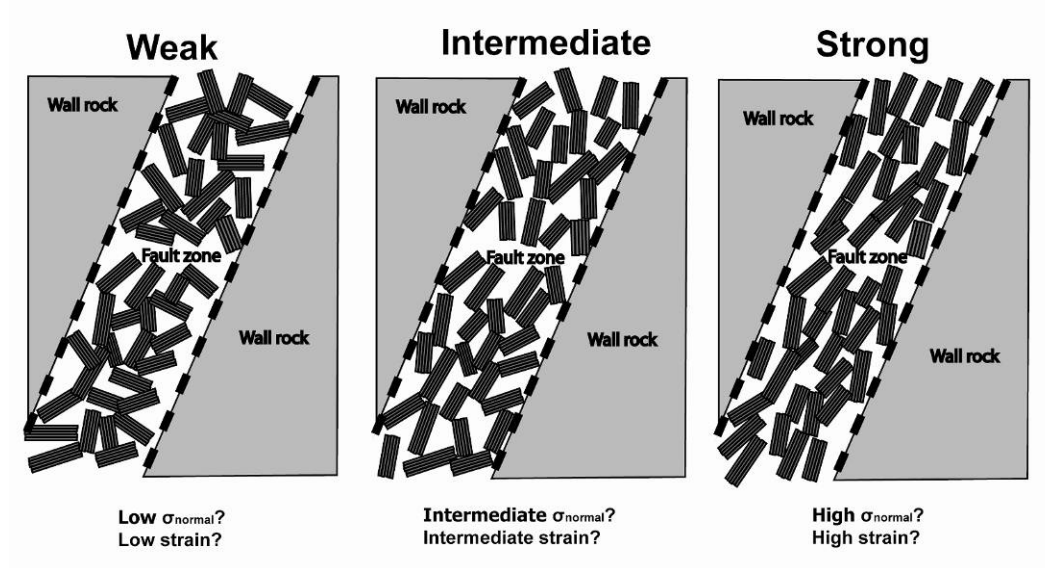


Figure 3-1: Schematic illustration of clay fabric orientation in fault zones.



Although numerous conceptual models for the compaction of clays in sedimentary environments depict a strong preferred orientation due to the mechanical effects of compaction and consolidation, few experimental validations for this view have been offered (Tullis, 1976). We demonstrate that fabrics obtained solely by compaction of clay-rich material are much weaker than those obtained by compacting and shearing the same clay-rich material, and that many conceptual illustrations of the effect of compaction processes on clay particle orientation are not supported by our laboratory measurements.

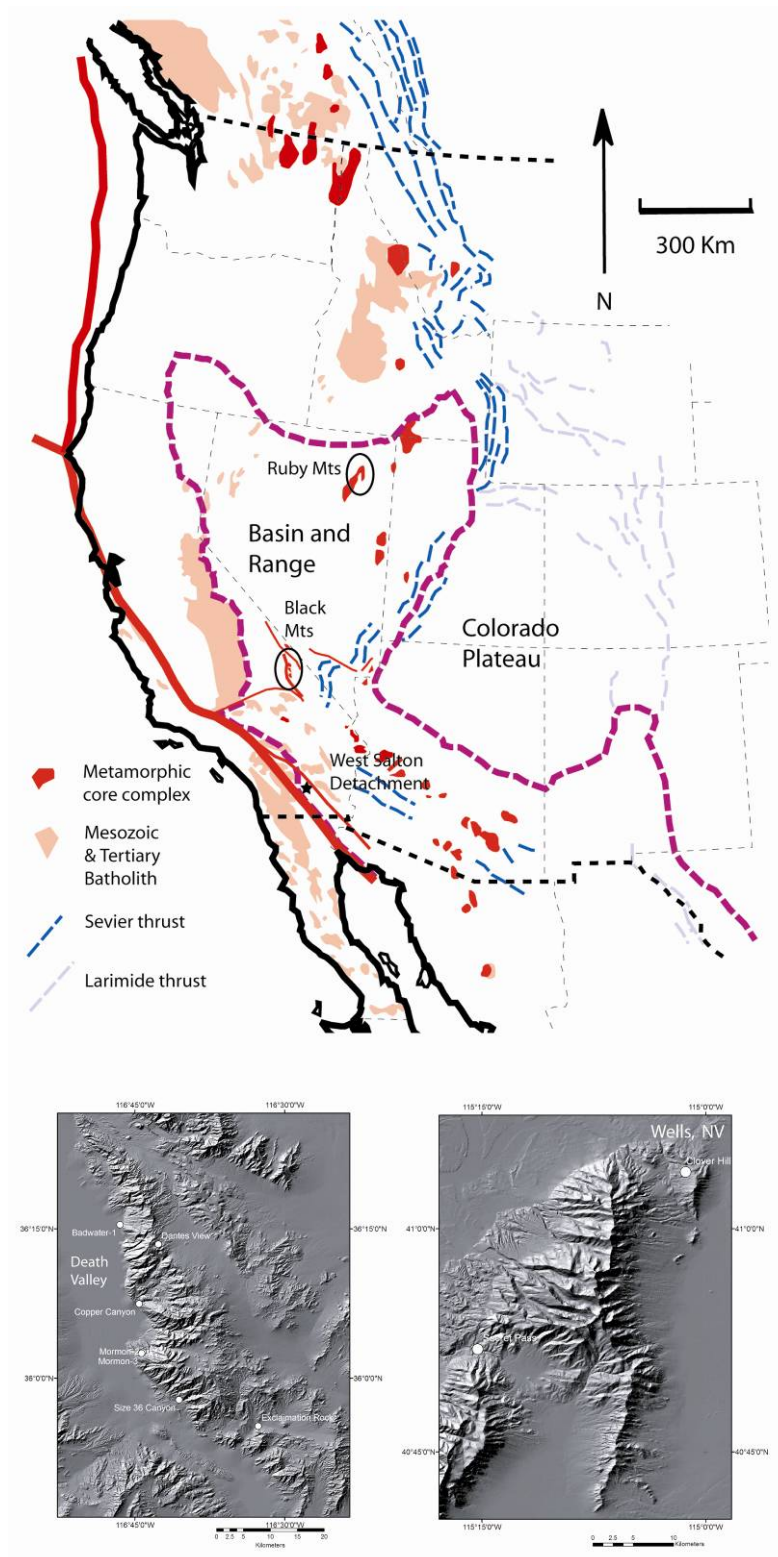
### **Clay Fabric**

The preferred orientation of minerals in rock is typically quantified using three techniques: 1) universal-stage optical microscopy (e.g. Turner & Weiss, 1963), 2) semi-automated optical microscopy (e.g. Price, 1973, Heilbronner & Pauli, 1983) and 3) X-ray texture goniometry (e.g. Schluz, 1949, Oertel, 1983, van der Pluijm et al., 1994). Additionally, bulk rock fabric quantification has been obtained by magnetic analysis of samples (e.g., Housen et al., 1993; Richter et al., 1993; Pares et al., 1999) and neutron diffraction analysis (Wenk, 2006). Because clay-rich rocks have crystallite sizes on the order of microns or smaller, which is below the resolution of optical microscopy, X-ray texture goniometry is our preferred technique for quantifying their fabric. XTG has been used to quantify phyllosilicate fabric intensity for four geologic topics: 1) Identifying the relative roles of compaction and authigenic mineral growth in the mud-to-shale transition (Sintubin, 1994b, Curtis et al., 1980, Ho et al., 1999, Aplin et al., 2006, Day-Stirrat et al., 2008), 2) Assessing the relative roles of mechanical rotation, dissolution, and

neocrystallization of micas in the shale-to-slate transition (Holeywell and Tullis, 1975, Tullis and Wood, 1975, Sintubin et al., 1994a, Ho et al., 1995, 1996, 2001, Jacob et al., 2000), 3) Assessing the symmetry of the preferred orientation of micas in phyllonitic and ultramytonitic mylonitic rocks (O'Brian et al., 1987), and 4) Quantifying phyllosilicate fabric intensities in clay-rich fault gouges (Yan et al., 2001, Solum et al., 2003, 2005, Schleicher et al. *in press*). The technique has also been used to study spatial variations of strain, on the mm to m scale, in phyllosilicate-rich rocks (Oertel & Curtis, 1972, Holewell & Tullis, 1975, Curtis et al., 1980, van der Pluijm et al., 1994, Ho, 1995). XTG is ideal for the quantification of fabric intensity in clay-rich fault gouges because it provides information of large numbers of small particles in three dimensions, and the analysis and sample preparation are relatively quick and straightforward.

### **Faults studied**

We measured fabric intensities from clay-rich gouges taken from nine different faults: six detachment faults in the Death Valley, CA area (the Badwater, Copper Canyon, Mormon Point, Gregory Peak Detachments, the basal fault of the Amargosa Chaos, and a low-angle detachment exposed near the Dante's View overview in Death Valley NP), the Ruby Mountains detachment fault in NE Nevada exposed at Secret Pass and Clover Hill, the Salton Detachment in SW California and the Peramola Thrust in NE Spain (Figure 3.2). These faults were selected because previously published XTG studies focused on normal faults (Moab Fault, UT, USA, Solum et al., 2005), thrust faults (Lewis Thrust, Alberta, Canada, Yan et al., 2001) and strike-slip faults (Punchbowl Fault, CA, USA, Solum et al., 2003). Low-angle normal faults have received little attention for fabric



**Figure 3-2:** Location map for samples used in this study. Top: regional map of the western US showing detachment faults examined in this study (redrawn after Coney, 1980). Bottom left: shaded-relief DEM showing the central Black Mountains and Death Valley area, CA. Bottom right: Shaded-relief DEM of the northern Ruby Mountains and East Humboldt Range, NV.

quantification, yet they are of considerable interest due to the mechanical paradox of their shallow dip and misorientation relative to predictions from laboratory rock friction experiments (e.g., Buck, 1988; Wernicke & Axen, 1988, Axen, 2004). None of the faults we sampled had significant veining or other visible evidence at outcrop of high fluid pressures.

The southern Death Valley area in SE California has exceptional exposure and preservation of clay-rich fault gouges along shallowly-dipping NW-directed normal faults of Miocene-to-Recent age that have been extensively studied (Pavlis et al., 1993, Miller, 1996, Cladouhos, 1999a, 1999b, Cowan, 1999, Cowan et al., 2003, Hayman et al., 2004, Hayman, 2006). We sampled a total of five localities along the three ‘turtlebacks’ on the west side of the Black Mountains, one locality in the southern Black Mountains in the Amargosa Chaos area, and one locality at a smaller detachment in the central Black Mountains near Dante’s View. At all localities, the faults juxtapose poorly sorted, moderately indurated Pliocene-Recent gravels against either highly fractured and chloritized Precambrian metamorphic rocks (as at Badwater, Copper Canyon & Mormon-3) or fractured mid-Miocene dioritic and granitic plutonic rocks at Mormon-2 and Size 36 Canyon (the Gregory Peak detachment). In outcrop, the gouges frequently, but not always, have a crude foliation defined by Y, R and P surfaces (using the terminology of Chester et al., 1985) and have been described in detail by Cladouhos (1999a, 1999b), Cowan (2003) and Hayman (2004). Gouge layers at all exposures range from 0.2 m to 2.0 m thick, and gouge zone thicknesses vary rapidly along strike. At Exclamation Rock on the Shoshone-Death Valley road, the Amargosa detachment places mid-Proterozoic Crystal Springs greenschist-facies quartzites over Mid-Proterozoic muscovite schistose gneisses. On the road to Dante’s View, (the fault at mile 11.3 of Miller & Wright, 2004), a

low-angle normal fault juxtaposes Miocene rhyolites in the hangingwall over Miocene white tuff in the footwall.

XRD analyses indicate that the Death Valley gouges are mineralogically quite variable (see Chapter 2 for a comprehensive discussion). Gouges have two characteristic clay mineral assemblages; one is dominated by an apparently detrital chlorite and its alteration products, corrensite and smectite, derived from pervasive chloritic alteration of the footwall. The second assemblage is dominated by authigenic  $1M_d$  illite, forming from the breakdown of feldspar derived from granitic footwall rocks. The distribution of the two assemblages is primarily a function of the distribution of footwall lithologies. At Mormon-3, a very distinctive gouge mineral assemblage of tri-octahedral smectite, sepiolite, talc and lizardite is found overprinting an apparently older detrital chloritic gouge based on field relationships. Field fabrics indicate that both assemblages pre-date the end of slip on the detachment. At Dante's View, the gouge contains a distinctive assemblage of di-octahedral smectite (montmorillonite) and palygorskite.

The Ruby Mountains metamorphic core complex is a well studied feature in NE Nevada (e.g. Snoke, 1980, Dallmeyer et al., 1986, Dokka et al., 1986, Mueller & Snoke, 1993, McGrew & Snee, 1994, McGrew et al., 2000). The complex was exhumed along a west-dipping mylonitic detachment that is exposed sporadically along the western margin of the range and at Clover Hill at the northern end of the East Humboldt Range. The detachment has a classical ductile-to-brittle structural history, and was active from the Eocene to the late Miocene (Dokka, 1986, McGrew et al., 2000). We sampled the detachment fault system gouges at two localities, on NV Rt 321 approximately 5 km southwest of Wells, NV (Stop 20 of Snoke & Howard, 1994), and at Secret Pass where the main detachment fault is exposed along NV Route 229 (Stop 12, locality H of Snoke

& Howard, 1994). At Clover Hill, the gouge zone is 1 m thick, reddish in color with white streaks along a crude foliation. XRD analysis of the gouge indicates that the Clover Hill gouge is dominated by illite, but has late alteration to kaolinite along the white streaks, which may post-date faulting based on field fabrics. At Secret Pass, the gouge zone of the main detachment fault is 1.0 – 1.5 m thick and XRD analysis indicates that the gouge contains discrete horizons of illite-rich illite-smectite (~90% I in I/S) and di-octahedral smectite. The illite-smectite is crudely foliated at outcrop and thus was present during the last slip event, whereas the smectite is not foliated and may post-date fault slip.

The West Salton Detachment Fault is one of a suite of east-dipping low-angle normal faults on the western side of the Miocene-to-Recent Salton Trough, which forms the northern end of the Gulf of California. The detachment juxtaposes Paleozoic greenschist- and amphibolite-facies metasediments in both the hangingwall and footwall. The fault strikes roughly NW-SE and accommodated ESE extension from the Miocene to early Pleistocene (Axen & Fletcher, 1998). The fault was sampled at UTM (CONUS NAD 27) 11N 0580316E 3689946N. Locally, the fault strikes NE-SW and dips ~25° to the east. The gouge zone is 0.25 to 0.5 m thick and displays a weak platy fabric. XRD analysis of the gouge shows that it consists primarily of a tri-octahedral smectite (saponite) and chlorite.

The Peramola thrust in the south-central Spanish Pyrenees is part of the Serres Marginals frontal thrust system. The thrust is exposed in a small roadcut (42° 3' 32", 1° 15' 43" E) at the village of Peramola, near the eastern termination of the Serres Marginals thrust system, where the fault places mid-Jurassic limestones over Eocene marls. The fault was active in the late Eocene during emplacement of the south-central Pyrenean thrust wedge (Puigdefabrigas et al., 1986, Sussman et al., 2004). Locally, the

thrust strikes NNW and dips west at 35°. The gouge zone is 2-3 m thick and is weakly foliated at outcrop. XRD analysis of the gouge indicates that it consists of corrensite (ordered chlorite-smectite) and minor illite.

### **Methods for X-Ray texture goniometry**

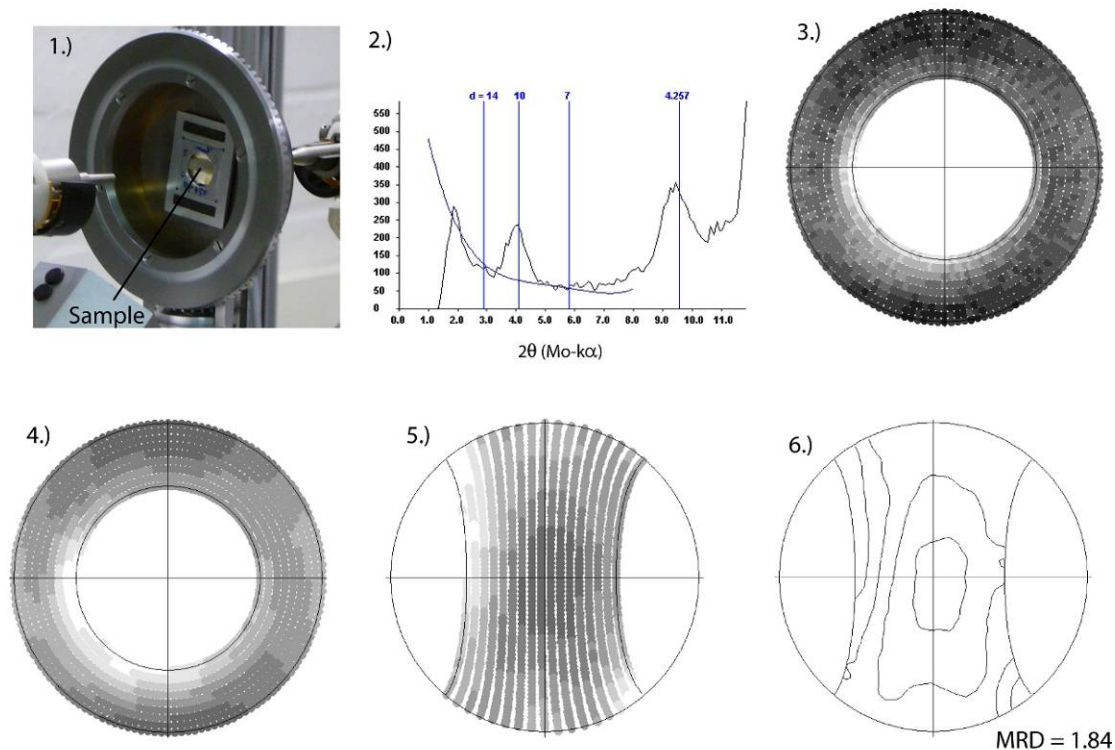
#### **Low-angle normal faults**

Oriented natural samples were either chiseled out of the fault zone or were teased out using a pocketknife or chisel along existing fractures, whereas laboratory gouge layers were oriented relative to the shear direction. Samples were set in a low viscosity epoxy resin (Struers EPOFIX) under low vacuum. The resin-impregnated samples were cut to thicknesses of between 0.2 and 0.8 mm on an oil-lubricated, low-speed saw in the X-Z plane of the strain ellipsoid (perpendicular to the planar fabric and parallel to any lineation or known fault slip direction) for both natural and experimental samples. Owing to the extremely friable nature of some natural gouges and most of the experimental gouges, samples were cut thicker than the 0.2 mm favored in van der Pluijm et al. (1994). Multiple analyses on samples from competent material that were cut both at 0.2 mm and 1.0 mm thick indicate that MRD varied by less than 10% between thin and thick samples. This minor difference in fabric intensity indicates that the relatively thick preparations necessitated by the friable nature of many of the samples does not significantly affect our fabric intensity measurements. For convenience, both natural and artificial samples were oriented in the XTG apparatus so that the shear sense was horizontal in the machine geometry and pole figure output, with either sinistral or dextral shear as indicated on figures.

Natural and synthetic gouge fabric intensities were measured on a modified Enraf-

Nonius CAD4 single crystal X-ray diffractometer in transmission mode using the method of van der Pluijm et al. (1994). The machine uses a molybdenum source and has a beam diameter of ~1 mm. The natural samples were measured at 23 mA and 43 kV, and the experimental samples were run at 15 mA and 35 kV, because the peak intensities for the higher purity experimental material were too high to permit accurate fabric quantification at higher voltages. XTG analysis for a gouge sample is a two-step process: first a  $2\theta$  scan over the range  $0.5 - 6.0^\circ$   $2\text{ Mo K}\alpha$  ( $2-26^\circ$   $\text{Cu K}\alpha$ ) identifies the (001) peaks of the clay phases in a sample. Then, we measure the intensity of the (*hkl*) of the clay phase of interest at ~1300 different positions to collect a pole figure measuring phyllosilicate fabric intensity (Figure 3.3). To collect a pole figure, the X-ray detector was first moved to the position that corresponds with the d-spacing of a prominent peak of the clay phase of interest [14 Å for smectite (001), 10 Å for illite (001), 9.8 Å for sepiolite (110), 10.5 Å for palygorskite (110) and 7 Å for both chlorite (002) and kaolinite (001)]. The sample was then rotated both in its plane and about a vertical axis through a total of 1296 positions, measuring the intensity of that peak at each position with a count time of 2 seconds, covering roughly 65% of a full hemisphere. When the scan was complete, the pole figure of the diffracted beam was smoothed using a two-cycle smoothing process and contoured using multiples of a random distribution (MRD), which is analogous to % of the data per 1% area of the pole figure (Wenk, 1985). That is, an MRD value of 3 means that 3% of the total corrected number of X-ray counts are in 1% of the pole figure. The pole figures are corrected for X-ray absorption using the procedures of van der Pluijm et al., (1994). The fabric intensity we report is the maximum measured MRD value of the pole figure. Each gouge sample was scanned at a minimum of two locations on the cut face surface. A total of 87 pole figures from natural gouges were collected for this study from analyses of 37 XTG samples cut from 22 hand specimens collected from 9 faults.



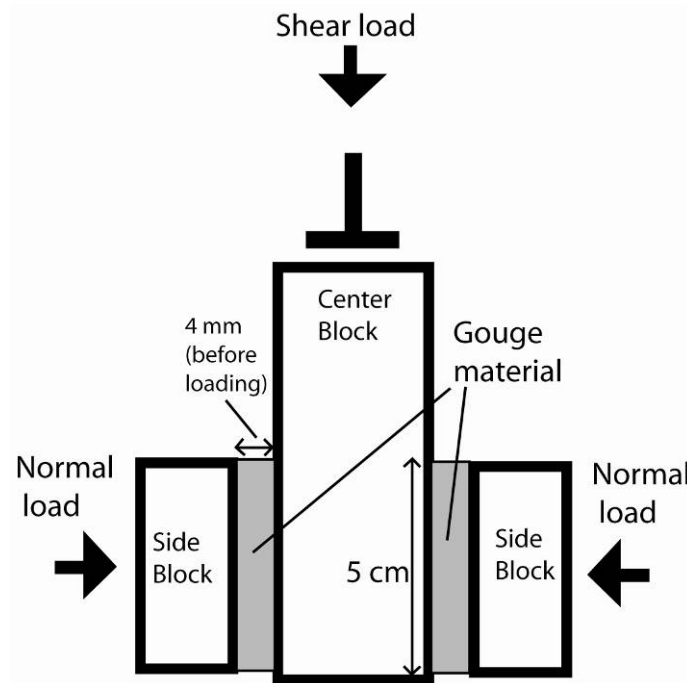


**Figure 3-3:** Illustration of X-ray goniometry data acquisition and reduction. 1.) View of sample in XTG apparatus, with source at right and detector to left. 2.)  $2\theta$  scan of sample showing strong illite/mica peak at 10 Å, along with quartz peak at 4.27 Å Mo K $\alpha$ . Background curve and d-spacings of common clay peaks are shown for convenience. 3.) Raw pole figure data of the intensity of the illite/mica 10 Å peak from the sample pictured in the XTG apparatus, orientation is the same as photo of sample, looking from the detector towards the X-ray source. 4.) 2-cycle smoothed data, view is same perspective as raw data. 5.) Smoothed data is rotated so that maximum is at center of figure. 6.) Line-contoured data with maximum at center. Contours are in intervals of 0.25 MRD.

## Laboratory shear experiments

Twenty-five laboratory experiments were performed on montmorillonite and montmorillonite-quartz mixtures using a servocontrolled, double-direct shear testing apparatus at room temperature and humidity. In this configuration, two layers of experimental gouge are sheared simultaneously while sandwiched between three steel blocks (see Figure 3.4). The side blocks are held in place by applying a horizontal normal stress, which is maintained via servocontrol, while the central block slides between the side blocks at a controlled displacement rate, inducing shear. Both the center and side blocks have roughened surfaces which consist of triangular grooves 0.8 mm deep that ensure slip in the gouge rather than along the boundary (see Saffer & Marone, 2003 for detailed description of the experimental setup). Gouge layers were prepared using a leveling jig to produce a uniform frictional contact area (5 x 5 cm) and uniform initial thickness (4 mm). Layers were compacted to 2-3 mm under normal load prior to shearing. We sheared a range of mixtures of commercially-available Ca-montmorillonite powder (acquired from GSA Resources) and Ottawa sand (F110, acquired from the U.S. Silica Glass company).

X-ray diffraction and SEM analysis of the montmorillonite powder indicates that it is predominantly a di-octahedral smectite (Ca-montmorillonite *sensu strictu*) which contains two partially-filled water interlayers at room humidity and which expands to two full water layers when solvated with ethylene glycol. The montmorillonite has a mean grain size of 60  $\mu\text{m}$  with 80% of the grain sizes between 3 and 142  $\mu\text{m}$  (Ikari et al., 2007). It contains trace amounts of heulandite and quartz (<1%). The F110 quartz has sub-angular grains that range in size from 50-250  $\mu\text{m}$  and is >99% pure (Anthony and Marone, 2005). Samples were tested at applied normal stresses ranging from 10 to 150 MPa, for a



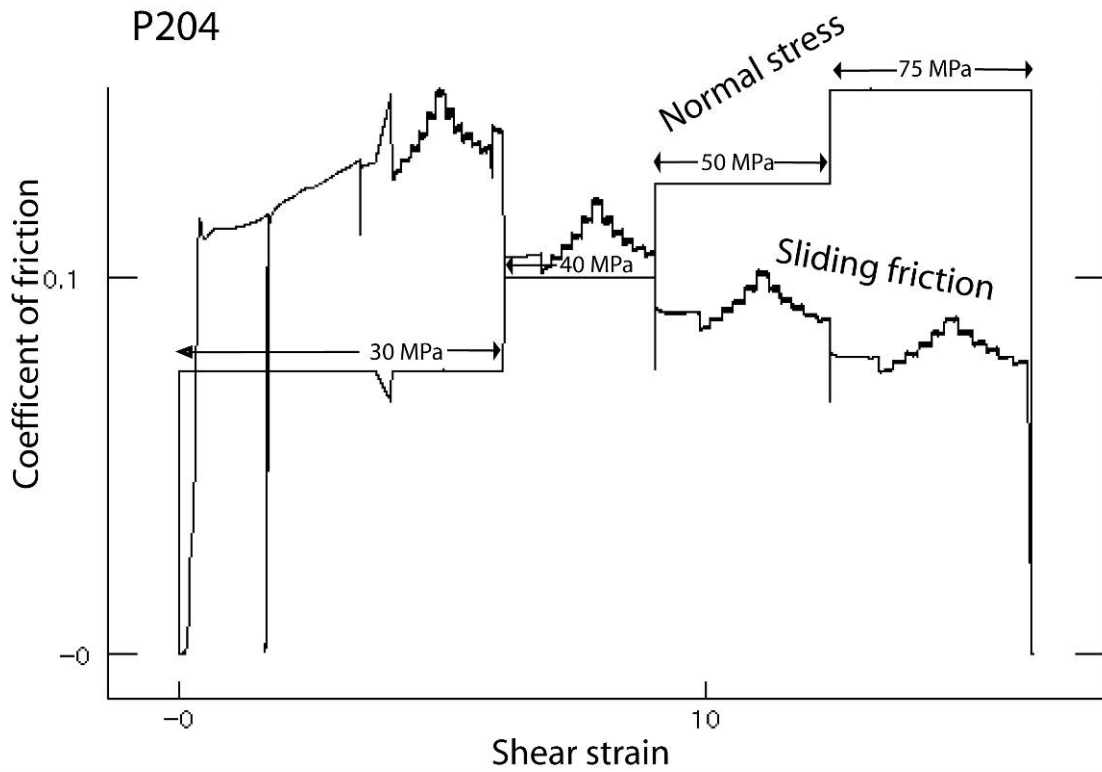
**Figure 3-4:** Sketch figure of biaxial double direct shear apparatus geometry. (after Saffer & Marone, 2003). A normal load is applied by horizontal rams, while a shear load is applied by driving the center block down using a separate ram. Synthetic gouge material is shown in grey.

series of gouge compositions ranging from 0 to 90 wt% quartz. In several of the experiments, normal stress was increased in steps; typical normal stress steps were 5, 10, 15 & 20 MPa, 30, 40, 50 & 75 MPa, and 100, 125 & 150 MPa (see Figure 3.5). The amount of shear strain accommodated at each normal stress was recorded and is listed in Table 3.1. Samples were sheared at sliding velocities from 1 to 300  $\mu\text{m}/\text{sec}$ . Gouge layers were subject to shear strains ranging from 0 (simple compaction) to  $\sim 22$ , which was calculated by integrating the measured slip increments divided by the instantaneous layer thickness. Load point displacement of the vertical loading ram, which applies shear load, was corrected for elastic stiffness of the apparatus to produce true shear displacement (e.g., Mair and Marone, 1999). A total of 69 XTG measurements were made from samples prepared from the friction experiments (Table 3.1).

## **Results**

### Natural gouges

Fabric intensity data from the natural gouges measured in this study are presented in Table 3.1 and in Figure 3.6. Our XTG clay fabric intensity measurements for natural fault gouges indicate that clay-rich gouges have uniformly weak fabrics. Clay fabrics in the 22 natural fault gouges measured in this study have an average MRD of 2.5 with a standard deviation of 0.5. The minimum observed MRD was 1.7, and the maximum was 4.0. These fabric strengths are low compared to those measured from rocks formed in other geologic environments, such as the transition from mud to shale in sedimentary basins, the transition from shale to slate as part of low-grade metamorphism, and high-T fault rocks such as mylonites (Figure 3.6). Previously published XTG data indicate that for rock in the mud-to-shale transition, MRDs range from 2 to  $\sim 7$  (Sintubin, 1994b, Ho et al., 1999, Aplin et al., 2006, Day-Stirrat et al., 2008) whereas for rocks in the shale-to-slate

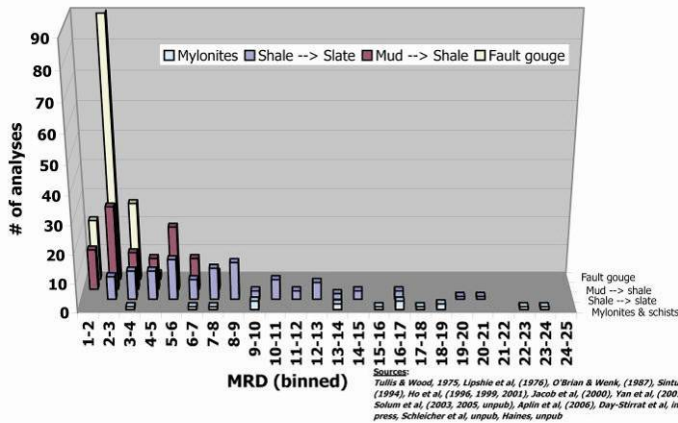


**Figure 3-5:** Plot of representative sliding friction test with stepped normal stress. Shown is a plot of normal stress versus shear strain (dotted line, right axis) superimposed over a plot of coefficient of sliding friction versus shear strain (solid line, left axis).

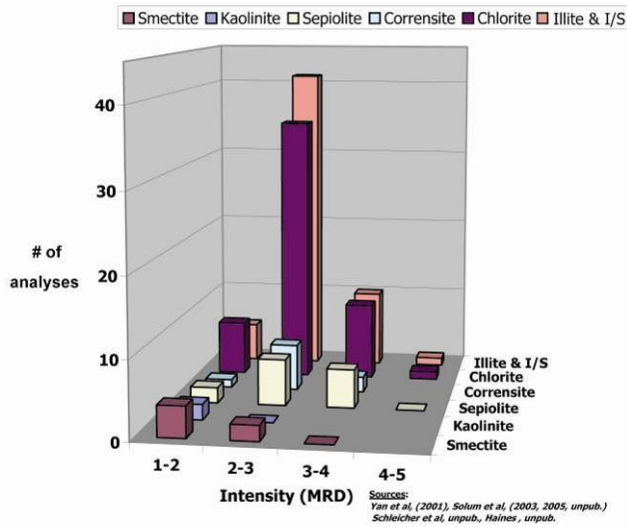
| Area                             | Outcrop                 | Field sample                | Sample chip    | Clay mineral | Fabric strength (MRD) |      |           |
|----------------------------------|-------------------------|-----------------------------|----------------|--------------|-----------------------|------|-----------|
| <b>Ruby Mountains, NV</b>        |                         |                             |                |              |                       |      |           |
|                                  | <b>Clover Hill</b>      | <b>Clover-1</b>             | CLO 1b         | Kaolinite    | 1.96                  | 1.79 |           |
|                                  |                         | <b>Clover-2</b>             | CLO 2a         | Illite       | 2.38                  | 2.42 |           |
|                                  | <b>Secret Pass</b>      | <b>Secret Pass 4-1</b>      | Sec 4-1 (1)    | Illite       | 2.57                  | 2.70 |           |
|                                  |                         |                             | SEC 4-1 (2)    | Illite       | 2.93                  | 2.78 |           |
|                                  |                         | <b>Secret Pass 4-3</b>      | SEC 4-3 (1)    | Smectite     | 1.77                  | 1.89 |           |
|                                  |                         |                             | SEC 4-3 (2)    | Smectite     | 1.75                  | 1.74 |           |
|                                  |                         | <b>Secret Pass 4-5</b>      | SEC 4-5 (3)    | Illite       | 1.92                  | 2.00 |           |
|                                  |                         | <b>Secret Pass 4-6</b>      | SEC 4-6 (3)    | Illite       | 2.51                  | 2.50 |           |
|                                  |                         |                             | SEC 4-6 (5)    | Illite       | 2.12                  | 1.80 |           |
| <b>Death Valley, CA</b>          |                         |                             |                |              |                       |      |           |
|                                  | <b>Badwater-1</b>       | <b>Badwater 1-1</b>         | Bad 1-1 (1)    | Illite       | 2.65                  |      |           |
|                                  |                         |                             | Bad 1-1 (1)    | Chlorite     | 2.05                  | 1.90 |           |
|                                  |                         |                             | Bad 1-1 (2)    | Chlorite     | 2.41                  | 2.15 |           |
|                                  |                         | <b>Badwater 1-2</b>         | Bad 2-1 (1)    | Illite       | 2.38                  | 2.54 |           |
|                                  |                         |                             | Bad 2-1 (2)    | Illite       | 2.50                  | 2.03 |           |
|                                  |                         | <b>Badwater 1-4</b>         | Bad-4a         | Illite       | 2.75                  | 2.49 |           |
|                                  | <b>Copper Canyon</b>    | <b>Copper Canyon-1</b>      | Cop-1a         | Chlorite     | 3.06                  | 3.02 | 3.17      |
|                                  |                         |                             | Cop-1a         | Corrensite   | 2.74                  | 3.92 | 3.22      |
|                                  |                         |                             | Cop-1b         | Chlorite     | 2.16                  | 3.28 | 3.67      |
|                                  |                         |                             | Cop-1b         | Corrensite   | 2.2                   | 2.97 |           |
|                                  |                         |                             | Cop-1b         | Illite       | 3.23                  |      |           |
|                                  | <b>Dante's View</b>     | <b>Dante-1</b>              | Dante-1        | Palygorskite | 2.32                  | 2.45 | 2.18      |
|                                  | <b>Exclamation Rock</b> | <b>Exclamation Rock W-1</b> | ! Rock W-1 (1) | Illite       | 3.62                  | 3.39 |           |
|                                  |                         |                             | ! Rock W-1 (2) | Illite       | 3.56                  | 3.00 |           |
|                                  |                         | <b>Exclamation Rock W-2</b> | ! Rock W-2 (1) | Illite       | 4.01                  | 2.41 |           |
|                                  |                         |                             | ! Rock W-2 (1) | Chlorite     | 2.04                  |      |           |
|                                  | <b>Size 36 canyon</b>   | <b>Size 36 Upper</b>        | 36-U (1)       | Illite       | 2.30                  | 2.36 |           |
|                                  |                         |                             | 36-U (2)       | Illite       | 2.40                  | 3.25 |           |
|                                  |                         | <b>Size 36 Lower</b>        | 36 L-1 (1)     | Illite       | 2.38                  | 2.27 |           |
|                                  |                         |                             | 36 L-1 (2)     | Illite       | 2.49                  | 3.16 |           |
|                                  |                         | <b>Size 36 FW breccia</b>   | 36 bx-1 (1)    | Illite       | 2.30                  |      |           |
|                                  |                         |                             | 36-bx-1 (2)    | Illite       | 2.22                  | 2.41 |           |
|                                  | <b>Mormon Point-2</b>   | <b>Mormon-2</b>             | Mor-2 (1)      | Chlorite     | 2.41                  | 2.44 |           |
|                                  |                         |                             | Mor-2 (2)      | Chlorite     | 1.99                  | 2.24 |           |
|                                  | <b>Mormon Point -3</b>  | <b>Mormon 3-1-1</b>         | MP31 1-1(1)    | Sepiolite    | 2.8                   | 3.15 |           |
|                                  |                         |                             | MP31 1-1(2)    | Sepiolite    | 2.75                  | 3.63 |           |
|                                  |                         |                             | MP31 1-2       | Sepiolite    | 3.26                  | 3.71 |           |
|                                  |                         | <b>Mormon 3-1-2</b>         | MP3-1 2-1 (1)  | Sepiolite    | 2.58                  | 1.94 | 2.36      |
|                                  |                         |                             | MP3-1 2-1 (1)  | Smectite     | 2.61                  |      |           |
|                                  |                         |                             | MP31 2-2       | Sepiolite    | 3.09                  | 2.49 | 1.92 2.44 |
|                                  |                         | <b>Mormon 3-1 (G)</b>       | MP31 G(1)      | Chlorite     | 2.02                  | 2.27 |           |
|                                  |                         |                             | MP31 G1(2)     | Chlorite     | 2.41                  | 2.35 |           |
| <b>Salton Sea Detachment, CA</b> |                         |                             |                |              |                       |      |           |
|                                  | <b>Salton Sea "571"</b> | <b>Salton 571</b>           | 571-1          | Smectite     | 2.69                  | 2.99 |           |
| <b>Peramola Thrust, NE Spain</b> |                         |                             |                |              |                       |      |           |
|                                  | <b>Peramola thrust</b>  | <b>Peramola-1</b>           | PER-1a         | Corrensite   | 1.83                  | 2.14 |           |
|                                  |                         |                             | PER-1b         | Corrensite   | 2.47                  | 2.20 |           |

**Table 3-1:** Fabric intensity measurements for natural faults sampled in this study.

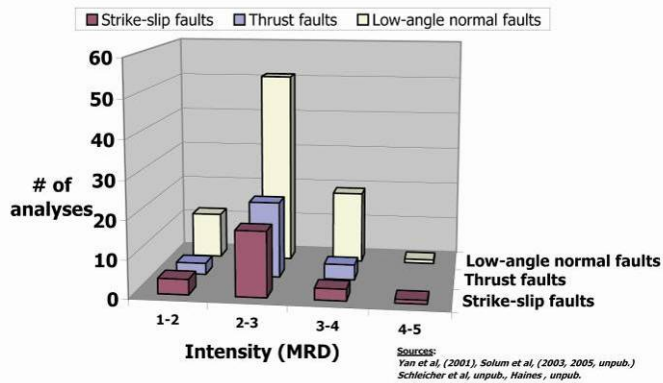
Phyllosilicate fabric intensities by geologic environment



Gouge phyllosilicate fabric intensities by primary clay mineral



Gouge phyllosilicate fabric intensities by tectonic environment



**Figure 3-6:** Natural clay fabric intensity data. Top: Phyllosilicate fabric strengths from various geologic environments. Note very weak fabric intensities of fault gouge fabrics compared to phyllosilicate fabrics in other geologic environments. Center: Fabric strength of fault gouges separated by predominant clay mineralogy of gouge. Note the consistency of the fabric strength distribution, irrespective of mineralogy. Bottom: Fabric strength of fault gouges from various tectonic environments; note consistency of fabric strength regardless of tectonic environment.

transformation, MRDs range from ~3 to ~20 (Tullis & Wood, 1975, Sintubin, 1994a, Ho et al., 1996, 2001, Jacob et al., 2000). Mylonites and schists have MRDs ranging from ~4 to as high as 24.0 (Lipshie et al., 1976, O'Brian & Wenk, 1987).

When the fabric intensity data from this study are combined with prior XTG data for other natural fault gouges (Yan et al., 2001, Solum et al., 2003, 2005, unpub., Schleicher et al., unpub.), the average fabric intensity distribution changes only very slightly. The merged data sets (N = 142 this study N = 90, preexisting data N = 52) have an average MRD of 2.6 with a standard deviation of 0.6. The minimum observed MRD in a clay-rich fault gouge was 1.7, and the maximum was 4.0 (Figure 3.6). The uniformly weak fabrics observed from gouges in a total of 15 faults from a variety of geologic environments indicate that weak clay fabrics are a universal characteristic of clay-rich fault gouges. When the fault gouge data are separated into distinct tectonic environments, such as thrust faults, low-angle normal faults and strike-slip faults, the fabric intensity distributions are surprisingly similar. Thrust faults have an average MRD of 2.6 (N = 27), low-angle normal faults have an average MRD of 2.7 (N = 90), and strike slip faults have an average MRD of 2.5. (N = 24) (see Figure 3.6). High angle normal faults have a similar average MRD of 2.4, although the data set is much smaller (N = 5). Standard deviations, minima and maxima are also very similar for the three larger distributions. The agreement among fabric intensities for gouges from differing tectonic environments indicate that the clay fabric-forming process is essentially independent of the tectonic environment (Figure 3.6).

When the gouge fabric intensity data are separated into distributions for various clay mineral assemblages, a similar pattern as above emerges. Illitic and chloritic gouges have essentially identical fabric intensities, 2.6 for illite and 2.5 for chlorite. Sepiolite and



palygorskite (both are phyllosilicates with a fibrous morphology as opposed to the platy morphology typical of most clay minerals) and corrensite-dominated gouges also have very similar average fabric intensities: 2.8 for sepiolite and palygorskite and 2.6 for corrensite. The fabric intensities for illite from fault gouge are, however, considerably weaker than those observed in illite-dominated shales, where the observed MRD's typically range from 3.0 to 6.0. Smectite and kaolinite fabric intensities for fault gouges are somewhat weaker than those for gouges that are dominated by other clay minerals; MRD's for gouges dominated by smectite and kaolinite average 2.18 for smectite and 1.88 for kaolinite. We suggest two possible explanations for the lower observed fabric intensities in smectitic and kaolinitic clay gouge. First, the data for smectite and kaolinite are derived from measurements on gouges from three 'low-angle' normal faults, two of which (Clover Hill and Secret Pass) have ambiguous field evidence that smectite-rich and kaolinite-rich horizons in the gouge zone were present at the time of faulting; thus, the very weak fabrics could have evolved as a result of clays that grew after fault slip ceased. If the fault surface was exhumed to higher levels in the crust, to a depth where differential stresses were lower, perhaps this led to a more isotropic clay fabric. Second, TEM images of smectite consistently show a distinctive wavy and irregular habit visible at very high magnifications (e.g. Schleicher et al., 2006), whereas illite and chlorite at the same high magnifications typically have more planar morphologies. It is likely that the lower measured fabric intensities for smectite are at least partly a function of the differing crystallite morphology of smectite, although more data are required to validate this hypothesis.

## Experimental gouges

The fabric intensity data from experiments are presented in Table 3.2 and Figure 3.7. The laboratory gouges have fabric intensities in the same range (MRD 1.7 – 4.6) as natural samples described above. The fabric strength intensities from the 100% montmorillonite samples, which were compressed but not sheared (P233, P234 & P1314), are very weak, and pole figures indicate maxima that are sub-vertical. Measured MRD's average 1.7, with a standard deviation of 0.1, and vary only slightly, with a minimum of 1.6 and a maximum of 1.8. MRD for the samples with zero shear strain does not vary systematically with normal stress; fabric intensities for samples compressed at 10 MPa, at 50 MPa and at 150 MPa are effectively identical and uniformly weak. The sub-vertical fabric intensity maxima in these samples indicate that the clay crystallites are aligning, albeit very weakly, perpendicular to the compressive stress (Figures 3.8 and 3.9). Samples that are both compressed and subjected to shear, however, exhibit substantially stronger fabrics, with MRDs averaging 2.9, and ranging from 1.7 to 4.6 (Figure 3.9). Fabric strength increases with increasing shear strain at shear strains from 0 to ~20.

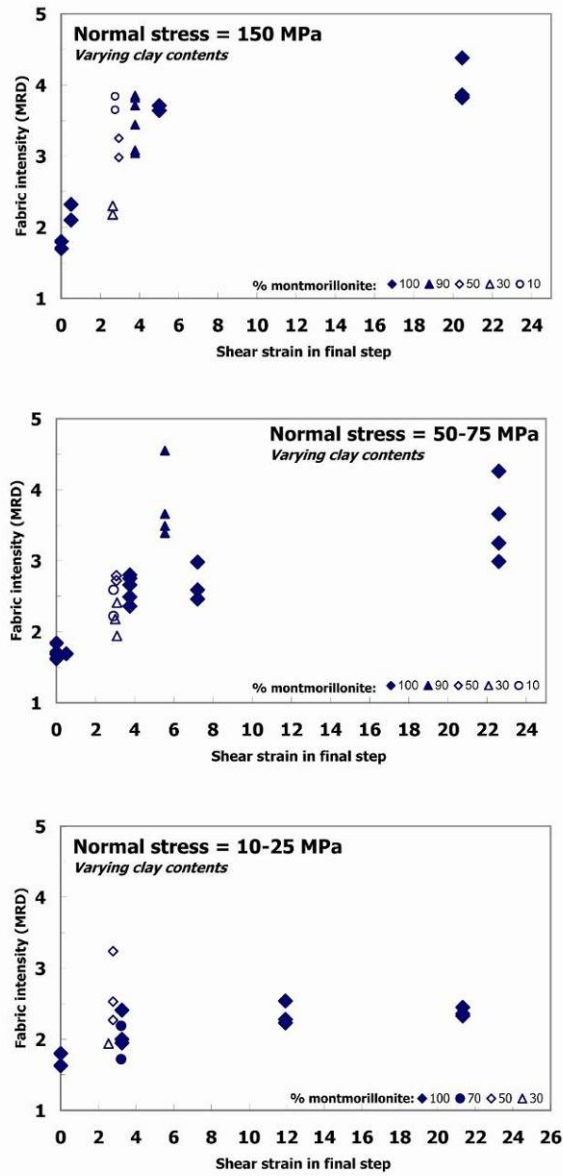
Several of our experiments were conducted at multiple normal stresses. To investigate the effect of strain history, we used only the shear strain at the highest normal stress for comparison. We posit that the frictional behavior and fabric development is primarily a function of the highest normal stress (Saffer & Marone, 2003), which is supported by the fabric measurements.

Unlike samples that were compressed without shear, sheared samples (Figure 3.9) exhibit fabric maxima that align at an angle both oblique to the maximum compressive

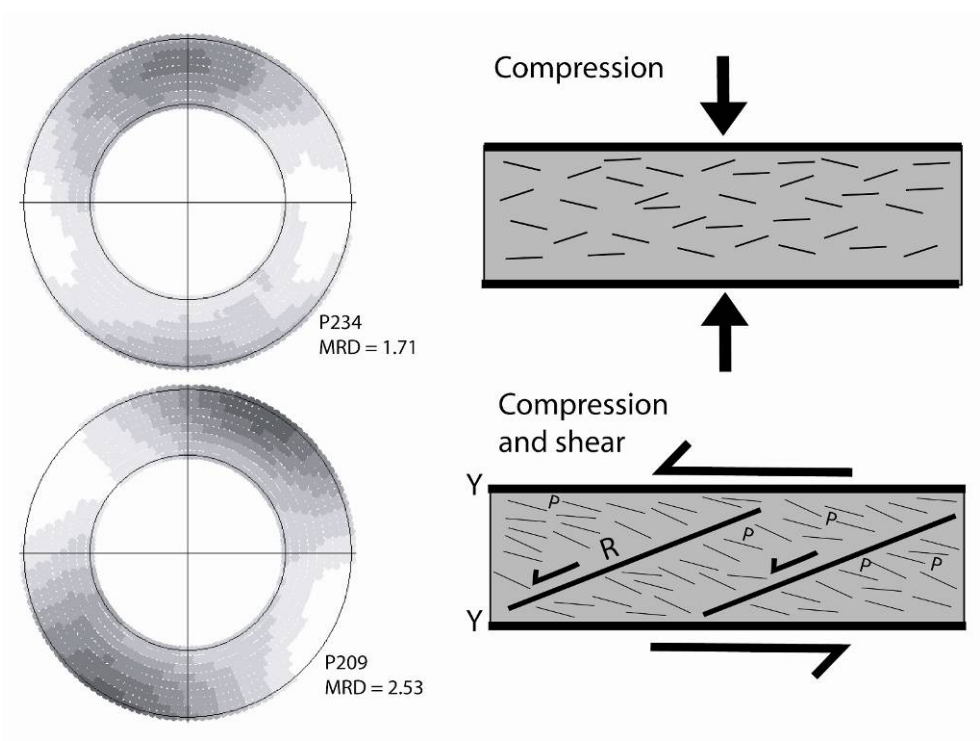
| Experiment | %<br>montmorillonite | $\sigma_n$ (MPa)   | Sliding velocity (mm/s)   | Shear strain<br>at end $S_{n1}$ | Shear strain<br>at end $S_{n2}$ | Shear strain<br>at end $S_{n3}$ | Shear strain<br>at end $S_{n4}$ | Final<br>shear<br>strain | Final $S_n$<br>(MPa) | Shear strain<br>during final $S_n$ |
|------------|----------------------|--------------------|---------------------------|---------------------------------|---------------------------------|---------------------------------|---------------------------------|--------------------------|----------------------|------------------------------------|
| P203       | 90                   | 20 - 30 - 40 - 50  | stepped 1,3,10,30,100,300 | 7.4                             | 11.2                            | 15.9                            | 21.5                            | 21.4                     | 50                   | 5.5                                |
| P204       | 90                   | 5 - 100 - 125 - 15 | stepped 1,3,10,30,100,300 | 6.2                             | 9.0                             | 12.4                            | 16.1                            | 16.1                     | 150                  | 3.8                                |
| P205       | 70                   | 5 - 10 - 15 - 20   | stepped 1,3,10,30,100,300 | 4.4                             | 6.6                             | 9.4                             | 12.6                            | 12.5                     | 20                   | 3.2                                |
| P209       | 50                   | 5 - 10 - 15 - 20   | stepped 1,3,10,30,100,300 | 3.7                             | 5.7                             | 8.0                             | 10.8                            | 10.8                     | 20                   | 2.8                                |
| P211       | 50                   | 30 - 40 - 50 - 75  | stepped 1,3,10,30,100,300 | 4.3                             | 6.4                             | 8.9                             | 12.0                            | 12.0                     | 75                   | 3.1                                |
| P212       | 50                   | 100 - 125 - 150    | stepped 1,3,10,30,100,300 | 4.6                             | 6.9                             | 9.9                             |                                 | 9.9                      | 150                  | 2.9                                |
| P213       | 30                   | 5 - 10 - 15 - 20   | stepped 1,3,10,30,100,300 | 3.5                             | 5.3                             | 7.5                             | 10.0                            | 10.1                     | 20                   | 2.5                                |
| P215       | 30                   | 30 - 40 - 50 - 75  | stepped 1,3,10,30,100,300 | 4.2                             | 6.4                             | 8.9                             | 12.0                            | 12.0                     | 75                   | 3.1                                |
| P216       | 30                   | 100 - 125 - 150    | stepped 1,3,10,30,100,300 | 4.2                             | 6.3                             | 8.9                             |                                 | 8.9                      | 150                  | 2.6                                |
| P220       | 10                   | 30 - 40 - 50 - 75  | stepped 1,3,10,30,100,300 | 3.7                             | 6.1                             | 8.2                             | 11.1                            | 11.1                     | 75                   | 2.9                                |
| P221       | 10                   | 100 - 125 - 150    | stepped 1,3,10,30,100,300 | 4.1                             | 6.1                             | 8.9                             |                                 | 8.6                      | 150                  | 2.8                                |
| P229       | 100                  | 5 - 10 - 15 - 20   | stepped 1,3,10,30,100,300 | 4.1                             | 6.3                             | 9.0                             | 12.3                            | 12.3                     | 20                   | 3.3                                |
| P233       | 100                  | 10                 | No displacement           | 0.0                             |                                 |                                 |                                 | 0.0                      | 10                   | 0.0                                |
| P234       | 100                  | 50                 | No displacement           | 0.0                             |                                 |                                 |                                 | 0.0                      | 50                   | 0.0                                |
| P241       | 100                  | 30 - 40 - 50 - 75  | stepped 1,3,10,30,100,300 | 5.3                             | 7.9                             | 11.1                            | 14.8                            | 14.8                     | 75                   | 3.8                                |
| P1313      | 100                  | 100 - 125 - 150    | stepped 1,3,10,30,100,300 | 6.0                             |                                 |                                 |                                 | 6.0                      | 150                  | 6.0                                |
| P1314      | 100                  | 150                | No displacement           | 0.0                             |                                 |                                 |                                 | 0.0                      | 150                  | 0.0                                |
| P1315      | 100                  | 150                | 10                        | 0.5                             |                                 |                                 |                                 | 0.5                      | 150                  | 0.5                                |
| P1528      | 100                  | 150                | 10                        | 20.5                            |                                 |                                 |                                 | 20.5                     | 150                  | 20.5                               |
| P1529      | 100                  | 75                 | 10                        | 7.2                             |                                 |                                 |                                 | 7.2                      | 75                   | 7.2                                |
| P1530      | 100                  | 75                 | 10                        | 22.6                            |                                 |                                 |                                 | 22.6                     | 75                   | 22.6                               |
| P1531      | 100                  | 20                 | 10                        | 11.9                            |                                 |                                 |                                 | 11.9                     | 20                   | 11.9                               |
| P1532      | 100                  | 20                 | 10                        | 0.3                             |                                 |                                 |                                 | 0.3                      | 20                   | 0.3                                |
| P1533      | 100                  | 20                 | 10                        | 0.3                             |                                 |                                 |                                 | 0.3                      | 75                   | 0.3                                |
| P1551      | 100                  | 20                 | 10                        | 21.3                            |                                 |                                 |                                 | 21.3                     | 20                   | 21.3                               |

| Experiment | MRD  | MRD  | MRD  | MRD  | MRD  | MRD  |
|------------|------|------|------|------|------|------|
| P203       | 3.66 | 4.55 | 3.39 | 3.49 |      |      |
| P204       | 3.71 | 3.85 | 3.82 | 3.44 | 3.08 | 3.04 |
| P205       | 2.19 | 1.72 |      |      |      |      |
| P209       | 3.24 | 2.53 | 2.27 |      |      |      |
| P211       | 2.72 | 2.79 |      |      |      |      |
| P212       | 2.98 | 3.25 |      |      |      |      |
| P213       | 1.94 |      |      |      |      |      |
| P215       | 2.41 | 2.18 |      |      |      |      |
| P216       | 2.30 | 2.18 |      |      |      |      |
| P220       | 2.59 | 2.22 |      |      |      |      |
| P221       | 3.65 | 3.84 |      |      |      |      |
| P229       | 1.95 | 2.00 | 2.41 |      |      |      |
| P233       | 1.80 | 1.63 |      |      |      |      |
| P234       | 1.69 | 1.62 | 1.84 | 1.71 |      |      |
| P241       | 2.75 | 2.49 | 2.80 | 2.36 | 2.66 |      |
| P1313      | 3.64 | 3.71 |      |      |      |      |
| P1314      | 1.70 | 1.69 |      |      |      |      |
| P1315      | 2.32 | 2.48 |      |      |      |      |
| P1528      | 3.86 | 4.38 | 3.83 | 3.82 |      |      |
| P1529      | 4.10 | 2.98 | 2.59 | 2.46 |      |      |
| P1530      | 2.99 | 3.66 | 4.36 | 3.25 |      |      |
| P1531      | 2.54 | 2.23 | 2.28 |      |      |      |
| P1532      | 1.77 | 2.00 |      |      |      |      |
| P1533      | 1.69 |      |      |      |      |      |
| P1551      | 2.36 | 2.43 | 2.33 |      |      |      |

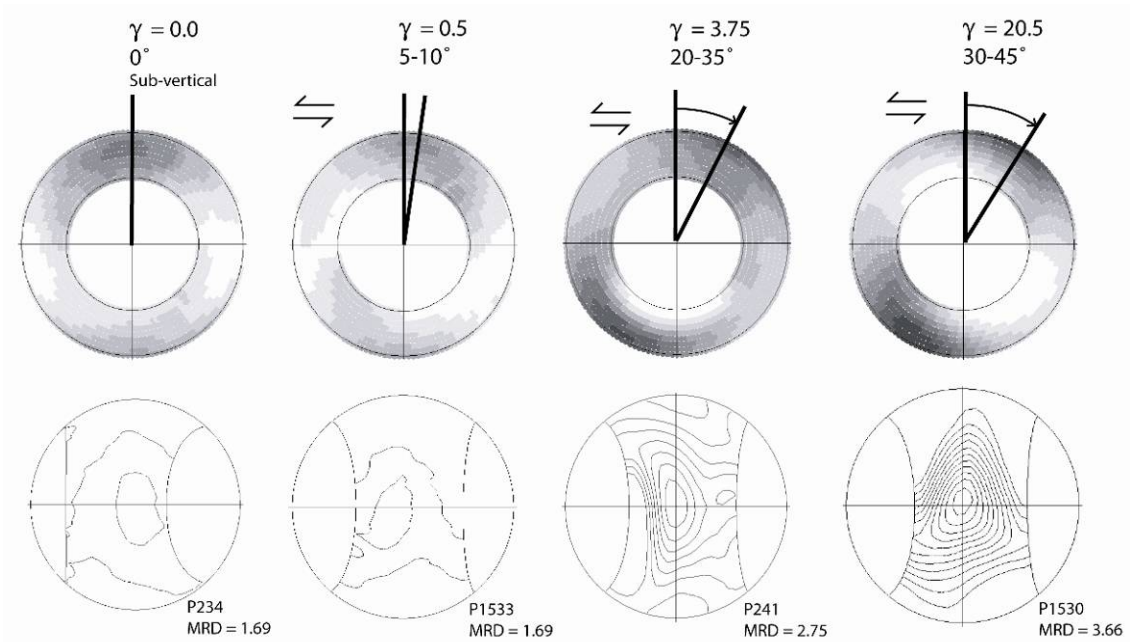
**Table 3-2:** Results of XTG measurements on experimental samples. Upper portion of table contains details of the stress and strain histories of the experimental samples. Lower portion of table shows fabric intensity data (MRD units) for same samples



**Figure 3-7:** Experimental clay fabric intensity data. Shown are three graphs of fabric intensity measurements made at three different normal stresses with a variety of clay contents. Each MRD measurement from a sample is plotted. All fabric intensities are plotted against the amount of shear strain in the final step of the experiment. Note the trend of increasing fabric intensities with increasing shear strain to a shear strain of ~5, then only minor further increases in fabric intensity at shear strains of ~20. Note also the absence of a correlation between clay content and fabric strength at a given shear strain.



**Figure 3-8:** Effect of compression versus shear on clay fabric orientation. Left: representative pole figures from samples subjected to compression (upper left) and subjected to compression and sinistral shear (lower left). Note difference of orientation of maxima with respect to normal stress, and tendency of clay platelets to align along P surfaces in shear. Right: sketches illustrating clay fabric inferred from pole figures.

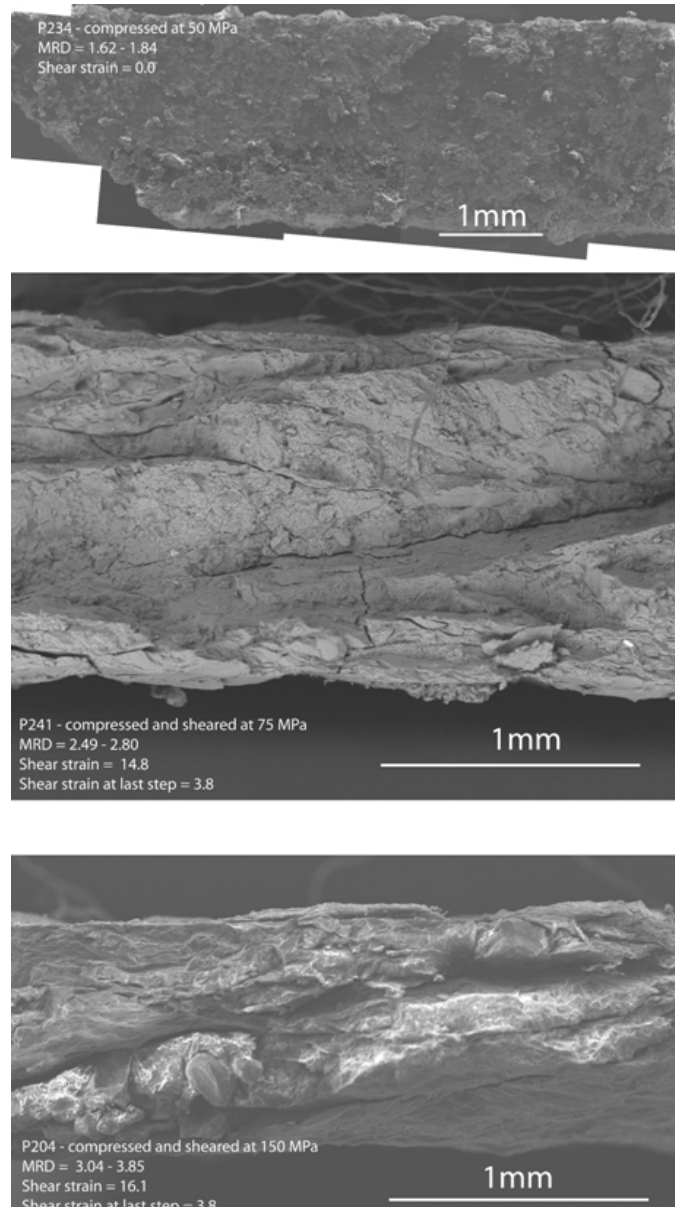


**Figure 3-9:** Effect of increasing shear strain on clay fabric orientation and strength. Pole figures shown are representative unrotated and smoothed pole figures from 100% montmorillonite mixtures at 4 different shear strains ( $\gamma = 0$ ,  $\gamma = 0.5$ ,  $\gamma = 3.8$  &  $\gamma = 20.5$ ). Normal stress is 75 MPa and vertical for all pole figures except for P234, where the maximum normal stress was 50 MPa. Sense of shear is sinistral for all samples (indicated by arrows), except upper left, which is unsheared. Range of angles indicated is the range of rotations of intensity maxima from vertical observed from samples with a given shear strain. Note gradual rotation of the maxima from  $\sigma_1$  with increasing shear strain, along with some increase of fabric strength with increasing strain at strains  $>3$ .

stress and to the shear direction, and parallel to the P shear orientation of Logan et al. (1979).

The orientation of clay fabrics in the experimental samples is analogous to observations of clay foliation in natural fault zones (Chester et al., 1985, Cladouhos, 1999b, Cowan, 2003, Hayman, 2006). The degree of rotation of the maxima from vertical toward  $\sigma_1$  in the experimental samples increases with increasing strain, ranging from  $\sim 0^\circ$  at 0 shear strain, to a maximum of  $30-45^\circ$  at shear strains of  $\sim 6$  (Figure 3.9). Maxima for samples with a shear strain of 0, i.e. simple compression, all have subvertical maxima. The samples with a shear strain of 0.5 exhibit either slightly inclined maxima or multiple maxima that are irregular and rotated at low angles ( $5-15^\circ$ ), both towards and away from  $\sigma_1$ . The two maxima were not perpendicular to each other, and may represent the onset of transition from a compression-dominated fabric to a shear-dominated fabric (e.g., Figure 3.1). Maxima for the samples with a shear strain of  $\sim 3$  are rotated  $20-35^\circ$  towards  $\sigma_1$  while the maxima for samples with a shear strain of  $\sim 20$  are rotated  $30-45^\circ$  towards  $\sigma_1$ .

SEM images further document fabric evolution with increasing strain (Figure 3.10). The samples subject to compression only, and zero shear, exhibit no visible fabric, consistent with MRD's of 1.6 to 1.8. These fabrics are only slightly more coherent than expected for a random distribution of clay grains. Samples that are compressed and sheared, however, are characterized by boundary parallel Y surfaces at the sample margins and clearly developed R shears with polished and striated surfaces (Figure 3.10). The sheared samples also have a crude P foliation, although, interestingly, the P foliation is at a lower angle to  $\sigma_1$  (typically  $5^\circ$  from horizontal), compared to the primary angle for phyllosilicate crystallites determined from XTG analysis, which is  $20-35^\circ$ .

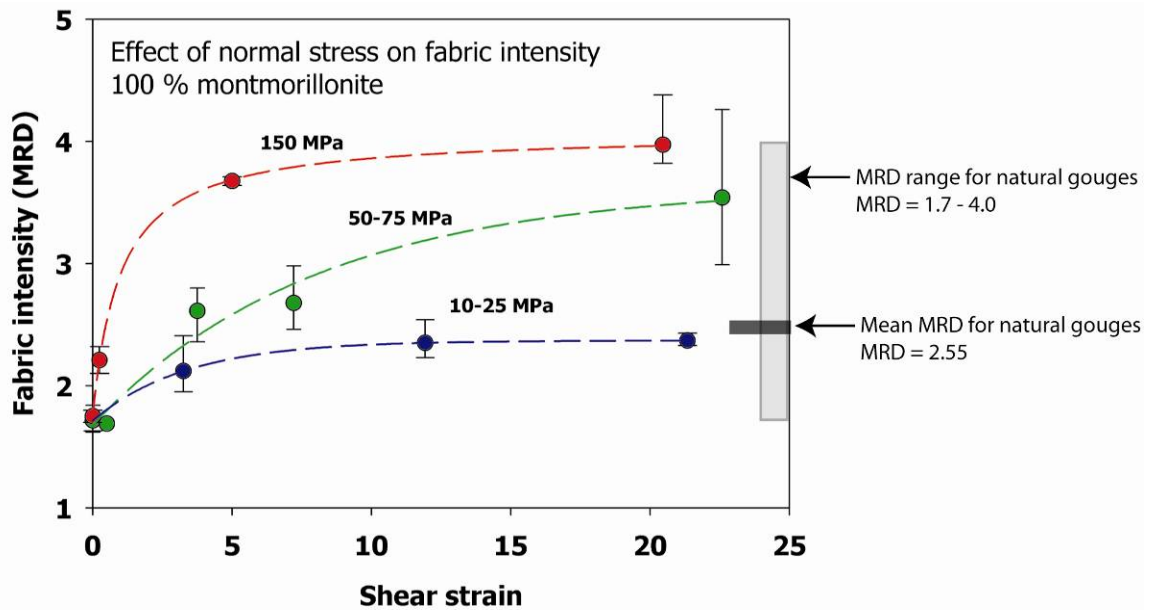


**Figure 3-10:** Scanning electron images of experimental samples used in this study. Top: photomosaic of SE images of sample P234, compressed at 50 MPa with no shear strain. Note the lack of a visible fabric. Middle: SE image of sample P204, compressed at a maximum of 75 MPa and sheared during its final normal stress step to a strain of 3.8. Note the development of a clay fabric, and R and Y surfaces. Bottom: SE image of sample P241, sheared at a maximum normal stress of 150 MPa and sheared during its final normal stress step to a shear strain of 3.8. Note the thinner nature of sample P241 compared to P204 and the stronger visible fabric, illustrating the role of normal stress in accelerating clay fabric development at a given shear strain.

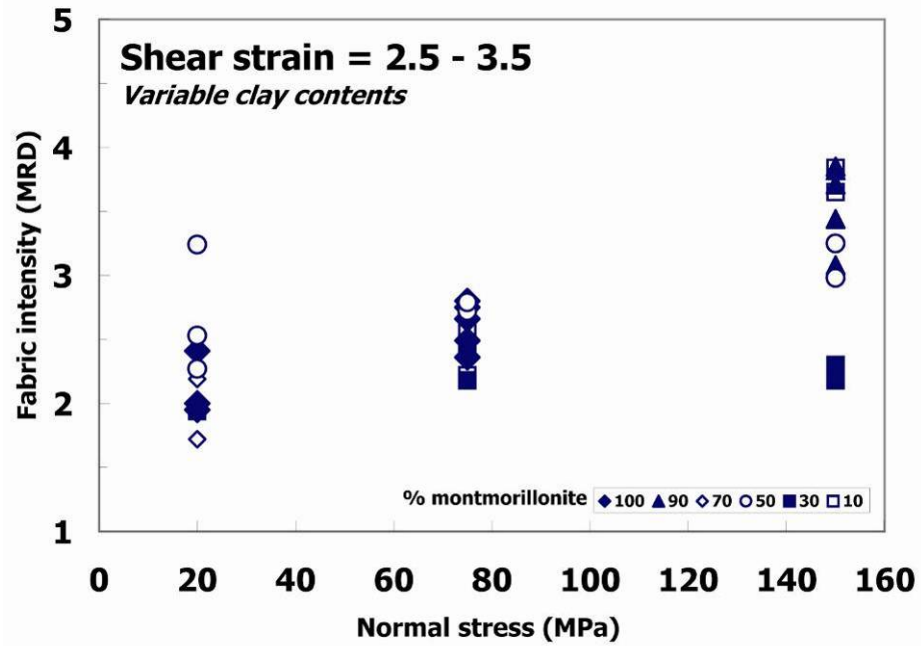


Clay fabric intensity in the experimentally deformed samples increases with increasing shear strain and normal stress. Normal stress dictated the fabric intensity achieved at a given strain and also the amount of strain required to acquire a given fabric strength (Figure 3.11). Samples subjected to compression but no shear exhibit MRD's from 1.6 to 1.8, whereas samples that were subjected to shear strains of ~20 exhibited MRD's of 3.4 to 4.6. Samples compressed at 10-25 MPa acquired a weak fabric at strains up to ~3 and maintained that fabric intensity up to a strain of 21; MRD's range from 1.7 (no fabric) to a maximum of 2.5, with most samples having an MRD of 2.1 to 2.4. Samples that were compressed at a maximum normal stress of 50-75 MPa and sheared to a shear strain of ~22 have MRD's that range from 2.3 to 4.3, with fabric intensity increasing with increasing strain from an average MRD of 2.6 at a strain of ~4, to an average MRD of 3.5 at a strain of 22.5. Samples that were compressed at a maximum normal stress of 150 MPa have MRD's from 2.2 to 4.0, with fabric intensity increasing systematically from an average intensity of 2.2 at a strain of 0.5 to an average fabric intensity of 4.0 at a shear strain of 20.5. At all normal stresses, the maximum fabric intensity is mostly reached within a shear strain of ~5, as suggested by experiments of Saffer and Marone (2003) from the evolution of the friction coefficient with shear strain.

The clay content of our laboratory samples has almost no resolvable effect on the phyllosilicate fabric intensity (Figure 3.12). The MRD values for clay-rich and clay-poor material are essentially identical for a given normal stress and shear strain. This observation is in contrast with findings from sedimentary basins where the fabric intensity decreases systematically with increasing quartz content (Curtis et al., 1980, Sintubin, 1994a, 1994b). Two possible explanations exist. First, the MRD values observed in experimental gouges are so low that the effect of varying clay content is below measurement resolution. A similar comment can be made about the natural fault



**Figure 3-11:** Experimental clay fabric intensity data. Shown are the average fabric intensity (filled circles), minimum and maximum fabric intensity measurements (vertical bars) for a particular friction experiment to highlight the role of shear strain in increasing fabric intensity at low shear strains, and of normal stress controlling the fabric intensity at high shear strains. Natural data are shown on the right-hand side for comparison. Note the average fabric intensities observed in natural gouges are similar to those generated at 10-25 MPa in the experimental material.



**Figure 3-12:** Graph showing the relationship of clay mineral content with fabric strength for samples with similar normal stress conditions and at similar shear strains. Note the lack of correlation of fabric strength with montmorillonite content of the mixture.

gouges, which also show low MRD values (Figure 3.6). For natural and laboratory gouge zones, a systematic difference of fabric strength with non-clay mineral content may be unresolvable within the limitations of the XTG technique. Another possibility is that fabrics in sedimentary rocks are dominated by authigenic clay that grows during burial and diagenesis, with a smaller contribution from detrital grains that may rotate by physical processes. Our laboratory experiments do not involve authigenic grain growth and thus rotation of clay grains is the only process for fabric development. However, authigenic grain growth does occur in natural fault zones (e.g., van der Pluijm et al., 2001). In sedimentary basins, the growth of authigenic phases at and below the smectite-to-illite transition can produce abrupt increases in fabric intensity with depth (e.g. Ho et al., 1996, Day-Stirrat et al., 2008). In these situations, it is possible that the presence of quartz or other non-platy particles hampers authigenic clay growth. In fault zones, if the preferred orientation of clay platelets is kept sufficiently weak by shearing, then the presence or absence of non-platy particles may not have a significant effect.

## **Discussion and Conclusion**

Three key points emerge from our fabric intensity measurements of natural fault gouge. 1) Natural fault gouges have uniformly weak fabrics when compared to the fabrics of phyllosilicate-rich rocks in other geologic environments. Fault gouge fabric intensities range from a low of about 1.8 to a maximum of about 4.4, with an average of 2.7. 2) Tectonic environment does not significantly impact clay fabric development in fault zones; thrust faults, strike-slip faults and both low-angle and high-angle normal faults all have similar fabric intensities. 3) The predominant clay mineralogy of a natural gouge

does not significantly affect fabric intensity; fabrics from chlorite-dominated clay gouges have similar fabric intensities to clay gouges dominated by illite or illite-rich illite-smectite (>75% I in I/S). Gouges dominated by corrensite or sepiolite have similarly weak fabrics compared to those dominated by chlorite or illite, although there are fewer data than from gouges with the former mineral assemblages. Natural gouges dominated by smectite and kaolinite have slightly weaker fabrics that may result from post-faulting growth of the clay phases or the wavy morphology of smectite clay phases.

Elevated fluid pressures in fault zones have been invoked as a possible mechanism for the apparent weakness of upper crustal faults when compared to typical laboratory values for coefficients of rock friction (e.g., Rice, 1992, Falkner & Rutter, 2001). This weakening mechanism requires that fault zone permeability is sufficiently anisotropic that fluids cannot escape into the surrounding wall rock, thus allowing elevated fluid pressure only in the fault core. However, for the faults we sampled, the low phyllosilicate fabric intensities observed and the lack of significant veining in either the gouge zones or the surrounding wall rock coupled indicates that fabric anisotropy cannot be invoked as a mechanism to confine fluids to the fault core. These observations support the findings of Solum et al., (2005) and Hayman (2006) and are consistent with recent studies that document little permeability anisotropy in some mudstones (Yang & Aplin, 2007).

The fabric intensity data from our experimental gouges indicate that the preferred orientation of phyllosilicates in clay-rich material is primarily a function of shear strain and the applied normal stress; fabric intensity does not vary systematically with clay content. Clay fabrics appear to develop almost completely by a shear strain of about 5, and increase only slightly with higher shear strains, suggesting that there is an 'upper limit' to clay fabric intensity generated by physical processes alone. At shear strains of

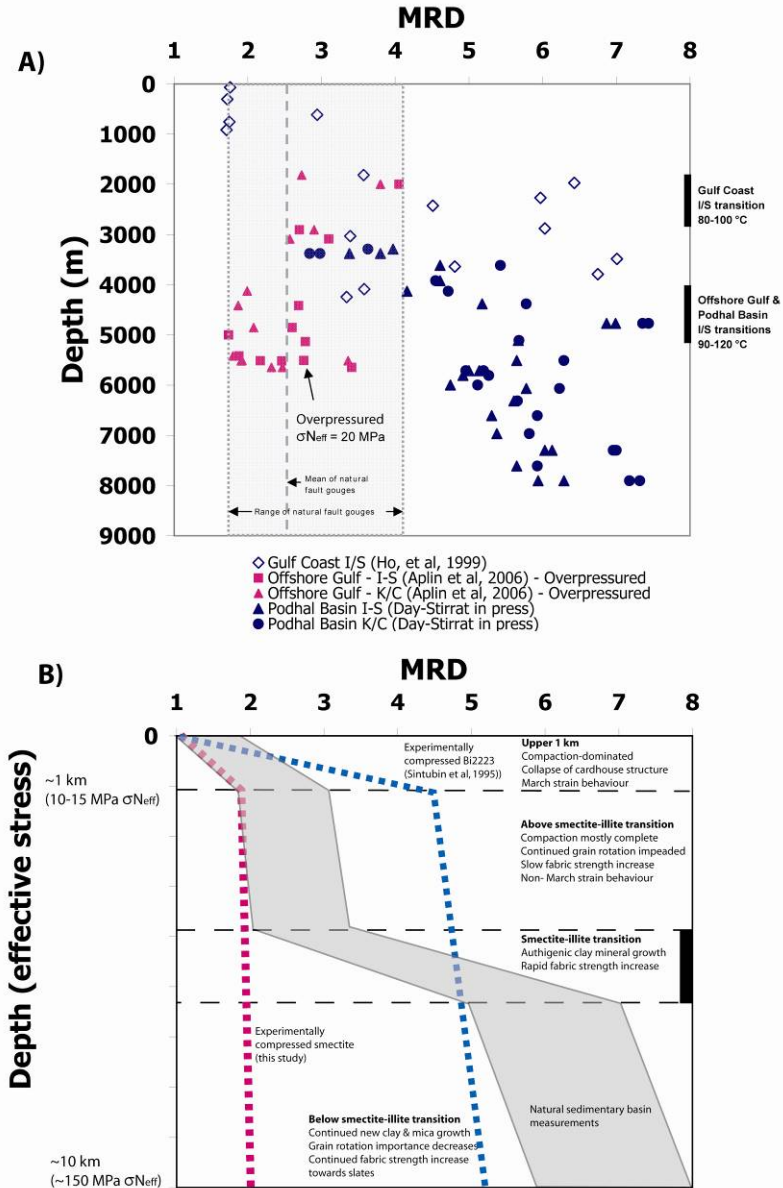
3.5, slip is already concentrated onto narrow R and Y surfaces, leaving the regions of P foliation as 'spectator regions' of low-strain material that are transported passively in the fault (e.g., Mair and Hazzard, 2007).

The existence of spectator regions would help to preserve low fabric intensities for the gouge zone as a whole. In contrast to our experimental conditions, natural clay-rich fault zones show evidence for authigenic growth of clays during deformation (e.g., Vrolijk & van der Pluijm, 1999, van der Pluijm et al., 2001, Solum et al., 2005). As new phyllosilicates grow in the fault zone, this material that has not previously been subjected to shear strain would also act to lower the average, or bulk shear strain in the fault zone.

We find that compression of smectitic material, without shear, does not produce a strong preferred orientation. This contrasts with the March (1932) model of passive particle rotation during compaction and porosity loss, which would predict that fabric intensity increases systematically with compaction alone. However, it is important to consider the range of stresses over which particle rotation is likely to dominate fabric development. During burial, porosity is reduced from initial values of > 50% to < 10% within the first kilometer or two of burial (e.g., Athy, 1930; Hamilton, 1978), where differential stresses are 1-10 MPa (e.g. Bowles et al., 1969, Vassuer et al., 1995). The differential stresses applied to the experimental gouge samples used in this study (10-150 MPa) are considerably higher than those at which the majority of compaction should occur; thus, it is likely that our experimental samples were already compressed to low porosity, even at the lowest stresses used, and that very little pore space remains for clay crystallites to rotate and further reorient with increasing normal stress. In this case, higher differential stress would not produce stronger clay fabrics at compressive stresses beyond ~10 MPa. Similar non-March strain behavior has been observed in fabric strength

measurements on compressed experimental aggregates of powdered phlogopite (Tullis, 1976) and Bi2223, a synthetic superconducting material ( $\text{Bi}_2\text{Sr}_2\text{Ca}_2\text{Cu}_3\text{O}_x$ ) with a platy crystal morphology (Sintubin, 1995). These studies indicated that the fabric strength of experimental aggregates increased rapidly at differential stresses lower than 10 MPa, and then rose only slightly with continued compression to >800 MPa. The phlogopite material asymptotically approached a fabric intensity of ~10.0 MRD with increasing normal stress, while the Bi2223 asymptotically approached a fabric intensity of ~6.0 MRD (Figure 3.13). Both materials exhibited March strain behavior at low compressive stresses (below 10 MPa) and then non-March behavior at higher stresses. A possibly analogous lack of increasing fabric preferred orientation with increasing loading stress has been observed in down-hole sedimentary sequences in the Gulf of Mexico and the Podhale Basin in Poland, where fabric intensity does not increase systematically with depth (i.e., increasing differential stress), but instead increases rapidly across the smectite-to-illite transition as a function of the growth of new minerals (Ho et al., 1995, Day-Stirrat et al., 2008). (Figure 3.13). Thus it seems likely that March strain behavior may not be realistic in geologic materials at compressive stresses much above ~10 MPa.

A key finding of our study is that prior work overestimates the role of mechanical rotation for compaction-induced fabric development in shales (e.g. Lambe, 1953, 1958, Ingles 1968, Yong, 1972). Prior work consistently depicts compaction-induced fabrics as similar to those in the 'strong' clay fabric of Figure 3.1. However, our study quantifies clay fabric intensity directly, and shows that mechanical rotation due to compaction is not a major factor in generating preferred orientation in clay particles. The fabrics obtained by mechanical rotation due to compaction are weak in comparison to those formed by

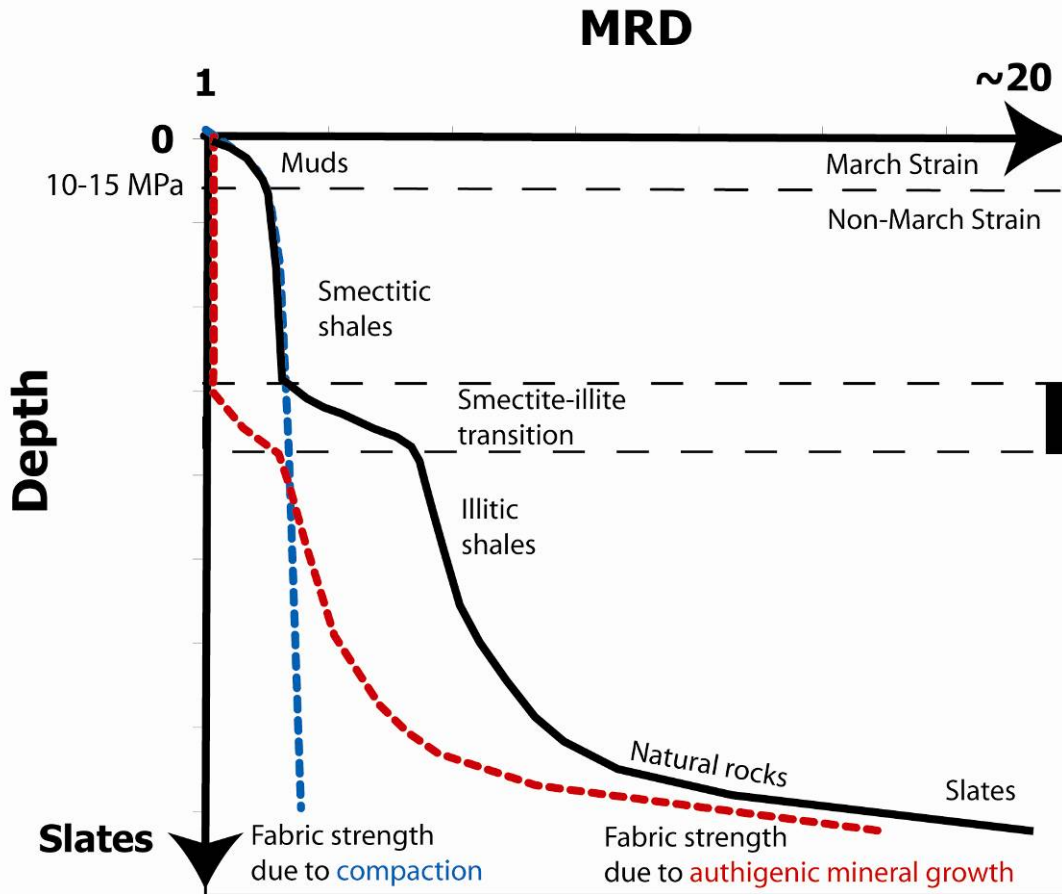


**Figure 3-13:** Comparison of published fabric intensity from sedimentary sequences with observed clay fabric intensities in clay gouges. Note that clay fabrics in both natural and experimental fault gouges never reach the intensities observed in shale with significant authigenic mineral growth. Note also that strong fabrics develop across mineral transformations in the Gulf Coast (Ho et al., 1999) and Podhale Basin sections (Day-Stirrat et al., 2008), whereas for the offshore gulf section (Aplin et al., 2006), where the I/S transformation is not complete, fabrics remain low with increasing depth. The offshore Gulf section is overpressured (effective stress ~20 MPa for the entire section) whereas the Gulf Coast and Podhal basin sections are normally pressured. **B.**) Schematic representation of the fabric development in shale from natural data to clarify processes in Figure A. Dashed lines are fabric measurements from experimentally-compressed material (smectite – this study, Bi2223, Sintubin et al., 1995). Tullis data is not plotted, as normal stresses used during compaction are not known. Grey field is fabric development in natural shales.



shearing in the laboratory and are very weak compared to those developed by diagenetic processes (Figure 3.14). During the latter, authigenic minerals grow with a preferred orientation in response to a differential stress, such as the transition from smectite to illite in sedimentary basins (e.g. Ho et al., 1995, Day-Stirrat et al., 2008) or the growth of new phyllosilicate phases during the transition from shales to slates in low-grade metamorphism (e.g. Ho et al., 2001).

We conclude that fault gouge fabric intensities are uniformly weak compared to those observed in shales, slates and sedimentary environments where diagenesis and metamorphism are active. Fabric intensities of natural fault gouge do not vary significantly as a function of tectonic environment or mineralogy of the dominant clay phase. Clay fabric intensities in natural gouges are sufficiently weak that highly anisotropic clay fabrics cannot be invoked to raise fluid pressures and weaken faults. Fabric intensity measurements from laboratory experiments with synthetic clay-quartz gouge lead to four main conclusions: 1) Although experimental clay gouge phyllosilicate fabrics are weak, fabric intensities vary systematically with shear strain. Fabric intensities for strained samples range from 1.7 to 4.6 and increase with increasing strain. 2) Gouges that are subject to compressive loading without shear acquire a weak fabric that is more or less perpendicular to the applied stress. Samples that are both compressed and sheared develop fabrics in which the clay crystallites are oriented obliquely, roughly  $15^\circ$  to  $\sigma_1$ , along P surfaces. 3) Samples that are compacted without shear have very weak fabrics, regardless of the applied normal stress. Samples subjected to compression at 10 MPa have essentially identically weak fabrics to those subjected solely to compression at 150 MPa; both having MRD's of 1.6 to 1.8. In light of these observations, the view that mudrocks acquire their preferred orientation primarily from compaction needs to be reconsidered, although the role of water saturation in



**Figure 3-14:** Schematic figure showing relative roles of compaction and authigenic mineral growth in diagenetic sequences as inferred from fabric intensity measurements. Note that at depths above the onset of the smectite-to-illite transformation, fabric strength is dominated by compaction, whereas at and below the smectite-to-illite transformation, fabric strength is almost entirely dominated by authigenic (mineral-forming) processes.

aiding grain boundary sliding has not been evaluated. 4) Samples both compressed and sheared to high shear strains develop fabric strengths that increase with higher applied normal stresses. Clay fabric intensities observed in natural gouges are similar to experimental material sheared at low normal stresses, and the experimental data suggest that most faults in the brittle regime do not experience high normal stresses during deformation.

**Acknowledgments:**

We are grateful to John Solum and Anja Schleicher for unpublished XTG data, and to Suzanne Janecke who provided sample material from the Salton Detachment. This work was made possible by NSF grants EAR-047707 (to BVDP), EAR-0545702 (to CM and DS), and OCE-0648331 (to CM and DS) and by an AAPG Grant-in-Aid to Haines.

## References

- Aplin, A., Matenaar, I., McCarty, D. & van der Pluijm, B. (2006). Influence of mechanical compaction and clay mineral diagenesis on the microfabric and pore-scale properties of deep-water Gulf of Mexico mudstones. *Clays and Clay Minerals* 54, No. 4, pp. 500-514.
- Axen, G. (2004). Mechanics of low-angle normal faults. In: Karener, G., Taylor, B., Driscoll, N., Kohlstedt, D. (eds), *Rheology and deformation of the lithosphere at continental margins*. Columbia University Press, pp. 46-91.
- Axen, G. & Fletcher, J., (1998). Late Miocene-Pliocene extensional faulting, northern California, Mexico, and Salton Trough, California: *International Geology Review* 40, pp. 219-244.
- Anthony, J. & Marone, C., (2003) Influence of particle characteristics on granular friction. *J. Geophysical Research*. 110, doi:10.1029/2004JB003399.
- Bolwes, F., Bryant, W. & Wallin, C. (1969). Microstructure of unconsolidated and consolidated marine sediments. *J. Sed. Petrol.* 39, pp. 1546-1551.
- Brown, K., Kopf, A., Underwood, M. & Weinberger., J., (2003). Compositional and fluid pressure controls on the state of stress on the Nankai subduction thrust: A weak plate boundary. *Earth and Planetary Science Letters* 214, pp. 589-603
- Bruce, C., (1984). Smectite dehydration – Its relation to structural development and hydrocarbon accumulation in northern Gulf of Mexico basin. *Amer. Assoc. Pet. Geol. Bull.* 68, pp. 673-683.
- Buck, W. (1988) Flexural rotation of normal faults, *Tectonics* 7 pp. 959-73.
- Byerlee, J., (1978). Friction of rocks. *Pure and Applied Geophysics* 116, pp. 615-626.
- Cladouhos, T., (1999a). Shape preferred orientations of survivor grains in fault gouge. *J. Structural Geology* 21, pp. 419-436.
- Cladouhos, T., (1999b). A kinematic model for deformation within brittle shear zones. *J. Structural Geology* 21, pp. 437-448.
- Chester, F., Friedman, M. & Logan, J., (1985) Foliated cataclasites. *Tectonophysics* 111, pp. 139-145.
- Coney, P. (1980) Cordilleran metamorphic core complexes: An overview in Crittenden, M. et al., (1980) eds. *Cordilleran metamorphic core complexes Geol. Soc. Amer. Memoir* 153, pp. 7-31
- Cowan, D., (1999). Do faults preserve a record of seismic slip? A field geologist's opinion. *J. Structural Geology* 21, pp. 995-1001.

- Cowan, D., Cladouhos, T., & Morgan, J., (2003). Structural geology and kinematic history of rocks formed along low-angle normal faults, Death Valley, California. *Geological Society of America Bulletin* 115, pp. 1230-1248.
- Curtis, C., Lipshie, S., Oertel, G & Pearson, M., (1980). Clay orientation in some Upper Carboniferous mudrocks, its relationship to quartz content and some inferences about fissility, porosity and compactional history. *Sedimentology* 27, pp. 333-339.
- Dallmeyer, R., Snoke, A., & McKee, E. (1986) The Mesozoic-Cenozoic tectonothermal evolution of the Ruby Mountains, East Humboldt range, Nevada: A cordilleran metamorphic core complex. *Tectonics* 5, pp. 931-54
- Day-Stirrat, R., Aplin, A., Środoń, J., & van der Pluijm, B., (2008). Diagenetic reorientation of phyllosilicate minerals in Paleogene mudstones of the Podhale Basin, southern Poland. *Clays and Clay Minerals* 56, pp. 100-111.
- Di Toro, G., Nielsen, S., & Pennacchioni, G., (2005). Earthquake rupture dynamics frozen in exhumed ancient faults. *Nature*, vol. 436, pp. 1009-1012
- Dokka, R., Mahaffie, M., & Snoke, A. (1986) Thermochronologic evidence of major tectonic denudation associated with detachment faulting, northern Ruby Mountains, East Humboldt Range, Nevada. *Tectonics* 5, pp. 995-1006
- Faulkner, D.R., & Rutter, E.H., (2001). Can the maintenance of overpressured fluids in large strike-slip fault zones explain their apparent weakness? *Geology* 29, 503–506.
- Falkner, D, Mitchell, T., Healy, D. & Heap, M., (2006) Slip on ‘weak’ faults by the rotation of regional stress in the fracture damage zone. *Nature* 444, pp. 922-925.
- Fitzgerald, P., Muñoz, J., Coney, P. & Baldwin, S. (1999). Asymmetric exhumation across the Pyrenean orogen: implications for the tectonic evolution of a collisional orogen. *Earth and Planetary Science Letters* 173, pp. 157-180.
- Hayman, N., Knott, J., Cowan, D., Nemser, E., & Sarna-Wojcicki, A., (2003). Quaternary low-angle slip on detachment faults in Death Valley, California. *Geology* 31, pp. 343-346.
- Hayman, N., Housen, B., Cladouhos, T., & Livi, K., (2004). Magnetic and clast fabrics as measurements of grain-scale processes within the Death Valley shallow-crustal detachment faults. *J. Geophysical Research* 109, B05409, doi:10.1029/2003JB002902.
- Hayman, N. (2006). Shallow crustal faults from the Black Mountain detachments, Death Valley, CA. *J. Structural Geology* 28, pp. 1767-1784.
- Heilbronner, R. & Pauli, C., (1993). Integrated spatial and orientation analysis of quartz c-axes by computer-aided microscopy. *J. Structural Geology* 15, pp. 369-382.

- Ho, N., Peacor, D. & van der Pluijm, B., (1995). Reorientation mechanisms of phyllosilicates in the mudstone-to-slate transition at Lehigh Gap, Pennsylvania. *J. Structural Geology* 17, pp. 345-356.
- Ho, N., Peacor, D. & van der Pluijm, B., (1996). Contrasting roles of authigenic and detrital phyllosilicates during slaty cleavage development. *J. Structural Geology* 18, pp. 615-623.
- Ho, N., Peacor, D. & van der Pluijm, B., (1999). Preferred orientation of phyllosilicates in Gulf Coast mudstones and relation to the smectite-illite transition. *Clays and Clay Minerals* 47, pp. 495-504.
- Ho, N., van der Pluijm, B. & Peacor, D. (2001) Static recrystallization and preferred orientation of phyllosilicates: Michigamme Formation, northern Michigan, USA. *J. Structural Geology* 23, pp. 887-893.
- Holeywell, R. & Tullis, T., (1975). Mineral reorientation and slaty cleavage in the Martinsburg formation, Lehigh Gap, Pennsylvania. *Geological Society of America Bulletin*. 86, pp. 1296-1304.
- Housen, B., Richter, C., & van der Pluijm, B., (1993). Composite magnetic anisotropy fabrics: experiments, numerical models, and implications for the quantification of rock fabrics. *Tectonophysics* 220, pp. 1-12.
- Ingles, O., (1968). Soil chemistry relevant to the engineering behavior of soils, in *Soil Mechanics – selected topics*, (Lee, I. ed.) Elsevier, New York, pp. 1-57.
- Ikari, M., Saffer, D., & Marone, C., (2007). Effect of hydration state of the frictional properties of montmorillonite-based fault gouge. *J. Geophysical Research*. B, 112, doi:10.1029/2006JB004748.
- Jacob, G., Kisch, H. & van der Pluijm, B., (2000). The relationship of phyllosilicate orientation, X-ray diffraction intensity ratios and c/b fissility ratios in metasedimentary rocks of the Helvetic zone of the Swiss Alps and the Caledonides of Jämtland, central western Sweeden. *J. Structural Geology* 22, pp. 245-258.
- Lambe, T., (1953). The structure of inorganic soil. *Proc. Amer. Soc Civ. Engineers* 79, pp. 1-49.
- Lambe, T., (1958). The structure of compacted clay. *Proc. Amer. Soc Civ. Engineers* 84, pp. 1654-1 to 1654-34.
- Lipshie, S., Oertel, G. & Christie, J. (1976). Measurement of preferred orientation of phyllosilicates in schists. *Tectonophysics* 34, pp. 91-99.
- Logan, J., Friedman, M., Higgs, M., Dengo, C. & Shimamoto, T., (1979). Experimental studies of stimulated gouge and their application to studies of natural fault zones. *Proc. Conf. VIII, Analysis of Actual Fault Zones in Bedrock*. U.S. Geol. Surv. Menlo Park, Calif., pp. 305-343.

- Logan, J. & Rauenzahn, K., (1987). Frictional dependence of gouge mixtures of quartz and montmorillonite on velocity, composition, and fabric, *Tectonophysics* 144, pp. 87-108.
- Lupini, J., Skinner, A., & Vaughan, P., (1981). The drained residual strength of cohesive soils, *Geotechnique* 31 pp. 181-213.
- Mair, K., & Hazzard, J.F., (2007) Nature of stress accommodation in sheared granular material: Insights from 3D numerical modeling, *Earth and Planetary Science Letters* 259, pp. 469-485, 10.1016/j.epsl.2007.05.006
- March, A., (1932). Mathematische Theorie der Regelung nach der Korngestalt bei affiner Deformation. 2. *Kristallogr.* 81, pp. 285-297.
- McGrew, A. & Snee, L. (1994)  $^{40}\text{Ar}/^{39}\text{Ar}$  thermochronologic constraints on the tectonothermal evolution of the northern East Humboldt Range metamorphic core complex, Nevada. *Tectonophysics* 238, pp. 425-50
- McGrew, A., Peters, M. & Wright, J. (2000) Thermobarometric constraints on the tectonothermal evolution of the East Humboldt Range metamorphic core complex, Nevada. *Geological Society of America Bulletin.* 112, pp. 45-60
- Miller, M., (1996). Ductility in fault gouge from a normal fault system, Death Valley, California: a mechanism for fault-zone strengthening and relevance to paleoseismicity. *Geology* 24, pp. 603-606.
- Miller, M., & Wright, L. (2004). Geology of Death Valley National Park, 2ed edition. Kendall Hall, Dubuque, 123 pp.
- Mitchell, J. K. (1993). Fundamentals of Soil Behavior, 2nd edition., John Wiley, New York, 437 pp.
- Morrow, C., Shi, L., & Byerlee, J., (1982). Strain hardening and strength of clay-rich fault gouges, *J. Geophysical Research B* 87 pp. 6771-6780.
- Morrow, C., Radney, B., & Byerlee, J., (1992). Frictional strength and the effective pressure law of montmorillonite and illite clays, *in: B. Evans (Ed.), Fault Mechanics and Transport Properties of Rocks; A Festschrift in Honor of W.F. Brace*, Academic Press, San Diego, CA, pp. 69-88.
- Morrow, C., Moore, D., & Lockner, D., (2000). The effect of mineral bond strength and absorbed water on fault gouge frictional strength, *Geophysical Research Letters* 27 pp. 815-818.
- Moore, D., Summers, R., & Byerlee, J., (1989). Sliding behavior and deformation textures of heated illite gouge, *J. Structural Geology* 11, pp. 329-342.
- Mueller, K., & Snoke, A. (1993) Progressive overprinting of normal fault systems and their role in Tertiary exhumation of the East Humboldt-Woods Hills metamorphic complex, northeast Nevada. *Tectonics* 12, pp. 361-71

- Numelin, T., Marone, C. & Kirby, E., (2005) Frictional properties of natural fault gouge from a low-angle normal fault, Panamint Valley, CA. *Tectonics* 26, doi:10.1029/2005TC001916
- O'Brian, D., Wenk, H., Ratschbacher, L. & You, Z., (1987). Preferred orientation of phyllosilicates in phyllonites and ultramylonites. *J. Structural Geology* 9, pp. 719-730.
- Oertel, G. & Curtis, C., (1972). Clay-ironstone concretions preserving fabrics due to progressive compaction. *Geol. Soc. Amer. Bull* 83, pp. 2597-2606.
- Oertel, G., (1983). The relationship of strain and preferred orientation of phyllosilicate grains in rocks – a review. *Tectonophysics* 100, pp. 413-447.
- van der Pluijm, B., Ho, N., & Peacor, D., (1994). High-resolution X-ray texture goniometry. *J. Structural Geology* 16, pp. 1029-1032, 1994.
- Pares, J., van der Pluijm, B., & Dinarès-Turell, J., (1999) Evolution of magnetic fabrics during incipient deformation of mudrocks (Pyrenees, Northern Spain). *Tectonophysics* 307, pp. 1-14.
- Pavlis, T., Serpa, L., & Keener, C., (1993). Role of seismogenic processes in fault-rock development; an example from Death Valley, California. *Geology* 21, pp. 267-270.
- Price, G., (1973). The photometric method used in microstructural analysis. *Amer. J. Sci.* 273, pp. 523-537.
- Puigdefàbregas, C., Muñoz, J., & Marzo, M. (1986). Thrust development in the eastern Pyrenees and related depositional sequences in the southern foreland basin. *In: Foreland Basins, eds. Allen, P. & Homewood, P. Int. Assoc. Sedimentologists Special Pub.* 8, pp. 229-46.
- Rice, J.R., (1992). Fault stress states, pore pressure distributions, and the weakness of the San Andreas Fault. *In: Evans, B., Wong, T.-F. (Eds.), Fault Mechanics and Transport Properties of Rocks; A Festschrift in honor of W.F. Brace. Academic Press, San Diego, pp. 475–503.*
- Richter, C., van der Pluijm, B., & Housen, B., (1993). The quantification of crystallographic preferred orientation using magnetic anisotropy. *J. Structural Geology* 15, pp. 113-116.
- Saffer, D., Frye, K., Marone, C. & Mair, K., (2001). Laboratory results indicating complex and potentially unstable frictional behavior of smectite clay, *Geophysical Research Letters* 28 pp. 2297-2300.
- Saffer, D. & Marone, C., (2003) Comparison of smectite- and illite-rich gouge frictional properties: application to the updip limit of the seismogenic zone along subduction megathrusts. *Earth and Planetary Science Letters* 215, pp. 219-235.



- Schleicher, A., van der Pluijm, B., Solum, J. & Warr, L., (2006). Origin and significance of clay-coated fractures in mudrock fragments of the SAFOD borehole (Parkfield California). *Geophysical Research Letters* 33, doi:10.1029/2006GL026505, 2006
- Schulz, L., (1949). Determination of preferred orientation in flat transmission samples using a Geiger Counter X-ray spectrometer. *J. Applied Physics* 20, pp. 1033-1036.
- Sibson, R., (1977). Fault rocks and fault mechanisms. *J. Geol. Soc. London* 133, pp. 191-213.
- Sintubin, M., (1994a). Phyllosilicate preferred orientation in relation to strain path determination in the lower Paleozoic Stavelot-Venn Massif (Ardennes, Belgium). *Tectonophysics* 237, pp. 215-231.
- Sintubin, M., (1994b). Clay fabrics in relation to the burial history of shales. *Sedimentology* 41, pp. 1161-1169.
- Sintubin, M., Wenk, H-R., & Phillips, D. (1995). Texture development in platy materials: comparison of Bi2223 aggregates with phyllosilicate fabrics. *Materials Science and Engineering A202*, pp. 157-171.
- Skempton, A., (1970). The consolidation of clays by gravitational compaction. *Q. J. Geol. Soc. London* 125, pp. 373-411.
- Snoke, A. (1980). Transition from infrastructure to superstructure in the Northern Ruby Mountains, Nevada. *in: Crittenden, M. et al., (1980) eds. Cordilleran metamorphic core complexes. Geol. Soc. Amer. Memoir* 153, pp. 287-333
- Snoke, A. & Howard, K. (1984). Geology of the Ruby Mountains-East Humboldt Range, Nevada: A Cordillerian metamorphic core complex. *In: Western geological excursions, Lintz, J. ed., GSA Ann. Meeting guidebook* volume 4, Reno Nevada, Mackay School of Mines, pp. 260-303.
- Solum, J., van der Pluijm, B., Peacor, D. & Warr, L., (2003). Influence of phyllosilicate mineral assemblages, fabrics and fluids on the behavior of the Punchbowl Fault, southern California. *J. Geophysical Research B108*, doi:10.1029/2002JB001858.
- Solum, J., van der Pluijm, B., & Peacor, D., (2005). Neocrystallization, fabrics and age of clay minerals from an exposure of the Moab Fault, Utah. *J. Structural Geology* 27, pp. 1563-1576.
- Sussman, A., Butler, R., Dinarès-Turell, J. & Verges, J. (2004) Vertical-axis rotation of a foreland fold and implications for orogenic curvature: an example from the Southern Pyrenees, Spain. *Earth and Planetary Science Letters* 218, pp. 435-49.
- Storti, F., Billi, A., & F. Salvini. (2003), Particle size distributions in natural carbonate fault rocks: insights for non-self-similar cataclasis, *Earth and Planetary Science Letters*, 206, 173-186.

- Tullis, T. & Wood, D. (1975). Correlation of finite strain from both reduction bodies and preferred orientation of mica in slate from Wales. *Geological Society of America Bulletin* 86, pp. 632-638.
- Tullis, T., (1976). Experiments on the origin of slaty cleavage and schistosity. *Geological Society of America Bulletin* 87, pp. 745-753.
- Turner, F. & Weiss, L. (1963) Structural analysis of metamorphic tectonites. McGraw-Hill, New York.
- van der Pluijm, B.A., Hall, C.M., Vrolijk, P.J., Pevear, D.R., & Covey, M.C., (2001). The dating of shallow faults in the Earth's crust: *Nature*, v. 412, 172-175, doi: 10.1038/35084053.
- Vrolijk, P., & van der Pluijm, B. (1999) Clay gouge. *J. Structural Geology* 21, 1039-1048.
- Wenk, H. (1985). Measurements of pole figures *in* Wenk, H. (ed.), Preferred orientation in deformed metals and rocks. Academic Press, Orlando p. 11-47.
- Wenk, H., (2006). Neutron diffraction texture analysis. *Reviews in Mineralogy* 63, pp. 399-426.
- Wernicke, B. & Axen, G. (1988) On the role of isostasy in the evolution of low-angle normal fault systems *Geology*, 16 pp. 848-51.
- Yan, Y., van der Pluijm, B., & Peacor, D., (2001). Deformational microfabrics of clay gouge, Lewsi Thrust, Canada: A case for fault weakening from clay transformation. In The nature and tectonic significance of fault zone weakening edited by R.E. Holdsworth et al.. *Geol. Soc. Spec. Publ.* 186, pp. 103-112.
- Yang, Y. & Aplin, A., (2007). Permeability and petrophysical properties in 30 natural mudstones. *J. Geophysical Research B* 112, B03206, doi:10.1029/2005JB004243, 2007
- Yong, R., (1972). Soil technology and stabilization: *Proceedings of the 4<sup>th</sup> Asian Regional Conference on Soil Mechanics and Foundation Engineering* 2, pp. 111-124.

## CHAPTER 4: CLAY QUANTIFICATION AND AR-AR DATING OF SYNTHETIC AND NATURAL GOUGE - APPLICATION TO THE MIOCENE SIERRA MAZATÁN DETACHMENT FAULT, SONORA, MEXICO

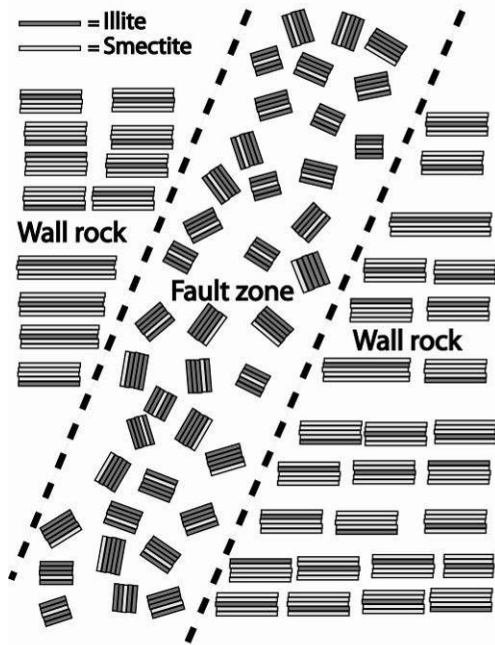
### **Abstract:**

Direct dating of brittle fault rocks has been predicated on the assumption that illite in fault gouge is a mixture of two populations of clays: one detrital, derived from the wall rock, and the other authigenic, forming in the brittle fault zone during faulting. Owing to complex diagenetic histories of wallrock shales in previous fault-dating studies, this assumption has remained largely untested. We demonstrate the validity of our clay quantification technique using calculated WILDFIRE© patterns to accurately model both artificial mixtures of  $2M_1$  and  $1M_d$  illite, and natural mixtures in young fault gouges. Using our quantification approach, we obtain well-defined detrital and authigenic ages from the Sierra Mazatán metamorphic core complex in Sonora, Mexico. Because the age population of the wall rock is well constrained by cooling ages, we confirm that the detrital component in the gouge is the age of the footwall granite, while the age of the authigenic component is the time at which faulting ceased, which is in agreement with field constraints. Based on the Ar-Ar age and the thermal conditions for the growth of the authigenic illite we also conclude that the Sierra Mazatán detachment continued slipping in the brittle regime at strain rates similar to those for the plastic regime (on the order of  $10^{-14} \text{ s}^{-1}$ ).

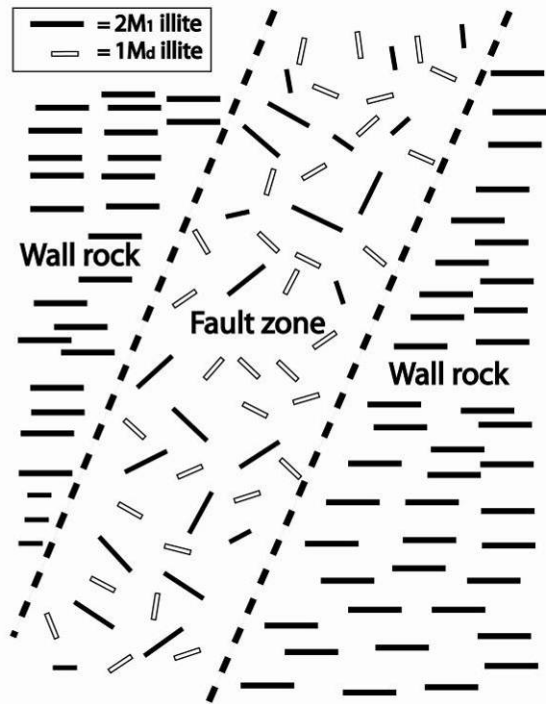
## Introduction

In recent years, mineral reactions related to faulting in the brittle regime have been recognized as an important process in fault zones (e.g., Pevear, 1999, Vrolijk and van der Pluijm, 1999, Yan et al., 2001). In clay gouge, earlier workers isolated a fine-grained fraction of illite ( $<2\mu\text{m}$ ) of the 1M or 1M<sub>0</sub> polytype, considered to be indicative of low-temperature authigenic growth. It was assumed that there was no detrital (2M<sub>1</sub>) illite in these samples (e.g. Lyons & Snellenburg, 1970, Kralik et al., 1987). Dating of the illite tended to overestimate the age of the faulting, however, as later work has shown that some detrital material is typically present even in very fine size fractions (Pevear, 1992, Grathoff, et al., 2001). Subsequent workers employed and modified modeling programs such as NEWMOD<sup>®</sup> (Reynolds, 1996) and WILDFIRE (Reynolds, 1993b) to quantitatively determine the amounts of authigenic and detrital clays in various size fractions in a gouge (Vrolijk and van der Pluijm, 1999, Ylagan et al., 2002; Solum et al., 2005; van der Pluijm et al., 2006; Solum & van der Pluijm, 2007). The percentage detrital illite of each of the size fractions is plotted against their apparent Ar-Ar total gas ages, and extrapolated to 0% and 100% to find the end-member ages. Two mineralogical reactions have been used for dating fault gouge: the illitization of illite/smectite (I/S) and the neocrystallization of authigenic 1M/1M<sub>0</sub> illite (shown diagrammatically in Figure 4.1). Clay-rich gouges have been observed to have higher percentage of illite in illite/smectite than the wall rocks on either side (Vrolijk and van der Pluijm, 1997). Using NEWMOD<sup>®</sup>, a program that generates calculated diffraction patterns for illite and illite/smectite, workers have been able to quantify authigenic illite in the illite/smectite in fault zones and reliably date the age of faulting by Ar/Ar chronology (van der Pluijm, et al., 2001). The illitization of illite/smectite approach is limited when illite (assumed to be detrital, either muscovite

A - Illitization of illite-smectite



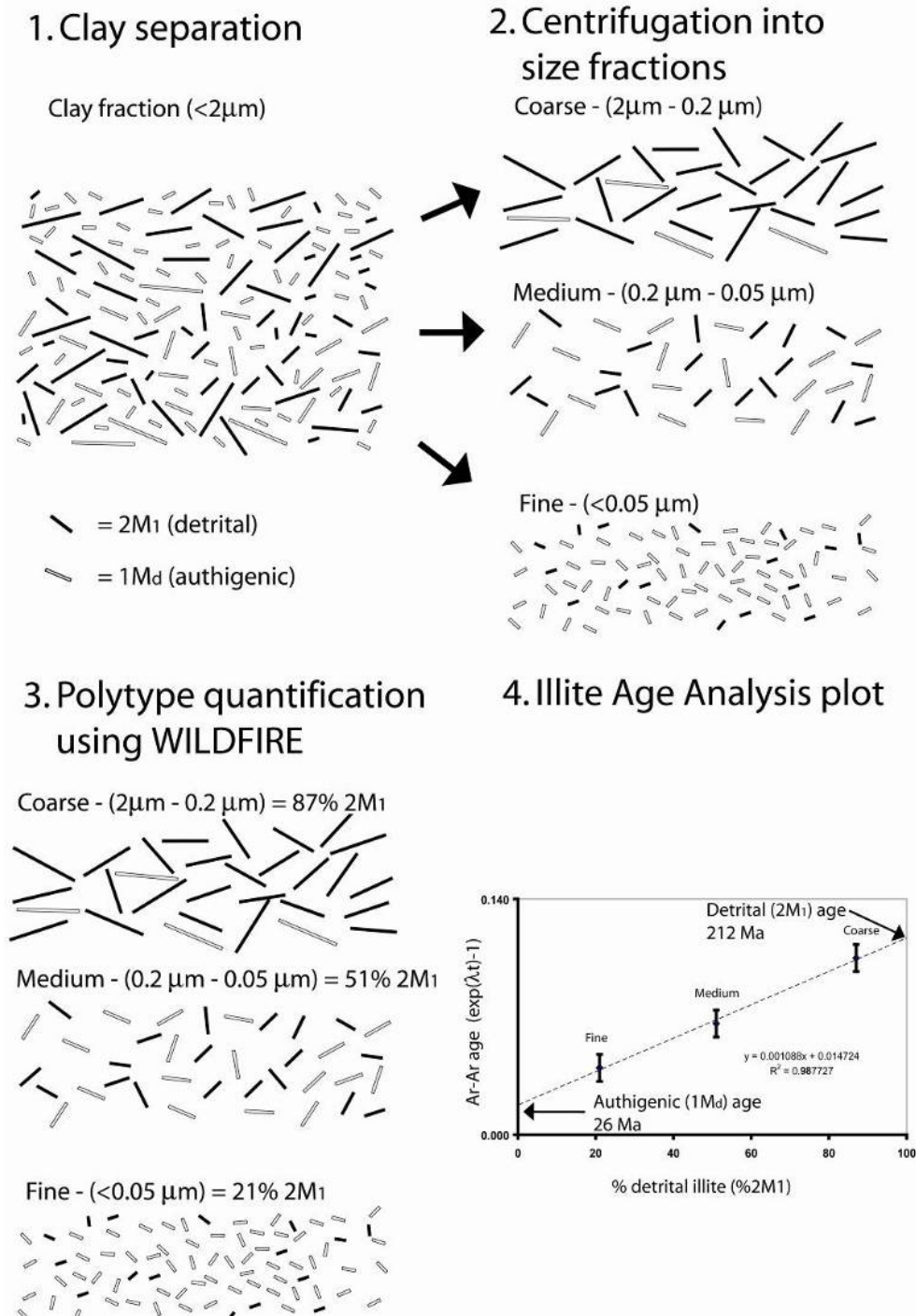
B - Growth of authigenic 1M<sub>d</sub> illite



**Figure 4-1:** Mineral transformations observed in clay gouges that are suitable for dating by illite age analysis. A. illitization of illite-smectite in fault gouge relative to the wall rock B. Growth of authigenic discrete 1M<sub>d</sub> illite in the gouge. 1M<sub>d</sub> illite grows below 150 °C.

or  $2M_1$  illite) occurs both in the wall rock and grows authigenically in the fault zone as the low-temperature  $1M/1M_d$  polytype (Solum et al., 2005). For this reason, our recent work has been focused on dating the observed  $1M/1M_d$  illite, discriminating it from the detrital  $2M_1$  polytype on the basis of XRD patterns and WILDFIRE<sup>®</sup>, a program that generates synthetic XRD patterns for clay minerals. WILDFIRE<sup>®</sup> patterns are used to iteratively model the percentage of the  $2M_1$  and  $1M_d$  polytypes in several size fractions, each with its own ratio of detrital to authigenic illite (Figure 4.2) (Ylagan, et al., 2002; Solum et al., 2005; Solum and van der Pluijm, 2007).

Our goals in this paper are threefold: to test our polytype quantification approach using experimental mixtures, to test our ability to date young gouges by applying our dating method to young, well-constrained faults, and to establish the significance of ages extracted for the detrital component of gouge. Using mixtures of standards, we aim to first demonstrate that a lowest-variance approach to modeling polytype ratios is appropriate at some ratios of polytypes, but at other ratios of polytypes, particularly  $2M_1$ -rich ratios, better results are obtained by matching the specific  $2M_1$  peaks, rather than the entire XRD pattern. We will then demonstrate the efficacy of our technique by dating gouge from the Sierra Mazatán metamorphic core complex in northwest Mexico, where the age of the detrital component is well established by a set of cooling histories from modeled K-feldspar Ar-Ar multi-domain diffusion modeling (Wong and Gans, 2003), and show that our approach accurately captures the age of authigenic clay in fault gouge. Dating the deformation related to the onset of exhumation of a core complex in the plastic regime has become relatively straightforward (e.g. McGrew and Snee, 1994, Vanderhaeghe et al., 2003), but determining when activity on a detachment ceases, critical to understanding the kinematics of core complex evolution, is much more difficult. Activity on brittle faults at core complexes has traditionally been dated by 'bracketing',



**Figure 4-2:** Cartoon illustrating fault gouge sample preparation and Illite Age Analysis process. 1. The clay-sized fraction of gouge is separated by settling in water. 2. The clay-sized fraction is centrifuged into three size fractions, spanning two orders of magnitude in grain size. 3. The relative abundance of 2M<sub>1</sub> and 1M<sub>d</sub> illite in each size fraction is determined using WILDFIRE©. 4. The percentage of detrital illite is plotted against the Ar-Ar age. The percentage detrital illite (2M<sub>1</sub>) is plotted against the function  $e^{\lambda t} - 1$ , where  $\lambda$  is the decay constant of potassium, and  $t$  is time; the percentage of detrital illite is actually linearly related to the exponential decay of potassium and not to chronological time.

dating events that preceded and followed the faulting (e.g. Miller and John, 1999, Wong and Gans, 2003), or by inferences from thermochronometer ages, (Miller et al., 1999, Carter et al., 2006). Frequently, the constraints placed on the termination of fault slip are not well defined when compared to the earlier evolution of these structures. The work presented herein provides a rigorous foundation to the Ar dating of gouge, and constrains the end of fault slip and extends the application of brittle fault dating to faults as young as mid-Miocene in age.

### **Fault dating and illite polytypism**

#### Fault dating

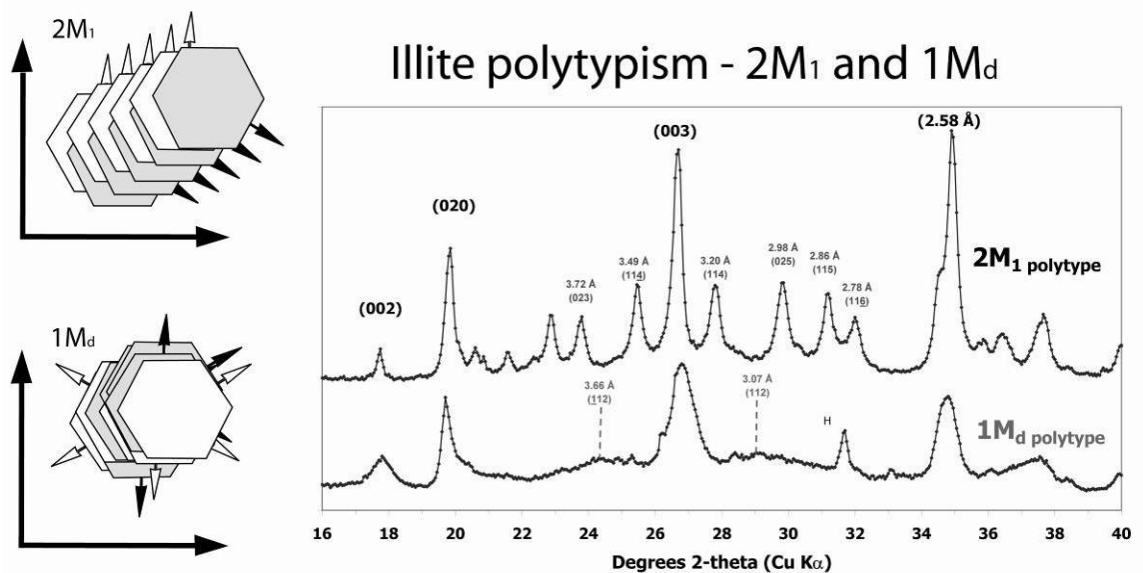
Previous work dating clay gouge has encountered two common obstacles. First, while the age of the authigenic component of clay gouge extrapolated from Illite Age Analysis could readily be related to the age of faulting, the extrapolated age of the detrital component is frequently difficult to interpret geologically, as it varies markedly from the depositional age of the hanging wall or footwall. In addition, all previous studies have focused on faults where the wall rock is sedimentary. It has long been known that illite in shale is a mixture of detrital mica, its weathering products and authigenic illite growing during diagenesis (Bailey, 1962). It also has long been recognized that the K-Ar age of a shale decreases systematically with grain size (Hower, 1963, Velde and Hower, 1963, Clauer et al., 1997) and that the abundance of the  $2M_1$  polytype relative to the  $1M/1M_d$  polytype also decreases systematically with grain size (Pevear, 1992, Grathoff et al., 1998). These paired observations led to the widely accepted interpretation that the  $2M_1$  component in a mixed illite population is detrital, while the  $1M/1M_d$  component is authigenic (Hower, 1963, Reynolds, 1963, Grathoff et al., 2001).



This distinction between illite polytypes is applied to fault dating by assuming that the  $2M_1$  component is detrital material derived from the wall rock, and the  $1M/1M_d$  component is authigenic material formed in the fault zone during fault slip. Given the potential complexity of the mica populations in shales, especially when both the hanging-wall and footwall are shales, the assumption that gouges are a binary mixture of detrital and authigenic illite may best be tested in an area where the age of the detrital component is well known, and the population of detrital minerals is functionally monotonic in age. A highly extended area, such as a metamorphic core complex is ideal for such an application in that the footwall rocks pass through the temperature ranges of detrital minerals for which Ar-Ar data can provide meaningful geological data (muscovite,  $375 \pm 25$  °C., and K-feldspar 100-500 °C. – McDougall and Harrison, 1999, Harrison et al., 2005) very rapidly, ensuring a nearly monotonic age population of detrital minerals.

### Illite Polytypism

Polytypism is a special case of polymorphism common to clay minerals and micas in that the two-dimensional arrangement of the silicate sheets remains unchanged, but the stacking sequence of the sheets varies. Traditionally, of the six possible mica polytypes (Smith and Yoder, 1956), five polytypes were identified in illite, the  $1M$ ,  $1M_d$ ,  $2M_1$ ,  $2M_2$ , and  $3T$  polytypes (Levenson, 1955, Shimoda 1970). The  $2M_1$  polytype stacking sequence is characterized by regular  $120^\circ$  rotations of the 2:1 layers with a two-layer repeat, e.g. each second layer is oriented the same way. This regular stacking produces a series of distinctive  $(11l)$  and  $(02l)$  reflections at 3.72, 3.49, 3.20, 2.98, 2.86, and 2.79 Å on an X-ray powder pattern (Moore & Reynolds, 1997), shown in Figure.4.3. The  $1M$  polytype, *sensu stricto*, has an ordered monoclinic symmetry, in which all sheets are oriented the same way, while the  $1M_d$  polytype stacking sequence is characterized by



**Figure 4-3:** Stacked XRD tracings for 2M<sub>1</sub> muscovite (Owl Creek pegmatite, Wind River Mts, WY, USA) and 1M<sub>d</sub> illite (IMt-1, Silver Hill, MT, USA). Note the 2M<sub>1</sub>-specific (111) and (021) peaks between 23 and 32° 2 $\theta$  produced by the 2M<sub>1</sub> ordered lattice layer stacking, and the 1M<sub>d</sub>-specific broad (112) and (112) peaks at 24.3 and 29.1 degrees 2 $\theta$ . (H) is halite. Polytype cartoons redrawn after Moore & Reynolds (1997).

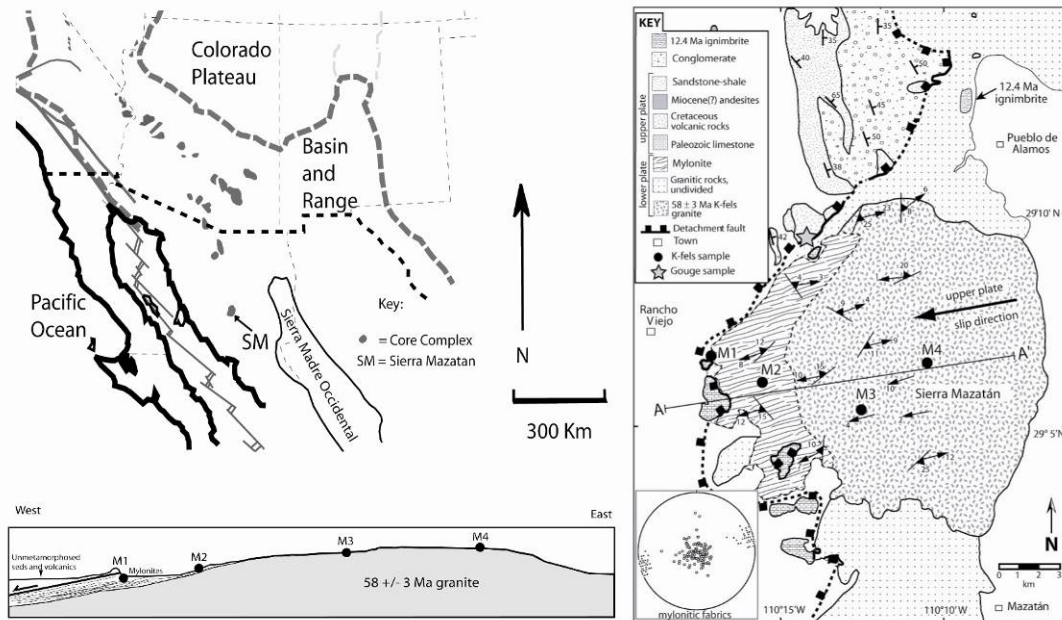
rotations of each silicate sheet in random multiples of  $120^\circ$ , or more rarely  $60^\circ$  relative to the sheet above and below. The 1M polytype is quite rare, and is generally only found in hydrothermal systems, where the 1M structure may be a function of anomalously high Mg contents (Peacor, et al., 2002). The  $1M_d$  polytype is identifiable by its lack of the  $2M_1$  peaks on XRD powder patterns, and instead has broad peaks on either side of the (003) peak at  $24.3^\circ$  and  $29.1^\circ$   $2\theta$  (Figure 4.3). The 1M and  $1M_d$  polytypes are not truly distinct polytypes, but rather end-members of a spectrum of ordering of rotation of the silicate sheets (Bailey, 1988), best thought of as a single 1M- $1M_d$  polytype. The degree of ordering of the silicate sheets is expressed in percentages of zero rotation; e.g. a sheet in a perfectly ordered 1M structure will have no rotations, so the percentage zero rotations = 1.0. A perfectly disordered  $1M_d$  structure will have a 1/3 chance of having a zero rotation, so the percentage of zero rotations = 0.33. For the sake of brevity and for consistency with previous work, hereafter, the subdivisions of the  $1M_d$ -1M series, the cv1m/ $1M_d$  and tv1M/ $1M_d$  polytypes of Drits et al., (1984) are collectively referred to as the 1M/ $1M_d$  polytype unless otherwise noted.

Illite polytypism is of geological interest because it has been linked to environmental conditions of clay formation. Experimental work indicates that the  $2M_1$  polytype is the most stable illite polytype and is thought to form above  $280^\circ\text{C}$  (Yoder and Eugster, 1955, Velde, 1965, Sroden and Ebrol, 1984), while the 1M/ $1M_d$  polytypes are thought to form at significantly lower temperatures, below approximately  $200^\circ\text{C}$  (Velde, 1965). The sequence  $1M_d$ -1M- $2M_1$  has been proposed to be indicative of increasing temperature and pressure, with the presence of authigenic  $2M_1$  indicating the onset of the lowest-temperature metamorphic zone (the anchizone –  $280$  to  $360^\circ\text{C}$ ) (Reynolds, 1963, Weaver and Brockstra, 1984). Apparently cogenetic  $1M_d$ , 1M and  $2M_1$  are known, however, from hydrothermal systems active at  $270$ - $330^\circ\text{C}$  (Lonker & Fitz Gerald, 1990).

While the upper limit on the conditions for growth of 1M/1M<sub>d</sub> is thus somewhat variable, the 1M/1M<sub>d</sub> polytypes are the only polytype observed in very low-grade sediments that lack a detrital illite or mica component, such as pore-filling 'hairy' illites in clean sandstones and illitized bentonites (Pevear, 1999). Work in sedimentary basins has found that the illite in sedimentary basins is nearly always a mixture of the 2M<sub>1</sub> and 1M/1M<sub>d</sub> polytypes (Grathoff, et al., 2001). The 2M<sub>1</sub> polytype is typically thought to be detrital material, while the 1M/1M<sub>d</sub> illite is formed during diagenesis, as the latter are the only polytypes observed to form at temperatures below 200°C (Grathoff, et al., 2001). This observation is of key importance in considering the observed presence of 1M/1M<sub>d</sub> illite in fault gouge. It is clear that the authigenic growth of 1M/1M<sub>d</sub> must be occurring well below 280 °C, which is in the brittle deformation realm.

### **Geologic setting**

To apply the clay quantification method to natural fault gouge and to test our ability to date faults as young as Miocene in age, we studied gouge from the Sierra Mazatán metamorphic core complex in Sonora, Mexico. Sierra Mazatán is the southernmost Cordilleran metamorphic core complex, one of a discontinuous band of highly extended domains from British Columbia to northwestern Mexico (Anderson, 1980, Nourse et al., 1994, Gans, 1997; Figure 4.4). The complex has a 'typical' metamorphic core complex geometry, with a topographically high shield-like lower plate of mid-crustal Paleocene (58 +/- 3 Ma U-Pb age, Anderson, 1980) granites and minor gneisses, separated from Cretaceous metavolcanics and unmetamorphosed Tertiary sedimentary strata by a shallowly west-dipping complex fault zone with a plastic-to-brittle deformation history (Vega Granillo & Calmus, 2003, Wong & Gans, 2003). The onset of exhumation at



**Figure 4-4:** Location map of northwest Mexico and surrounding areas showing location of study area and selected geographic and tectonic features. Boundaries of the Basin and Range (hachured line) and relatively un-extended Sierra Madre Occidental are modified from *Coney, (1980), Gans (1997) and Wong & Gans (2003)*. Solid lines are faults. Geologic map and section of Sierra Mazatán courtesy of Martin Wong.

Sierra Mazatán is well constrained by K-feldspar  $^{40}\text{Ar}/^{39}\text{Ar}$  ages, which indicate rapid west-directed exhumation, beginning at 20 Ma in the east, and at 18 Ma in the west. The end of exhumation is only constrained by a 12.4 Ma ignimbrite outcropping on the mylonitic carapace, indicating the mylonites were at the surface by that time (Vega Granillo & Calmus, 2003, Wong and Gans, 2003). The detachment fault is exposed on the northwest side of the core complex at the base of Cerro Pelon (UTM 0574600 E, 3226750 N, NAD 1927 Mexico UTM datum), about 10 km north along strike from the sample locations described in Wong and Gans (2003). The gouge zone is 0.5-2 m thick, and separates Cretaceous metavolcanics from weakly mylonitized and extensively fractured Paleocene granite. The gouge is a yellowish-brown hard clayey gouge with a crude visible fabric, and contains rounded and abraded clasts of granite and grains of quartz and feldspar in a matrix of very fine clay. Two K-feldspar Ar-Ar ages from footwall constrain the cooling history of the footwall in the vicinity of the detachment fault. The M1 sample of Wong & Gans (2003) is taken from the immediate vicinity of the fault, and records rapid cooling of the footwall of the detachment from 350°C at 18 Ma to 200°C at 16 Ma. The M2 locality, ~ 3km up-dip from the M1 locality, and ~500m below the detachment surface in true section, records rapid cooling from 350°C at 19.5 Ma to 200°C at 17.5 Ma. Both the published Ar-Ar ages, and paleomagnetic constraints on a set of post-mylonitization basaltic dikes (Wong, pers. com.) clearly indicate that the fault was initiated at a dip of ~60 degrees, and was then passively rotated in a domino fashion to its current dip of 10-20°. Dating the deformation related to the onset of exhumation of a core complex in the plastic regime has become relatively straightforward (e.g. McGrew and Snee, 1994, Vanderhaeghe et al., 2003, Wong & Gans, 2003), but determining when activity on a detachment ceases, critical in understanding the kinematics of core complex evolution, is much more difficult. Activity on brittle faults at core complexes has traditionally been dated by 'bracketing', dating

events that preceded and followed the faulting (e.g. Miller and John, 1999, Wong and Gans, 2003), or by inferences from thermochronometer ages, (Miller et al., 1999, Carter et al., 2006). Frequently, the constraints placed on the termination of fault slip are not well defined when compared to the earlier evolution of these structures. Key questions therefore remain, how long the core complex was active, both in the plastic and brittle regimes, and when various parts of a detachment were active.

## **Methods**

### Standard sample preparation

Because most commercial illite standards are taken from sedimentary basins, where illites are nearly always a mixture of polytypes (Grathoff, et al., 1998), we used muscovite as a proxy for 2M<sub>1</sub> illite. Muscovite has the same crystallographic structure as 2M<sub>1</sub> illite and is chemically very similar. Muscovite has only slightly less Si, Mg and H<sub>2</sub>O than illite and only slightly more tetrahedral Al and 1.0 interlayer K<sup>+</sup> per (Si,Al)<sub>4</sub>O<sub>10</sub>(OH)<sub>2</sub> formula unit, where illite has 0.89 K<sup>+</sup> per formula unit (Srodon, et al., 1992). Muscovite collected from the Owl Creek pegmatite, Wind River Range, WY was ground in a shatter box for 1 minute, and then suspended in water. The clay component of the ground muscovite (<2 μm spherical equivalent) was separated using Stokes' Law for the settling of particles in water. For the 1M<sub>d</sub> standard we used the IMt-1 standard from Silver Hill, MT, available from the Clay Minerals Society Source Clay Repository and characterized by Hower and Mowatt (1963). The IMt-1 illite was disaggregated in water, suspended and the clay fraction poured off in the same manner as the muscovite. The clay fraction was centrifuged to <1μm in size, and dried by evaporation. Prior to detailed quantification, both the IMt-1 and muscovite were analyzed for the presence of non-clay

phases and interlayered smectite using oriented smear preparations on a glass slide. Both standards were then X-rayed twice, once air-dried and again after solvation for 72 hours in ethylene glycol from  $2-35^{\circ} 2\Theta$  at 1 degree/minute using a Scintag X1  $\Theta-\Theta$  powder diffractometer, with an accelerating voltage of 40.0 kV, a filament current of 35.0 mA, and a Cu  $K\alpha$  source. XRD analysis indicates that both the Owl Creek muscovite and the  $< 1\mu\text{m}$  fraction of the IMt-1 standard are nearly monomineralic muscovite and illite, respectively. Some halite was noted in the IMt-1 material, probably derived from laboratory water used in centrifugation. Neither the peaks for the  $2M_1$  sample nor for the IMt-1 sample shifted upon glycol solvation, but the IMt-1 sample had some broadening of the (001) reflection and a sloping shoulder on the low-angle side of the peak upon solvation, indicating that some smectite interlayers were present. The percentage of interlayered smectite was checked using the  $\Delta 2\Theta$  method of Sroden (1980) and was found to be  $< 5\%$ . The  $2M_1$  muscovite and the 1Md illite were then mixed in 6 different weight-percentage mixtures, 0%  $2M_1$ , 14%  $2M_1$ , 23%  $2M_1$ , 50%  $2M_1$ , 77%  $2M_1$  and pure  $2M_1$  (Figure 4.5). Samples were side-loaded into an Al sample holder to achieve a high degree of particle randomness in the sample (Moore and Reynolds, 1997). Each mixture was then scanned from  $16-44^{\circ} 2\Theta$ . Because of the low intensity of the polytype-specific peaks and the resolution of XRD increases with longer counting time at each step, we used the step-scanning mode with a step size of  $0.05^{\circ}$  and a count time of 40 seconds per step. Several XRD analyses of the same mixture were performed to assure that the samples were thoroughly mixed.

#### Sierra Mazatán sample preparation

About 0.5 kg of clay gouge material from the Sierra Mazatán detachment fault was disaggregated by soaking in water and suspended repeatedly until the sample was free



of salts. The clay-sized material was separated using the same Stoke's law techniques as for the gouge sample. The accumulated clay fraction was centrifuged into a total of five different size fractions, (2  $\mu\text{m}$  – 1 $\mu\text{m}$ , 1  $\mu\text{m}$  – 0.5 $\mu\text{m}$ , 0.5  $\mu\text{m}$  – 0.1 $\mu\text{m}$ , 0.1  $\mu\text{m}$  - 0.05  $\mu\text{m}$  – and <0.05 $\mu\text{m}$ ) spanning roughly two orders of magnitude in grain size, to obtain multiple samples, each with a distinct ratio of relatively coarse-grained detrital and fine-grained authigenic illite. As the effects of chemical treatments to remove carbonate, quartz, or organic material on the retention of Ar by illite are not known (Moore and Reynolds, 1997), we did not treat our samples.

#### WILDFIRE modeling

Several methods have been used to quantify the amount of  $2M_1$  and  $1M/1M_d$  in illite mixtures using properties of the polytype-specific peaks. Early approaches were empirical, using standards mixed in various ratios and ratioing the area of one or two polytype-specific peaks to the area of the 2.58 Å peak at  $36^\circ 2\Theta$  (see summary in Dalla Torre et al., 1994). A significant improvement was proposed by Grathoff and Moore (1996) who used a combination of physical mixtures and WILDFIRE<sup>©</sup> calculated XRD patterns to ratio the area of five polytype-specific peaks to the area of the 2.58 Å peak. WILDFIRE<sup>©</sup> calculates three-dimensional X-ray diffraction patterns for randomly oriented grains and allows the user to experiment with many mineralogic variables to fully capture the variability of structure ordering in illites described earlier. WILDFIRE<sup>©</sup> also allows the user to vary the thickness of the diffracting crystallites, the randomness of the sample (also known as the Dollase factor), the percentage of interlayered smectite, its hydration state, and any ordering of the illite/smectite (Reichweite). This multitude of options potentially allows for better matching of real powder patterns than empirical ratios of peak areas derived from a single set of standards. More recently, workers have

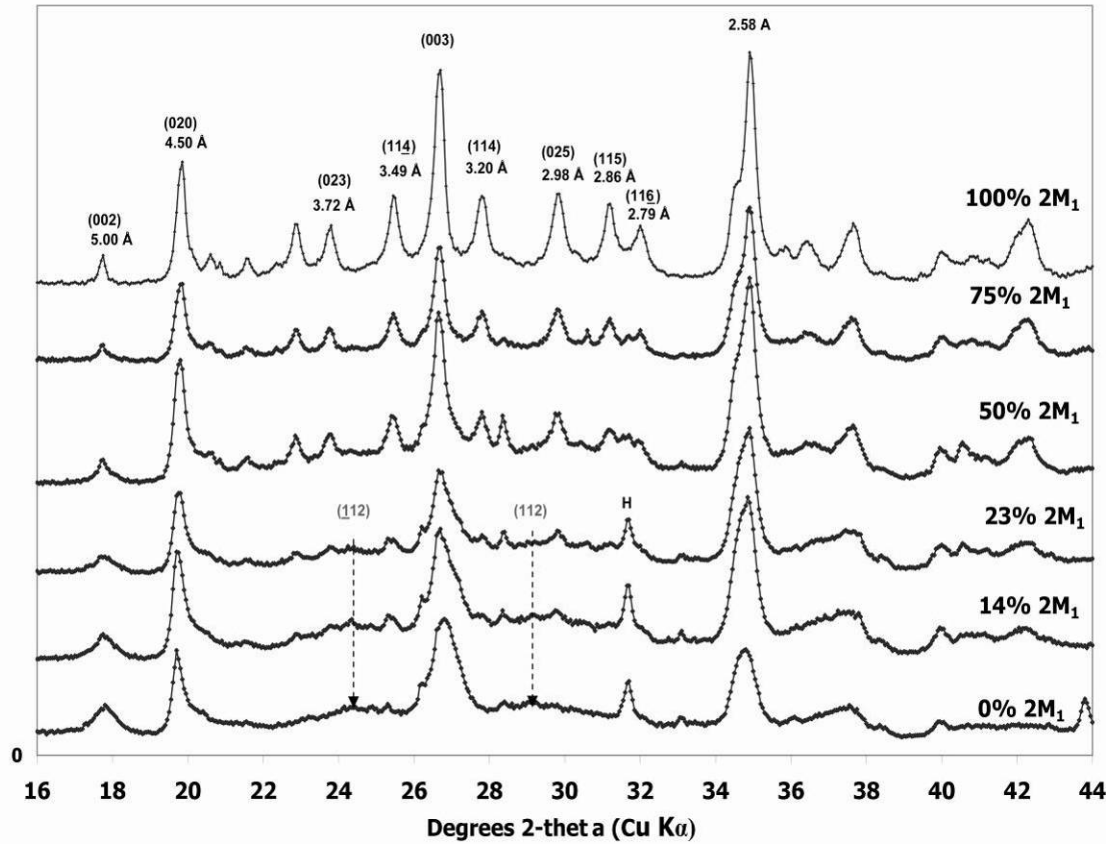
exclusively used mixtures of WILDFIRE<sup>®</sup>-generated patterns to quantify the proportions of polytypes in a sample (Ylagan, et al., 2002; Solum et al., 2005; Solum and van der Pluijm, 2007). This WILDFIRE<sup>®</sup>-based approach uses a least-squares lowest-variance approach to determine the best match between the sample and calculated patterns. Although the absolute number of counts recorded by an XRD unit for a given diffraction angle and sample are largely a function of machine settings and sample preparation, and are not in themselves geologically meaningful (the relative numbers of counts at different diffraction angles are however extremely meaningful), the absolute number of counts for a given diffraction angle calculated in WILDFIRE are usually much lower than the number of counts recorded by an XRD, so a scale factor must be used to multiply each WILDFIRE 'count' so that it is similar to those recorded by the XRD for the natural samples. Scale factors appropriate for our apparatus typically range from 5.0 to 30.0 and are used in increments of 0.1. At each step (0.05°) in the XRD scan of the sample pattern between 21 and 36° 2 $\theta$ , the region with the 2M<sub>1</sub> polytype-specific peaks, a variance is calculated between the sample and the scaled mixture of WILDFIRE patterns in a spreadsheet. The square of the variance at each step is calculated, the squares of the variances are then summed, giving a total 'variance' for the mixture of theoretical patterns. Our approach was first to apply the lowest variance approach to the mixtures, as a test of this approach, and then to modify it where appropriate. We observe that the absolute magnitude of the scale factor rarely affects which mixture of 2M<sub>1</sub> and 1M<sub>d</sub> patterns has the lowest variance with the natural sample. We do however, compare results with many scale factors and for the lowest-variance approach we use the scale factor which produces the lowest absolute variance. Until now, this approach of using WILDFIRE<sup>®</sup>-generated patterns has not been tested against standards to demonstrate its validity.

## Argon dating

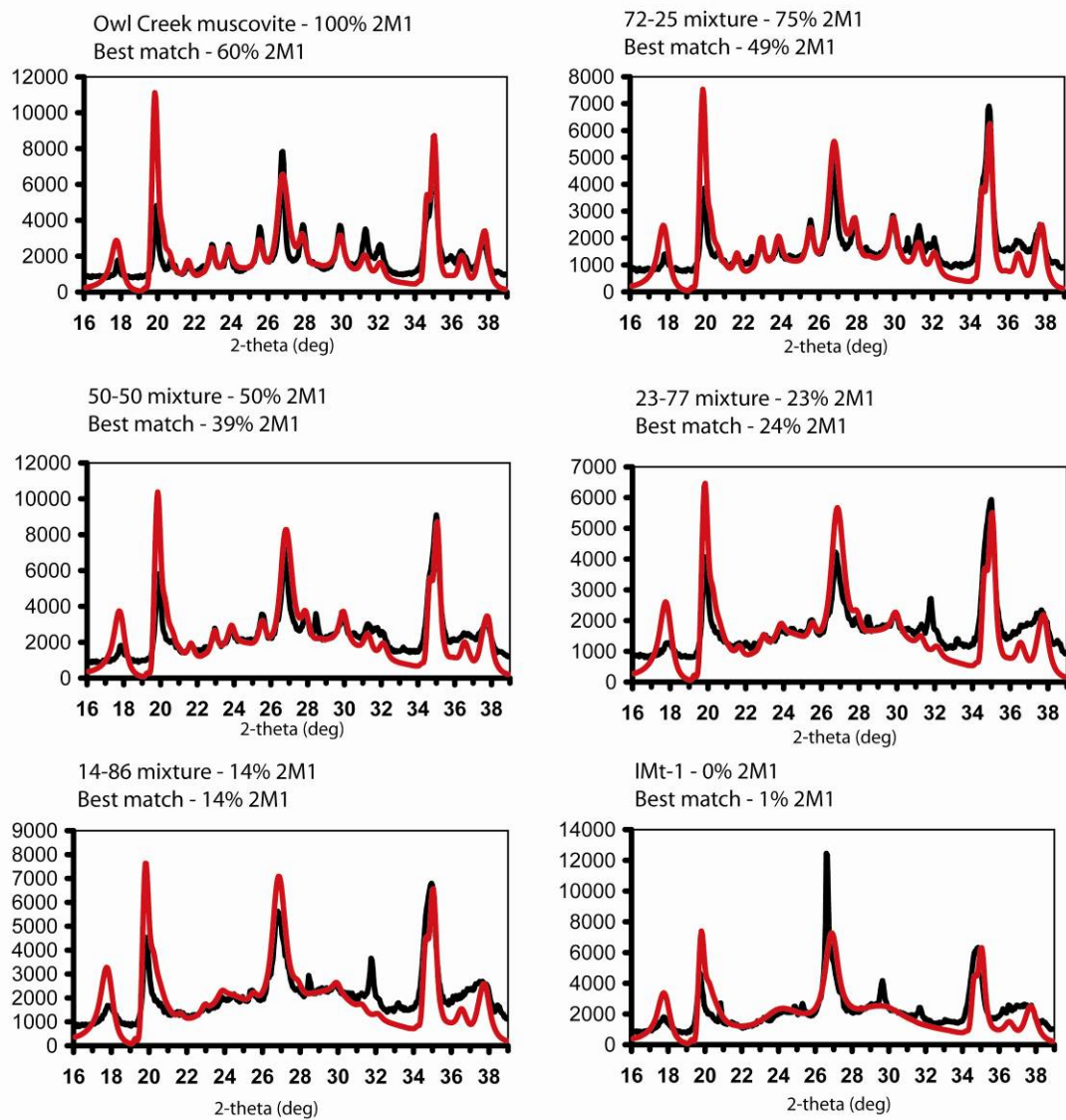
As the momentum transfer that occurs during the  $^{39}\text{K} (n,p) - ^{39}\text{Ar}$  reaction is sufficient to move the produced Ar atom  $\sim 0.1 \mu\text{m}$ , (a significant percentage of the effective diameter of most clay crystallites), large amounts of  $^{39}\text{Ar}$  might be lost during irradiation, producing erroneously old ages. To avoid this problem, the samples were packaged into fused silica vials and sealed prior to irradiation (van der Pluijm et al., 2001). Thus, the  $^{39}\text{Ar}$  expelled from the crystallites during irradiation is retained for analysis (see Dong et al., 1995 for a rigorous treatment of the issue). The sample vials were broken open; the initial gas was analyzed; the vials were then step-heated under a defocused laser until sample fusion occurred. The total gas age obtained from the vacuum-encapsulated sample is equivalent to that obtained from a conventional K-Ar age (Dong, 1995, 1997).

## Results and quantification.

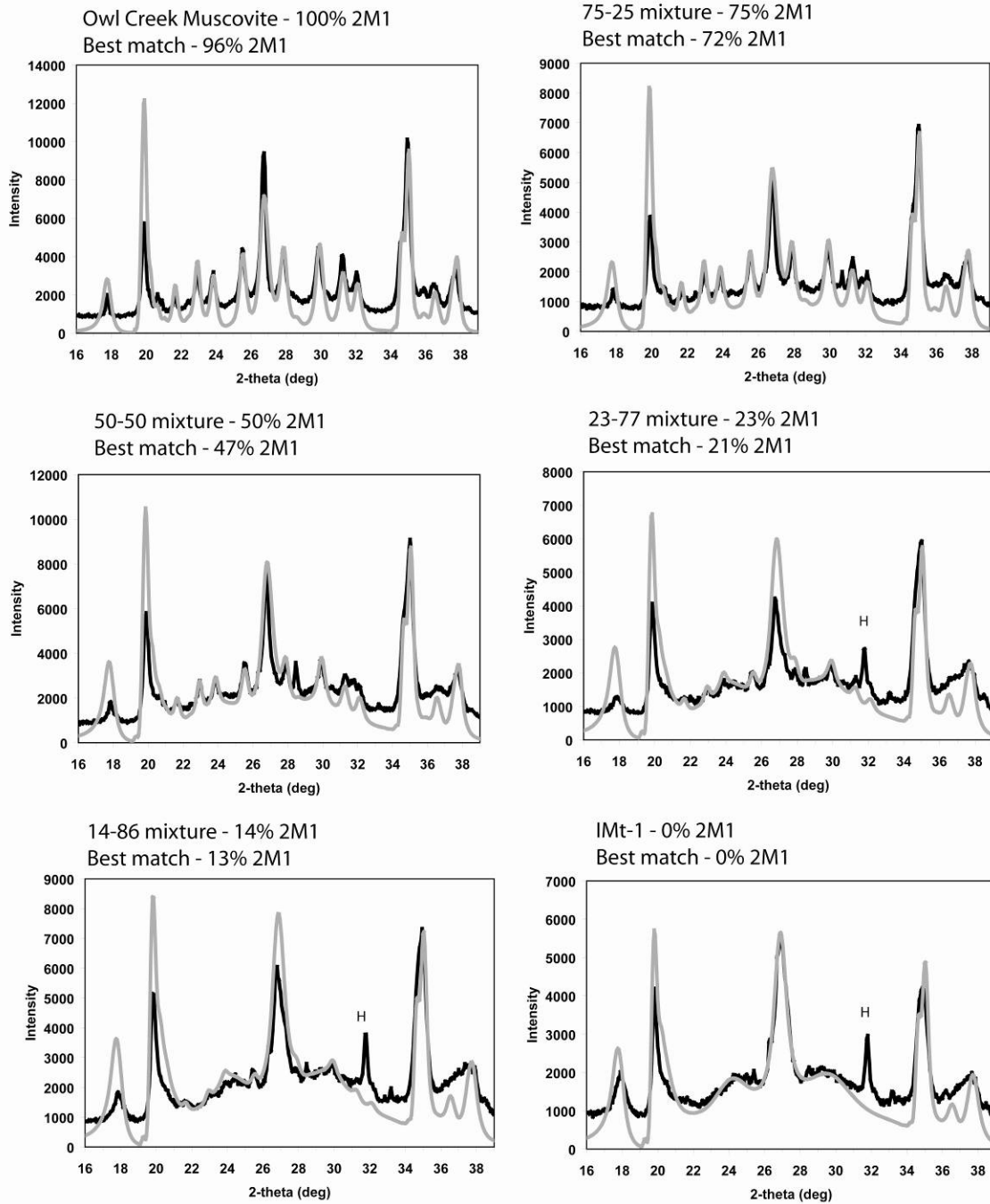
The XRD peaks of interest for polytype determination are non-(00 $l$ ) peaks and are only visible on powder patterns taken from samples with a near-random orientation of the crystallites. For all mixtures of standards, the (020) peak at 4.5 Å (19.8° 2 $\Theta$  Cu K $\alpha$ ) is significantly higher than the (002) peak at 5.0 Å (17.8° 2 $\Theta$ ), indicating that acceptable sample randomness was achieved (Grathoff and Moore, 1996). The intensity of the 2M $_1$ -specific peaks decreases consistently with decreasing 2M $_1$  content of the mixtures (Figure 4.5). We applied the lowest variance modeling approach to all 6 mixtures, and then applied our approach, which fits the entire profile from 21 to 36° 2 $\Theta$  when the 2M $_1$  peaks are weak or absent, but fits only the 2M $_1$  peaks when they are strong. Figure 4.6 shows the best matches using the lowest-variance method, while Figure 4.7 shows the best matches using our method. For the 1M $_0$ -rich mixtures the lowest variance approach



**Figure 4-5:** Stacked XRD tracings for six artificial mixtures of Owl Creek muscovite ( $2M_1$ ) and IMt-1 illite ( $1M_d$ ). Note the gradual decrease in intensity of the  $2M_1$ -specific peaks with decreasing abundance of  $2M_1$  in the mixture.



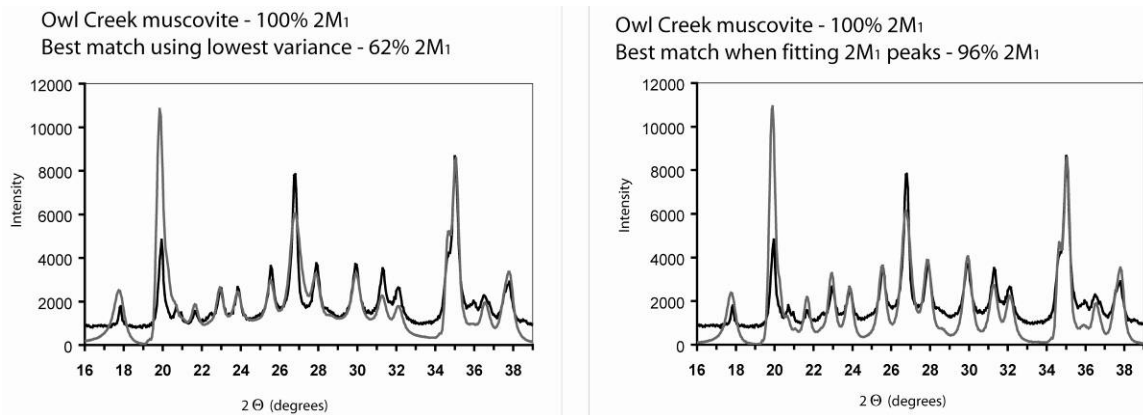
**Figure 4-6:** Best matches of WILDFIRE patterns using WILDFIRE and a lowest-variance approach. Note the excellent visual correspondence, but that the percentage of  $2M_1$  in  $2M_1$ -rich mixtures is severely underestimated.



**Figure 4-7:** XRD tracings for six artificial mixtures of Owl Creek muscovite (2M1) and IMt-1 illite (1Md) and best matches calculated using WILDFIRE and our approach. Note that especially for the 2M<sub>1</sub>-rich mixtures, the best match matches the 2M<sub>1</sub>-specific peaks, while for 1M<sub>d</sub>-rich mixtures, the best match matches the entire pattern between 21 and 36 degrees 2 $\theta$ . H is hematite.

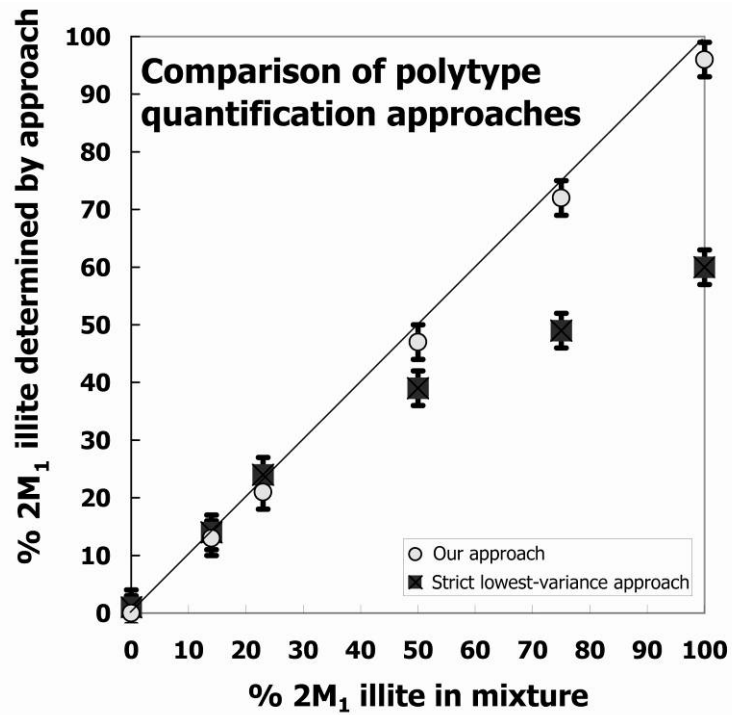
generates very good fits; the figures for the 23%  $2M_1$ , 14%  $2M_1$  and 0%  $2M_1$  mixtures needed only very minor iterative adjustment to produce visually satisfying matches. However, at high percentages of  $2M_1$ , (50%  $2M_1$ , 75%  $2M_1$  and 100%  $2M_1$ ), a lowest variance approach significantly underestimates the actual percentage of  $2M_1$  in the mixture. The reason for this is clear in Figure 4.8 which shows best matches calculated using the two different approaches. The effect of background broadening on the real XRD pattern is immediately apparent. WILDFIRE© patterns do not calculate a background level of scatter that replicates the peak broadening from amorphous phases, such as oxides and oxy-hydroxides, inevitably found in nature. The effect of the background produced by these phases is to generate anomalously  $1M_d$ -rich matches for  $2M_1$ -rich mixtures, shown in Figure 4.9. The transition from matching the entire sample pattern between  $21$  and  $36^\circ 2\theta$  and matching only the  $2M_1$ -specific peaks is gradational and occurs between a whole-profile best match of 30%  $2M_1$  and 50%  $2M_1$ . Of the many variables involved in matching calculated patterns to real mixtures using our approach, the relative amounts of the two end-members, the crystallite size of the calculated end-members and the Dollase factor are the most important. The results of our experiments show excellent correspondence between prepared and calculated mixtures, demonstrating the validity of our method.

Each size fraction of the sample from Sierra Mazatán was then X-rayed in the same manner as the standards and modeled using our approach; matches for the Sierra Mazatán size fractions are shown in Figure 4.10. The very coarse and coarse size fractions contain an assemblage of quartz + dolomite +  $2M_1$  illite +  $1M_d$  illite. The medium, fine and very fine fractions have an assemblage of  $2M_1$  illite or muscovite and  $1M_d$  illite in varying percentages. The relative abundance of quartz and dolomite both decrease systematically with grain size of the size fraction. Significantly, none of the size

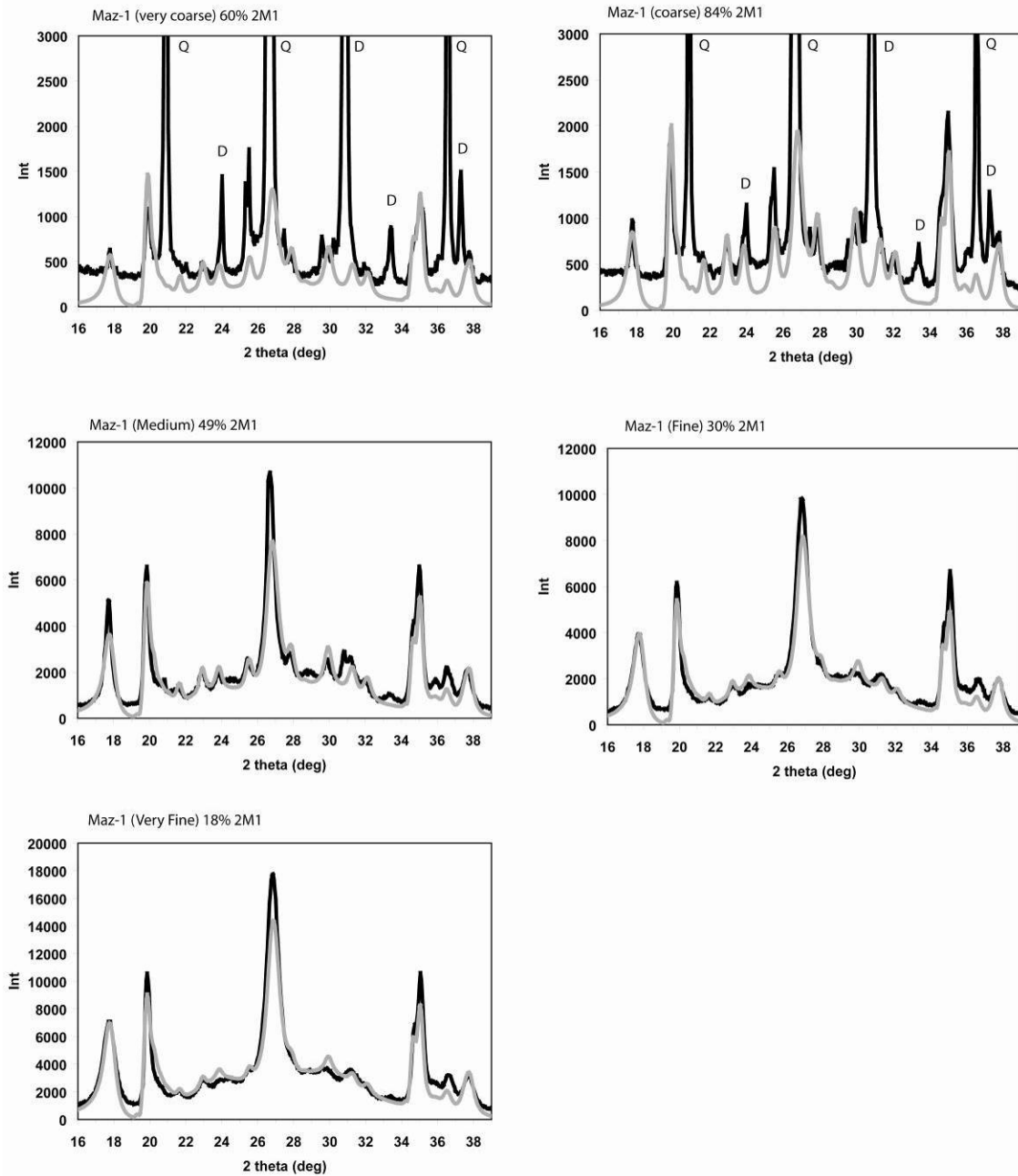


**Figure 4-8:** Best matches of WILDFIRE patterns to XRD tracings of Owl Creek muscovite (2M<sub>1</sub> - black) calculated using WILDFIRE (grey) using two different approaches. The figure on the left is calculated using a strict lowest-variance approach, while the right-hand figure is calculated using our approach. Note that the lowest-variance approach does not take into account the background broadening from the real XRD pattern between the 2M<sub>1</sub>-specific peaks.





**Figure 4-9:** Predicted vs. actual comparison of polytype quantification using a strict lowest-variance approach and our approach, which uses the entire pattern between 21 and 36 degrees  $2\theta$  for  $1M_0$ -rich mixtures, while for the  $2M_1$ -rich mixtures, our approach focuses on matching the  $2M_1$ -specific peaks. Our approach is similar to the lowest-variance approach in identifying small quantities of  $2M_1$  well, but is much better at identifying  $2M_1$ -rich mixtures than a strict lowest-variance approach. Error bars are  $\pm 3\%$ .



**Figure 4-10:** XRD patterns (black) and best matches (grey) for size fractions of gouge from Sierra Mazatan. The prominent peaks extending off the graph for the very coarse and coarse fractions are peaks from non-clay phases (Q = quartz, D = dolomite).

fractions contains any detectable feldspar; feldspar peaks can overlap the polytype-specific peaks used for modeling, and in addition, most feldspar contains  $K^+$ , greatly complicating any attempt to date feldspar-clay mixtures using Ar-Ar methods. The modeling of the sample powder patterns indicates the samples have widely varying ratios of  $1M_d$  and  $2M_1$ , with the percentage of  $2M_1$  decreasing with decreasing grain size. The very coarse and coarse fractions contained 60% and 84%  $2M_1$  respectively. The finest fraction contains only 18%  $2M_1$  and consists primarily of a disordered  $tv1M_d$  illite (percent zero rotations = 0.4, much closer to  $tv1M_d$  than  $tv1M$ ) with very few smectite interlayers (<10%).

The Ar-Ar data from the Sierra Mazatán samples are shown in Figure 4.11. The Ar-release spectra for each size fraction do not have plateaus due to the effects of Ar recoil (Dong, 1995), and because they are composed of mixtures of grains of different ages and grain sizes. All the spectra have an initial near-zero-age component, interpreted to be  $^{39}\text{Ar}$  released during irradiation due to recoil. The percentage of Ar released during the initial 'recoil' fraction increases with progressively finer size fractions, consistent with finer-grained clays having a higher surface-to-volume area and thus potential for  $^{39}\text{Ar}$  loss during irradiation. 'Spikes' in the spectra are heating steps in which relatively little argon was released and thus have large analytical uncertainties. The very coarse size fraction released comparatively little argon and thus has large analytical errors relative to the other size fractions. XRD analysis indicated that the very coarse size fraction was composed primarily of quartz and dolomite, with relatively little illite. The coarse size fraction spectrum contains a 19.9 +/- 0.3 Ma plateau-like component interpreted to be the cooling age of the  $2M_1$  material in that sample vial, and is similar to the 18-20 Ma cooling ages interpolated from the same temperature ranges of the K-feldspar data of Wong & Gans (2003), taken from the vicinity of the detachment. As our polytype

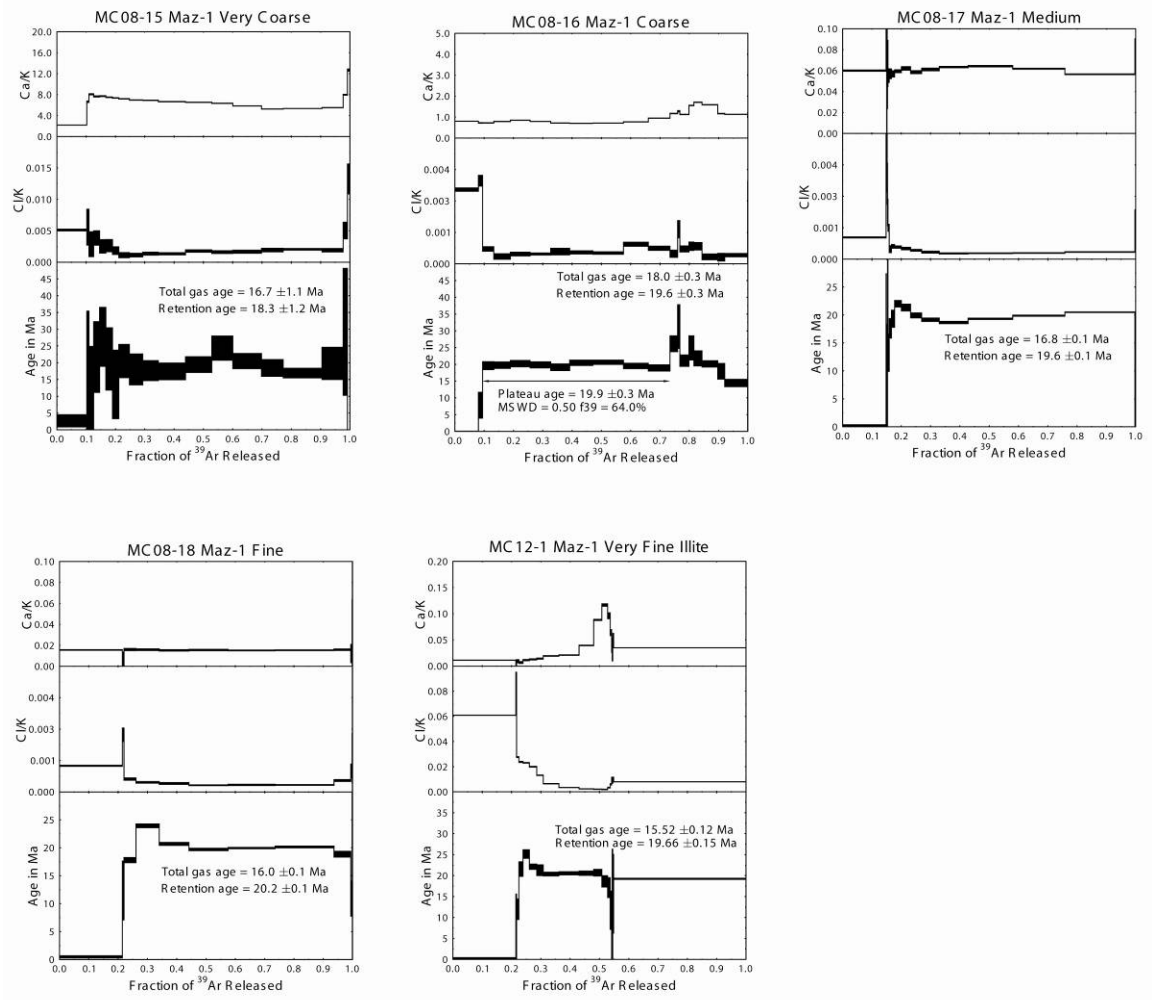
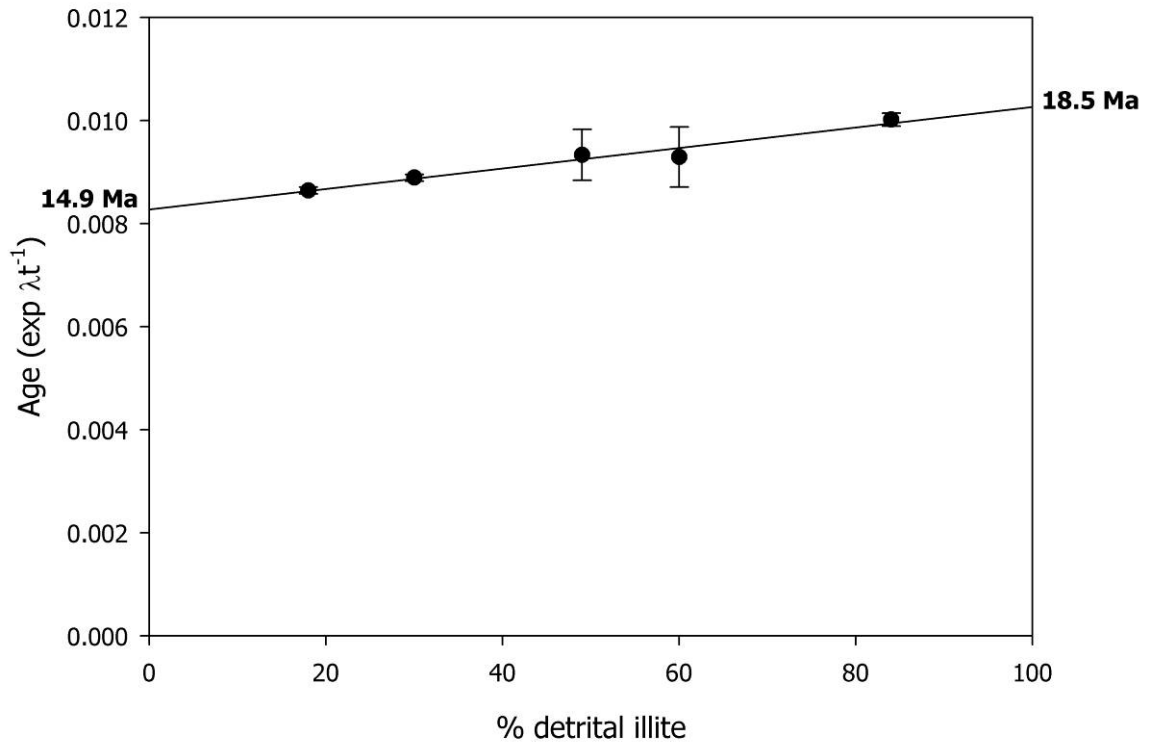


Figure 4-11: Ar-Ar spectra for the five size fractions of gouge from Sierra Mazatán.

modeling indicates a change in the predominant illite polytype from  $2M_1$  in the coarser size fractions to  $1M_d$  in the finer fractions, and the Ar-Ar ages decrease as the percentage of  $2M_1$  increases, it is apparent that the size fractions contain varying components of a two illite populations, an older  $2M_1$  polytype (probably detrital muscovite from the footwall granite) and a younger  $1M_d$  formed during brittle faulting. Such transitions have been noted in brittle faults elsewhere (van der Pluijm et al., 2001, Ylagan, 2002, Solum et al., 2005; Solum & van der Pluijm, 2007) and have been dated by illite age analysis, which correlates the percentage of the  $2M_1$  polytype and apparent argon age of each size and extrapolates the ages of the  $1M_d$  and  $2M_1$  (authigenic and detrital components). The illite age analysis plot plots the percentage detrital component against the function  $e^{\lambda t} - 1$ , where  $\lambda$  is the decay constant of argon and  $t$  is apparent age, as it is the decay constant of argon that is linearly proportional to the percentage detrital mica. The illite age analysis plot for the gouge sample from Sierra Mazatán is shown in Figure 4.12, and indicates a 14.9 Ma for the age of the authigenic component, and an 18.9 Ma age for the detrital component.

### **Interpretation and discussion**

The 14.9 Ma age of the  $1M_d$  component of the gouge is the age of authigenic illite growing in the fault gouge. As the gouge sample was crudely foliated and but was not itself brecciated, it can be inferred that the illitic gouge formed under conditions of significant differential stress, and thus during the period the fault was active. The preservation of this syn-tectonic fabric also indicates that any post-illite-growth slip was extremely minor. Thus it is clear that the age of the authigenic illite is also the age of the last major slip episode on the fault, and that the currently outcropping portion of the fault

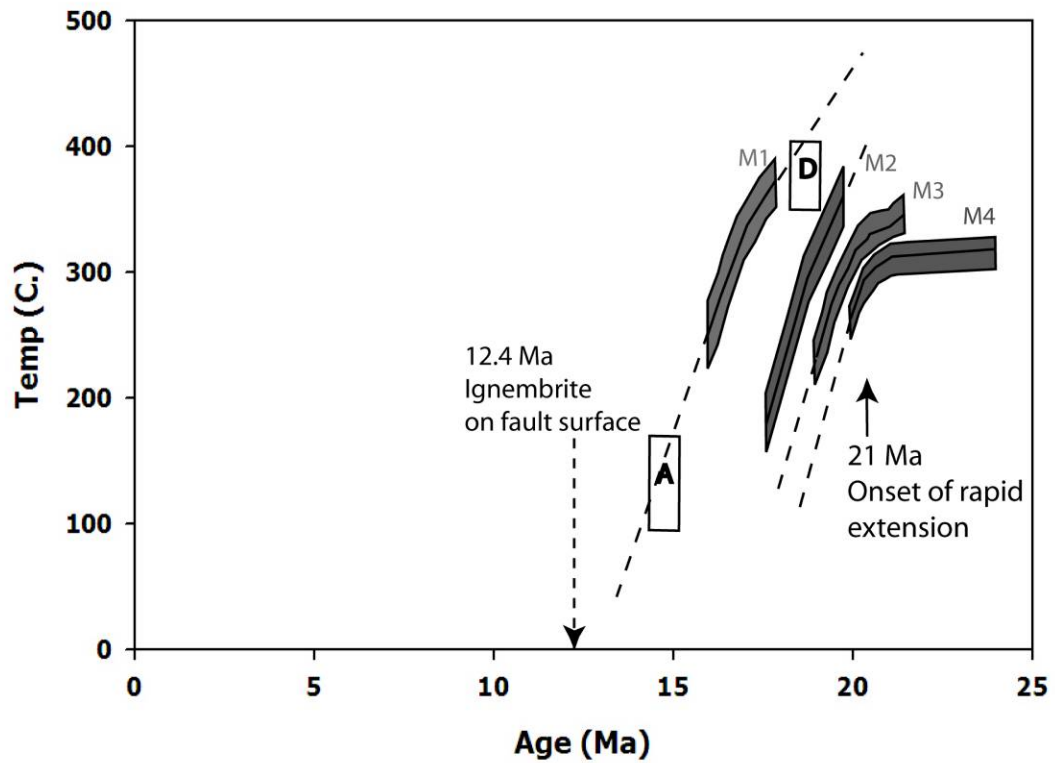


**Figure 4-12:** Illite age analysis plot for gouge from Sierra Mazatán detachment fault. Numbers in **bold** are the extrapolated ages for the authigenic (14.9 Ma) and detrital illite populations (18.5 Ma) mixed in the gouge. Percentage detrital illite ( $2M_1$ ) is plotted against function  $e^{\lambda t}-1$ , where  $\lambda$  is the decay constant of potassium, and  $t$  is time; the percentage of detrital illite is linearly related to the decay constant of potassium and not to chronological time.

surface was last active at temperatures between 50 and 150°C, the growth conditions for 1M<sub>d</sub> illite (Grathoff et al., 2001). Whether the authigenic illite formed during individual slip events, gradually during aseismic creep, or between individual seismic events due to fluid flow along the fault, remains unclear.

The 14.9 Ma gouge age (Figure 4.12) fits very well with known field constraints on faulting and demonstrates the reliability of the technique. The gouge age is clearly younger than the constraints imposed by the feldspar age and older than the field constraint on the fault surface imposed by the 12.4 Ma ignimbrite (Wong and Gans, 2003). The cooling history of Wong and Gans (2003) from the M1 locality in the immediate vicinity of the footwall records cooling from 350 °C at 18 Ma to 200 °C at 16 Ma. The 18.5 Ma age of the 2M<sub>1</sub> component of the gouge extrapolated from the illite age analysis agrees well with the constraints from the M1 feldspar age. The history for the M1 locality records rapid cooling of the immediate footwall of the detachment from 350°C at 18 Ma, a temperature very close to the 375 +/- 25 °C Ar blocking temperature of muscovite (Figure 4.13).

The age of the authigenic illite also has implications for the rate of fault slip. While Wong and Gans (2003) proposed that rapid slip ceased shortly after 16 Ma, our gouge age indicates slip on the detachment into the purely brittle regime to ~14.9 Ma. The 1M<sub>d</sub> age indicates cessation of the fault at conditions of 50-150°C. Wong and Gans (2003) determined slip rates in the plastic regime of 3.3 – 7.7 mm/year, broadly consistent with those known from other core complexes (Brady, et al. 2002, Carter et al., 2006). Assuming a geothermal gradient of 25°C/km, an initial fault dip of 60° and growth conditions for 1M<sub>d</sub> illite to be ~100 °C., the fault accommodated 4 km of slip between 16 Ma and 14.9 Ma, implying a net slip rate of 4.2 +/- 2.1 mm/yr and a strain rate on the



**Figure 4-13:** Summary plot of age data from the Sierra Mazatán detachment. K-feldspar cooling data are from Wong & Gans, (2003), “A” is age of authigenic component extrapolated from Illite Age Analysis of gouge (14.9 Ma), “D” is age of detrital component (18.5 Ma).



order of  $10^{-14} \text{ s}^{-1}$ . It appears that the Sierra Mazatán detachment continued slipping well into the brittle regime at rates similar to those for the plastic regime. Another consequence of the 18.5 Ma age of the detrital component is that the hanging wall of the detachment contributed little or no detrital material to the gouge. The hanging-wall of the Sierra Mazatán detachment in the vicinity of the gouge outcrop is Cretaceous in age (Vega Granillo and Calmus, 2003, Wong and Gans, 2003). Should any appreciable amount of hanging-wall material have contributed to the gouge, the age of the detrital component would have been significantly older than the 18.5 Ma age of the detrital component determined by illite age analysis. This observation of only one wall of a fault zone contributing the vast majority of detrital material in gouge is at variance with the widely described fault structure of a high-strain fault core surrounded by a symmetrical lower-strain damage zone (cf. Chester and Logan, 1997), but is consistent with macroscopic observations in other metamorphic core complexes (Hayman, 2006).

## **Conclusions**

Illite polytype quantification using calculated WILDFIRE© patterns accurately quantifies artificial mixtures of  $2M_1$  and  $1M_d$  illite and supports the application to natural mixtures in real fault gouge. Polytype quantification is significantly improved when the effects of background broadening are considered, particularly with  $2M_1$ -rich mixtures.

Both the ages of the detrital and authigenic components at Sierra Mazatán extrapolated from illite age analysis of gouge fit remarkably well with regional constraints. The assumption in illite age analysis that gouge is a mixture of two populations of illites, one detrital, derived from the wall rock, and one authigenic forming in the brittle fault zone is

therefore supported, as well. The 18.5 Ma age extrapolated for the detrital component ( $2M_1$  illite or muscovite) matches well with the time at which the footwall of the detachment passed through the closure temperature of muscovite. The 14.9 Ma age for the age of the latest period of faulting and fluid flow at the Sierra Mazatán metamorphic core complex directly constrains the end of activity on the detachment of this metamorphic core complex. The gouge age indicates that high slip rates from 2.1 mm/yr to 6.9 mm/yr inferred from the plastic regime continued into the brittle regime.

### **Acknowledgments**

This study was funded by NSF grants EAR-0230055 and EAR-0345985, and the Turner Fund of the Department of Geological Sciences at the University of Michigan. In particular, we wish to thank Martin Wong for his help in providing sample material and advice on the geology of Sierra Mazatán. We also thank Chris Hall and Marcus Johnson for assistance with Ar dating, and Carl Henderson for maintenance of the EMAL-XRD facility. Thoughtful reviews by Sarah Sherlock and Laurence Warr helped us to clarify the presentation and arguments of the paper.

## References

- Anderson, T., Silver, L., & Salas, G., (1980). Distribution and U-Pb isotopic ages of some lineated plutons, northwest Mexico. *Geological Society of America Memoir* 153, 269-283.
- Bailey, S., Hurley, P., Fairbairn, H., & Pinson, W., (1962). K-Ar dating of sedimentary illite polytypes: *Geological Society of America Bulletin* 73, p. 1167–1170.
- Bailey, S., (1988). X-ray diffraction identification of the polytypes of mica, serpentine, and chlorite. *Clays and Clay Minerals* 36, 193-213.
- Carter, T., Kohn, B., Foster, D., Gleadow, A., Woodhead, J., (2006). Late stage evolution of the Chemehuevi and Sacramento detachment faults from apatite (U/Th)/He thermochronometry – Evidence for mid-Miocene accelerated slip. *Geological Society of America Bulletin* 118, 689-709.
- Chester, F., Logan, J., (1987). Composite planar fabric of gouge from the Punchbowl Fault, California. *J. Structural Geology* 9, 621-634.
- Dalla Torre, M., Stern, W., Frey, M., (1994). Determination of white mica polytype ratios: Comparison of different XRD methods. *Clay Minerals* 29, 717-726.
- Dong, H., Hall, C., Peacor, D., Halliday, A., (1995). Mechanism of argon retention in clays revealed by laser  $^{40}\text{Ar}$ - $^{39}\text{Ar}$  dating. *Science* 267, pp. 355-359.
- Dong, H., Hall, C., Halliday, A., Peacor, D., (1997).  $^{40}\text{Ar}$ - $^{39}\text{Ar}$  dating of late-Caledonide (Acadian) metamorphism and cooling of K-bentonites and slates from the Welsh Basin, UK. *Earth and Planetary Sciences* 150, pp. 337-351.
- Drits, V.A., Plançon A., Sakharov, B.A., Besson, G., Tsipursky, S.I., & Tchoubar, C., (1984). Diffraction effects calculated for structural models of K-saturated montmorillonite containing different types of defects. *Clay Minerals* 19, 541-562.
- Gans, P., (1997). Large-magnitude Oligo-Miocene extension in southern Sonora: Implications for the tectonic evolution of northwest Mexico. *Tectonics* 16, 388-403.
- Grathoff, G., Moore, D., (1996). Illite polytype quantification using WILDFIRE—calculated patterns. *Clays and Clay Minerals* 44, 835–842.
- Grathoff, G., Moore, D., Hay, R., & Wemmer, K., (1998). Illite polytype quantification in Paleozoic shales: A technique to quantify diagenetic and detrital illite *in* Schieber, J., et al., eds., Shale and mudstones II. Petrography, petrophysics, geochemistry, and economic geology: Stuttgart, Germany, Schweizerbart'sche Verlagsbuchhandlung, p. 161–175.

- Grathoff, G., Moore, D., Hay, R., Wemmer, K., (2001). Origin of illite in the lower Paleozoic of the Illinois Basin: Evidence for brine migration. *Geological Society of America Bulletin* 113, 1092-1104.
- Harrison, M., Grovem M., Lovera, O., Zeitler, P. (2005). Continuous thermal histories from inversion of closure profiles. *Reviews in Mineralogy and Geochemistry* 58, pp. 389-409.
- Hayman, N., (2006). Shallow crustal fault rocks from the Black Mountain detachments, Death Valley, CA. *J. Structural Geology* 28, 1767-1784.
- Hower, J., Hurley, P. M., Pinson, W. H. and Fairbairn, H. W. (1963). The dependence of K-Ar age on the mineralogy of various particle size ranges in a shale. *Geochimica et Cosmochimica Acta* 27, 405-410.
- Kralik, M., Klima, K., Riedmueller, G., (1987). Dating fault gouges. *Nature* 327, 315-317.
- Levenson, A.A., (1955). Studies in the mica group: Polymorphism among illites and hydrous micas. *American Mineralogist* 40, 41-49.
- Lonker, S., Fitz Gerald, J., (1990). Formation of coexisting 1M and 2M polytypes in illite from an active hydrothermal system. *American Mineralogist* 75, 1282-1290.
- Lyons, J., Snellenburg, J., (1970). Dating faults. *Geological Society of America Bulletin* 82, 1749-1752.
- McDougall, I. & Harrison, M. (1999). Geochronology and thermochronology by the  $^{40}\text{Ar}/^{39}\text{Ar}$  method. 2ed edition. Oxford Monographs on Geology and Geophysics no. 9. New York: Oxford University Press, 212 pp.
- McGrew, A., Snee, L. (1994).  $^{40}\text{Ar}/^{39}\text{Ar}$  thermochronologic constraints on the tectonothermal evolution of the northern East Humboldt Range metamorphic core complex, Nevada. *Tectonophysics* 238, 425-450.
- Miller, E. Dumitru, T., Brown, R., Gans, P., (1999). Rapid Miocene slip on the Snake Range-Deep Creek fault system, east-central Nevada. *Geological Society of America Bulletin* 111, 886-905.
- Miller, J., John, B., (1999). Sedimentation patterns support seismogenic low-angle normal faulting, southeastern California and western Arizona. *Geological Society of America Bulletin* 111, 1350-1370.
- Moore, D. M., Reynolds, R. C., Jr. (1997). X-ray Diffraction and the Identification and Analysis of Clay Minerals. Oxford University Press, New York.
- Nourse, J., Anderson, T., Silver, L., (1994). Tertiary metamorphic core complexes in Sonora, northwest Mexico. *Tectonics* 13, 1161-1182.
- Peacor, D.R., Bauluz, B., Dong, H., Tillick, D., Yan, Y., (2002). TEM and AEM evidence for high Mg contents of 1M illite. Absence of 1M polytypism in normal prograde diagenetic sequences. *Clays & Clay Minerals* 50, 757-765.

- Pevear, D.R., (1992), Illite age analysis, a new tool for basin thermal history analysis, *in* Kharaka, Y.K., and Maest, A.S., eds., *Proceedings of the 7th International Symposium on Water-Rock Interaction: Rotterdam, Netherlands, Balkema*, p.1251–1254.
- Pevear, D.R., (1999). Illite and hydrocarbon exploration. *Proceedings of the National Academy of Sciences* 96, 3440–3446.
- Reynolds, R. (1963). Potassium-rubidium ratios and polymorphism in illites and microclines from the clay size fractions of proterozoic carbonate rocks. *Geochimica et Cosmochimica Acta* 27, 1097-1112.
- Reynolds, R. C., Jr. (1993a). Three-dimensional powder X-ray diffraction from disordered illite: simulation and interpretation of the diffraction patterns. *In: Computer Applications to X-Ray Powder Diffraction Analysis of Clay Minerals*, Reynolds, R., & Walker, J, eds., CMS Workshop Lectures Vol 5. The Clay Minerals Society, Aurora, Colorado, 43-78.
- R. Reynolds, R. C., Jr. (1993b). WILDFIRE - A computer program for the calculation of three-dimensional powder X-ray diffraction patterns for mica polytypes and their disordered variations, Hanover, New Hampshire.
- Reynolds Jr., R., Reynolds III., R.C., (1996). NEWMOD-for-Windows. The Calculation of One-Dimensional X-ray Diffraction Patterns of Mixed-layered Clay Minerals, Hanover, New Hampshire 1996.
- Shimoda, S., (1970). A hydromuscovite from the Shakani mine, Akita Prefecture, Japan. *Clays and Clay Minerals* 18, 267-274.
- Smith, J. Yoder, H., (1956). Experimental and theoretical studies of the mica polymorphs. *Mineralogical Magazine* 31, 209-231.
- Solum J., van der Pluijm, B., Peacor, D., (2005). Neocrystalization, fabrics and age of clay minerals from an exposure of the Moab fault zone, Utah. *J. Structural Geology* 27, 1563-1576.
- Solum, J., van der Pluijm, B. (2007). Reconstructing the Snake River/Hoback Canyon segment of the Wyoming thrust Belt through direct dating of fault rocks. In *Whence the Mountains? Inquiries into the Evolution of Orogenic Systems: A volume in Honor of Ray Price. Geological Society of America Memoir* 433
- Sroden, J. (1980). Precise identification of illite/smectite interstratifications by X ray powder diffraction. *Clays and Clay Minerals* 28, 401-11
- Srodon, J., Eberl, D., (1984). Illite, *in* Micas, Mineralogical Society of America *Reviews in Mineralogy* 13, Bailey, S. ed.
- Vanderhaeghe, O., Teyssier, C., McDougall, Dunlap, , W. (2003). Cooling and exhumation of the Shuswap Metamorphic Core Complex constrained by  $^{40}\text{Ar}/^{39}\text{Ar}$  thermochronology. *Geological Society of America Bulletin* 115, 200-216.

- Vega Granillo R. & Calums, T., (2003). Mazatan metamorphic core complex (Sonora, Mexico): structures along the detachment fault and its exhumation evolution. *Journal of South. American Earth Sciences* 16, 193-204.
- Velde, B. and Hower, J. (1963). Petrological significance of illite polymorphism in Paleozoic sedimentary rocks. *American Mineralogist* 48, 1239-1254.
- Velde, B., (1965). Experimental determination of muscovite polymorph stabilities. *American Mineralogist* 50, 436-449.
- Vrolijk, P., van der Pluijm, B., (1999). Clay gouge. *J. Structural Geology* 21, 1039-1048.
- Weaver, C., Brockstra, B., (1984). Illite-mica: *in* Weaver, C. et al., eds. Shale Slate metamorphism in the Southern Appalachian Mountains, Elsevier, Amsterdam, 67-199.
- Wong, M., Gans, P., (2003). Tectonic implications of early Miocene extensional unroofing of the Sierra Mazatán metamorphic core complex, Sonora, Mexico. *Geology* 31, 953-956
- Wong, M., Gans, P., (2005). Constraining the slip history and initial dip of low-angle normal faults using  $^{40}\text{Ar}/^{39}\text{Ar}$  K-feldspar thermochronology: a case study from the Sierra Mazatán core complex, Sonora, Mexico *Abstracts, Goldschmidt conference* A293.
- Yan, Y., van der Pluijm, B., Peacor, D. (2001). Deformational microfabrics of clay gouge, Lewis Thrust, Canada: a case for fault weakening from clay transformation. *Geological Society Special Publication* 186, pp. 103-112.
- Ylagan, R. Kim, C., Pevear, D., Vrolijk, P., (2002). Illite polytype quantification for accurate K-Ar determination. *American Mineralogist* 87, 1536-1545.
- Yoder, H., Eugster, H., (1955). Synthetic and natural muscovites. *Geochemica et Cosmochemica Acta* 8, 225-280.

## CHAPTER 5: FAULT AND PROVENANCE AGES IN THE PYRENEES – CONSTRAINTS FROM FAULT GOUGE DATING.

### **Abstract**

Dating brittle faults by the growth of authigenic illite in fault gouge allows for direct testing of kinematic models of orogenic evolution. We present fault gouge ages from 9 faults in the south-central and south-eastern Pyrenees. Four thrusting events occurred during the Pyrenean orogeny: 1.) Late Cretaceous thrusting (Boixols) 2.) Latest Paleocene-Early Eocene (Nogueres Zone & Freser antiformal stack). 3.) Middle-Late Eocene (Ripoll syncline, Vallfogona thrust, Gavarnie thrust, Abocador thrust and L'Escala thrust) and 4.) Middle Oligocene thrusting in the central portion of the Axial Zone (Llavorsi-Senet thrust). The Paleocene-Early Eocene and Middle-Late Eocene events may or may not be one single event, due to slightly overlapping error estimates for fault gouge ages. Our ages indicate a pulse of thrusting during the Middle and Late Eocene at multiple positions in the orogenic wedge, demonstrating that the range was simultaneously active along most of its length. In the central region the faults record overlapping ages, so the orogen was behaving as a critical wedge, while elsewhere foreland progression of ages is preserved. We also find late slip on thrusts in the central regions of the range, which was predicted from kinematic reconstructions to explain the distinctive antiformal stack geometry of the central part of the range, but not previously demonstrated from syntectonic sedimentation. The Late Paleozoic ages of the detrital component of many

of the foreland basin thrusts indicate that Hercynian-age micas were deposited in the Southern Pyrenean foreland basin as early as the Cretaceous.

## **Introduction**

The Pyrenees have been a testing ground for theories concerning the origin of mountain ranges since the beginning of the 19<sup>th</sup> century. At various points in time, theories such as Neptunism (Ramond, 1801), uplift due to volcanism, (Leymerie, 1849) and gravity sliding (de Sitter, 1954, Deramond, 1979) as well as modern ideas about Iberian-European collision (Choukroune et al., 1973, Muñoz, 1992, Beaumont et al., 2000) have all been invoked to explain the distinctive structural geometries preserved in this well-exposed, partially exhumed mountain belt. The belt is asymmetrical with a central basement core flanked by south and north-verging foreland fold-and-thrust belts, with the south-verging thrust belt wider and more complex than the northern segment (Muñoz, 1992, Vergès, 2002) (Figure 5.1). The foreland fold-and-thrust belt, especially along its outboard southern margin, has exceptional preservation of syn-orogenic strata, which has permitted timing of structural events in the foreland (e.g. Puigdefàbrigas et al., 1986, Burbank et al., 1992a, Sussman et al., 2004) and permitted the estimation of rates of shortening processes (Burbank et al., 1992b, Vergés et al., 1995, 1998, Meigs et al., 1996). Brittle thrusting involving basement units is also preserved in the inner portion of the range (Muñoz et al., 1986, Saura & Teixell, 2006).

The tendency of thrusts to young in age towards the foreland has long been recognized (e.g., Armstrong & Oriol, 1965) and has been interpreted in terms of a forward-propagating, critically tapered orogenic wedge (e.g. Dahlen et al., 1984, DeCelles &



Mitra, 1995, Meigs, 1996). Thrusting can also occur on faults inboard of the thrust front, called “out-of-sequence thrusting” (e.g. Morley, 1988). Out-of-sequence thrusting on new thrusts forming at deeper orogenic levels on inboard thrusts in the central core has been invoked to explain the distinctive antiformal stack structural geometry of the central and eastern Pyrenees (Parish, 1984, Muñoz et al., 1986, Muñoz 1992), (see section in Figure 5.1). While the outboard thrusts in the Pyrenees have an extensive syn-tectonic sedimentary record that permits indirect timing of fault slip (e.g. Burbank et al., 1992a, Burbank et al., 1992b, Meigs et al., 1996, Meigs 1997a, 1997b, Sussman et al., 2004), thrusting in the inner portion of the range, in the Axial Zone, occurred in the brittle regime, but lacks preserved syntectonic strata. As a consequence, establishing the timing of brittle deformation in this portion of the range, and directly testing out-of-sequence models over the entire extent of the range, has been limited to inferences from thermochronometer data (Fitzgerald et al., 1999), balanced cross-section constraints (Muñoz, 1992) or by clast provenance analysis of conglomerates in the outboard portion of the thrust belt (Puigdefàbrigas et al., 1986).

While the timing of some thrusting events has been broadly constrained using paleomagnetic and biostratigraphic correlations, close evaluation of many of the lines of evidence indicates that constraints of the period of activity on many thrusts are actually quite broad. The ability to date fault rocks in the brittle regime has made direct testing of geometric and kinematic scenarios of regional thrusting possible (e.g., van der Pluijm et al., 2006, Haines and van der Pluijm, 2008), and offers a new technique to test the validity of previous (inferred) ages of thrusts ages. We analyzed fault rocks in the Pyrenees with three objectives: 1) to directly establish the timing of brittle thrusting on both outboard and inboard thrusts in the south-central and southeastern Pyrenees by dating authigenic mineralization related to faulting, 2) to test the proposed presence of

young thrusting deep in the orogenic belt; and 3) to examine the presence of a regional mid-late Eocene orogenic pulse, consistent with the proposal that the entire range was behaving as a critically-tapered orogenic wedge during that time.

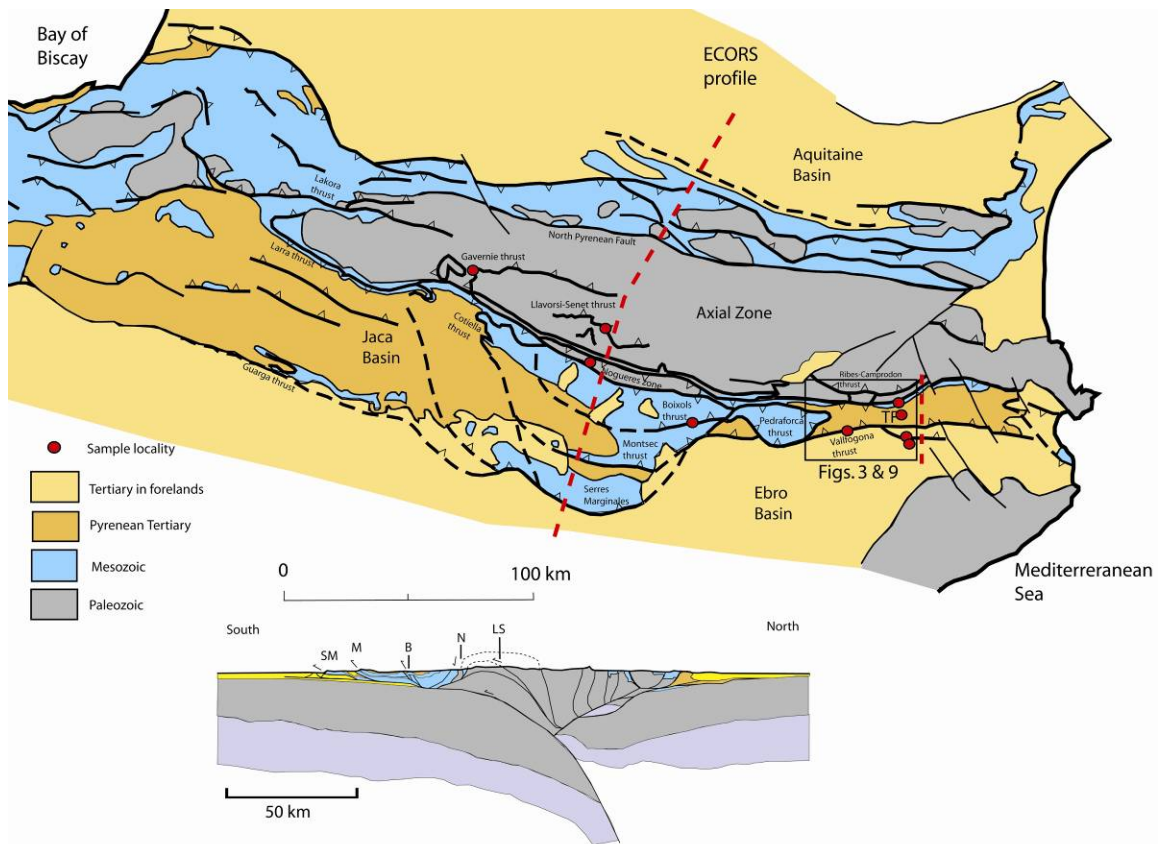
### **Fault dating**

The age of the movement of brittle faults in fold and thrust belts has traditionally been dated by 'bracketing' the age of the fault, by establishing the age of events that preceded and followed fault motion (e.g. Armstrong & Oriel, 1965, Williams, 1985, Puigdefàbrigas & Souquet, 1986, Farrell et al., 1987), by inferences from seismic lines (e.g. Ardèvol et al., 2000), or biostratigraphic and paleomagnetic data from syntectonic sediments (e.g. Burbank et al., 1992a, 1992b, Meigs et al., 1996, Meigs, 1997, Sussman et al., 2004). Frequently, the constraints placed on the age of fault slip are not well defined when syntectonic sedimentary basins lack appropriate biostratigraphic or magnetostratigraphic constraints, or are absent entirely due to subsequent erosion. Direct dating of authigenic clay mineralization in clay-rich gouges (van der Pluijm et al., 2001) offers a new approach in that the age of the fault rock is established directly. In recent years, the growth of authigenic minerals, particularly the low-temperature  $1M_d$  polytype of illite, in the brittle regime ( $\ll 300$  °C.) has been recognized as a significant process in clay-rich gouges (Vrolijk & van der Pluijm, 1999). Identifying the age of the authigenic illite by dating several size fractions of a gouge and characterizing the relative abundances of both the low-temperature  $1M_d$  polytype and the high-temperature (detrital)  $2M_1$  polytype of illite in each size fraction has been used to date reliably date faults from a variety of geologic settings (Ylagan, 2002; Solum et al., 2005; van der Pluijm et al., 2006; Solum & van der Pluijm, 2007; Haines & van der Pluijm, 2008). As the kinetics for the growth of

large clay crystallites at low temperatures are unfavourable, authigenic clays in gouges are typically very fine-grained ( $< 1\mu\text{m}$ ) and thus tend to concentrate in the finest size fraction. Each size fraction of clay from a gouge is treated as a point on a binary mixing line between the Ar-Ar age of the  $2M_1$  (detrital) component (derived from the wall rock during slip) and the Ar-Ar age of the  $1M_d$  (authigenic) component that grows during faulting. The percentage of detrital illite in each size fraction is established by quantitative modeling of XRD patterns using synthetic XRD patterns generated using WILDFIRE©, a program that calculates XRD patterns for illitic clays with a variety of crystallographic variables. The percentage of detrital illite is then plotted against the apparent Ar-Ar age for each size fraction, and the ages of the authigenic and detrital components are obtained by extrapolation.

### **Geological setting**

The Pyrenees, which straddle the border between France and Spain, are the westernmost expression of the Alpine-Himalayan orogeny and are the result of interactions between the Iberian, African and European plates during the late Mesozoic and Cenozoic. Collision occurred from the late Cretaceous to the earliest Miocene, as the Iberian microplate collided with, and was partially subducted under the European plate (Choukroune, 1989, Muñoz, 1992, Beaumont et al., 2000). The range is about 600 km long and approximately 150 km wide, and consists of a roughly east-west striking central core, commonly referred to as the Axial Zone, which is flanked by two foreland basins, the Aquitanian Basin to the north, and the Ebro Basin to the south (see Figure 5.1). Balanced sections based on the ECORS deep seismic profile across the central



**Figure 5-1:** Location map of faults studied (red circles) and approximate projection onto ECORS seismic profile. Letters refer to faults mentioned in text. LS = Llavorsi-Senet thrust, N = Nogueres zone, B = Boixols thrust, M = Montsec thrust, P = Pedraforca nappe, V = Vallfogona. The area of Figure 5.3 is shown as a box. Note traces of ECORS seismic profile (Muñoz, 1992) and the balanced cross-section of Travé et al., (2007) used in Figure 5.3.

portion of the range (Muñoz, 1992) and the Ansó-Arzacq transect across the western portion of the range indicate that the central portion of the range experienced ~150 km of shortening (Muñoz, 1992), while the western portion of the range experienced only 75-80 km of shortening (Teixell, 1998).

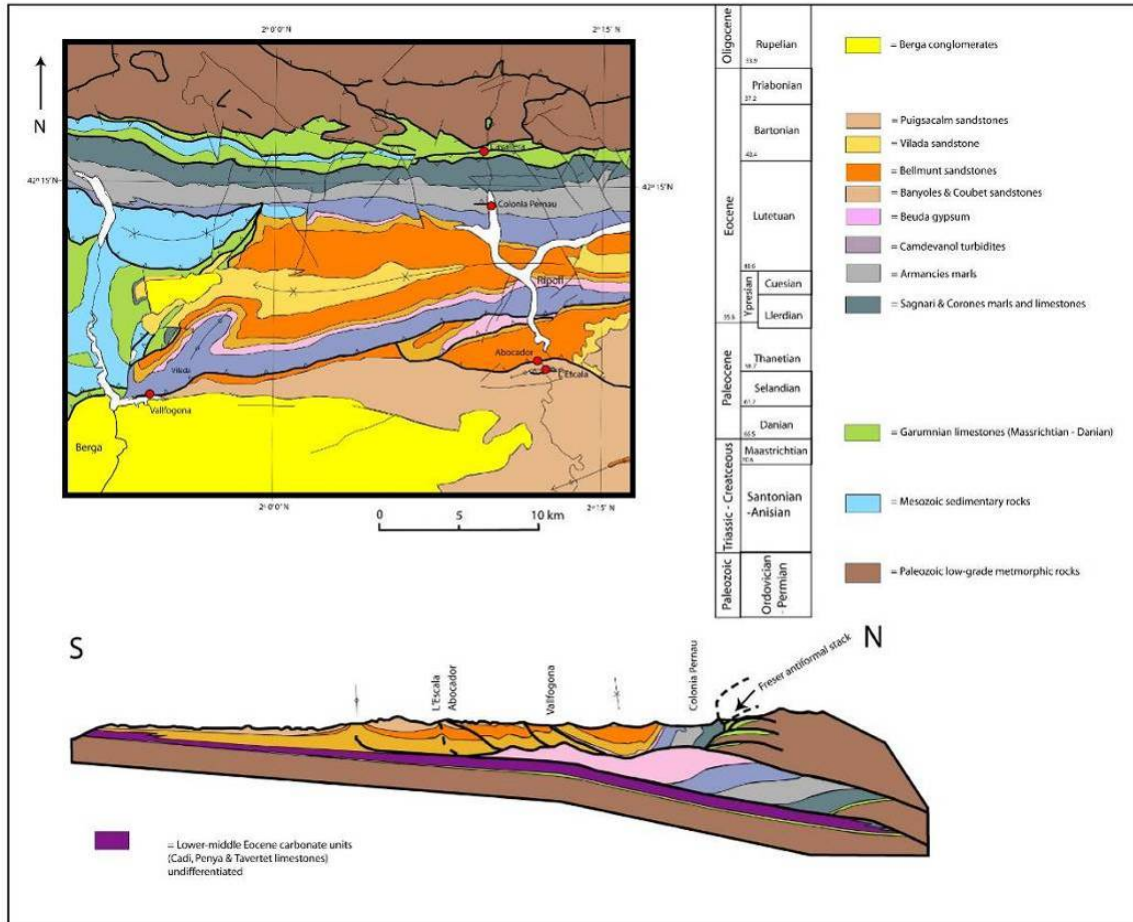
Along strike, the range can be separated into three distinct regions. The western segment has undergone relatively little shortening and has only limited exposure of Paleozoic rocks deformed during the Hercynian orogeny in the core of the segment (Teixell, 1996). The central segment has experienced more shortening, with extensive exposure of Paleozoic rocks in the Axial Zone and a relatively wide southern foreland fold and thrust belt. The south-central foreland fold-and-thrust belt can be divided into an outer imbricate thrust stack of Mesozoic and Tertiary rocks and an inner antiformal stack of basement rocks (Muñoz et al., 1986, Muñoz, 1992.) The eastern segment has a very narrow (15 km) foreland fold-and-thrust belt, yet extensive exposure of Paleozoic rocks in the core of the range, and has been partially re-worked by Neogene extensional faulting during the opening of the Gulf of Lyon (e.g. Maurel et al., 2007). The Pyrenees are asymmetrical in cross-section, with most structures verging to the south. The wide south-central foreland fold-and-thrust belt is thought to have formed generally in sequence from the late Cretaceous inboard Boixols thrust to the Eocene-to-Oligocene Serres Marginals foreland boundary thrust, although out-of sequence thrusting has been noted (Vergés & Muñoz, 1990, Muñoz, 1992, Meigs et al., 1996). A distinctive feature of the central and eastern portions of the Pyrenees is the presence of south-dipping faults (e.g. the south-dipping portions of the Cotella Nappe and the Gavarnie Nappe, the Nogueres zone, and the Serra Cavallera thrust) near the southern edge of the antiformal stack that juxtaposes older, apparent hanging-wall rocks over younger, footwall rocks. Prior to the plate tectonic paradigm, these fault geometries were interpreted as

gravity slides (e.g. de Sitter, 1954). Based on section-balancing constraints and subsequent seismic imaging, the structures are now widely accepted as overturned thrusts in a hindward-imbrecating antiformal stack (Muñoz et al., 1986, Muñoz, 1992) that has been displaced and overturned by younger thrusts deeper in the orogen. As the deeper thrusts juxtapose primarily Paleozoic rocks, establishing their age directly has proved problematic, however. We present direct ages of thrust faults from the south-central and southeastern Pyrenees that constrain the timing of hindward-imbrecating thrusting in the central portion of the range. As our approach also determines the age of the detrital component in fault gouge, we demonstrate that the provenance of the wall rock can be determined and insights into pre-Pyrenean exhumation history can be made.

## **Methods**

### Sample locations

The fault gouges sampled for this study are taken from faults along two transects (Figures 5.1 and 5.2), one along faults that either directly intersect the ECORS profile, or have lateral extensions to the ECORS profile in the south-central Pyrenees (Boixols, Gavarnie, Noguères zone and Llavorsi-Senet thrusts), and a second transect across the southern fold-and-thrust belt in the easternmost Pyrenees along the Ter and Freser rivers (Serra Cavallera, Rialp syncline, Vallfogona, Abocador and L'Escala thrusts). Geology and outcrops photos are shown in Figures 5.2 and 5.3. Coordinates of sample localities are shown in Table 5.1.



**Figure 5-2:** Geologic map with sample locations, cross-section and stratigraphic column for the Ter-Freser river section shown. Map is redrawn after the Mapa Geològic de Catalunya, (2002) and the section is redrawn after Travé et al., (2007). The line of the section is approximately 2 km E of the map area.



**Figure 5-3:** Outcrop photographs of some thrusts sampled for this study. A.) Abocador thrust outcrop on route C-17, ~25 km north of Vic. B.) Vallfogona thrust on route C-26, ~5 km W of Vilada. C.) Boixols thrust on route L-511, 3 km E of Boixols. D.) Gavarnie thrust outcrops on the Plan de Llari, ~15 km NW of Bielsa.



| <b>Fault</b>             | <b>Northing</b><br>(Deg, min. decimal sec) | <b>Easting</b><br>(Deg, min. decimal sec) |
|--------------------------|--|---|
| Gavarnie thrust          | 42° 41.766'                                | 0° 4.746'                                 |
| L'Escala thrust          | 42° 8.827'                                 | 2° 12.436'                                |
| Abocador thrust          | 42° 9.078'                                 | 2° 12.043'                                |
| Ripoll syncline thrust   | 42° 16.179'                                | 2° 9.548'                                 |
| Boixols thrust           | 42° 10.405'                                | 1° 10.871'                                |
| Vallfogona thrust        | 42° 7.806'                                 | 1° 54.36'                                 |
| Pont de les Coves thrust | 42° 16.179'                                | 2° 9.548'                                 |
| Rialp zone               | 42° 31.430'                                | 0° 49.715'                                |
| Nogueres zone            | 42° 24.925'                                | 0° 45.355'                                |

**Table 5-1:** Locations of faults sampled in this study. Datum is WGS 1984.

## South-central transect

### Boixols thrust

The Boixols thrust was sampled at a roadcut near km 21.6 on carretera L-511, 3 km E of the village of Boixols and 12 km W of Coll de Narga. See Figure 5.3C. Locally the thrust strikes 085, dips 65° N and juxtaposes hanging wall Jurassic (Dogger) dolomitic limestones against a footwall Cretaceous (Santonian) interbedded limestone and shale sequence. The fault zone outcrop consists from hangingwall to footwall of a ~15 m thick fractured damage zone in the hanging wall, a 0.5 m thick brown hard clayey gouge, a 6 m thick lens of dolomitic limestone and a 0.5 m thick greenish hard clayey gouge at the contact with the footwall, which was sampled for age dating. The footwall limestone and shale sequence is significantly less fractured than the hangingwall dolomites.

### Gavarnie thrust

The Gavarnie thrust is exposed at the west side of the Plan de Llari, 14.1 km northwest of Bielsa, Aragon. See Figure 5.3D). Locally, the thrust places upper Devonian phyllites over upper Cretaceous (Coniacian - Santonian) limestones and Triassic redbeds (von Lith, 1965). The fault zone at Plan de Llari is >10 m thick and the internal architecture is complex. The fault zone contains 1-5 m thick dolomitic carbonate mylonites at its margins, and a 1-2 m thick cohesive pressure solution-cemented fault breccia sandwiched between. The breccia contains clasts of the carbonate mylonite and the overlying phyllites, indicating the deformation history was from predominantly plastic to entirely brittle. Immediately underlying the breccia and above the lower mylonite is a 2 m thick black, fractured greasy-textured phyllite, which was sampled for dating.

## Nogueres Zone

An overturned thrust in the Nogueres thrust system is exposed along a minor road leading east from Pont de Suert towards the village of Gotarta. The fault zone is ~10 m thick and dips steeply to the south. The fault juxtaposes Devonian limestones of the Fontjanina and Manyanet formations against Carboniferous-Permian tuffs of the Guiro formation. Detailed mapping and balanced section constraints described by Saura, (2004) indicate about 160 m of S-directed transport along the structure, which is sub-parallel to, and kinematically related to the kilometer-scale Gotarta thrust, located ~1 km to the north.

## Llavorsi-Senet thrust

A thrust in the Llavorsi-Senet thrust system is exposed in a roadcut on Route L-500, 0.5 km west of the village of Boi. The thrust zone is ~10 m wide, dips steeply to the north and juxtaposes Cambro-Ordovician metapelites of the Orri thrust sheet over Cambro-Ordovician metapelites of the Erta thrust sheet (Poblet, 1991, Saura & Teixell, 1996). Clayey gouge was sampled near the northern edge of the outcrop.

## Ter-Freser section

## L'Escala thrust

The L'Escala thrust is exposed in a roadcut along Rt. C-17, about 7 km south of the village of Ripoll. The thrust is developed at the tip of a breached anticline, and has 100-200 m of displacement, and places reddish sandstones and siltstones of the middle

Eocene Bellmunt formation over grey sandstones of the upper Eocene Puigsacalm formation. About 10 cm of firm clayey gouge is developed along the fault surface.

#### Abocador thrust

The Abocador thrust is exposed in a roadcut along Rt. C-17, about 6 km south of the village of Ripoll. See Figure 5.3a. The thrust places reddish sandstones and siltstones of the middle Eocene (Lutetian) Bellmunt formation over grey sandstones of the upper Eocene (Bartonian) Puigsacalm formation, with about 1 km of displacement. 10-50 cm of hard clayey gouge is locally developed along the fault surface.

#### Vallfogona thrust

The Vallfogona thrust was sampled at a roadcut on carretera C-26 near km 154.4, 5.5 km northeast of Berga and 2.5 km southwest of Vilada. See Figure 5.3b. Locally the Vallfogona thrust strikes WNW-ESE, dips vertically and places steeply north-dipping Eocene Campdevánol turbidites over steeply south-dipping carbonate-derived conglomerates, variously described as upper Eocene (Lutetian – Priabian) (*Institute Cartographic de Catalunya*) or Oligocene in age (Burbank et al., 1992). About 10 cm of firm clayey gouge is developed along the fault contact.

#### Colonia Pernau – Ripoll syncline thrust

The lower Eocene marls of the Armànies formation in the northern limb of the Ripoll syncline are cut by numerous 10's of meters to 100's of meters scale thrusts and folds. These structures are best exposed in a railway embankment 0.5 km west of the village

of Colonia Pernau (3.5 km south of the leading edge of the Freser antiformal stack). The thrusts dip moderately to the north, although some are tightly folded. Gouge from an unfolded north-dipping thrust in the marls was sampled from a 10 cm thick gouge layer. The amount of offset could not be determined in the field, but is probably on the order of 10's of meters.

#### Freser antiformal stack

Deformation in the Freser antiformal stack (Muñoz et al., 1986) is exposed in a cliff face at the Pont de les Coves bridge on the River Freser, approximately 5 km south of the village of Ribes de Freser along Rt N-152. The cliff face exposes middle and upper Garumnian (Maastrichtian - Paleocene) silty limestones which are structurally thickened and located in the southernmost (highest) slice of the four slices of the antiformal stack. The exposure is complex and the limestone is cut by several small (meter-scale to 10's of meters) faults, duplexes and backthrusts, many with well-developed 1-20 cm thick clayey gouges. 10-20 cm of firm clayey gouge from one of the backthrusts immediately above the horse-bounding thrust was sampled for age dating.

#### **Gouge sample preparation**

To characterize the main clay minerals present in each fault exposure, oriented clay slurry mounts of the <2  $\mu\text{m}$  fraction were used. Samples were scanned from 2-35° 2 $\Theta$  (Cu-K $\alpha$ ) at a scan rate of 1°/minute both air dried and after ethylene glycol saturation for periods of 24 hours to 7 days. All XRD work was performed on a Scintag X1  $\Theta$ - $\Theta$  powder diffractometer, with an accelerating voltage of 40.0 kV, a filament current of 35.0

mA, and a Cu K $\alpha$  source. Once the principle clay minerals were identified, illitic material was then selected for polytypism analysis. As polytype-specific peaks used to establish the polytypism of illite are non-00l peaks and are suppressed by the oriented mounts used to identify the main clay minerals present, random sample preparations of the same material using a side-loaded sample packer (Moore & Reynolds, 1997) were used to accentuate the non-00l peaks. Samples were then step-scanned from 16-44° 2 $\theta$  with a step size of 0.05° and a count time of 40 seconds per step.

#### WILDFIRE modeling

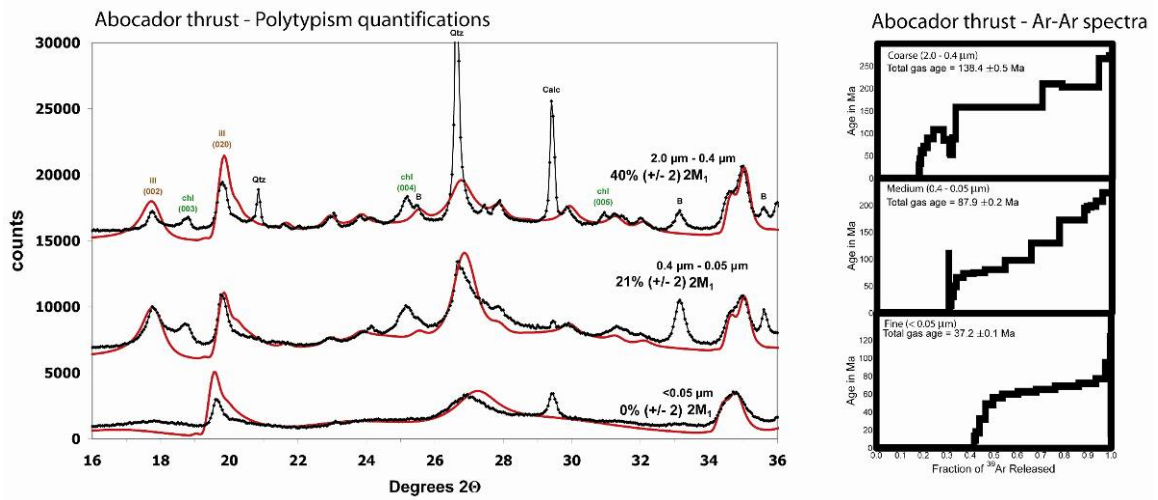
To determine the relative abundance of the two polytypes of illite (2M<sub>1</sub> and 1M<sub>d</sub>) in each size fraction of gouge, diffraction patterns obtained from random XRD scans were modeled in a spreadsheet using calculated XRD patterns generated by WILDFIRE<sup>®</sup> (Reynolds, 1993). WILDFIRE<sup>®</sup> calculates three-dimensional X-ray diffraction patterns for randomly oriented grains and allows the user to experiment with many mineralogic variables to fully capture the variability of structure ordering in illite, along with allowing the user to vary thickness of the diffracting crystallites, randomness of the sample (also known as the Dollase factor), percentage of interlayered smectite, its hydration state and any ordering of the illite/smectite (Reichweite). This multitude of options allows for optimal matching of real powder patterns, relative to early approaches that used empirical ratios of peak areas derived from a single set of standards (e.g. Velde & Hower, 1963). The precision of the polytype modeling is within 2-3 % (Haines & van der Pluijm, 2008), so we use a 1 $\sigma$  range of 2% for the subsequent illite age analysis. The only exception to the 2% error range is for the fine fraction of fault rocks from the Gavarnie thrust, where, owing to obtaining very small amounts of material for the powder pattern, we use a 1 $\sigma$  error of +/- 5%.

## Ar-Ar dating

A total of 30 size fractions from 9 faults were dated by Ar-Ar methods at the University of Michigan. To avoid the problem of argon recoil, the samples were packaged into fused silica vials and sealed prior to irradiation (van der Pluijm et al., 2001). Thus, the  $^{39}\text{Ar}$  expelled from the crystallites during irradiation is retained for analysis (see Dong et al., 1995 for a treatment of the issue). The sample vials were broken open, the initial gas was analyzed, and the vials were then step-heated under a defocused laser until sample fusion occurred. The total gas age obtained from the vacuum-encapsulated sample is equivalent to a conventional K-Ar age (Dong, 1995, 1997).

## Results

The XRD modeling of the various size fractions from gouges shows that all samples along both transects display a clear change in polytypism from relatively  $2M_1$ -rich (detrital polytype) in the coarse size fractions to relatively  $1M_d$ -rich (authigenic polytype) in the finest size fractions of the gouge, consistent with authigenic illite growth in fault gouge. Host rocks do not show this progression. A typical polytype quantification and Ar-Ar degassing spectra for the same material is shown in Figure 5.4. The polytype quantification shows a decrease in the amount of the  $2M_1$  polytype and an increase in the authigenic  $1M_d$  component, with decreasing grain size. The Ar-release spectra for each size fraction do not have plateaus, because they are composed of mixtures of grains of different ages and grain sizes and due to the effects of Ar recoil. All the spectra have an initial near-zero-age component, representing  $^{39}\text{Ar}$  released during irradiation due to recoil. The percentage of Ar released during the initial 'recoil' fraction increases



**Figure 5-4:** Typical quantification of the relative abundance of the 2M<sub>1</sub> and 1M<sub>d</sub> polytypes of illite in the coarse, medium and fine fractions size fractions of a fault gouge, and associated Ar-Ar spectra. Note the decreasing amount of the 2M<sub>1</sub> (detrital) component in progressively finer size fractions, and that the finest fraction consists almost entirely of the 1M<sub>d</sub> polytype. The Ar-Ar spectra for the <0.05 m fraction does indicate a very small amount of older material in the last degassing step, but below the 2-3% (by volume) detection limit of XRD. B = Berthierine.



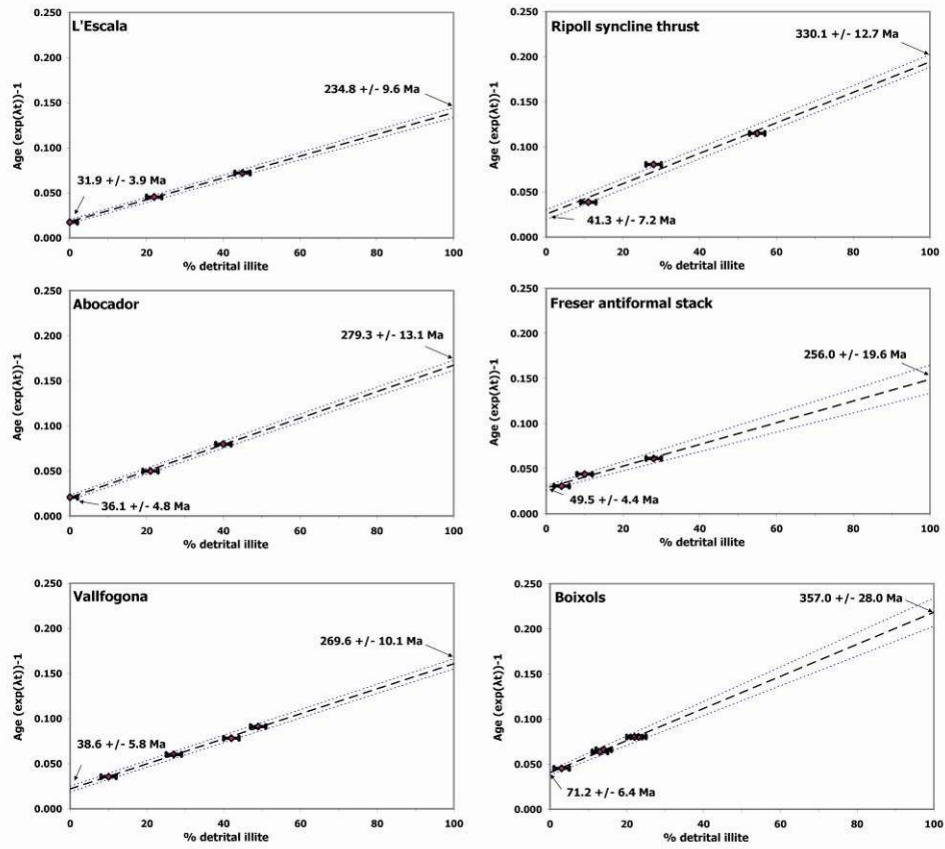
with progressively finer size fractions, consistent with finer-grained clays having a higher surface-to-volume area and thus more potential for  $^{39}\text{Ar}$  loss during irradiation. Clay polytype quantification results and Ar-Ar ages for the various size fractions of the 9 gouges sampled in this study are shown in Figure 5.4. Illite age analysis plots of the % detrital ( $2M_1$  polytype) versus the apparent Ar-Ar age of each size fraction are shown in Figure 5.5. A map showing the ages of the faults is in Figure 5.6, with the inset showing faults in the Ter-Freser transect.

### South-central Pyrenees

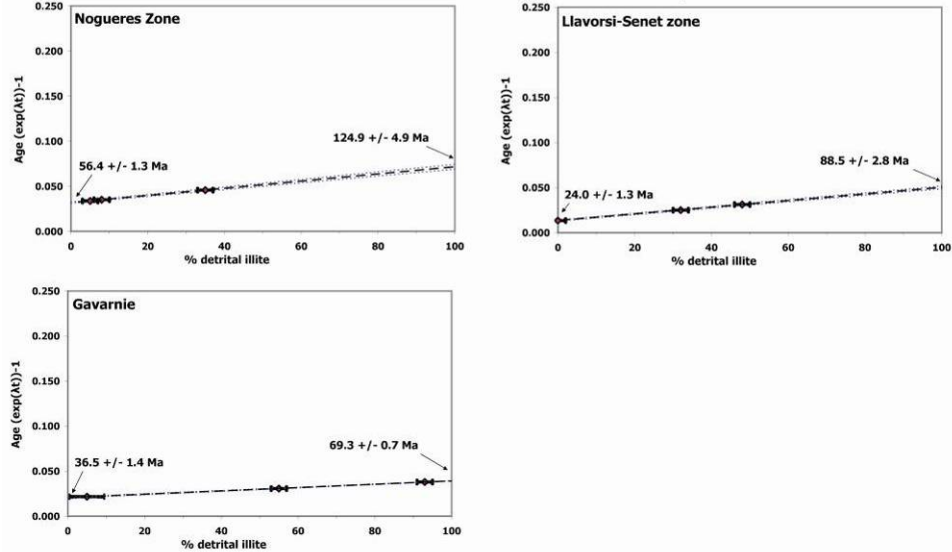
#### Boixols thrust

The Boixols thrust *sensu stricto* is exposed for ~32 km along strike where it juxtaposes Jurassic (Dogger) to Cretaceous (Coniacian-Santonian) shelf carbonates in the hangingwall against late Cretaceous (Santonian-Campanian) foredeep carbonates and shales in the footwall (Simo, 1986, Deramond et al., 1993, Ardèvol et al., 2000). The fault is considered the result of inversion on an early Cretaceous extensional basin (Bond & McClay, 1995). The surface expression of the Boixols thrust dies out at its western end in the Sant Corneli anticline, a fault-propagation growth anticline in Campanian and Maastrichtian shelf sediments. The fault extends further to the west as a blind structure on seismic lines where it tips out in Maastrichtian sediments (Ardèvol et al., 2000, Guillaume et al., 2008). Blind splays of the Boixols thrust (Riu, Turbón and Campanué thrusts) continue to the west where they cut progressively further upsection on seismic lines as far as the earliest Eocene (Ardèvol et al., 2000). Stratigraphic constraints therefore indicate that the Boixols thrust was active during the Campanian

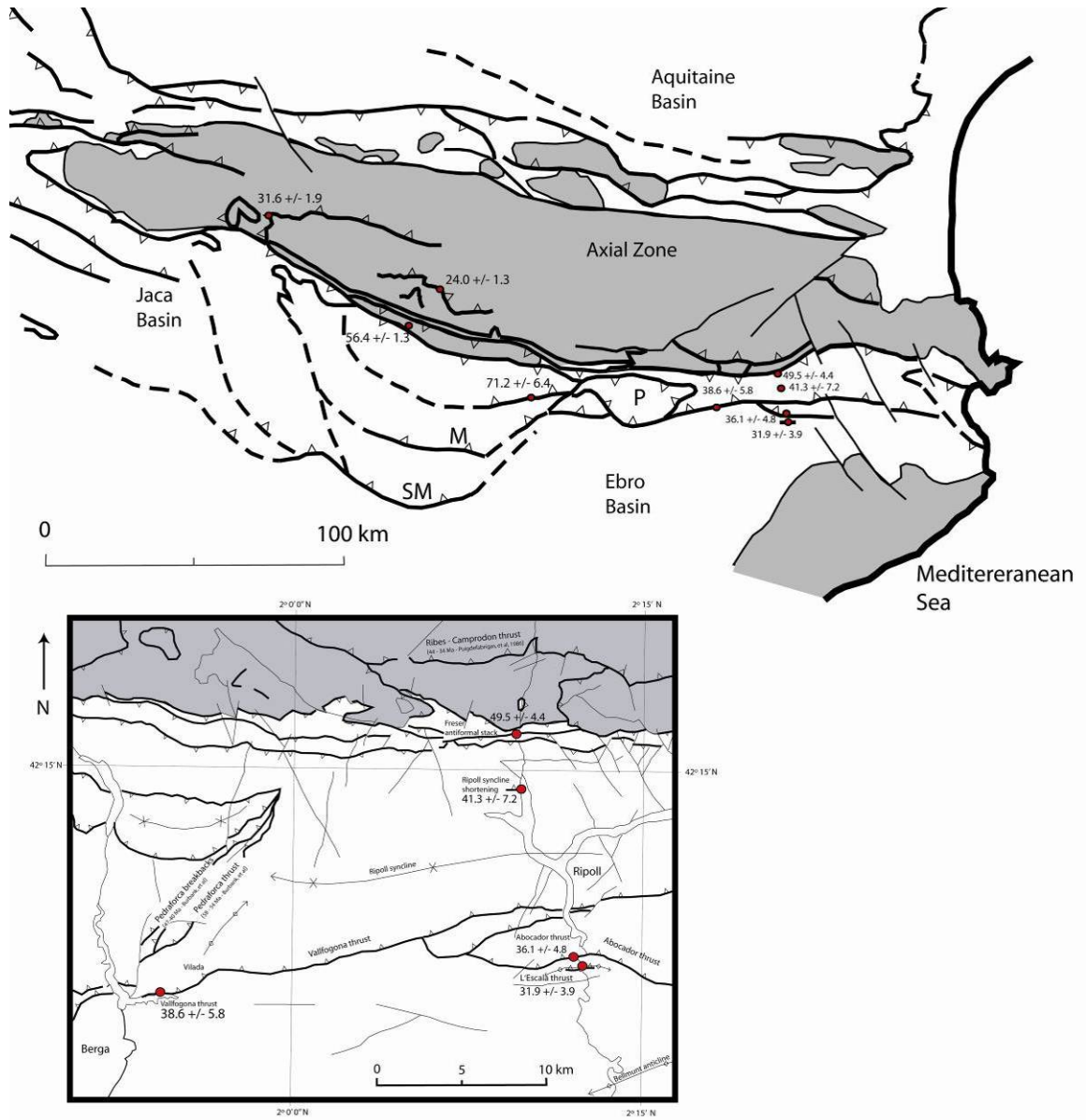
Outboard thrusts - sedimentary on sedimentary



Inboard thrusts - metamorphic on metamorphic



**Figure 5-5:** Illite age analyses plots of the nine gouges sampled in this study. Note the faults that juxtapose sedimentary rocks against sedimentary rocks give Hercynian ages for the detrital component, whereas rocks that juxtapose metamorphic rocks on metamorphic rocks (Nogueres & Llavorsi-Senet) or metamorphic rocks on sedimentary rocks (Gavarnie) give Cretaceous ages for the detrital component.



**Figure 5-6:** Map showing distribution of fault gouge ages for the 9 faults sampled. Grey is Paleozoic Axial Zone rocks. Inset box is same as on Figure 5.2

(83-70 Ma) and became inactive shortly thereafter, at the end of the Campanian or early Maastrichtian (70-65.5 Ma) (Deramond et al., 1993). The 71.2 +/- 6.4 Ma age (latest Campanian) of authigenic illite in fault gouge of the Boixols thrust is therefore fully consistent with these estimates for the age of the Boixols thrust, confirming a latest Cretaceous contractional event. The age of the detrital component in the gouge is 357.0 +/- 28.0 Ma, which is consistent with a Hercynian cooling age for the source region of phyllosilicates in the footwall and hangingwalls,.

#### Gavarnie thrust

The Gavarnie thrust marks the southern edge of the Axial zone where it juxtaposes Devonian and Silurian phyllites and slates (unconformably overlain by upper Cretaceous limestones) over Triassic to Cretaceous redbeds and limestones. At the Plan de Llari, the fault places Devonian phyllites over Cretaceous (Coniacian – Santonian) limestones (von Lith, 1965). The outcrop sampled is 200 m. north of the hangingwall cutoff for the Gavarnie nappe where Cretaceous limestones unconformably overlie Devonian phyllites. The timing of movement on the Gavarnie fault is not well constrained, based mostly on cross-cutting relationships of the thrust with late Eocene Hecho Group turbidites to the south in the Jaca Basin (Labuame et al., 1983, 1985). Here, the thrust is observed to cut Cuesian (52-48 Ma) turbidites, but not to cut latest Eocene and Oligocene turbidites (Labaume et al., 1983), thus constraining fault activity from earliest to latest Eocene. The age of authigenic illite in the sheared phyllite of 36.5 +/- 1.4 Ma, tightly constrains the last major phase of activity on the Gavarnie thrust to the latest Eocene . The very small amount of material obtained for the <0.05 µm size fraction resulted in a lower-quality XRD pattern than typical for polytype modeling, so a 1σ estimate of 5% was used for this size fraction in the error analysis. The age of the

detrital component extrapolated from illite age analysis is 69.3 +/- 0.7 Ma. The age of the detrital component indicates a late Cretaceous cooling age for the detrital component of the sheared phyllite. As the hangingwall phyllites at outcrop are located only 300 m below an unconformity with Coniacian-Santonian (89-83 Ma) limestones, and must therefore have been at or near the surface during the late Cretaceous, the sheared phyllite must be an exotic block from significantly deeper in the crust that was entrained and transported a distance of at least several kilometers. The sheared phyllite is bounded both above and below by mylonite zones from the overlying hangingwall phyllites and footwall Cretaceous limestones. The Cretaceous age of the detrital component demonstrates the capacity of faults to entrain and transport material long distances.

It has been argued that the Gavarnie thrust has a complex history of fluid flow (Grant et al., 1990, Banks et al., 1991, McCaig et al., 1995, McCaig et al., 2000) and the authigenic age of illite from the Gavarnie thrust could be considered problematic. At least two periods of significant fluid flow along the fault of saline sedimentary brines derived from underlying Triassic redbeds and Silurian phyllites are recognized. Temperatures for these fluid-flow events, which are recorded in the isotopic compositions of mylonites, are thought to be 250-300 °C (Banks et al., 1990). Field relations indicate that brittle deformation postdates earlier mylonization, so gouge formation occurred after the passage of these fluids. Were hot fluids responsible for authigenic illite growth, the illite would have grown as the high-temperature 2M<sub>1</sub> polytype, as its crystallization temperature exceeds 280 °C, while the low-temperature 1M<sub>d</sub> polytype typically grows <200 °C. (Sroden & Eberl, 1984). While the high-temperature fluid flow was hot enough to have produced 2M<sub>1</sub> illite, this would require that the fluid flow be latest Cretaceous in age and that the Gavarnie thrust therefore have been active since the Cretaceous,

inconsistent with field constraints imposed by the Coniacian-Santonian (89-83 Ma) depositional age of the footwall carbonates (now mylonitized). The authigenic illite therefore is cogenetic with the lower-temperature deformation also recorded by the cohesive fault breccia, and dates the last major event on this fault.

#### Nogueres zone thrust

The overturned thrust in the Nogueres zone is a small-scale overturned southward-facing thrust found in a kilometer-scale region of south-dipping overturned thrusts which juxtapose Paleozoic and Mesozoic units at the southern margin of the Axial Zone. The thrust has a relatively minor displacement of ~160 meters (Saura, 2004), although it is sub-parallel to the major Gotarta thrust to which it is kinematically linked (Saura & Teixell, 2006). Prior constraints on the timing of thrust movement were limited, except that fault movement must predate deposition of the upper Eocene Sarroca conglomerate, which unconformably overlies the Mesozoic and Paleozoic rocks of the Nogueres thrust slice. The age of authigenic illite in the fault gouge is 56.4 +/- 1.3 Ma, consistent with a latest Paleocene – earliest Eocene period of activity on the Gotarta thrust. The age for the detrital component of the gouge is 124.9 +/- 4.9 Ma, which is older than the onset of collision and Pyrenean tectonic exhumation, which is typically understood to be Santonian (Puigdefàbrigas & Souquet, 1986). This age of the detrital component indicates the detrital component is a probable mixture of material with Cretaceous and Hercynian cooling ages.

#### Llavorsi-Senet zone thrust

The thrust in the Llavorsi-Senet thrust zone is the most inboard of the thrusts sampled in this study and juxtaposes Cambro-Ordovician metapelites of the Orri and Erta thrustsheets. The age of the thrust has been uncertain, as it juxtaposes Paleozoic rocks over its entire length. Section-balancing constraints require that it be younger than the Nogueres thrusts to explain the southward overtilting of the Nogueres thrusts (Muñoz, 1992), and motion on the Llavorsi-Senet thrust may be contemporaneous with the deposition of the Lower Oligocene Senterada conglomerates found to the south, which unconformably overly strongly tilted Nogueres Zone structures and contain clasts derived from the hangingwall Orri thrust sheet (Saura & Teixell, 2000). The age of the authigenic illite in the fault gouge is 24.0 $\pm$  1.3 Ma, or a Late Oligocene period of activity on the Llavorsi-Senet thrust. The age of the detrital component of the gouge is 88.5  $\pm$  2.8 Ma, reflecting late Cretaceous cooling age for micas in wall-rock pelites.

#### Ter-Freser section

#### Freser antiformal stack

The Freser antiformal stack (Puigdefàbrigas et al., 1986, Muñoz, et al., 1986) is a kilometer-scale structure of south-dipping, overturned, thin thrust sheets. Each sheet is ~500 m thick and is comprised of Paleozoic basement lithologies and their Garumnian-to-Eocene cover sediments (Vergès et al., 2002). The thrust sampled is at the base of the fourth (highest preserved) thrust sheet (diagrammed in Muñoz, et al., 1988). Prior age constraints for the timing of thrusting are only the depositional age of the Garumnian (latest Cretaceous – Paleocene) and cross-cutting of the antiformal stack by a north-dipping, south-vergent, out-of-sequence thrust (Ribes-Camprodon thrust). The Ribes-Camprodon thrust sheet is thought to be the source of basement-derived clasts that

appear with increasing frequency in upper Eocene syn-tectonic conglomerates and sandstones of the Bellmunt and Puigsacalm formations to the south (Puigdefàbrigas et al., 1986). The age of authigenic illite in the fault gouge in the antiformal stack is 49.5 +/- 4.3 Ma, defining an early Eocene period of thrusting forming the duplex, then being cut by the later Ribes-Camprodon thrust and overturning the duplex to its present-day south-facing orientation during the Upper Eocene. The age of the detrital component of the gouge is 256.1 +/- 19.5 Ma, recording the Hercynian age for source phyllosilicates contained within the silty Garumnian limestone.

#### Colonia Pernau - Ripoll syncline thrust

The thrust exposed in the railway cut at Colonia Pernau is a minor thrust within the Cuesian Armàncies marls in the north limb of the Ripoll syncline, south of the Freser antiformal stack, and juxtaposes two different levels within the Armàncies marls. The north limb of the syncline is internally folded and thrust by numerous 10's to 100meter-scale ENE-WSW striking structures (Muñoz et al., 1988). The age of faulting is not constrained by field relations. The age of authigenic illite in fault gouge at Colonia Pernau is 41.3 +/- 7.2 Ma, dating the age of faulting in the north limb of the Ripoll syncline, which is very similar to the age of the Vallfogona thrust immediately to the south (see below). Some thrusts are themselves folded, although the fault zone sampled was not, so some deformation in the syncline occurred (shortly?) afterward. The age of the detrital illite in the gouge is 330.1 +/- 12.7 Ma, reflecting Hercynian detrital clays in the Armàncies marls.

#### Vallfogona thrust



The Vallfogona thrust juxtaposes early to middle Eocene (Cuesian - Lutetian ) turbidites and gypseferous shales against Bartonian to, perhaps, Oligocene (40.4 – 33.9 Ma) sandstones and conglomerates, and is found at the base of the south limb of the Ripoll Syncline. The age of the hangingwall turbidites was reported as 49-46 Ma on the basis on integrated magneto- and biostratigraphy (Verges, et al., 1998). The age of conglomerates in the younger part of the hangingwall sequence is not well constrained (Burbank et al., 1992a), but is upper Eocene to lower Oligocene (Verges & Burbank, 1996). Stratigraphic constraints and paleomagnetic data (Burbank et al., 1992a) require that the fault was active in the late Eocene to perhaps the earliest Oligocene. Three periods of activity on the Vallfogona thrust were inferred by Burbank et al.. (1992a), 44-42.5 Ma, 41.5 – 40.5 and <39 Ma, on the basis of magnetostratigraphy and sedimentary relations in the Ripoll syncline and hangingwall conglomerates. The age of authigenic illite in fault gouge from the Vallfogona thrust is 38.9 +/- 5.8 Ma, consistent with the age of the final period of thrust activity inferred by Burbank et al., (1992a), although a progressive unconformity in the lower Oligocene Solsona conglomerates in the footwall to the west has been used to argue that the fault was active until at least 36 Ma and possibly as late as 30 Ma (Vergés & Burbank, 1996). The age of the detrital component of the gouge is 269 +/- 12.6 Ma, consistent with the 2M<sub>1</sub> illite in the wall rocks being derived from micas that cooled below the closure temperature for Ar diffusion (375 +/- 25 °C) during the Hercynian orogeny.

#### Abocador thrust

The Abocador thrust is a small thrust outboard of the Vallfogona thrust with an outcrop trace of ~25 km. The thrust places middle Eocene (upper Lutetian) Bellmunt redbeds over middle-to upper Eocene (Bartonian) Puigsacalm sandstones and has a

displacement of ~1 km (Muñoz et al., 1988). Age constraints for thrust movement are scarce, except that it is assumed to have formed shortly after deposition of the footwall Puigsacalm sandstones (Travé et al., 2007). The age of authigenic illite in the fault gouge is 36.1 +/- 4.8 Ma, giving a Priabonian age for fault slip (see Figure 5.5). The age of the detrital component is 279.4 +/- 10.1 Ma, consistent with a Hercynian age for the detrital micas in the Puigsacalm and Bellmunt formations.

### L'Escala thrust

The L'Escala thrust is the most outboard structure in the transect through the southeastern Pyrenean fold and thrust belt along the Ter and Freser rivers. The structure is an anticline-tip thrust that locally developed along the crest of the L'Escala anticline, and juxtaposes the same middle Eocene Bellmunt redbeds over Middle to Upper Puigsacalm sandstones as the Abocador thrust (see above). The magnitude of displacement is uncertain, but is probably on the order of 100's of meters (Muñoz et al., 1988). Age constraints for displacement are unclear, but must be younger than the Bartonian (40.4 – 37.2 Ma) age of the footwall, and slip has been assigned to the Middle Eocene (Travé et al., 2007), although the grounds for such timing are unclear. Authigenic illite in fault gouge is 31.9 +/- 3.9 Ma, giving an earliest Oligocene age for the L'Escala thrust, indicating that thrusting probably remained active as the L'Escala anticline grew in the earliest Oligocene. The gouge age also indicates that the L'Escala thrust is the youngest and most outboard thrust in the Ter-Freser section. The age of the detrital material is 238.4 +/- 9.6 Ma, somewhat younger than the age of the detrital component for the same units for the Abocador thrust, which we interpret as a mixture of Hercynian rocks and somewhat younger material.

## Discussion

### Fault ages

The direct dating of gouge from thrusts in the south-central and south-eastern Pyrenees indicates a general progression of in-sequence thrusting that youngs towards the foreland, but also that out-of-sequence thrusting, particularly at deep structural levels, is an important process. The ages show a distinct contrast in thrust propagation style between the south-central portion of the range (out-of-sequence thrusting) and the southeastern portion of the range (in-sequence thrusting). The gouge ages also show that thrusts at several different structural positions were active in the mid-to-late Eocene, consistent with the Pyrenees behaving as a critically tapered orogenic wedge during that time.

The timing of thrusting in the outboard portion of the south-central Pyrenees was already well constrained, and our results for the Boixols thrust (71.2 +/- 6.8 Ma), the most outboard thrust sampled in this study, support previous published ages based on biostratigraphy and paleomagnetism. The ages of the more inboard thrusts have been more difficult to constrain by these methods, which benefit from our direct dating approach. Our deformation age in the Nogueres zone (56.4 +/- 1.3 Ma), kinematically linked to the Gotarta and Nogueres thrusts (Saura, 2004), constrains a late Cretaceous – Middle Eocene age estimate (Muñoz, 1992) as Late Paleocene to Early Eocene. Our age of 49.9 +/- 4.4 Ma for the Freser antiformal stack along with the initial emplacement of the Pedraforca (Burbank et al., 1992a), Montsec (Farrell et al., 1985), and Lakhora (Teixell, 1990) thrusts in the same latest Paleocene-earliest Eocene time interval, as well as a rapid increase in subsidence rate in the South Pyrenean Basin (Vergés et al., 1995), define a significant orogenic pulse of thrusting during this time. The Paleocene is

a time of tectonic quiescence and low convergence rates, accommodated primarily on inverted Cretaceous extensional faults (Vergés et al., 2002), but at the end of the Paleocene and beginning of the Eocene significant thrusting occurred at several places in the orogenic wedge, as the tip of the wedge migrated to the south from the Boixols thrust towards the Montsec and Serres Marginales thrusts during the middle Eocene. An Early Eocene orogenic pulse would have been sufficient to load the basin margin and trigger rapid subsidence in the South Pyrenean foreland basin, as recorded by the onset of marine sedimentation at the beginning of the Eocene. Because these fault rocks typically preserve the final major period of movement (Solum et al., 2005), it is unknown from our dating whether thrusts were active prior to the Paleocene-Eocene pulse.

During the Eocene, thrusting along the south-central transect occurred both at the southern tip of the southward-propagating orogenic wedge (translation of the Serres Marginales thrust sheet; Meigs, 1997) and inboard, recorded by continued movement on the Montsec thrust (Meigs 1997) and initiation of the Gavarnie thrust (Labaume et al., 1985). The Gavarnie thrust has a protracted history spanning the Eocene, and records both early plastic deformation (carbonate mylonites) and later brittle deformation (cohesive fault breccias and sheared phyllite). Our ages constrain the later, brittle deformation at the Plan de Llari to the Priabonian. During this middle-late Eocene time interval, thrusts were active at a wide variety of positions in the orogenic wedge (see Figure 5.10B in outboard positions on both the north and south sides of the range, and also on inboard thrusts (e.g. Gavarnie and the Larra thrust, Martinez-Peña & Casa-Sanz, 2003). The coeval ages of thrusting on many faults in both the southern foreland thrust belt (this study), northern foreland thrust belt (Fischer, 1984) and the interior portion of the range (this study, Martinez-Peña & Casa-Sanz, 2003), demonstrate that the Pyrenees were effectively behaving as a doubly tapered critical wedge as predicted by

the critical wedge model (e.g. Dahlen et al., 1984). The separation of a Paleocene-earliest Eocene pulse from a Middle-Late Eocene orogenic pulse may not be justified on the basis of slightly overlapping error estimates, but the two events have different structural styles and occur at different places in the orogenic wedge. Structures associated with the Paleocene-Early Eocene event typically have multiple thin thrust sheets (<2 km thick) that involve basement and are located mostly behind the (then) wedge tip of the Boixols thrust. By contrast, the Middle-Late Eocene event is associated with a major period of wedge tip advance (Meigs, 1997) and involves much larger, thicker thrust sheets, especially in the south-central portion of the range.

A final period of early Oligocene faulting in the central portion of the Axial Zone is recorded by the 24.0 +/- 1.3 Ma gouge age on the Llavorsi-Senet thrust. The Llavorsi-Senet is the first thrust immediately to the south of the Maladeta Pluton, a Hercynian pluton exhumed rapidly during the early Oligocene (35-30 Ma), as inferred by apatite fission-track cooling data (Fitzgerald et al., 1999). The final slip event recorded by the fault may not have accommodated sufficient displacement to disrupt the thermal profile of the <28 Ma apatite partial-annealing zone inferred from the Maladeta fission-track data. While the age for the Llavorsi-Senet thrust is too young to directly correlate with the end of rapid exhumation of the Maladeta pluton at ~30 Ma, it is consistent with the pluton having been partially tectonically exhumed by the Llavorsi-Senet thrust until 24 Ma when slip on the Llavorsi-Senet thrust ceased, with exhumation then accommodated along another thrust further to the south. Subsequent tectonic exhumation of the thrust sheet immediately to the south of the Llavorsi-Senet thrust to ~20 Ma is indicated by 22-20 Ma apatite fission-track ages at Barruera, 2 km SW of the Llavorsi-Senet sample site in the footwall (Gibson et al., 2007). These young cooling ages in the footwall of the Llavorsi-Senet thrust indicate that another thrust to the south of the Llavorsi-Senet must

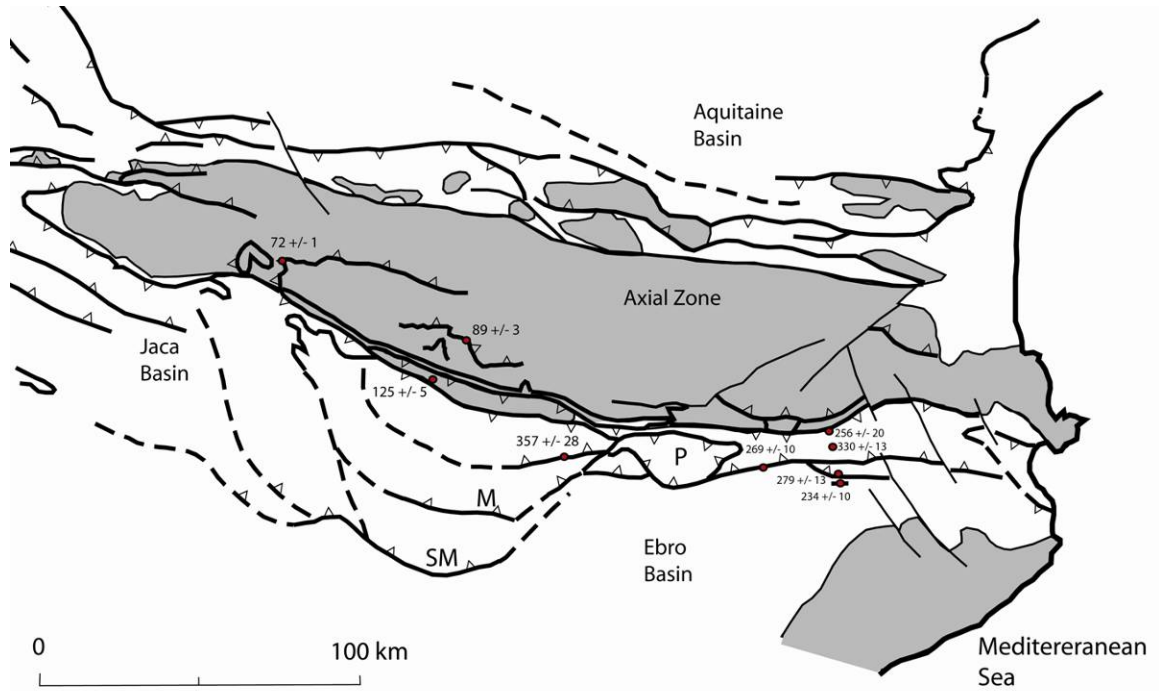
have remained active until ~19 Ma (Gibson et al., 2007), probably the Bono thrust. The young age of the Llavorsi-Senet thrust confirms the presence of young thrusting at deep structural levels, consistent both with models of Pyrenean or Pyreneal evolution that require out-of-sequence hindward-imbrecating thrusts (e.g. Muñoz, 1992) and with critical-wedge predictions that multiple thrusts in a range will be active at the same time.

In the eastern Ter-Freser transect, a sequence of southward-propagating in-sequence thrusting began in the early Eocene and ended in the earliest Oligocene. The in-sequence thrusting is in contrast with the out-of-sequence thrusting recorded in the south-central transect (Figure 5.6). Activity on the on the now south-dipping thrusts in the Freser antiformal stack occurred at 49.9 +/- 4.4 Ma, an age coinciding with the Early Eocene timing of the onset of subsidence at the northern edge of the Ebro Basin, as recorded by deposition of the glauconitic marls of the Lleridian and Cuesian Sagnari and Coronas formations. These thrusts were then overturned by the out-of-sequence, south-vergent Ribes-Camprodon thrust during the middle and late Eocene (Puigdefàbrigas et al., 1986) into their present south-dipping position. Shortening in the lower Eocene marls of the Ripoll syncline was a gradual process during the middle Eocene, but thrusting of an already folded sequence occurred at 41.3 +/- 7.2 Ma, which likely dates the deformation in the Ripoll syncline to the Lutetian and Bartonian. The Vallfogona thrust has a complex history spanning at least 10 Ma (Burbank, 1992a), and the 38.6 +/- 5.8 Ma age is equivalent to the final <39 Ma period of activity identified by Burbank et al. (1992a), consistent with fault-gouge dating of the last major episode of slip on a fault. The Abocador thrust is immediately outboard of the Vallfogona thrust and records an age of 36.1 +/- 4.8 Ma, within error of the ages of both the Vallfogona and Gavarnie thrusts, demonstrating coeval thrust activity at a variety of positions in the orogenic wedge. Numerous other thrusts were also active at this time: the Larra thrust in the west-

central Pyrenees, and many of the thrusts in the northern Pyrenean foreland belt. The L'Escala thrust is the most outboard thrust, and appears to record the final period of thrusting in the southeastern Pyrenees at 31.9 +/- 3.9 Ma. The gouge age is consistent with a posited east-to-west cessation of thrusting observed by extending from early Oligocene in the east to early Miocene in the west, (Vergès 1993, Hernaiz & Solé, 2000).

#### Provenance Ages

The age extrapolated for the detrital component of fault gouge is potentially an 'age' of a mixture of grains derived from both the footwall and hangingwall. Although a single age detrital age extrapolated from illite age analysis may not be not geologically meaningful, especially if it is probable that the detrital component is a mixture of both footwall-derived and hangingwall-derived grains, the consistency of the 234-330 Ma ages of the detrital component from wall rocks of the five faults in the Ter-Freser transect argues convincingly that detrital clays in the wall rocks in both the Garumnian and Eocene units in the eastern Ebro Basin are Hercynian in origin, and that micas with Hercynian ages had already been exhumed to the surface by the late Cretaceous (Figure 5.7). The age range extrapolated for the detrital component of the southeastern profile gouges is consistent with 290-250 Ma muscovite Ar-Ar ages from schists in the eastern Axial zone in Andorra, (McCaig & Miller, 1986) and 266 – 303 Ma muscovite Ar-Ar ages from gneisses of the Canigou massif, France (Maurel et al., 2007). Some fault rocks only received significant detrital mica input from an exotic block in the fault zone, as for example at the Gavarnie outcrop. At the Plan de Llari, the detrital age extrapolated from fault gouge is equivalent to the age of the 2M<sub>1</sub> mica derived from a mylonite-bounded block and not from the wall rock, where a late Cretaceous muscovite cooling age for the Devonian phyllites in the Plan de Llari area is impossible owing to the late-Cretaceous unconformity 300 m from the fault rock outcrop.



**Figure 5-7:** Map showing the age of the detrital component of fault gouge. Note that the outboard thrusts all have Hercynian ages for the detrital component, while the inboard thrusts which juxtapose primarily metamorphic units give Cretaceous ages for the detrital component which is the apparent cooling age of the wallrocks. Note that Gavarnie age is in parentheses, as it dates the Ar-Ar cooling age of an exotic block within the fault zone and not the Ar-Ar age of the wallrock



## Summary and conclusions

Direct dating of authigenic illite in fault gouges from nine faults in the southeastern and south-central Pyrenees has identified four discrete thrusting events during the Pyrenean orogen: 1) Late Cretaceous thrusting (Boixols); 2) Latest Paleocene-Early Eocene (Nogueres Zone & Freser antiformal stack); 3) Middle-Late Eocene (Ripoll syncline, Vallfogona thrust, Gavarnie thrust, Abocador thrust and L'Escala thrust); and 4) Middle Oligocene thrusting in the central portion of the Axial Zone (Llavorsi-Senet thrust). The Paleocene-Early Eocene and Middle-Late Eocene thrusting events may also have been one single event, due to slightly overlapping error estimates for fault gouge ages. However, as the Paleocene-Early Eocene event is confined to a single laterally continuous region of south-dipping overturned thrusts, we maintain a distinction between the two events. The Middle-Late Eocene event involves thrusting in widely varying portions of the orogenic wedge. Our finding of clustered fault movements in the Pyrenees add to a growing body of evidence for mountain ranges behaving as predicted by the critical wedge model (e.g. Willet et al., 2003 - Taiwan, van der Pluijm, 2006 – Canadian Rockies, Solum & van der Pluijm, 2007 – Wyoming Rockies).

The thrust ages also reveal a marked contrast in thrust propagation style between the south-central and southeastern portions of the range, with out-of-sequence thrusting dominating the south-central transect and in-sequence thrusting dominating the southeastern transect. It is thus evident that structural style can vary significantly even on the scale of <150 km along strike, perhaps in response to lateral variations in foreland basin architecture. The south-central transect is propagated through a 5000 m+ thick Mesozoic sequence dominated by thick banks of relatively rigid carbonate rocks, while the

southeastern transect is propagated through a relatively thin sequence of Tertiary vertically heterogeneous sediments lying unconformably over Paleozoic basement.

We also demonstrate the presence of young thrust ages in the central portion of the orogen, where stratigraphic constraints have not so far constrained the time of fault motions. The pervasively Hercynian ages of the detrital component of fault gouges in rocks in the southern Pyrenean foreland basin show that the southern Pyrenean foreland basin was receiving detrital clay input derived from exhumed Hercynian rocks in the central portion of the eastern range. The Cretaceous cooling ages inferred for the  $2M_1$  component of faults in the Axial Zone indicates that some rocks in the central portion of the range may have recorded more Pyrenean (Cretaceous-Tertiary) exhumation than the eastern portion of the range.

### **Acknowledgments**

This work was supported by NSF grants EAR-0629331 and EAR-0738435 and the Scott Turner Fund at Michigan. We thank Josep Pares for introducing us to the area and to Spanish colleagues during several field trips. Jeff Rahl was involved with the inception of the Pyrenees project, in collaboration with UM's Todd Ehlers; discussion with them helped to clarify the goals and outcomes of the fault dating study. We are grateful to J. Muñoz and J. Vergés for sample site advice. We are also grateful to Chris Hall and Marcus Johnson for Ar-dating and to Carl Henderson for maintenance of the EMAL facility at Michigan.

## References

- Ardèvol, L., Klimowitz, J., Malagón, J. & Nagteggal, P., (2000). Depositional sequence response to foreland deformation in the Upper Cretaceous of the Southern Pyrenees, Spain. *AAPG Bulletin* 84, pp. 566-587.
- Armstrong, F. & Oriel, S., (1965). Tectonic development of Idaho-Wyoming thrust belt. *AAPG Bulletin* 49, pp. 1847-1866.
- Banks, D., Davies, G., Yardley, B., McCaig, a. & Grant, N., (1991). The chemistry of brines from an alpine thrust system in the central Pyrenees: An application of fluid inclusion analysis to the study of fluid behaviour in orogenesis. *Geo. Et Cosmo. Acta.* 55, pp. 1021-1030.
- Beaumont, C., Muñoz, J., Hamilton, J. & Fullsack, P., (2000). Factors controlling the Alpine evolution of the central Pyrenees inferred from a comparison of observations and geodynamical models. *J. Geophysical Research B*, 105, pp. 8121-8145.
- Bond, R. & McClay, K., (1995). Inversion of a Lower Cretaceous extensional basin, south central Pyrenees, Spain. *In: Buchanan, J & Buchanan, P., eds., Basin Inversion. Geological Society Special Publication; v. 88; p. 415-431.*
- Burbank, D., Vergés, J., Muñoz, J. & Bentham, P., (1992a). Coeval hindward and forward-imbrecating thrusting in the south-central Pyrenees, Spain: Timing and rates of shortening and deposition. *Geological Society of America Bulletin.* 104, pp. 3-17.
- Burbank, D., Puigdefábrigas, C. & Munoz, J. (1992b). The chronology of the Eocene tectonic and stratigraphic development of the eastern Pyrenean foreland basin, northeast Spain. *Geological Society of America Bulletin.* 104, pp. 1101-1120.
- Choukroune, P., Séguret, M. & Galdéano, A., (1973). Caractéristiques et evolution des Pyrénées, *Bull. Soc. Geol. Fr.*, 7, pp. 601-611.
- Choukroune, P., (1989) the ECOURS Pyrenean deep seismic profile reflection data and the overall structure of an orogenic belt. *Tectonics* 8, pp. 23-39.
- Dahlen, F., Suppe, J., & Davis, D. (1984). Mechanics of fold-and-thrust belts and accretionary wedges. *J. Geophysical Research B* 89, pp. 10,087-10,101.
- DeCelles, P., Mitra, G., (1995). History of the Sevier orogenic wedge in terms of critical taper models, northeast Utah and southeast Wyoming. *Geological Society of America Bulletin.* 107, pp. 454-462.
- Deramond, J. (1979) Mécanismes de déformation en mise en place des nappes: exemple de la nappe de Gaernie (Pyrenees Centrales) These 3ed cycle. Toulouse.

- Deramond, J., Souquet, P., Fondecave-Wallez, M. & Specht, M. (1993). Relationships between thrust tectonics and sequence stratigraphy in foredeeps: model and examples from the Pyrenees (Cretaceous-Eocene, France, Spain). *In: Tectonics and seismic sequence stratigraphy*. Williams, G. & Dodd, A., eds. *Geological Society special publication* 71, pp. 193-219.
- Dong, H., Hall, C., Peacor, D. & Halliday, A., (1995). Mechanism of argon retention in clays revealed by laser  $^{40}\text{Ar}$ - $^{39}\text{Ar}$  dating. *Science* 267, pp. 355-359.
- Dong, H., Hall, C., Halliday, A. & Peacor, D., (1997).  $^{40}\text{Ar}$ - $^{39}\text{Ar}$  dating of late-Caledonide (Acadian) metamorphism and cooling of K-bentonites and slates from the Welsh Basin, UK. *Earth and Planetary Science Letters* 150, pp. 337-351.
- Farrell, S., Williams, G. & Atkinson, C., (1985). Constraints on the age of movement of the Montsech and Cotiella thrusts, south central Pyrenees, Spain. *J. Geological Society London*, 144, pp. 907-914.
- Fischer, M., (1984). Thrust tectonics in the North Pyrenees. *J. Structural Geology* 6, pp. 721-726.
- Fitzgerald, P., Muñoz, J., Coney, P., & Baldwin, S., (1999). Asymmetric exhumation across the Pyrenean orogen: implications for the tectonic evolution of a collisional orogen. *Earth and Planetary Sciences Letters* 173, pp. 157-170.
- Gibson, M., Sinclair, H., Lynn, G. & Stuart, F., (2007). Late-to-post-orogenic exhumation of the Central Pyrenees revealed through combined thermochronological data and modeling. *Basin Research* 19, pp. 323-334.
- Grant, N., Banks, D., McCaig, A. & Yardley, B., (1990). Chemistry, source and behavior of fluids in Alpine thrusting of the Central Pyrenees. *J. Geophysical Research B*, 95, pp. 9,123 – 9,131.
- Guillaume, B., Dhont, D. & Brusset, S. (2008). Three-dimensional geologic imaging and tectonic control on stratigraphic architecture: Upper Cretaceous of the Tresp Basin (south-central Pyrenees, Spain). *AAPG Bulletin* 92, pp. 249-69.
- Hernaiz, H., Solé, P., (2000). Las estructuras del diapiro de salinas de Rosio y del alto de San Pedro-Iglesias y sus implicaciones en la evolución tectónica de la transversal burgalesa de la cordillera vascocantábrica-cuenca del Duero. *Revista de la Sociedad Geológica de España*, 13, pp.471-486.
- Lababe, P., Mutti, E., Séguet, M. & Rosell, J., (1983). Mégaturbidites carbonates du bassin turbiditique de L'Eocène inférieur et moyen sud-pyrénéen. *Bull. Geol. Soc. Fr.* 7, 25, pp. 927-941.
- Lababe, P., Séguet, M. & Seyve, C., (1985). Evolution of a turbiditic foreland basin and analogy with an accretionary prism: example of the Eocene south-central Pyrenean basin. *Tectonics* 4, pp. 661-685.

- Leymerie, A., (1849). Voyage au Marboré et au Mont Perdu. *C. R. Acad. Sci. Paris*, 29, 308-310.
- Martinez-Peña, M. & Casas-Sanz, A., (2003). Cretaceous-Tertiary inversion of the Cotiella Basin (southern Pyrenees, Spain). *Int. J. Earth Science*, 92, pp. 99-113.
- Maurel, O., Moniè, P., Pik, R., Arnaud, N. Brunel, M., & Jolivet, M., (2007) the Mesozoic thermal-tectonic evolution of the Eastern Pyrenees: An  $^{40}\text{Ar}$ - $^{39}\text{Ar}$  Ar fission track and (U-Th)/He thermochronological study of the Canigou and Mont-Louis massifs. *Int. J Earth Sci.* DOI 10.1007/s00531-007-0179-x.
- McCaig, A. & Miller, J., (1986).  $^{40}\text{Ar}$ - $^{39}\text{Ar}$  ages of mylonites along the Merens fault, central Pyrenees. *Tectonophysics* 129, pp. 149-172.
- McCaig, A., Wayne, D., Marshall, J., Banks, D. & Henderson, I., (1995). Isotopic and fluid inclusion studies of fluid movement along the Gavarnie Thrust, central Pyrenees: reaction fronts in carbonate mylonites. *American Journal of Science* 295, pp. 309-343.
- McCaig, A., Wayne, D. & Rosenblum, J., (2000). Fluid expulsion and dilatancy plumbing during thrusting in the Pyrenees: Pb and Sr isotopic evidence. *Geological Society of America Bulletin*. 112, pp. 1199-1208.
- Meigs, A., Vergés, J. & Burbank, D., (1996). Ten-million history of a thrust sheet. *Geological Society of America Bulletin*. 108, pp. 1609-1625.
- Meigs, A., (1997a). Sequential development of selected Pyrenean thrusts. *J. Structural Geology* 19, pp. 481-502.
- Meigs, A., (1997b). Growth of the South Pyrenean orogenic wedge. *Tectonics* 16, pp. 239-58.
- Moore, D. M. & Reynolds, R. C., Jr. (1997). X-ray Diffraction and the Identification and Analysis of Clay Minerals. Oxford University Press, New York. 378 pp.
- Morley, C., (1988). Out-of-sequence thrusts. *Tectonics* 7, pp. 539-561.
- Muñoz, J., Martinez, A. & Verges, J. (1986) Thrust sequences in the eastern Spanish Pyrenees. *J. Structural Geology* 8, pp. 399-405.
- Muñoz, J., Casas, J., Martínez, A., & Vergés, J. (1988) An introduction to the structure of the southeastern Pyrenees the Ter-Freser cross-section *Excursion guidebook*. Symposium on the Geology of the Pyrenees and Betics, 85 p., Barcelona
- Muñoz, J., (1992) Evolution of a continental collision belt: ECOURS-Pyrenees crustal balanced cross-section. In *Thrust Tectonics*, McClay, K., ed, Chapman and Hall, New York, pp. 235-246.
- Parish, M., (1984). A structural interpretation of a section of the Gavarnie nappe and its implications for Pyrenean geology. *J. Structural Geology* 6, pp. 247-255.

- Poblet, J., (1991). Estructura de les unitats del vessant sud de la zona axial del Pirineu central. *Unpublished PhD thesis, University of Barcelona*, 604 pp.
- Piugdefàbrigas, C. (1975). La sedimentación Molassica en la cuenca de Jaca. *Mongrafías del instituto de estudios Pirenaicos* 104.
- Piugdefàbrigas, C. & Souquet, P., (1986). Tectonosedimentary cycles and depositional sequences of the Mesozoic and Tertiary from the Pyrenees. *Tectonophysics* 129, pp. 173-203.
- Piugdefàbrigas, C., Muñoz, J. & Marzo, M. (1986). Thrust belt development and related depositional sequences in the southern foreland basin. *Spec. Publs. Int. Ass. Sediment.* 8, pp. 229-246.
- Ramond, L., (1801). Voyages au Mont Perdu et dans la partie adjacente des Hautes-Pyrénées. Belin, Paris, 392 pp.
- Reynolds, R. C., Jr. (1993). WILDFIRE - A computer program for the calculation of three-dimensional powder X-ray diffraction patterns for mica polytypes and their disordered variations, Hanover, New Hampshire.
- Saura, L., (2004). Anàlisi estructural de la zona de los Nogueros. *Unpublished PhD thesis, University of Barcelona*. 398 pp.
- Saura, L. & Teixell, A., (2000). Relación entre los conglomerados oligocenos y las estructuras tectónicas en la Zona de los Nogueros, Pirineo central. *Geotemas* 2, pp. 201-203.
- Saura, L. & Teixell, A., (2006). Inversion of small basins – effects on structural variations at the leading edge of the axial zone antiformal stack (southern Pyrenees, Spain). *J. Structural Geology* 28, pp. 1909-1920.
- Simo, A., (1986). Carbonate platform depositional sequences, upper Cretaceous, south-central Pyrenees (Spain). *Tectonophysics* 129, pp. 205-231.
- De Sitter, L., (1954). Gravitational gliding tectonics, an essay on comparative structural geology. *American Journal of Science* 252, pp. 321-344.
- Solum, J., van der Pluijm, B. & Peacor, D. (2005) Neocrystallization, fabrics and age of clay minerals from an exposure of the Moab Fault, Utah. *J. Structural Geology* 27, pp. 1563-76.
- Solum, J., van der Pluijm, B., (2007). Reconstructing the Snake River/Hoback Canyon segment of the Wyoming thrust Belt through direct dating of fault rocks. In *Whence the Mountains? Inquiries into the Evolution of Orogenic Systems: A volume in honor of Ray Price. Geological Society of America Memoir* 433, pp. 183-196.
- Sroden, J. & Eberl, D., (1984). Illite, in Micas, Mineralogical Society of America *Reviews in Mineralogy*, 13, Bailey, S. ed.

- Sussman, A., Butler, R., Dinarès-Turell, J., & Vergés, J., (2004). Vertical-axis rotation of a foreland fold and implications for orogenic curvature: an example from the Southern Pyrenees, Spain. *Earth and Planetary Science Letters* 218, pp. 435-449.
- Teixell, A., (1998). Crustal structure and orogenic budget in the west central Pyrenees. *Tectonics* 17, pp. 395-406.
- Travé, A., Labaume, P. & Vergés, J., (2007). Fluid systems in foreland fold-and-thrust belts: An overview from the Southern Pyrenees. *In: Thrust belts and foreland basins: from fold kinematics to hydrocarbon systems*, Lacombe, O. et al., eds. Springer, Berlin, pp. 93-115.
- van der Pluijm, B., Hall, C., Vrolijk, P., Pevear, D. & Covey, M., (2001). The dating of shallow faults in the Earth's crust. *Nature* 412, pp. 172-175.
- van der Pluijm, B., Vrolijk, P., Pevear, D., Hall, C., Solum, J., 2006. Fault dating in the Canadian Rocky Mountains: Evidence for late Cretaceous and early Eocene orogenic pulses. *Geology* 34, 837-840.
- Velde, B. & Hower, J., (1963). Petrological significance of illite polytypism in Paleozoic sedimentary rocks. *American Mineralogist* 48, pp. 1239-1254.
- Vergès, J., (1993). Estudi tectònic del vessant sud del pirineu oriental i central: Evolució cinemàtica in 3D, Ph.D. thesis, Universitat de Barcelona. 203 pp.
- Vergés, J. & Muñoz, J., (1990). Thrust sequences in the southern central Pyrenees. *Bull. Soc. Geol. Fr.* 8, pp. 265-271.
- Vergés, J., Muñoz, J. A., and Martínez, A., (1992), South Pyrenean fold-and-thrust belt: Role of foreland evaporitic levels in thrust geometry, *in* McClay, K. R., ed., *Thrust Tectonics*: London, Chapman and Hall, p. 255-264.
- Vergés, J., Millán, H., Roca, E., Muñoz, J. A., Marzo, M., Cirés, J., den Bezemer, T., Zoetemeijer, R., and Cloetingh, S., (1995), Eastern Pyrenees and related foreland basins: Pre-, syn- and post-collisional crustal-scale cross-sections., *in* Cloetingh, S., Durand, B., and Puigdefàbregas, C., eds., *Marine and Petroleum Geology*, p. 903-916.
- Vergés, J. & Burbank, D., (1996). Eocene-Oligocene thrusting and basin configuration in the eastern and central Pyrenees (Spain). *In: Tertiary basins of Spain*, Friend, P. & Dabrio, C., eds., Cambridge University Press, World and regional geology, E11, pp. 120-133.
- Vergés, J., Marzo, M., Santaaulària, Serra-Kiel, J., Burbank, D., Muñoz, J. & Giménez-Montsant, J. (1998). Quantified vertical motions and tectonic evolution of the SE Pyrenean foreland basin. *In: Cenozoic foreland basins of western Europe*, Mascle, A. et al., eds. *Geological Society special publication* 134, pp. 107-134.

- Vergés, J., Fernández, M., & Martínez, A., (2002). The Pyrenean orogen: pre-, syn- and post-colisional evolution. *J. Virtual Explorer* 8, pp. 57-76.
- Von Lirrh, J., (1965). Geology of the Spanish part of the Gavarnie Nappe
- Vrolijk, P. and van der Pluijm, B. A. (1999). Clay gouge. *J. Structural Geology* 21, 1039-1048.
- Williams, G., (1985). Thrust tectonics in the south central Pyrenees. *J. Structural Geology* 7, pp. 11-17.
- Willett, S, Fisher, D., Fuller, C., En-Chao, Y., & Lu, C.Y., 2003, Erosion rates and orogenic wedge kinematics in Taiwan inferred from fission-track thermochronometry: *Geology*, 31, p. 945–948.
- Ylagan, R. Kim, C., Pevear, D., Vrolijk, P., 2002. Illite polytype quantification for accurate K-Ar determination. *American Mineralogist* 87, 1536-1545.



## CHAPTER 6: DATING THE DETACHMENT FAULT SYSTEM OF THE RUBY MOUNTAINS, NEVADA – SIGNIFICANCE FOR KINEMATICS OF LOW-ANGLE NORMAL FAULTS

### Abstract

The growth and evolution of low-angle normal faults and metamorphic core complexes is a subject of considerable debate in the geological community. We report 6 Ar-Ar ages of authigenic illite-rich illite-smectite in gouge from four faults in the Ruby Mountains metamorphic core complex detachment fault system, as well as 4 muscovite and 4 coexisting biotite  $^{40}\text{Ar}$ - $^{39}\text{Ar}$  ages from footwall mylonites in the vicinity of the brittle detachment system. The ages constrain the evolution of juxtaposed plastic and brittle segments of the detachment system during the Miocene. The ages place important constraints on two aspects of core complex evolution, the dip of the brittle fault at the time of slip, and the rate at which mylonites in the footwall are exhumed. We have tested the hypothesis that low-angle slip occurred on the Ruby Mountains detachment fault by dating authigenic illite in 3 gouge samples from both the low-angle detachment system and a high-angle normal fault that soles into the main detachment fault system, to determine their relative ages. Authigenic illite-rich illite-smectite (I/S) in gouge in three faults at Secret Pass is distinguishable from similar phases in both the footwall and hangingwall rocks because the authigenic I/S in gouge contains only 1 water layer as opposed to the more common 2-water I/S phases that occur as detrital phases in both the hangingwall and footwall. An  $^{40}\text{Ar}$ - $^{39}\text{Ar}$  age of monomineralic, 1-water I/S in the main detachment is 12.3 +/- 0.1 Ma, while monomineralic, 1-water I/S in the high-angle normal

fault is 11.6 +/- 0.1 Ma, and monomineralic, 1-water I/S in a low-angle normal fault above the main detachment is 13.8 +/- 0.2 Ma or younger. The similarity of all three ages leads to the conclusion that these faults were active coevally as part of a kinematically-linked detachment fault system. The ages also indicate that since the time of gouge formation, the fault system could not have rotated more than 20°, as the high-angle fault (current dip 52°) could not have formed as a normal fault at dips much above 70°. Post-faulting rotation of the low-angle detachment (current dip ~10°) must therefore be less than 20°, thus requiring a fault dip on the main brittle detachment of  $\leq 30^\circ$  at the time of slip. These gouge ages are consistent with slip at a low dip on the main detachment at the latest stages of detachment evolution and do not support the passage of a 'rolling hinge'. Conventional Ar<sup>40</sup>-Ar<sup>39</sup> ages of coexisting muscovite and biotite in footwall mylonites in the vicinity of the brittle fault exposures indicate that the mylonites cooled below 375 +/- 25 °C at 20.7 – 20.5 Ma. Exhumation from 375 +/- 25 °C to 275 +/- 25 °C occurred at relatively slow fault slip rates of 0.5 to 7.5 mm/yr, while exhumation from 275 +/- 25 °C to 100 +/- 50 °C occurred at slip rates of 2.1 to >>10 mm/yr. Complex biotite Ar-Ar spectra prevent a more precise rate estimate. 3 size fractions of gouge from a second outcrop of the Ruby Mountains detachment were also dated, but the gouge 'age' obtained was Cretaceous, indicating an unrecognized detrital population of the low-temperature 1M<sub>d</sub> polytype of illite in the gouge.

## **Introduction**

The evolution of metamorphic core complexes, particularly their evolution in the brittle regime, remains one of the major controversies of structural geology. Metamorphic core complexes are most prominently known from the eastern Basin and Range province,

extending from southern British Columbia to northwest Mexico, recording large-magnitude extension (e.g. *Coney, 1980, Snoke et al., 1980*). Most core complexes have a gently-dipping dome-shaped metamorphic 'core' of mid-crustal rocks, which are topped by a 'carapace' of mylonitic quartzo-feldspathic rocks, quartzites or mylonitic carbonate rocks. The mylonites are overlain and cut by brittle fault rocks (breccias, cataclasites and clay-rich gouges), collectively recording a distinctive plastic-to-brittle strain history. The hangingwall blocks of the detachments are often un- or weakly metamorphosed and are cut by high angle normal faults which sole onto the main detachment surface. Core complex detachments have accommodated large amounts of horizontal displacement, typically 10-50 km, and are responsible for the removal of a significant portion of the crustal section, in the range of 5-15 km (*Axen, 2004*).

Core complex detachments have garnered considerable geological attention because many detachment fault surfaces have dips  $<30^\circ$  in the field, (*John, 1987*). Such low dips contradict our understanding of rock mechanics as the normal faults responsible for the exhumation of these structures should not slip in the brittle regime ( $<300^\circ\text{C}$ ) at these low dips (*Anderson, 1942, Scholz, 2002*), assuming a vertical maximum compressive stress and typical values of sliding friction for rock ( $\mu = 0.65 - 0.8$ , *Byerlee, 1978*). Moreover, there is no clear evidence of seismic focal mechanisms on a low-angle normal fault (*Jackson, 1987, Jackson & White, 1989, Wernicke, 1995, Collettini & Sibson, 2001*) although several ambiguous fault-plane solutions have been proposed (e.g. *Eyidogan & Jackson, 1986, Abers, 1991, Rietbrock, et al., 1997*). The geometry also adds to the debate about the frictional strength of faults (e.g. *Rice, 1992*) as slip of detachment faults at dips  $<30^\circ$  would require low apparent fault zone friction compared to laboratory values.

Three main mechanisms have been advanced to explain slip on low-angle normal faults: 1.) the fault was initially active at a higher dip – the ‘rolling hinge’ model (*Wernicke & Axen, 1988, Buck, 1988*). 2.) The principal stresses rotate from vertical in the vicinity of the fault (*Chery, 2002*), or 3.) The fault zone is weakened, either by a.) high fluid pressure (*Axen, 1992*) or b.) low-friction materials in the fault zone (*Tullis, 1986*). Field evidence from the orientations of fractures in the vicinity of detachment fault planes does not support the mechanism of rotation of principle stresses in the vicinity of the fault zone (*Reynolds & Lister, 1987, Axen, 2004*), thus favoring a ‘rolling hinge’ or low-friction fault zones to explain the paradox of low-angle detachment faults. The ‘rolling hinge’ mechanism removes the mechanical problem of slip at low dips through large amounts of crustal flexure, whereas the low-friction mechanisms require unusual physical conditions in the vicinity of the fault zone to avoid the mechanical problems of slip at low dips in the brittle regime. Testing between these models has been difficult as field evidence frequently permits a ‘rolling hinge’, but does not require it (*Axen & Bartley, 1997*) while other, such as paleomagnetic evidence at core complexes, requires slip at dips at or near the current dip (*Liviccari, et al., 1995*).

The two contrasting hypotheses for the evolution of detachment faults can be tested if the ages of both the main detachment and the high-angle faults that sole into the detachment are known. As the high-angle normal faults in the hanging-wall blocks have a more ‘typical’ (e.g., listric) geometry and are reasonably inferred to have formed under a vertical maximum compressive stress regime, their age relations to the main detachment are key in determining if the main low-angle detachment was active at the same time and presumably the same stress field. If the main detachment is older than high-angle faults, then the main detachment could have formed earlier, at a high angle, and then passively rotated to a low angle as part of the passage of a ‘rolling hinge’. Until

recently, the lack of a reliable method to directly date brittle fault rocks prohibited testing such a hypothesis through geochronology. While it is fairly common to be able to find field exposures of the main detachment and hanging-wall normal faults in a metamorphic core complex, and the main detachment frequently contains clay gouge, it is rare to find faults in the hanging-wall that also contain gouge. Many core-complex hanging walls lack the appropriate phyllosilicate-rich wall rocks or sufficient offset along the fault to generate clay-rich fault gouges amenable to dating. However, the Secret Pass area of the Ruby-East Humboldt metamorphic core complex in northeastern Nevada is unusual in that an exposed hanging-wall normal fault has well-developed clay gouge that is suitable for dating by Ar-Ar methods. The age of clay gouge from the hanging-wall normal fault can then be compared with the age of gouge from the main detachment to elucidate the temporal relationship of normal faults currently found at high and low-angles, which is the goal of this study.

### **Fault dating**

Key to dating fault gouges by the Ar-Ar or K-Ar methods is the ability to compensate for the effect of the 'contamination' of gouge by detrital material and its effect on the ages obtained. Early attempts to date fault gouges directly isolated a fine-grained fraction of illite (<2  $\mu\text{m}$ ) (Lyons & Snellenburg, 1970, Kralik et al., 1987, Damon & Shaqfullah., 2006). It was assumed, but not demonstrated, that these samples were free of detrital illite derived from the wallrocks. Dating of illite tended to over-estimate the age of the faulting, however, as later work showed that some detrital material can remain present in even very fine size fractions (Pevear, 1992, Grathoff, et al., 2001). Subsequent applications of geochronological methods to date fault gouge (e.g., van der Pluijm et al.,

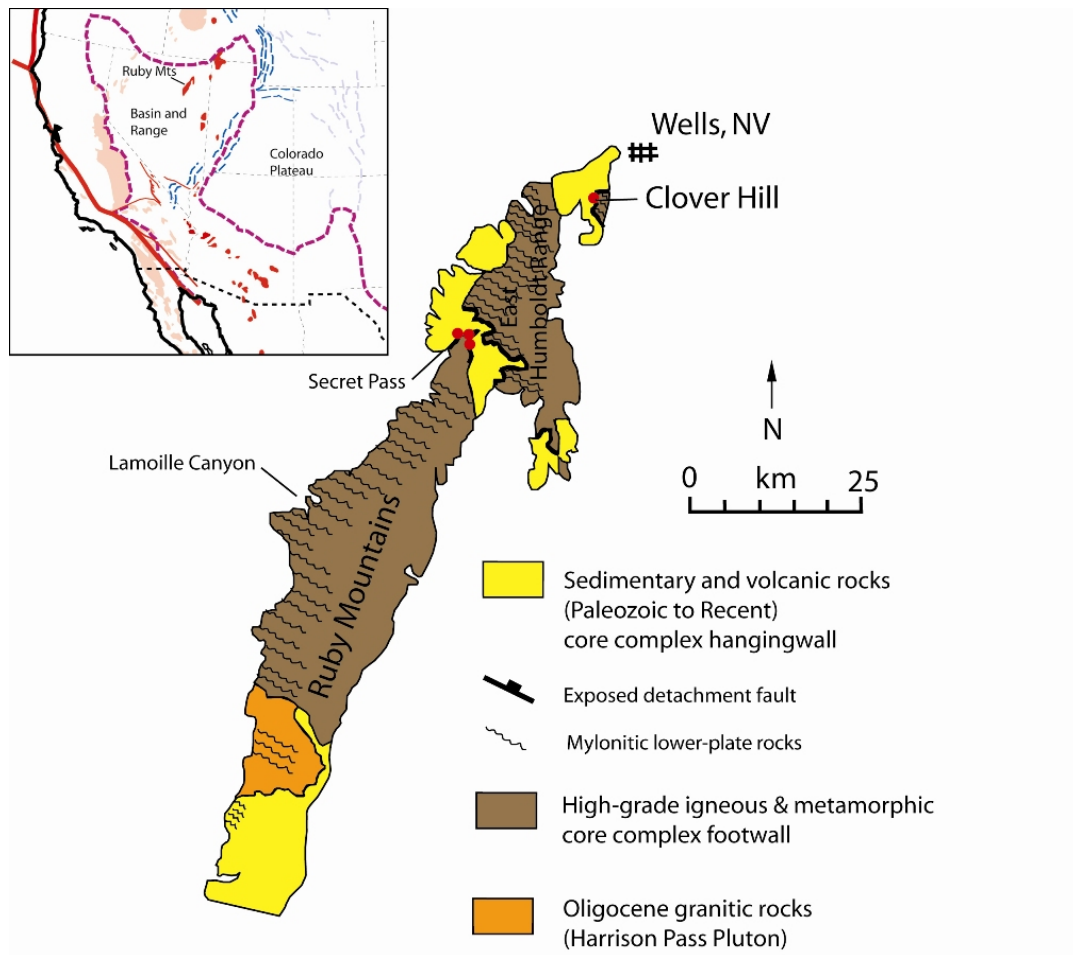
2001, 2006, Ylagan et al., 2002, Solum et al., 2005, Haines & van der Pluijm, 2008) have compensated for the problem of detrital contamination by separating the gouge into several size fractions, each having a separate ratio of detrital and authigenic material, and iteratively modeling XRD patterns of the various size fractions to determine the percentage of authigenic and detrital material in each prior to vacuum-encapsulated Ar-Ar dating. Using an approach known as Illite Age Analysis, the percentage of detrital illite in each of the size fractions is plotted against its apparent Ar-Ar total gas ages, and then extrapolated to 0% and 100% to find the end-member ages. Modeling programs NEWMOD<sup>®</sup> (Reynolds, 1996) and WILDFIRE<sup>®</sup> (Reynolds, 1993b) are used to quantitatively determine the amounts of authigenic ( $1M_d$ ) and detrital ( $2M_1$ ) clays present in each size fractions of a gouge. Two clay mineral transformations lent themselves to this approach, the age of the illitization of illite/smectite (van der Pluijm et al., 2001, Solum et al., 2005), and the growth of the authigenic, low-temperature  $1M_d$  polytype of illite (Solum et al., 2005, Solum & van der Pluijm, 2007, Haines & van der Pluijm, 2008). While the percentage of illite in interlayered illite/smectite has been shown to increase in clay gouges relative to that found in the wall rock (Vrolijk & van der Pluijm, 1999), and the illitization of illite/smectite approach has been successfully used to date fault gouges, the illitization of illite/smectite approach is limited when illite (assumed to be detrital) occurs both in the wall rock and grows authigenically in the fault zone as the low-temperature  $1M/1M_d$  polytype (Solum and van der Pluijm, 2005).

Because some clay gouges can contain almost exclusively the authigenic  $1M_d$  polytype of illite and lack either 1.) enough of the  $2M_1$  polytype to permit the conventional illite age analysis approach using the growth of authigenic  $1M_d$ , or 2.) enough of a difference in the amount of illite in illite-rich illite-smectite between coarse and fine size fractions of the gouge to permit dating using the illitization of illite/smectite approach, we demonstrate

that isolating, characterizing and dating a single fine fraction of the authigenic illite or illite-rich smectite alone can date authigenic clay growth in clay gouge. We model XRD patterns of the fine fraction material using WILDFIRE<sup>©</sup> and NEWMOD<sup>©</sup> to demonstrate that the fine fraction material is indeed monomineralic and contains only the 1M<sub>d</sub> polytype. We demonstrate that the fine fraction illite in the gouge is distinct from authigenic fine fraction 1M<sub>d</sub> illite that is observed in the wallrock. Based on WILDFIRE<sup>©</sup> modeling, we have been able to isolate essentially pure authigenic 1M<sub>d</sub> illite in three fault gouges from the Ruby Mts detachment at Secret Pass and dated them by Ar-Ar methods.

### **Field area**

The Ruby Mountains are a well-exposed core complex in northeastern Nevada (*Howard, 1980, Snoke, 1980*) extending ~150 km along strike from SW to NE (See Figure 6.1). The complex was exhumed along a large WNW-dipping, 1-2 km thick shear zone that strikes along the NW side of the range. The detachment was active from the late Cretaceous to the Miocene (*Snoke & Lush, 1984, Dallmeyer et al., 1986, Dokka et al., 1986, Mueller & Snoke, 1993, McGrew & Snee, 1994, McGrew et al., 2000*) and has a 'typical' core complex plastic-to-brittle history. The onset of exhumation is somewhat unclear, as studies reported highly discordant hornblende <sup>40</sup>Ar/<sup>39</sup>Ar ages ranging in age from Triassic to the upper Eocene (*Dallmeyer et al., 1986, McGrew & Snee, 1994*), but exhumation probably was underway by the early Eocene in the eastern (up-dip) portion of the detachment with a crude trend of hornblende Ar-Ar younging towards the northwest, consistent with a SE-NW exhumation direction (*McGrew & Snee, 1994*). Early deformation occurred at temperatures >500 °C evidenced by high-grade synkinematic



**Figure 6-1:** Generalized geologic map of the Ruby Mountains-East Humboldt Range in northeastern Nevada. Distribution of mylonitic lower-plate rocks is shown by lines. Redrawn from Snoke & Lush, (1984). Inset at left: regional map showing major structural elements of the western US, redrawn from Coney, (1980).



mineral assemblages, sub-grain development and ductile recrystallization of feldspar (Snook, 1980, Peters & Wickham, 1995). Exhumation to predominantly brittle conditions occurred quite rapidly during the late Oligocene and early Miocene, evidenced by 30-23 Ma  $^{40}\text{Ar}/^{39}\text{Ar}$  cooling ages from muscovite and biotite (Dallmeyer et al., 1986, McGrew & Snee, 1994), with a clearer trend of younger ages towards the northwest (downdip). The end of tectonic exhumation however is very poorly constrained, as the age of Miocene sediments in the hanging wall is not well known. Several rhyolites in the hanging-wall of the detachment have been dated at between 14 and 12 Ma, but their relation to the detachment surface (whether cross-cutting or truncated by the detachment) is unclear. A 26.5 +/- 6.3 Ma apatite-fission track age (closure temperature ~110 °C) from Clover Hill is nearly concordant with the biotite  $^{40}\text{Ar}/^{39}\text{Ar}$  and sphene fission track ages (both with closure temperatures 240-300 °C, Coyle & Wagner, 1998). Low-temperature thermochronometers, such as apatite fission-track may have yielded ambiguous results, due to the extremely high slip rates for these structures (2.5 km/My to ~30 km/My; Brady, 2002, Carter, et al., 2004), and the resultant possibility of advection of footwall rocks towards the surface faster than the isotherms can re-equilibrate.

The core complex detachment fault in the Ruby-East Humboldt Mountains is well-exposed at only two localities, at Secret Pass (between the Ruby Mountains and the East Humboldt range), and at Clover Hill at the NE corner of the East Humboldt range. We have characterized and dated gouges from the exposure at Clover Hill and at three faults at Secret Pass, the main detachment fault, a subsidiary detachment above the main detachment and a high-angle normal fault in the hangingwall that soles into the low-angle detachment system.

## Methods

### Sampling and clay separation

About 0.5 kg of clay gouge material was collected along a traverse across the fault core of each of the three detachment fault exposures and the hanging-wall normal fault, sampling each visibly distinct region at outcrop. Samples were disaggregated by soaking in water and suspended repeatedly until the sample was free of salts. The clay-sized material ( $<2 \mu\text{m}$ ) was separated using Stoke's law techniques. The accumulated clay fraction was centrifuged into three different size fractions, ( $2 \mu\text{m} - 0.4 \mu\text{m}$ ,  $0.4 \mu\text{m} - 0.05 \mu\text{m}$  – and  $<0.05 \mu\text{m}$ ) spanning roughly two orders of magnitude in grain size, to obtain multiple samples, each with a distinct ratio of relatively coarse-grained detrital and fine-grained authigenic illite. As the effects of chemical treatment to remove carbonate, quartz or organic material on the retention of Ar by illite are not well known (Moore and Reynolds, 1997), we did not treat our samples further.

### X-ray diffraction

To characterize the main clay minerals present in each sub-region of a fault exposure, oriented clay slurry mounts of the  $<2 \mu\text{m}$  fraction were used. Samples were scanned from  $2-35^\circ 2\theta$  (Cu- $\alpha$ ) at a scan rate of  $1^\circ/\text{minute}$  both air dried and after ethylene glycol saturation for periods of 24 hours to 7 days. The nature of illite in any illite-smectite (I/S) and the effect of any ordering (R0, R1, etc) were determined using NEWMOD (Reynolds & Reynolds, 1996). NEWMOD calculates 1-dimensional XRD patterns for (00l) reflections of illite and illite-smectite (I/S) and allows the user to vary the crystallite size, the composition of the clay phase, the percentage of illite in an illite-smectite (I in I/S) and the hydration state of that smectite, as well as any ordering in the I/S. Once the

principle clay minerals were identified, illitic material was then selected for polytypism analysis. As the polytype-specific peaks used to establish the polytypism of illite are non-00l peaks and are suppressed by the oriented mounts used to identify the main clay minerals present, random sample preparations of the same material using a side-loaded sample packer (Moore & Reynolds, 1997) were used to accentuate the non-00l peaks. Samples were then step-scanned from 16-44° 2 $\theta$  with a step size of 0.05° and a count time of 40 seconds per step.

#### WILDFIRE modeling

To determine the relative abundance of the various polytypes of illite (2M<sub>1</sub> and 1M<sub>d</sub>) in each size fraction of illitic gouge identified by XRD scans of the oriented mounts, diffraction patterns from random XRD patterns of the same material were modeled using WILDFIRE<sup>®</sup>. WILDFIRE<sup>®</sup> calculates three-dimensional X-ray diffraction patterns for randomly oriented grains and allows the user to experiment with many mineralogic variables to fully capture the variability of structure ordering in illites described earlier, along with allowing the user to vary the thickness of the diffracting crystallites, the randomness of the sample (also known as the Dollase factor), the percentage of interlayered smectite, its hydration state and any ordering of the illite/smectite (Reichweite) (Reynolds, 1993). This multitude of options allows for better matching of real powder patterns than early approaches which used empirical ratios of peak areas derived from a single set of standards (see summary in Dalla Torre et al., 1994).

#### Ar-Ar dating

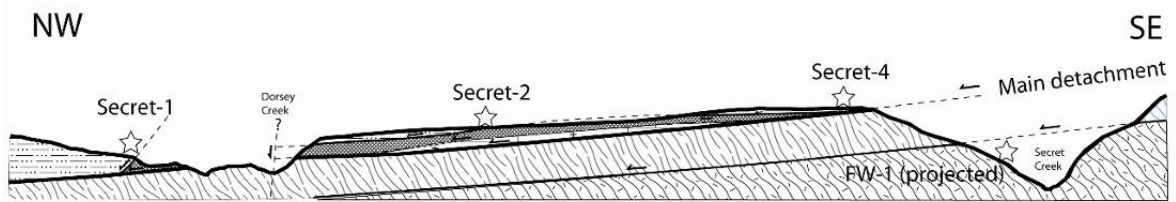
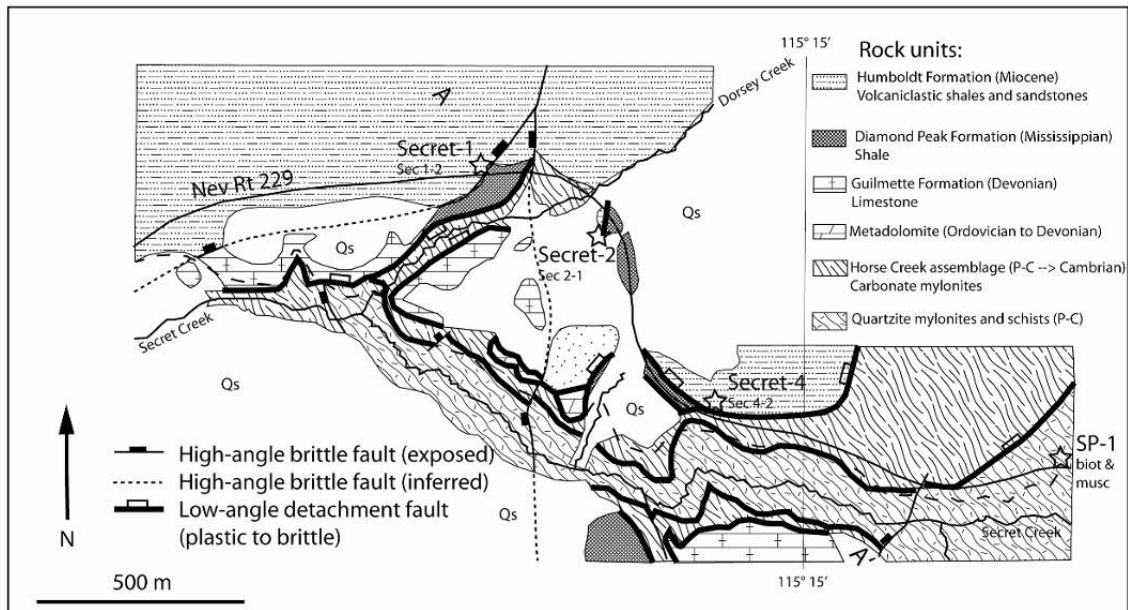
A total of 9 clay samples from the Ruby Mountains faults were dated by Ar-Ar methods at the University of Michigan. To avoid the problem of argon recoil, the samples were

packaged into fused silica vials and sealed prior to irradiation (van der Pluijm et al., 2001). Thus, the  $^{39}\text{Ar}$  expelled from the crystallites during irradiation is retained for analysis (see Dong et al., 1995 for a rigorous treatment of the issue). The sample vials were broken open; the initial gas was analyzed and the vials were then step-heated under a defocused laser until sample fusion occurred. The total gas age obtained from the vacuum-encapsulated sample is functionally equivalent to a conventional K-Ar age (Dong, 1995, 1997). Coexisting muscovite and biotite grains from footwall mylonites were also dated using standard (unencapsulated) laser step-heating techniques.

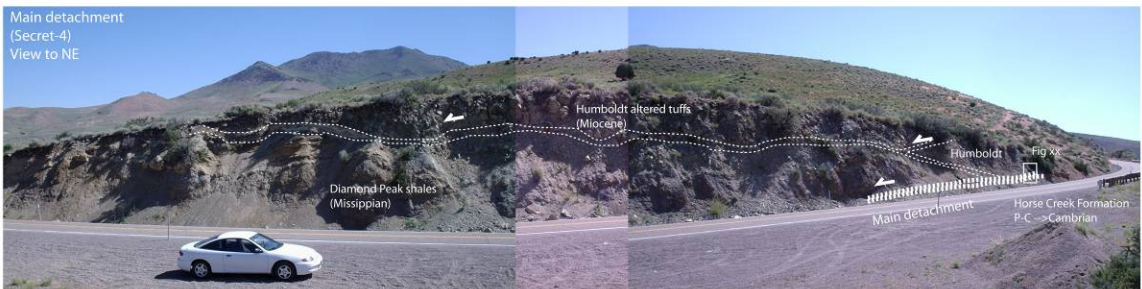
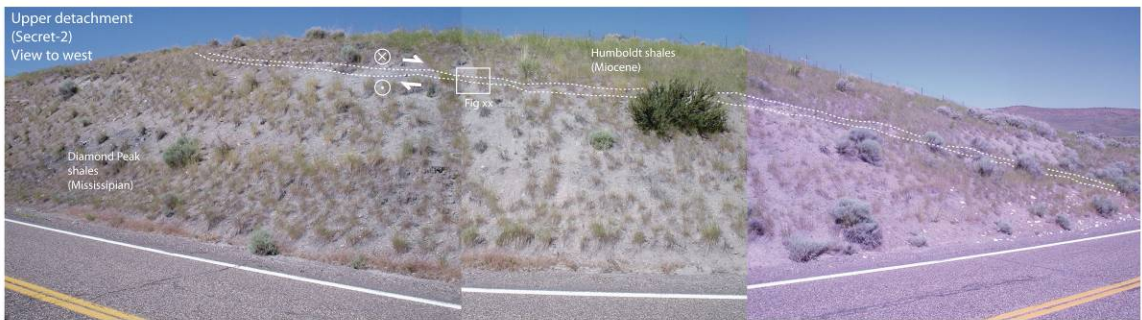
## **Results**

### Outcrop and gouge characterization - Secret Pass

The Ruby Mountains detachment exposure in Secret Pass along Nevada Route 229 is complex, with at least three sub-parallel NW-dipping detachments that are exposed in roadcuts within 1 km of each other (see Figures 6.2 and 6.3). The brittle detachments are stacked vertically and are separated by <100 m in true section (see Figure 6.2). Similar geometries of stacked low-angle detachments have been observed in the Chemehuvi Mountains of SE California and the Amargosa Chaos area of the southern Black Mountains, SE CA (Stewart, 1983, Miller & John, 1999). In addition, a higher-angle normal fault in the hanging-wall, which soles out onto the low-angle main detachment, is exposed. Because both the hangingwall and footwall sediments of the high-angle normal fault (Secret-1) and the upper detachment (Secret-2) show evidence for authigenic illite growth due to diagenetic process in sedimentary basins prior to tectonic juxtaposition, detailed characterization of both the gouge and wall rocks is required.



**Figure 6-2:** Simplified geologic map of the Secret Creek Gorge area and cross section showing the locations of the three detachment faults described in this paper, along with a simplified cross section along A – A'. Map redrawn from Snoke et al., (1984).



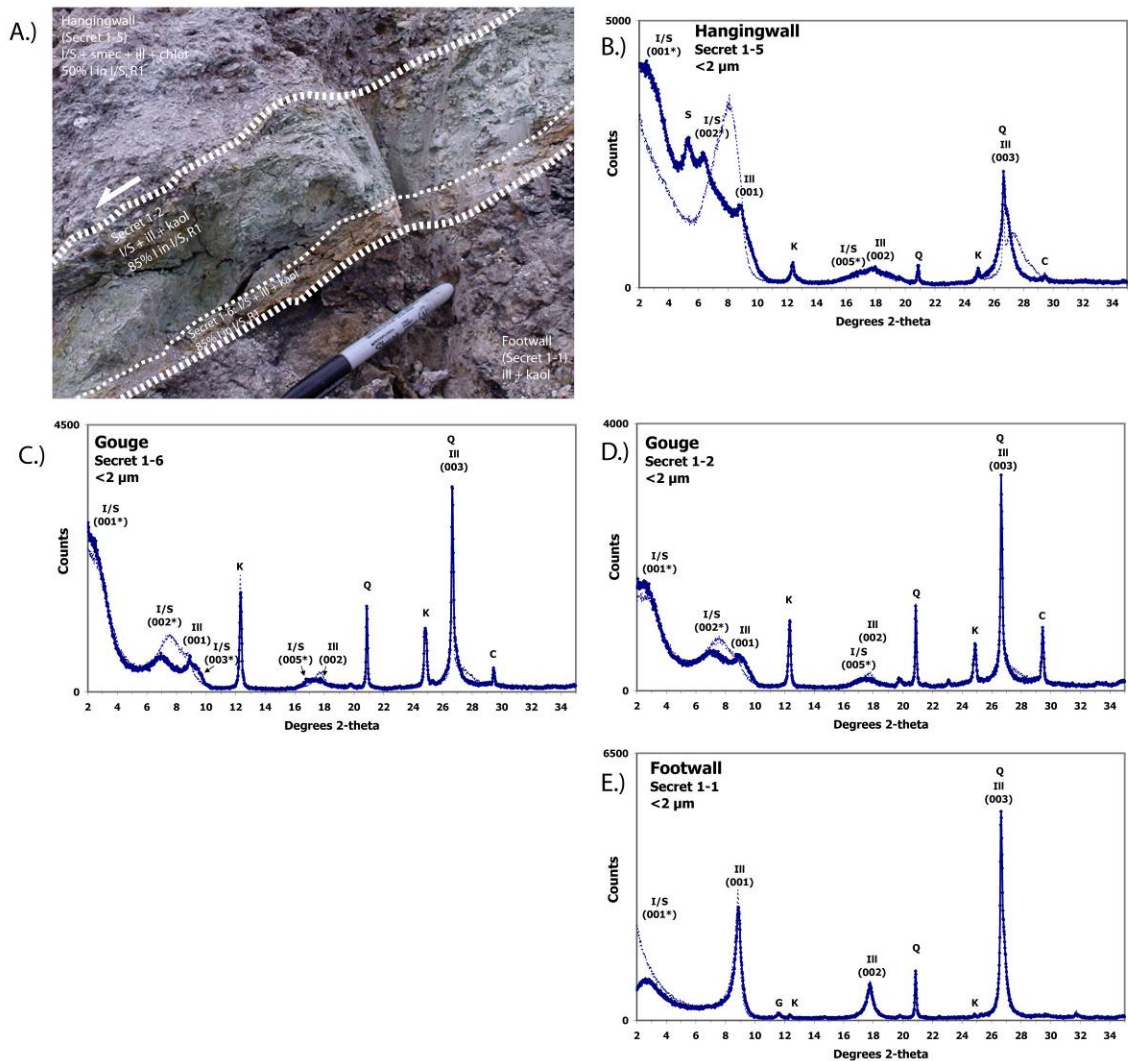
**Figure 6-3:** Field photos showing outcrops of faults at Secret Pass sampled in this study. All exposures are along NV Route 229.

## High-angle normal fault

The high-angle fault that soles out into the main detachment is exposed in a roadcut 200 m west of Dorsey Creek (40° 52' 12" N, 15° 15' 36" W). The fault zone dips moderately to the northwest (52 → 320) and consists of 20-30 cm of clay-rich gouge. Visually the gouge can be separated into two regions, an upper greenish unit and a lower brownish unit (see Figure 6.4). XRD patterns from oriented preparations indicate that the two units (samples Secret 1-2 and Secret 1-6) are essentially identical in composition. Secret 1-2 consists of an illite-rich 1-water I/S (80-85% I in I/S, R1) in all size fractions (see Figure 6.4). The one-water-layer-nature of the I/S suggests that the expandable component may be a vermiculite-like mineral or a high-charge beidellite, rather than smectite *sensu stricto*. Random powder mount XRD patterns of the same size fractions indicate that the illite-rich I/S in Secret 1-2 is almost exclusively the 1M<sub>d</sub> polytype in all size fractions (see Figure 6.5).

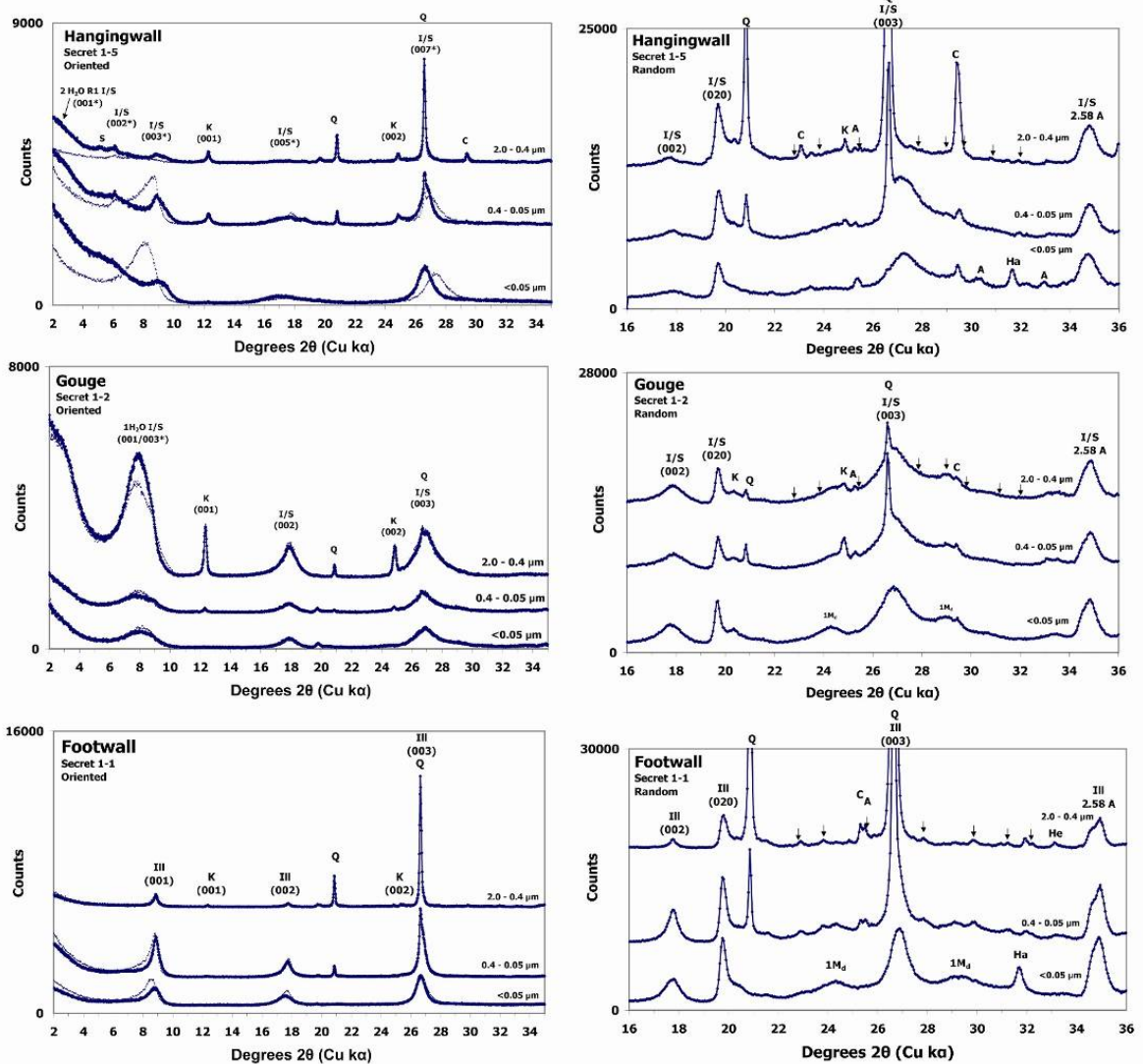
The hangingwall Humboldt formation (sample Secret 1-5) consists of a mixture of 2-water I/S (50% I in I/S, R1), discrete illite, discrete smectite and kaolinite (see Figure 6.5). When separated into size fractions, the hangingwall shales show a transition from a coarse fraction dominated by R1 I/S with 50-55% I in I/S to an R0 2-water illite-rich I/S with 80-85% I in I/S in the fine fraction. Random powder mounts of the same size fractions indicate that the illitic portion of I/S in all size fractions consists almost exclusively of the 1M<sub>d</sub> polytype of illite (see Figure 6.5)

The footwall Diamond Peak shale (sample Secret 1-1) consists almost exclusively of discrete illite. A hump at 3.2 °2 $\theta$  (27 Å) indicates the presence of some ordered R1 I/S interlayers with the illite (see Figure 6.5). A random powder mount XRD pattern of Secret



**Figure 6-4:** Field photograph and XRD patterns of <2μm fraction from upper-plate normal fault rocks (Secret-1). A.) Field photo showing regions sampled. B.) Hangingwall Miocene siltstone (Secret 1-5), Note presence of discrete smectite, illite-smectite, illite and kaolinite. C.) Lower region of gouge (Secret 1-6), gouge consists of illite-smectite, illite and kaolinite. D.) Upper region of gouge (Secret 1-2). Note same assemblage as C.) E.) Footwall Mississippian shale. Note shale consists entirely of illite. Dotted line is air-dried, solid line is after ethylene glycol salivation. Note the gouge mineralogy (R1 illite-rich I/S) is distinct from the wall rock on either side and is not a mechanical mixture of the footwall (illite) and hangingwall (50% I in I/S + illite + smectite). I/S = illite-smectite, S = smectite, ill = illite, K = kaolinite, Q = quartz, C = calcite, G = gypsum.





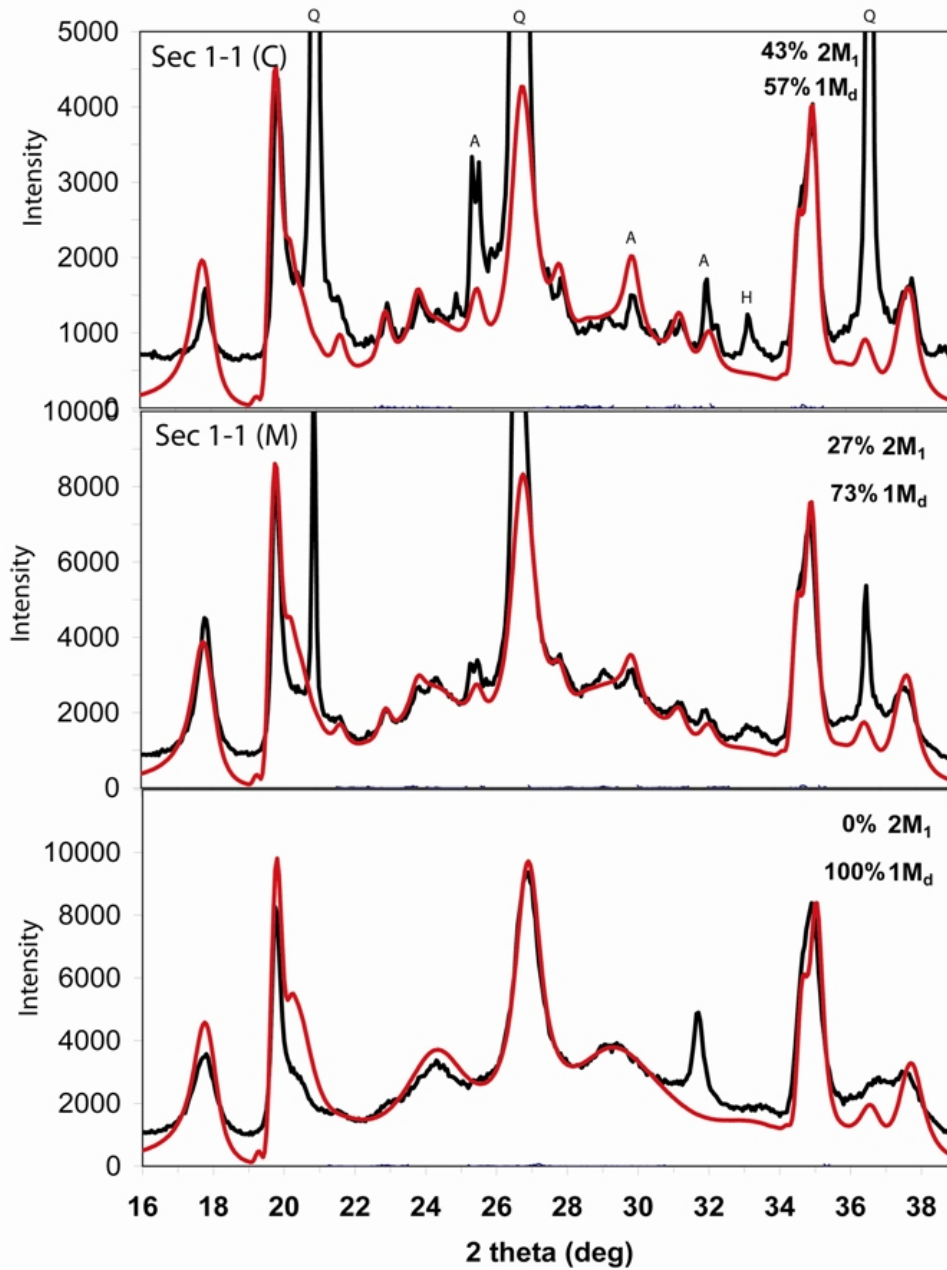
**Figure 6-5:** XRD patterns of gouge and wall rocks of upper-plate normal fault, separated into size fractions. Left hand column are oriented preparations (to accentuate (00 $\ell$ ) reflections), right-hand column is random preparations of same material (to accentuate 1M $_d$  and 2M $_1$ -polytype-specific peaks). Dotted line is air-dried, solid line is after ethylene glycol saturation. Arrows indicate illite 2M $_1$ -specific peaks. Hangingwall (Secret 1-5 – Miocene Humboldt formation siltstone): Note transition from multiple clay phases (R1 I/S, smectite & kaolinite) in the coarse size fraction to a single clay phase (R0 – R1 illite-rich I/S) in the fine size fraction. Note also the absence of 2M $_1$ -specific illite peaks in all size fractions. Gouge: Note transition from I/S + kaolinite assemblage in coarser size fractions to 1-water illite-rich I/S in the <0.05  $\mu$ m fraction. Note also the absence of 2M $_1$ -specific peaks and presence of 1M $_d$  humps in all size fractions. Footwall (Secret 1-1 – Mississippian Diamond Peak shale): Note the transition from illite + kaolinite in coarser size fractions to illite in the <0.05  $\mu$ m size fraction. Note also the clear transition from a mixture of the 2M $_1$  and 1M $_d$  polytypes in the coarsest size fraction to pure 1M $_d$  in the finest size fraction. I/S = illite-smectite, K = kaolinite, III = illite, A = analcime, H = halite. Q = quartz, C = calcite.

1-1 indicates a clear transition from a mixture of the  $2M_1$  and  $1M_d$  polytypes of illite in the coarse and medium size fractions to a pure *tv* (trans-vacant)  $1M_d$  illite in the fine size fraction (see Figure 6.5). WILDFIRE modeling indicated a transition from 43%  $2M_1$  in the coarse fraction to 0%  $2M_1$  in the fine fraction, e.g. the fine fraction of the shale consists entirely of authigenic  $1M_d$  illite, which presumably grew during diagenesis of the Diamond Peak shale (See Figure 6.6). This hypothesis is being tested by Ar-Ar dating.

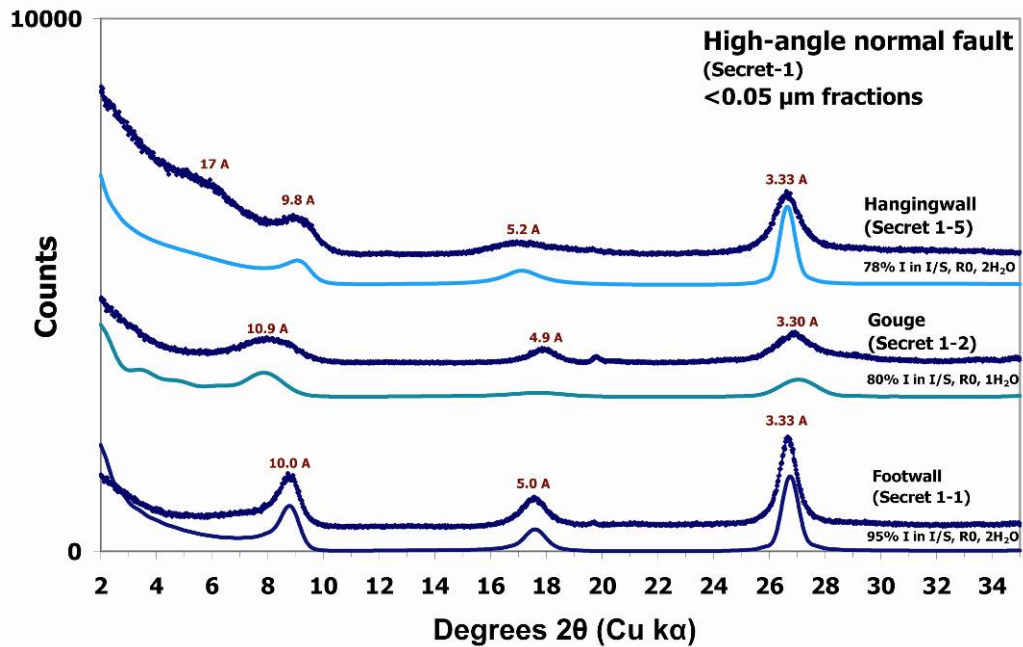
The authigenic illite-rich I/S in the gouge (sample Secret 1-2) is an essentially pure 1-water illite-rich I/S (80-85% I in I/S, R0) and is thus distinct from the authigenic  $1M_d$  discrete illite in the footwall (sample Secret 1-1) and the authigenic 2-water illite-rich I/S (80-85% I in I/S, R0) in the hangingwall (sample Secret 1-5), as authigenic phases in the footwall and hangingwall are both 2-water phases. See Figure 6.7.

#### Upper detachment

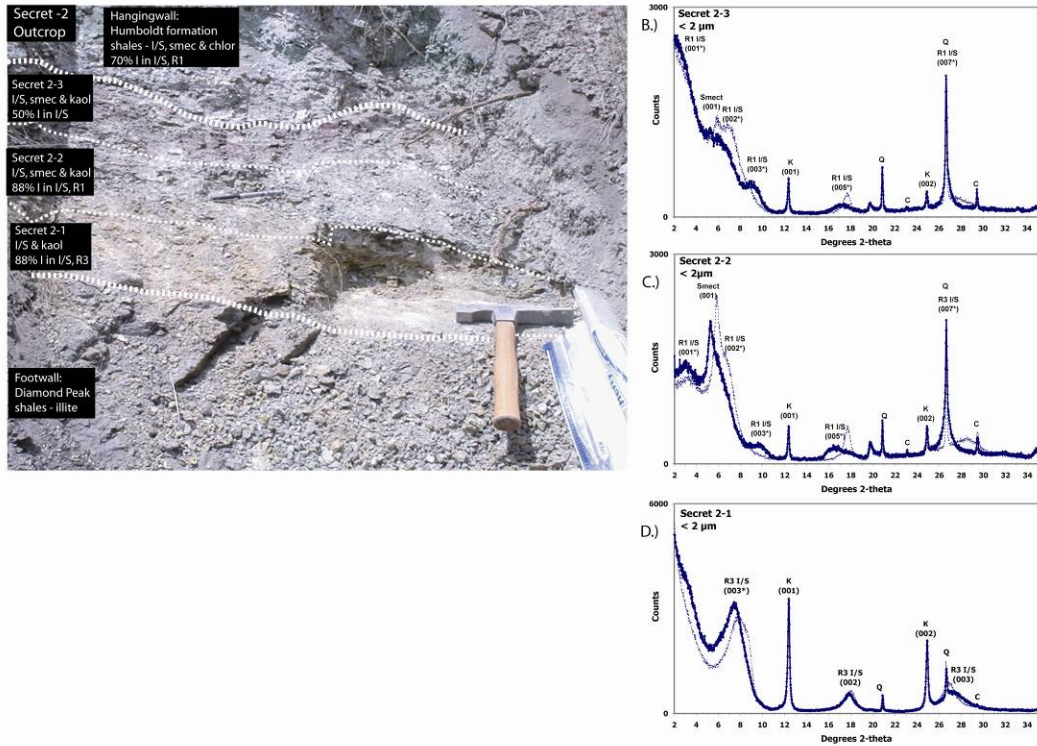
A low-angle detachment above the main detachment is poorly exposed on the west side of Rt 229 near the top of a roadcut ( $40^\circ 52' 5''$  N,  $115^\circ 15' 36''$  W) where it dips gently to the northwest ( $20 \rightarrow 306$ ). The fault zone is about 50 cm thick, clay-rich, and has relatively sharp contacts with the same footwall Diamond Peak shales and hangingwall Humboldt siltstones as the high-angle normal fault. The gouge zone can be divided into three distinct clay-rich regions, both visually and on the basis of XRD patterns. (see Figure 6.8). The upper region (sample Secret 2-3) consists of predominantly of R1 ordered 2-water layer illite-smectite and kaolinite, with minor smectite. The illite/smectite is 50-55% I in I/S, as determined by the  $^\circ\Delta 2\theta$  method of Sroden, (1980). The central region of the gouge zone (sample Secret 2-2) is composed predominantly of R1 ordered I/S and kaolinite, with minor smectite. Unlike the upper region, the I/S in the central



**Figure 6-6:** XRD patterns from Secret 1-1 with polytype quantifications determined using WILDFIRE-generated patterns. Note the clear transition from a mixture of the 2M<sub>1</sub> and 1M<sub>d</sub> polytypes in the coarsest size fraction to pure 1M<sub>d</sub> in the finest size fraction. A = analcime, H = halite.



**Figure 6-7:** XRD patterns and NEWMOD matches of fine fractions from gouge and wallrocks of hanging-wall high-angle normal fault (Secret-1). Note 2-water nature of hangingwall and footwall authigenic phases and the 1-water nature of the gouge authigenic phase. Oriented, glycol-solvated preparations.

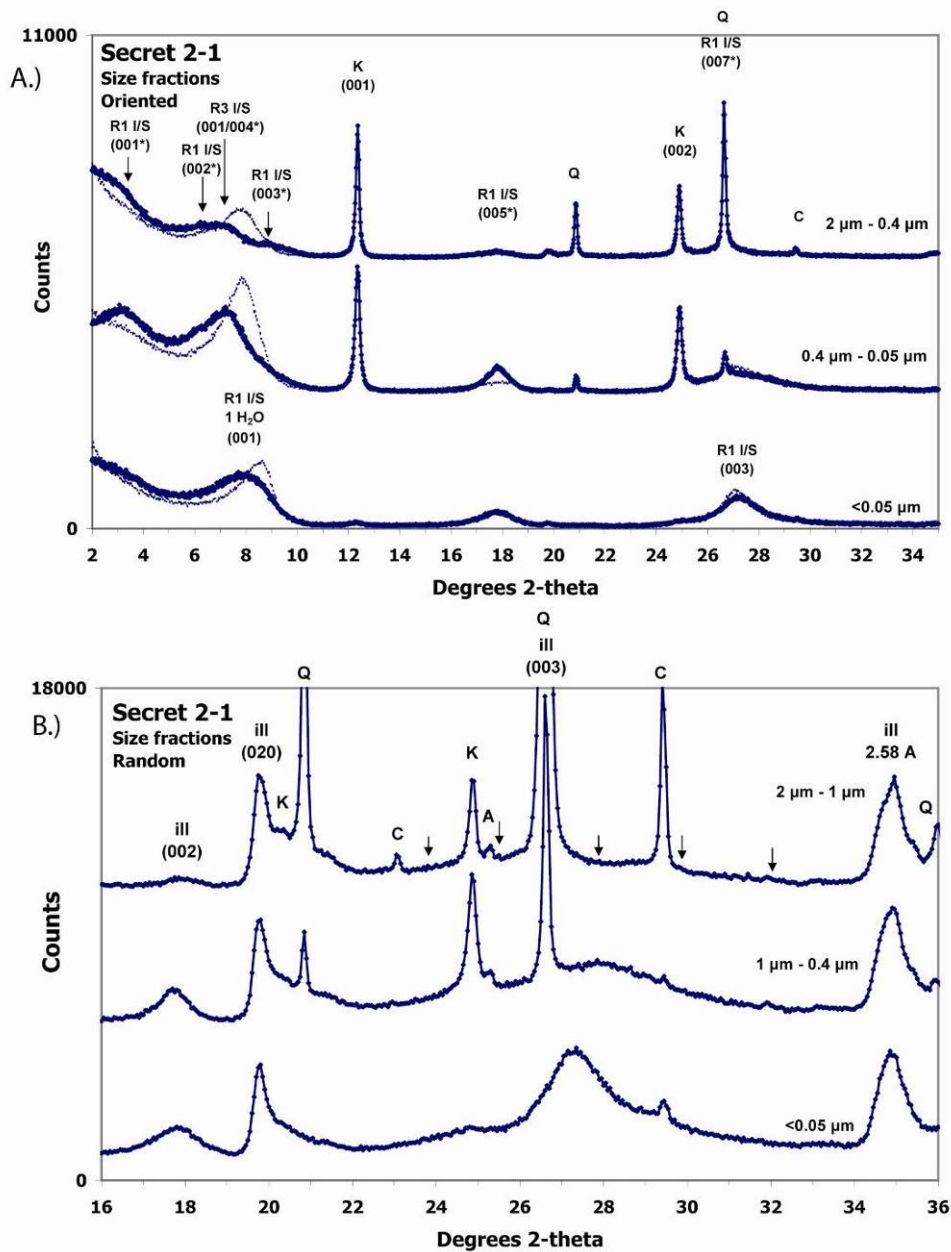


**Figure 6-8:** Outcrop photograph and XRD patterns of the <2 μm fraction of the gouge of the upper low-angle detachment (Secret 2-1). A.) Outcrop photo of the main detachment, showing three sub-regions sampled. B-D.) XRD patterns from each region of the gouge dashed line is air-dried pattern, solid is glycol-solvated (Secret-4-1). B.) Gouge is a mixture of smectite and kaolinite. C.) central greenish region of the gouge zone (Secret 4-3), Material is essentially pure montmorillonite. D.) Dark grey region at base of gouge zone. Material is R3 illite-rich I/S and kaolinite.

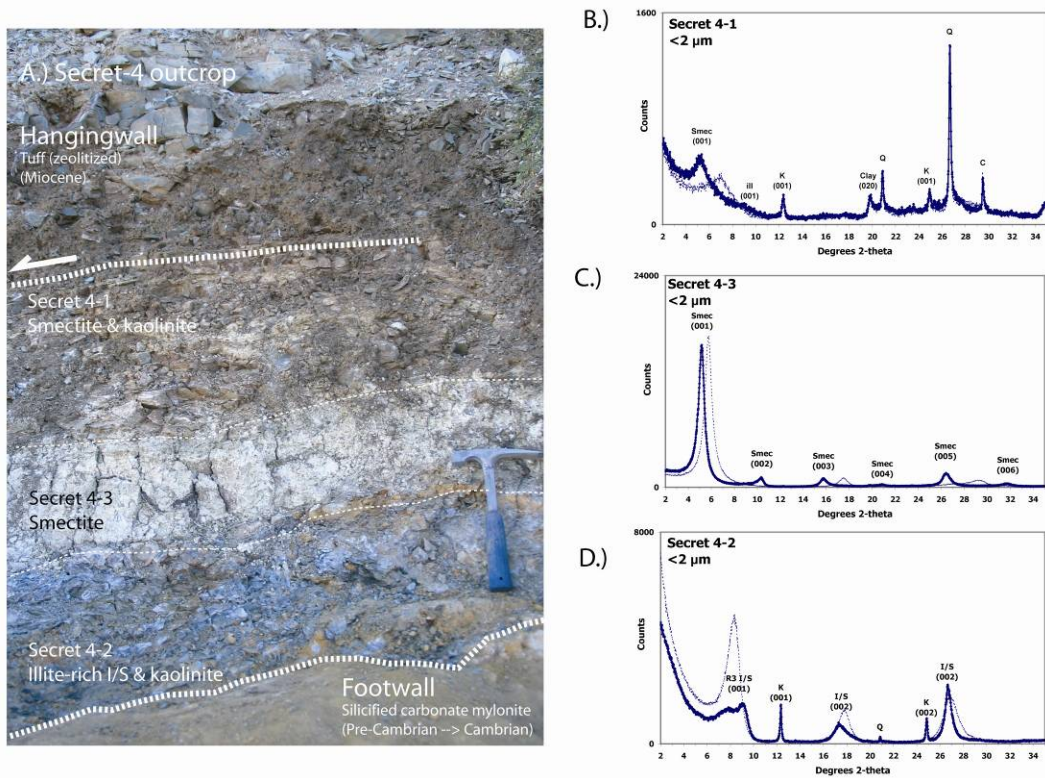
region is much more illitic, 85-90% I in I/S as determined by the  $^{\circ}\Delta 2\theta$  method. The lower region (sample Secret 2-1) consists mostly of an illite-rich I/S that is a mixture of R1 and R3 ordering, and minor discrete kaolinite. Oriented XRD patterns from the coarse size fraction from Secret 2-1 indicate the presence of peaks at 27 Å, 13.5 Å, 12 Å and 9.4 Å, consistent with a mixture of R1 and R3 mixtures (see Figure 6.9). The finest grain size of the gouge consists almost entirely of an illite-rich 1-water layer illite-smectite (85% I in I/S, R0-R1). A random powder XRD scan of Secret 2-1 shows that the illite-smectite consists almost entirely of the  $1M_d$  polytype in all size fractions, and that the  $2M_1$  polytype is absent to the detection limits of XRD (see Figure 6.9). The finest fraction of the gouge from the upper detachment (sample Sec 2-1) is thus essentially a monomineralic  $1M_d$  1-water illite-rich illite smectite (R0-R1), very similar to that of the main detachment. The progression from top to bottom of 50% I in I/S, R1 to 85% I in I/S, R1, to 85% I in I/S, R0 indicates that the authigenic clay-forming reaction likely involves solid-state illitization of detrital R1 I/S and the transformation of the interlayer smectite to a more vermiculate-like composition.

#### Main detachment

The main detachment fault is exposed in a roadcut along Nevada Rt 229 (40° 51' 53" N, 115° 15' 15" W - see Figures 6.3 & 6.10), where the fault juxtaposes Miocene water-lain tuffs of the Humboldt Formation (heavily altered to clinoptilite and heulandite) against silicified carbonate mylonites of the Horse Creek assemblage. The gouge zone is approximately 1 m thick and is mineralogically diverse. Three distinct zones can be distinguished in the gouge zone, both visually and on the basis of clay composition determined by XRD (See figure 6.10). The upper region of the gouge zone (sample Sec 4-1) consists of a hard light brown mixture of smectite and kaolinite, with very minor illite



**Figure 6-9:** Upper figure: patterns from oriented preparations. Dotted line is air-dried, solid is after glycol salvation. Note transition from assemblage of R1 + R3 I/S + kaolinite to monomineralic assemblage in fine fraction of R1 1-water I/S. Lower figure: patterns from random preparations. Arrow show 2M<sub>1</sub>-specific peaks. Note absence of 2M<sub>1</sub> peaks in all size fractions and pure 1Md polype in the finest size fraction. K = kaolinite, C = calcite, Q = quartz, A = analcime.

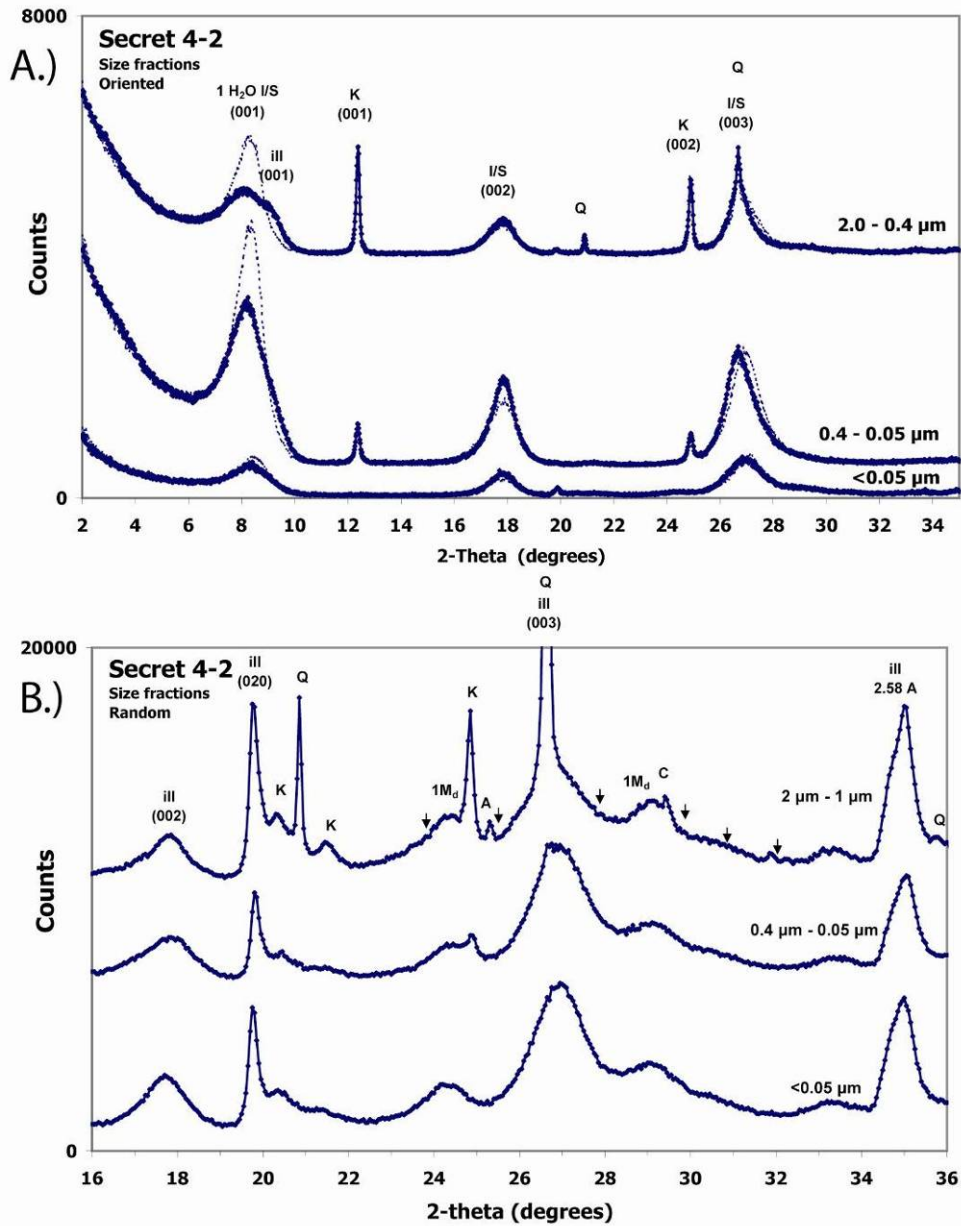


**Figure 6-10:** Outcrop photo and XRD patterns of the <2 μm fraction of each region visible in photo. A.) Outcrop photo of the main detachment, showing three sub-regions sampled. B-D.) XRD patterns from each region of the gouge dashed line is air-dried pattern, solid is glycol-solvated (Secret-4-1). B.) Gouge is a mixture of smectite and kaolinite. C.) central greenish region of the gouge zone (Secret 4-3), Material is essentially pure montmorillonite. D.) Dark grey region at base of gouge zone. Material is R3 illite-rich I/S and kaolinite.

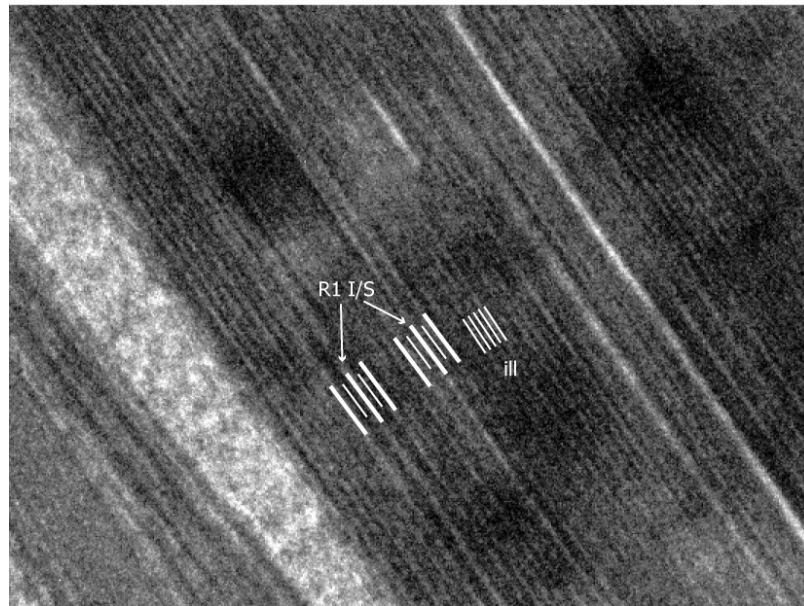
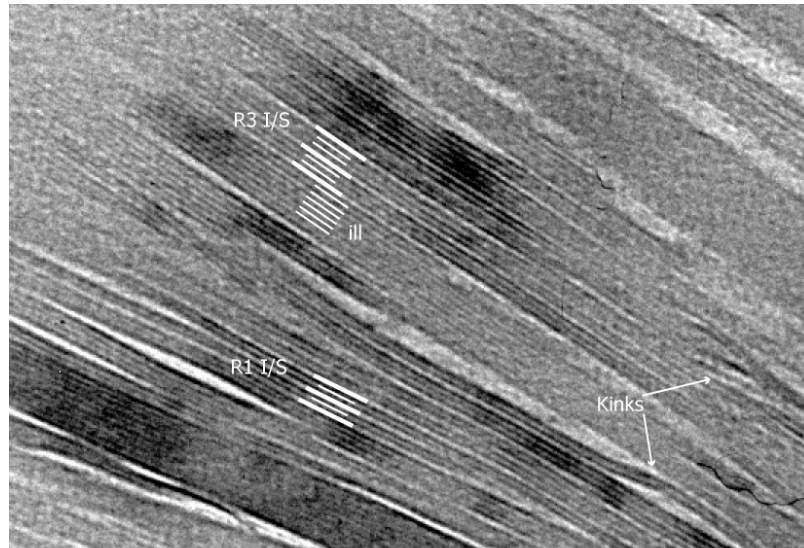


and quartz. The central region of the gouge zone (sample Sec 4-3) is a light green, very stiff, essentially pure smectite. The smectite is dioctahedral on the basis of a (060) reflection at 1.499 Å (61.88° Cu K $\alpha$ ), and SEM/EDS analysis indicates that the primary cations are Mg and Fe with subordinate K and Ca, warranting the montmorillonite designation. The lower region (sample Sec 4-2) is a dark grey, hard clay consisting of illite-rich illite/smectite and quartz. XRD patterns of the separated size fractions of the lower region (Sec 4-2) show a distinct 'shoulder' at 7.9° on the low-angle side of the illite (001) peak, indicative of R3 ordering. When Sec 4-2 is separated into size fractions, a transition is evident from predominantly an R3 illite-smectite in the coarse size fraction to an R0 1-water layer illite-smectite within the medium and fine size fractions (See Figure 6.11). The finest size fraction of Sec 4-2 consists exclusively of 1-water illite-rich illite-smectite (85% I in I/S, R0). HR-TEM observations of the clay from Secret 4-2 indicate the presence of both R1 and R3 ordering in illite smectite together with packets of discrete illite. (see Figure 6.12). Kinks and layer terminations, indicative of lattice defects and strain, are common. XTG data (x-ray texture goniometry) measuring clay fabric intensity, show that both the smectitic and illitic clays in the main detachment have a very weak preferred orientation (Haines et al., in submission; Chapter 3). An XRD random powder mount shows that the illite-smectite in Secret 4-2 consists almost exclusively of the 1M<sub>d</sub> polytype in all size fractions, and that the 2M<sub>1</sub> polytype is either absent or present below the detection limits of XRD (typically <2-3%; Figure 6.11). The finest fraction of the gouge from the main detachment (sample Sec 4-2) is thus functionally a monomineralic 1M<sub>d</sub> 1-water illite-rich I/S, similar to those found in the high-angle normal fault and upper detachment.

Clover Hill

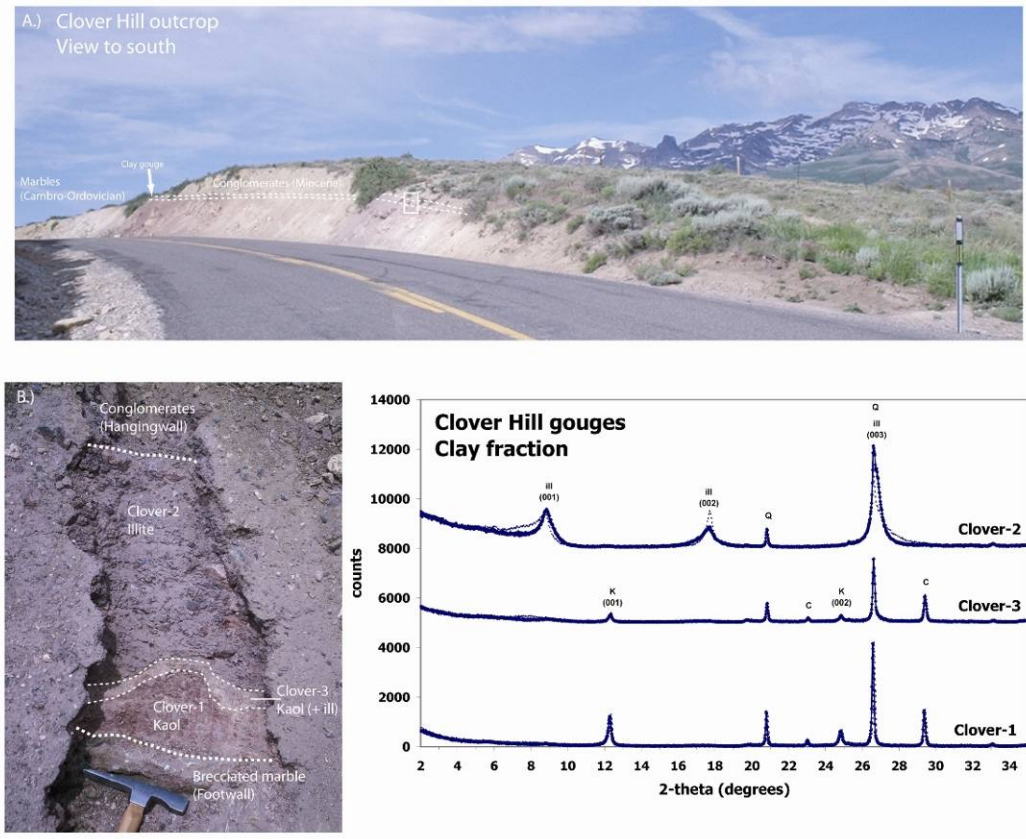


**Figure 6-11:** XRD patterns from size fractions of the gouge of the main low-angle detachment (Secret 4-2). Upper figure: patterns from oriented preparations. Dotted line is air-dried, solid is after glycol salivation. Note transition from assemblage of R3 I/S + kaolinite to monomineralic assemblage in fine fraction of R1 1-water I/S. Lower figure: patterns from random preparations. Arrow show 2M<sub>1</sub>-specific peaks. Note absence of 2M<sub>1</sub> peaks in all size fractions and pure 1M<sub>d</sub> polytype in the finest size fraction. K = kaolinite, C = calcite, Q = quartz, A = analcime.

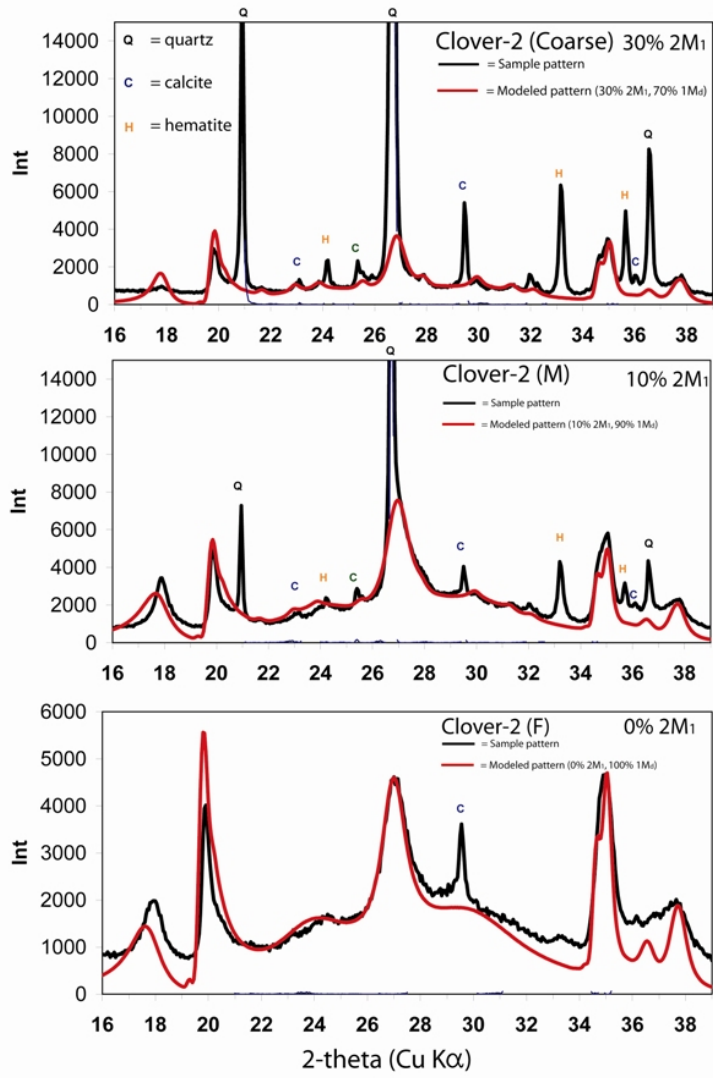


**Figure 6-12:** HD-TEM lattice fringe images of clays from the main detachment (Secret 4-2). Thin (5-10 nm) packets of ordered illite-smectite (both R1 and R3) are visible together with 8-20 nm packets of illite. Kinked layers, indicative of strain, are visible in the upper image.

The detachment fault at Clover Hill strikes NNE and dips gently to the WNW at 20-40°. The outcrop is in a road cut on Nevada Rt 231 that is now heavily eroded, (see Figure 6.13, a photo of the fresh outcrop can be found in Mueller & Snoke, 1993). The fault surface is undulatory on a meter scale and dips gently to the west; measured strikes range from 015 to 040. The gouge zone is approximately 1 meter thick, and is a thick, hard (resists thumbnail indentation), reddish-brown illitic gouge with visible alteration near the bottom of the gouge to white kaolinite (see Figure 6.13). The gouge zone can be separated into three regions, both visible at outcrop and in XRD patterns. The XRD patterns from oriented mounts indicate that the upper portion of the gouge (sample Clover-2) is primarily discrete illite, whereas the lower third is heavily altered to kaolinite (samples Clover-1 and Clover-3, see Figure 6.13). The diffraction pattern of the illite that dominates the upper two-thirds of the gouge (Clover-2) shows that it has some smectite interlayers, based on the low-angle shoulder to the illite (001) peak and the broadening of the (002) peak upon glycolation; the lack of shifting of the (001) or (002) peaks upon glycolation indicates that the amount of interlayered smectite is no more than a few percent. Diffraction patterns from oriented mounts (Clover-1 & Clover-3, Fig 13) of clays in the lower third of the gouge indicate that it is predominantly kaolinite with only a very small amount of illite and discrete smectite. The illitic material (Clover-2) was separated into size fractions and random powder diffraction patterns were collected (see Figure 6.14). The percentage of the 2M<sub>1</sub> polytype decreases with decreasing grain size and for the finest size fraction, the 2M<sub>1</sub> polytype is undetectable, e.g. the fine fraction consists entirely of 1M<sub>d</sub> illite and a small amount of calcite, indicating a transformation of detrital 2M<sub>1</sub> illite to authigenic 1M<sub>d</sub> illite.



**Figure 6-13:** Outcrop photo and XRD patterns from the gouge zone at Clover Hill. of the  $<2 \mu\text{m}$  fraction of each region visible in the photo. A.) Outcrop photo of the main detachment, showing three sub-regions sampled. B.) Closeup of outcrop showing sub-regions sampled. C.) XRD patterns from each region of the gouge dashed line is air-dried pattern, solid is glycol-solvated. Clover-2 is illite, Clover-3 and Clover-1 are predominantly kaolinite.



**Figure 6-14:** XRD patterns from random preparations of size fractions of Clover-2 and illite polytype quantifications done using WILDFIRE. Note the clear transition from a mixture of the 2M<sub>1</sub> and 1M<sub>d</sub> polytypes in the coarse and medium fractions and the pure 1M<sub>d</sub> nature of the fine fraction.

## Illite Ar-Ar ages

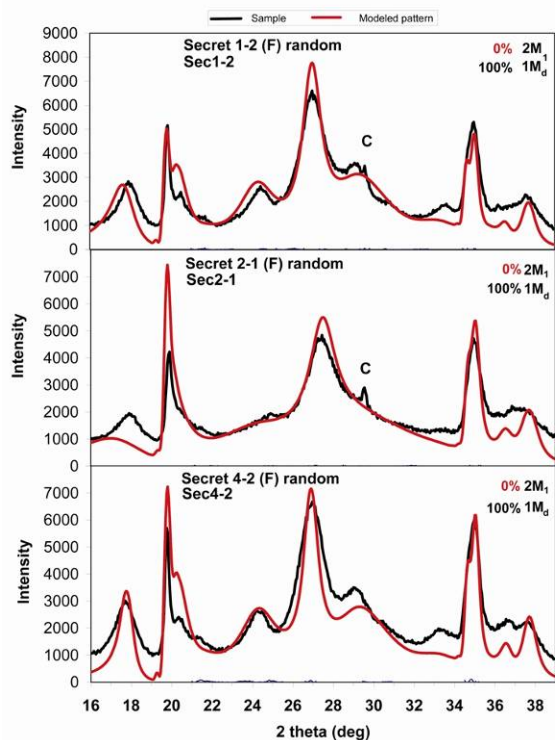
### Secret Pass

Spectra for Ar-Ar ages of the authigenic 1-water, illite-rich illite-smectite isolated in the Secret Pass samples are given in Figure 6.15, along with clay polytype quantification using WILDFIRE calculated XRD patterns. All the spectra have an initial near-zero-age component, reflecting  $^{39}\text{Ar}$  released during irradiation due to recoil. The percentage of Ar released during the initial 'recoil' fraction ranges from 30-40% in all size fractions, consistent with fine-grained clays having a high surface-to-volume area and thus potential for  $^{39}\text{Ar}$  loss during irradiation. The Ar-release spectra for the main detachment and the high-angle normal fault (Secret 1-2 and Secret 4-2) do not have classic 'plateaus' due to the effects of Ar recoil (Dong, 1995), but both have a near-plateau component in the later degassing steps, consistent with XRD observations that both samples are functionally monomineralic authigenic 1-water illite-rich illite-smectite of one age population that grew between 11.5 and 12.3 Ma. The sample from the upper detachment (Secret 2-1) has a 'stair-step' profile often observed in dating of authigenic illite in fault gouge (e.g. van der Pluijm et al., 2001). The stair-step geometry of the release spectra is a function of samples being composed of mixtures of grains of different ages and grain sizes. It is apparent that the Ar ages for the fine fractions of Secret 1-2 and Secret 4-2 are very close to the age of the authigenic illite-smectite growing in the fault gouge of the detachment system during fault slip, if not dating it directly. The Secret 2-1 age of 13.8 +/- 0.15 Ma is thus a maximum age for slip on the upper detachment.

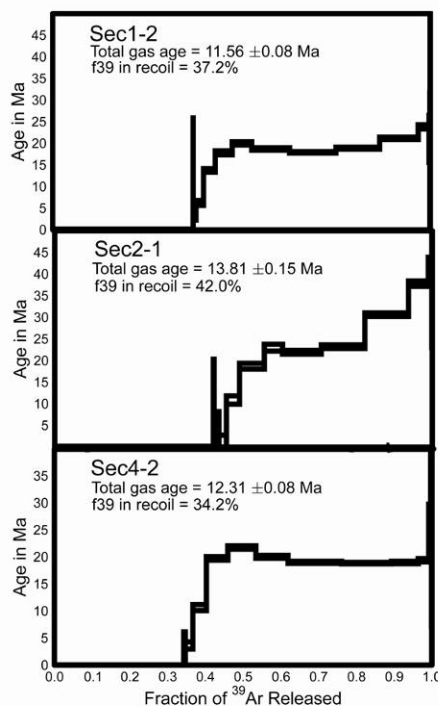
### Secret Pass muscovite and biotite ages

Coexisting muscovite and biotite 'fish' were dated from a footwall mylonite collected 800

Polytype quantifications for finest size fractions of clay gouges at Secret Pass



Ar-Ar ages for finest size fractions of clay gouges at Secret Pass



**Figure 6-15:** Illite polytypism quantifications and  $^{40}\text{Ar}$ - $^{39}\text{Ar}$  illite step-heating spectra from fine-grained sized fractions of the three gouges (<0.05 m) from the three detachment faults exposed at Secret Pass. Note samples are very fine-grained and thus have a large recoil fraction of Ar during degassing. The total gas ages for the three samples are similar and indicate both the high-angle and the main low-angle detachment were active within a time interval of 0.75 +/- 0.16 Ma.

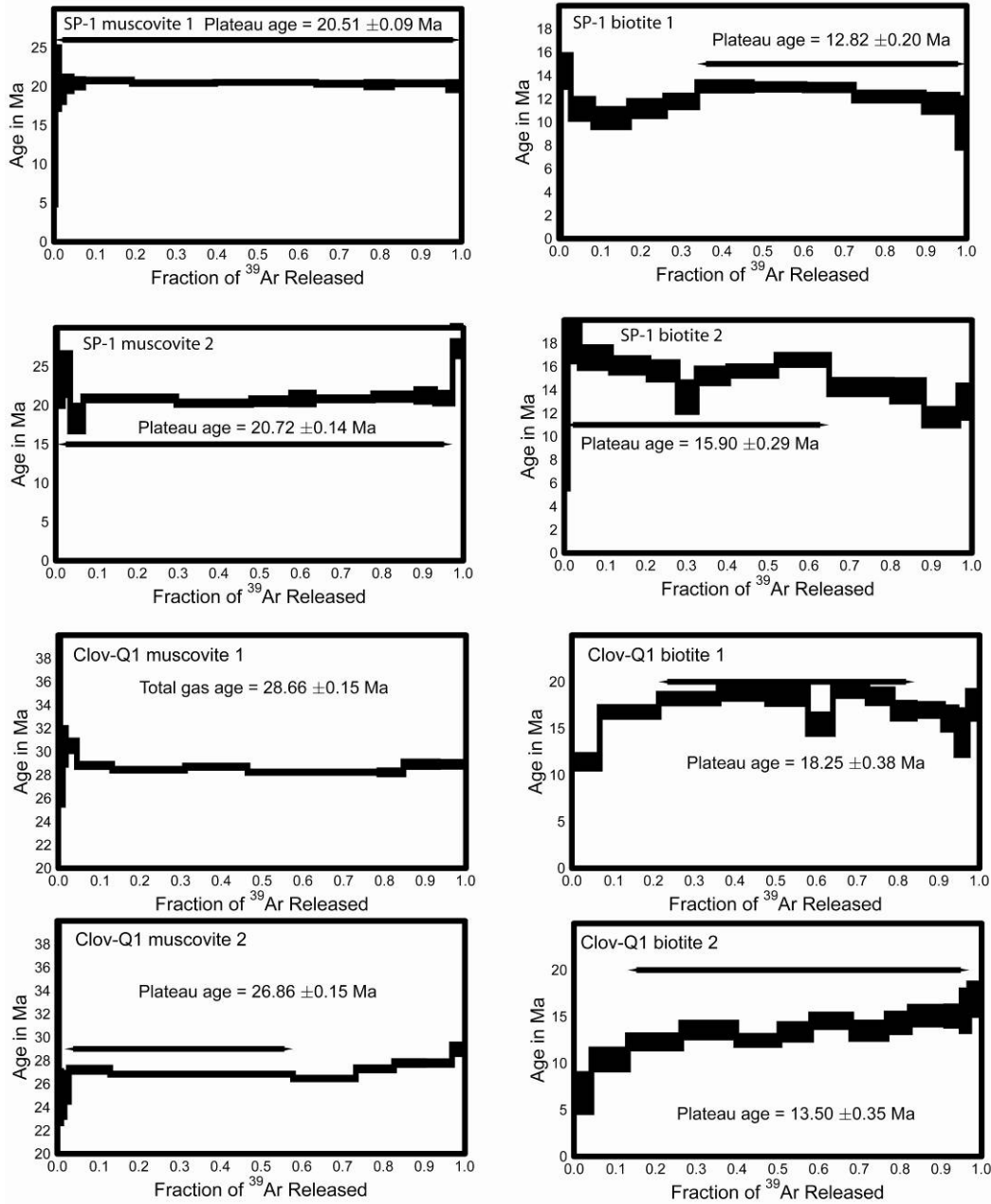


m east of Secret-4 and ~150 m below the detachment surface in true section (locality FW-1). Ar release spectra are shown in Figure 6.16. The muscovites give good plateau ages of 20.5 +/- 0.1 Ma and 20.7 +/- 0.1 Ma. The biotites do not have good plateaus and give apparently conflicting ages of 12.8 +/- 0.2 Ma and 15.9 +/- 0.3 Ma. As these release spectra do not have good plateaus, and the ages are significantly different for two mica grains taken from the same hand sample, it is possible that the biotites were variably altered or that each grain has a different closure temperature. Petrography indicates that both quartz and feldspar deformed plastically, indicating deformation above 500 °C (Voll, 1976, Simpson, 1985). As the micas clearly were in equilibrium with mylonitic deformation at temperatures above the blocking temperature of muscovite (375 +/- 25 °C) and biotite (275 +/- 25 °C) (Hames & Bowring, 1994), the Ar-Ar ages of both the muscovite and biotite are interpreted as cooling ages and not the age of mylonization.

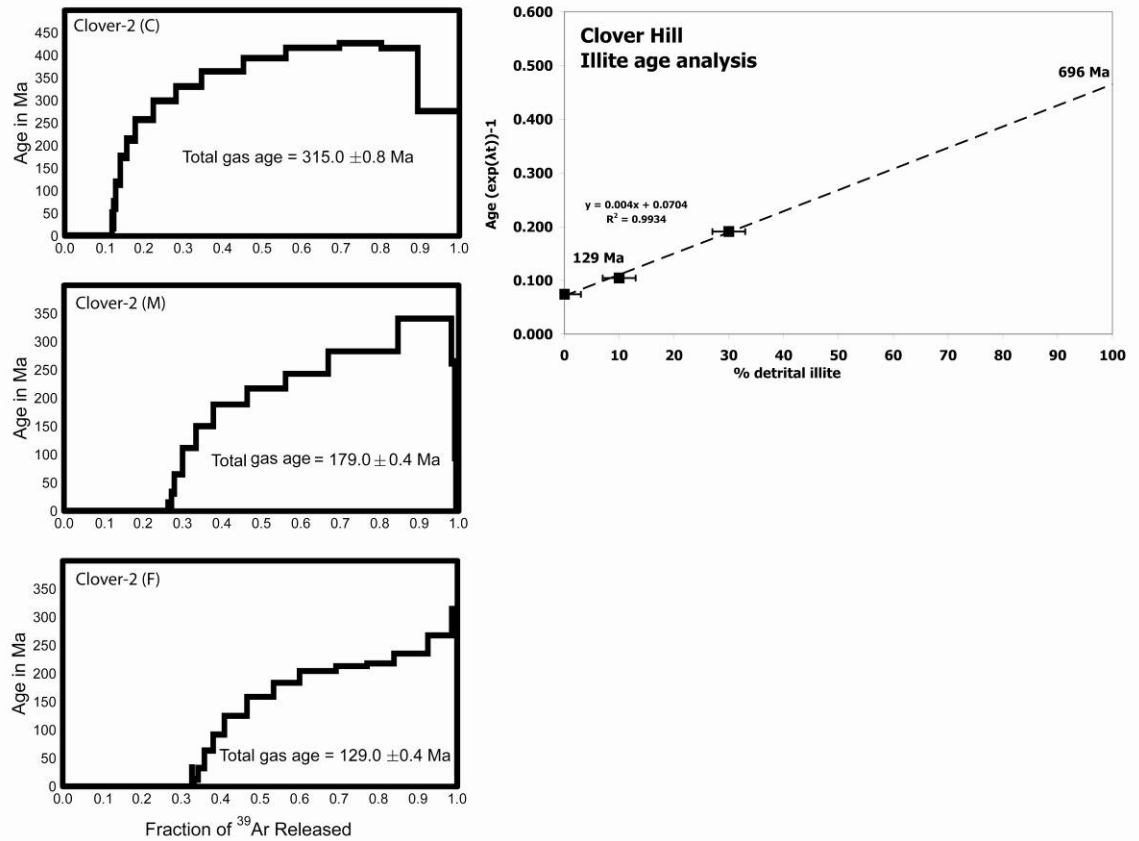
Clover Hill ages

Gouge ages

The Clover Hill gouge ages are old and thus reflect the presence of detrital 1M<sub>d</sub> illite in the gouge. The gouge mineralogy appeared to be a transition from predominantly 2M<sub>1</sub> illite in the coarse fraction (2.0 – 0.4 µm) to almost pure 1M<sub>d</sub> in the finest size fraction (<0.05 µm), but the Ar-Ar ages for the various size fractions ranged from 315 Ma to 129 Ma, indicating a Cretaceous age for the finest fraction illite in the gouge (see Figure 6.17). The most logical explanation for the old ages is that Miocene conglomerates in the hangingwall, which are almost entirely carbonate clasts sourced from the Woods Hills (Snoke, pers. comm.), contained significant amounts of 1M<sub>d</sub> illite. As WILDFIRE© modeling indicates that the <0.05 µm fraction of the gouge is essentially pure 1M<sub>d</sub> illite



**Figure 6-16:**  $^{40}\text{Ar}$ - $^{39}\text{Ar}$  illite step-heating spectra for coexisting muscovite and biotite from quartzite mylonites at Secret Pass (locality SP-1, Figure 6.2) and at Clover Hill (sample Clov-Q1). Note excellent plateau ages for the muscovite and more irregular spectra for the biotites. Ages clearly point to Early-Mid- Miocene cooling from  $375 \pm 25 \text{ }^\circ\text{C}$  to  $275 \pm 25 \text{ }^\circ\text{C}$ (?) at Secret Pass and Late Oligocene to Mid- Miocene cooling at Clover Hill.



**Figure 6-17:**  $^{40}\text{Ar}$ - $^{39}\text{Ar}$  illite step-heating spectra for size fractions of illitic gouge at Clover Hill (Clover-2) and illite age analysis plot. The plot indicates an apparent Cretaceous for the 1M<sub>d</sub> illite in the gouge. 'Age' is probably the result of mixing of two or more 1M<sub>d</sub> illite age populations, one detrital and one authigenic in the gouge. See text for discussion.

and has a Cretaceous age, the presence of a detrital  $1M_d$  illite population in the gouge, derived from the Paleozoic limestone clasts is probable. The Cretaceous age would indicate a mixture of a Paleozoic population and a Miocene population. The Ar-Ar spectra of the  $<0.05 \mu\text{m}$  fraction supports this interpretation in that the profile steps up continuously indicating a mixture of age populations, and the oldest age steps indicate degassing of material that is Late Paleozoic in age (Figure 6.17). The footwall marble mylonites are clean and contain no clay. Indeed, XRD work on crushed clasts of the hangingwall conglomerates indicates significant amounts of illite present in the clasts.

#### Clover Hill muscovite and biotite ages

Coexisting muscovite and biotite 'fish' were dated from a footwall mylonite collected 200 m east of the gouge outcrop and ~50 m below the detachment surface in true section. Ar release spectra are shown in Figure 6.16. The muscovites give good plateau ages of  $28.7 \pm 0.2 \text{ Ma}$  and  $26.9 \pm 0.2 \text{ Ma}$ . The biotites do not have good plateaus and give apparently conflicting ages of  $18.3 \pm 0.4 \text{ Ma}$  and  $13.5 \pm 0.4 \text{ Ma}$ . As the Clover Hill biotite release spectra do not have good plateaus, it is possible that the Clover Hill biotites were variably altered, or that each grain has a separate blocking temperature. These ages clearly date Oligocene exhumation of the Ruby Mountain complex at Clover Hill, agreeing with previous interpretations (Mueller & Snoke, 1993, McGrew et al., 2000).

#### **Interpretation and discussion**

Key to the success of brittle fault dating is demonstrating that we have isolated and dated the authigenic illitic phase growing during deformation. As both the upper

detachment and hangingwall normal faults at Secret Pass juxtapose rocks that themselves contain more than one generation of an illitic phase, careful clay characterization of both wall rocks and gouge is required for these rocks. The footwall, hangingwall and gouge in the upper detachment and high-angle upper-plate fault all contain illite-rich I/S or discrete  $1M_d$  illite. The hangingwall at the high-angle normal fault and the upper detachment contain detrital  $R1$  I/S (50% I in I/S) and authigenic  $R0$  2-water I/S (80-85% I in I/S). The footwall at the high-angle normal fault and the upper detachment contain detrital  $2M_1$  illite and authigenic  $1M_d$  illite; the latter presumably formed during diagenesis of the Diamond Peak shales. The illite in the gouges, however, is recognizably distinct from the  $1M_d$  or illite-rich I/S in the wall rocks, as it is a 1-water I/S (see Figure 6.9). A further test of this hypothesis by dating illite in the footwall by the  $2M_1$ - $1M_d$  method and the hangingwall shale by the illite-in-illite-smectite method is ongoing. This work will date the growth of the  $1M_d$  populations in the footwall and hangingwall.

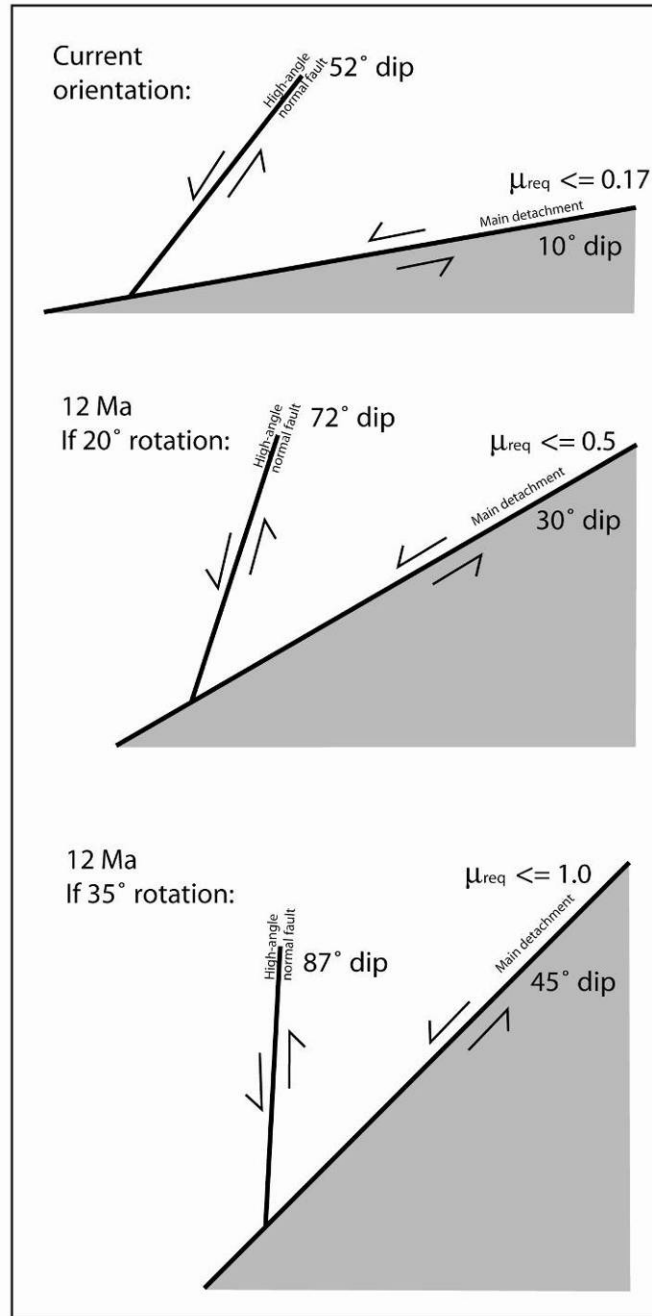
The illite-rich nature of authigenic I/S places constraints on the conditions of authigenic clay growth in the gouge. The smectite-illite transition has been extensively studied in sedimentary basins, (e.g., Hower et al., 1976, Ahn & Peacor, 1986, Freed & Peacor, 1989a, 1989b, Li et al., 1997; Kim et al., 2004; Huggett & Cuadros, 2005; Sandler & Saar, 2007). While the transformation is generally agreed to be a prograde diagenetic series of reactions below 200 °C., numerous factors besides temperature can control the progress of the reactions. Time (Pytte & Reynolds, 1989),  $K^+$  availability (Huang et al., 1993), water/ rock ratio (Whitney, 1990), and microbial interactions (Kim et al., 2004) have all been shown to affect reaction progress. As discrete un-illitized smectite can form in soils and has been shown to be stable to temperatures as high as ~135 °C (Aplin et al., 2006), and authigenic ordered I/S to form in evaporative environments at

temperatures < 45 °C (Sandler & Saar, 2007), constraints on the temperature of I/S growth are thus poor, save that clay growth occurred < 200 °C and probably between 50 and 150 °C. Several possible sources exist for components of the authigenic illite-smectite, either the authigenic I/S is forming by illitization of I/S in the hangingwall shales, or by dissolution and reprecipitation of illite derived from the footwall Diamond Peak shales. At Secret-4 the footwall at the sampled outcrop is a carbonate mylonite, and not Diamond Peak shale, but the outcrop is only 20 meters updip from outcrops of Diamond Peak in the hangingwall, and thus Diamond Peak shale could have been smeared along the fault surface at the sampled location. I/S formation by illitization of detrital R1 I/S seems likely in the high-angle normal fault and the upper low-angle detachment, as a transition can be observed from top to bottom across the outcrop. The origin of the illite in the main detachment may be different. Field relations of the illite-rich layer and the smectite-rich layer do not indicate any clear age relationship, and thus it is possible that the smectite-rich layer is derived from alteration of the hangingwall silicified tuffs, while the I/S is derived from retrograde alteration of smeared Diamond Peak shale.

The  $^{40}\text{Ar}$ - $^{39}\text{Ar}$  ages of illite in the finest size fractions from the gouges at Secret Pass, which date the age of fault gouge formation, show that the last major period of activity on the main detachment fault occurred at 12.3 Ma and that the last major period of activity on the hangingwall high-angle normal fault occurred at 11.5 Ma. The upper detachment was last active at some point after 13.8 Ma. These remarkably similar ages indicate that the two low-angle faults and the high-angle normal fault were all active at the same time as part of a kinematically linked fault system. If the currently low-angle detachments had been active at an angle 'typical' of a high-angle normal fault (55-70°), then became inactive and passively rotated to their low dips (10°), the rotation associated with the passage of a 'rolling hinge' would have occurred in <800,000 years, an average rotation

rate of  $1^\circ/20,000$  years. Such a rapid rotation, associated with a  $40^\circ$  flexure of the upper crust would surely have resulted in pervasively deformed footwall rocks, which are not observed.

A simpler explanation for our illite ages is that both the high-angle upper-plate normal fault and both low-angle detachments were all active at the same time at about 12 Ma. The simultaneous activity of normal faults with contrasting orientations places clear constraints on the dip of both faults at the time of slip. The current dip of the high angle fault ( $52^\circ$ ) is at the low end of the typical dips observed for high-angle normal faulting ( $45\text{-}70^\circ$ , Jackson & White, 1989). The dip of the high-angle normal fault therefore could have been no more than  $20^\circ$  higher than current, as both faults were active at the same time, the low-angle detachments also could not have rotated more than  $20^\circ$ . Assuming a maximum  $20^\circ$  rotation of the footwall to account for a  $52\text{-}72^\circ$  range in possible dips the dip of the current low-angle detachments would rise to no more than  $\sim 30^\circ$  at the time of fault slip (Figure 6.18). If the high-angle fault had been rotated much more than  $20^\circ$  since the time of active slip, it would have been sub-vertical at the time of slip, a mechanically very unfavorable orientation for listric normal fault initiation and growth. We thus suggest that the degree of post-slip rotation of the normal faults in the Secret Pass area is  $<20^\circ$ . A  $<20^\circ$  post-faulting rotation of the Secret Pass detachment system is consistent with geometric constraints on the angle of initiation of the high-angle listric fault in the upper plate. It is thus concluded that the low-angle detachments in the Secret Pass area were active in the brittle regime at dips  $<30^\circ$  around 12 Ma, which is inconsistent with the passage of a 'rolling hinge' with large footwall rotation in the Secret Pass area. The fault ages are consistent with large-magnitude extension, but accommodating extension on a primary low-angle normal fault surface as envisaged by

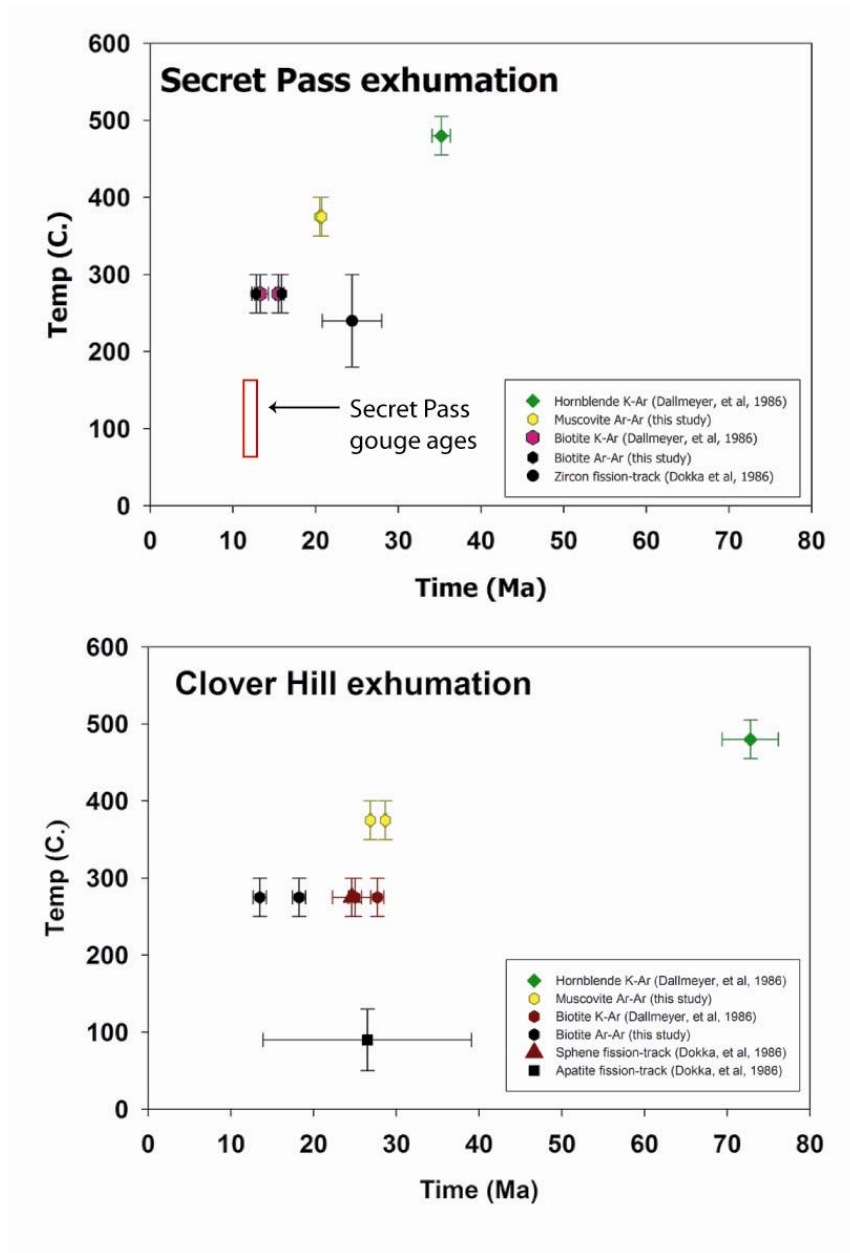


**Figure 6-18:** Sketch showing constraints on the amount of post-faulting footwall rotation on dips of Secret Pass faults active at 12 Ma, and thus the dips at which the detachment fault system was active. The Ar-Ar ages of the gouge demonstrate that both the low- and high-angle faults were active at roughly the same time around 12 Ma. A rotation of 20° both permits slip on the main detachment, and allows the upper-plate normal fault to initiate at 70°, a feasible angle for a high-angle normal fault. 35° of post-faulting rotation requires that the high-angle normal fault initiate at an unfeasibly high angle.



Spencer, (1984), rather than with large-magnitude flexural rotation of the footwall, as envisaged by Wernicke & Axen, (1988), Buck (1998), or Hamilton, (1998). It is important to note that our ages do not constrain the dip of the detachment at its initiation in the Middle Eocene, but rather the dip at the final stages of detachment evolution during the Middle Miocene.

The higher-temperature muscovite and biotite Ar-Ar ages provide important constraints on the rate of exhumation of older portions of the detachment system. The mylonites at Secret Pass clearly formed earlier than 20 Ma, as they record amphibolite-facies conditions during mylonization, significantly higher than the Ar-Ar closure temperature of muscovite. Figure 6.19 shows the time-temperature history of the footwall from the Secret Pass area from this study and previously published data. The coexisting muscovite and biotite ages, together with the gouge ages at Secret Pass define a coherent time-temperature path extending from the onset of exhumation in the latest Eocene and extending to the middle-late Miocene, with an increase in cooling rate between biotite closure at 13-15 Ma and gouge formation at ~12 Ma. However, the zircon fission track age of Dokka et al. (1986) from the same locality as our muscovite and biotite ages does not fall on the time-temperature path defined by our multiple Ar-Ar ages and more recently reported ages from the western Ruby Mountains (Colgan et al., 2006, Gifford et al., 2007). Apatite fission-track ages from the Harrison Pass pluton, found in the footwall 20 km to the south along strike recording cooling of the footwall through ~110 °C from 12 to 14 Ma (Colgan & Metcalf, 2006). Instead of mid-late Miocene exhumation documented by several isotopic systems, the zircon fission-track age implies very rapid exhumation during the late Oligocene. We submit that the Dokka et al. zircon fission-track age is erroneous in some way and is not geologically meaningful. Assuming a geothermal gradient of 25°C/km, a fault dip of 30° and growth



**Figure 6-19:** Exhumation histories for Secret Pass and Clover Hill as inferred from data from this study and published sources. Gouge ages, and muscovite ages are from this study. Biotite ages are from this study and Dallmeyer et al., (1986). Hornblende Ar-Ar ages are from Dallmeyer et al., (1986), Zircon, sphene and apatite fission-track ages are from Dokka et al., (1986).

conditions for illite-rich I/S of  $\sim 100$  °C, the detachment fault accommodated 22 km of slip between 20.5 Ma and 12.0 Ma, implying a net slip rate of  $2.6 \pm 0.7$  mm/yr and a strain rate on the order of  $10^{-14}$  s $^{-1}$ . As the age relationships of the brittle faults prohibit a dip  $>30^\circ$  for the main detachment at the time of gouge growth, the dip of the detachment could be as low as current values,  $\sim 10^\circ$ . In that case, the mean fault slip rate would have been  $7.5 \pm 2.0$  mm/yr. Similar mean slip velocities on the order of mm/yr have been reported from other core complex detachment faults (Carter et al., 2006, Haines & van der Pluijm, 2008, Chapter 4). The muscovite and biotite ages from Clover Hill offer a less clear picture of the exhumation history, but demonstrate that the area cooled through  $375 \pm 25$  °C at around 26-28 Ma, consistent with previous studies (McGrew et al., 2000).

## Conclusions

Authigenic 1-water layer illite-rich I/S grew in fault gouge from the Secret Pass area of the Ruby Mountains, Nevada. The authigenic illite in the gouge is distinguishable from illite and illite-smectite derived from the wall rocks on the basis of mineralogy and hydration state as determined by XRD and TEM analyses. An interpretation that illite-smectites and  $1M_d$  illite in both the gouge and the wallrock are the products of a common post-faulting diagenetic event is unlikely, as the rocks do not show any evidence for a post-faulting hydrothermal event, and the area has been exhumed post-12 Ma, and not buried. Ar-Ar ages of the authigenic illite in 2 detachment faults and a high-angle fault that soles into the detachment system show that the high-angle normal fault and the main detachment fault formed from  $\sim 11.5$  Ma to  $\sim 12.3$  Ma, and that gouge in the upper

detachment formed <13.8 Ma. Exhumation of the Ruby Mountain metamorphic core complex in the vicinity of Secret Pass occurred during the middle-late Miocene, fault slip averaged 2.6 +/- 0.25 mm/yr and the last major period of fault slip was around 12 Ma. These gouge ages indicate that all three faults were active at the same time and thus active in a kinematically-linked system. As the high-angle fault normal fault currently dips 52°, but may have been as much as 70°, the low-angle faults that now dip ~10° (and never exceeded <35°) are all of the same age. We conclude that the low dip of the detachment fault required by the gouge ages argues against a 'rolling hinge' evolution for the Secret Pass area, but instead shows that the main detachment fault was active at shallow dip in the brittle regime.

### **Acknowledgments**

This work was supported by NSF grant EAR 0738435, exploratory funding by a GSA Grant-in-Aid to Haines, and the Scott Turner Fund at the University of Michigan. We are grateful to Chris Hall and Marcus Johnson for assistance with Ar-dating, to Carl Henderson for maintenance of the EMAL X-ray facility at Michigan and to Anja Schleicher for assistance with microscopic characterization.

## References

- Abers, G. (1991) Possible seismogenic shallow-dipping normal faults in the Woodlark-D'Entrecasteaux extensional environment, Papua New Guinea. *Geology* 19, pp.1205-1208.
- Ahn, J., & Peacor, D., (1986). Transmission and analytical electron microscopy of the smectite-to-illite transition. *Clays and Clay Minerals*, 34, pp. 165-179.
- Anderson, E. (1942) The mechanics of faulting and dyke formation with respect to Britain: Edinburgh, Oliver and Boyd, 191 pp.
- Aplin, A., Matenaar, I., McCarty, D. & van der Pluijm, B. (2006). Influence of mechanical compaction and clay mineral diagenesis on the microfabric and pore-scale properties of deep-water Gulf of Mexico mudstones. *Clays and Clay Minerals* 54, No. 4, pp. 500-514.
- Axen, G. (2004) Mechanics of low-angle normal faults. *In* Rheology and deformation of the lithosphere at continental margins, Karner, et al., eds. Columbia, pp. 45-91.
- Axen, G., & Bartley, J., (1997). Field tests of rolling hinges: Existence, mechanical types, and implications for extensional tectonics. *J. Geophysical Research B* 102, pp. 20,515-20,537.
- Brady, R. (2002) Very high slip rates on continental extensional faults: New evidence. From U-Th/(He) dating. *Earth and Planetary Sciences Letters* 197, pp. 95-104.
- Byerlee, J. (1978) Friction of rocks. *Pure and Applied Geophysics*, 16, pp. 615-626.
- Buck, W. (1988) Flexural rotation of normal faults, *Tectonics* 7, pp. 959-973.
- Carter, T., Kohn, B., Foster, D., & Gleadow, A. (2004). How the Harcuvar Mountains became cool: Evidence from apatite (U/Th)/He thermochronometry. *Geology*, 32, pp. 985-988.
- Carter, T., Kohn, B., Foster, D., Gleadow, A., & Woodhead, J., (2006). Late stage evolution of the Chemehuevi and Sacramento detachment faults from apatite (U/Th)/He thermochronometry – Evidence for mid-Miocene accelerated slip. *Geological Society of America Bulletin* 118, 689-709.
- Chery, J. (2002) Core complex mechanics: From the Gulf of Corinth to the Snake Range. *Geology* 29, pp. 439-442.
- Collettini, C. & Sibson, R. (2001) Normal faults, normal friction? *Geology* 29, pp. 927-930.

- Colgan, J., & Metcalf, J. (2006) Rapid middle Miocene unroofing of the southern Ruby Mountains, Nevada: *Geological Society of America Abstracts with Programs*, v. 38, no. 7, p. 417.
- Coney, P. (1980) Cordilleran metamorphic core complexes: An overview. *in: Cordilleran metamorphic core complexes*, Crittenden, M. et al. eds. *Geological Society of America Memoir* 153, pp. 7-31.
- Coyle, D. & Wagner, G., (1998). Positioning the titanite fission-track partial annealing zone. *Chemical Geology* 149, pp 117-125.
- Dallmeyer, R., Snoke, A., & McKee, E. (1986). The Mesozoic-Cenozoic tectonothermal evolution of the Ruby Mountains, East Humboldt range, Nevada: A cordilleran metamorphic core complex. *Tectonics* 5, pp. 931-954.
- Dalla Torre, M., Stern, W., & Frey, M., (1994). Determination of white mica polytype ratios: Comparison of different XRD methods. *Clay Minerals* 29, 717-726.
- Damon, P. & Shafiqullah, M., (2006). K-Ar ages of fault rocks along the Catalina detachment fault, Tanque Verde Ridge, Rincon Mountains, Arizona. *Arizona Geological Survey Contributed Report* CR-06-A. Arizona Geological Survey, Tuscon, AZ, 18 pp.
- Dokka, R., Mahaffie, M., & Snoke, A. (1986) Thermochronologic evidence of major tectonic denudation associated with detachment faulting, northern Ruby Mountains, East Humboldt Range, Nevada. *Tectonics* 5, pp. 995-1006.
- Dong, H., Hall, C., Peacor, D., & Halliday, A., (1995). Mechanism of argon retention in clays revealed by laser  $^{40}\text{Ar}$ - $^{39}\text{Ar}$  dating. *Science* 267, pp. 355-359.
- Dong, H., Hall, C., Halliday, A., & Peacor, D., (1997).  $^{40}\text{Ar}$ - $^{39}\text{Ar}$  dating of late-Caledonide (Acadian) metamorphism and cooling of K-bentonites and slates from the Welsh Basin, UK. *Earth and Planetary Sciences Letters* 150, pp. 337-351.
- Eyidogan, H. & Jackson, J. (1985), A seismological study of normal faulting in the Demirci, Alasehir and Gediz earthquakes of 1969-1970 in western Turkey: Implications for the nature and geometry of deformation in continental crust, *Journal of the Royal Astronomical Society* 81, 569-607.
- Freed, R. & Peacor, D., (1989a). Diagenesis and the formation of illite-rich I/S crystals in Gulf Coast shales: A TEM study of clay separates. *J. Sedimentary Petrology*. 62, pp 220-234.
- Freed, R., & Peacor, D., (1989b). Variability in temperature of the smectite/illite reactions in Gulf Coast sediments. *Clay Minerals* 24, pp. 171-180.
- Gifford, L., Newman, V., Foster, D., Howard, K., & Donelick, R., (2007). Quantifying Eocene and Miocene extension in the Sevier hinterland with implications for mineral and energy resources in northeastern Nevada. *Geological Society of America Abstracts with Programs*, 39, p. 226.

- Hames, W., & Bowring, S., (1994). An empirical evaluation of the argon diffusion geometry in muscovite. *Earth and Planetary Sciences Letters* 124, pp. 161-167.
- Hamilton, W., (1988). Detachment faulting in the Death Valley region, California and Nevada. *U. S. Geological Survey Bulletin* 1790, pp. 51-85.
- Howard, K. (1980) Metamorphic infrastructure in the northern Ruby Mountains, Nevada, *in: Cordilleran metamorphic core complexes*. Crittenden, M. et al. eds., *Geological Society of America Memoir* 153, pp. 335-347.
- Hower, J, Eslinger, E., Hower, M. & Perry, E., (1976). Mechanism of burial metamorphism of argillaceous sediment: Mineralogical and chemical evidence. *Geological Society of America Bulletin* 87, pp. 725-737.
- Huang, W, Longo, J., & Peaver, D., (1993). An experimentally derived kinetic model for smectite-to-illite transformation and its use as a geothermometer. *Clays and Clay Minerals* 41, pp. 162-177.
- Huggett, J., & Cuadros, J., (2005). Low-temperature illitization of smectite in the late Eocene and early Oligocene of the Isle of Wight (Hampshire Basin), UK. *American Mineralogist* 90, pp. 1192-1202.
- Jackson, J. (1991). Active normal faulting and crustal extension, *in Continental extensional tectonics*, eds. Coward, M, Dewey, J., & Hancock, P.. pp. 3-18
- Jackson, J. & White, N. (1989) Normal faulting in the upper continental crust: observations in regions of active extension. *J. Structural Geology* 11, pp. 15-36.
- John, B. (1987) Geometry and evolution of a mid-crustal extensional fault system, *in Continental Extensional Tectonics*, eds., Coward, M. et al., *Geological Society Special Publication* 28 pp. 313-336.
- Li, G., Peacor, D., & Coombs, D., (1997). Transformation of smectite to illite in bentonite and associated sediments from Kaka Point, New Zealand: Contrasts in rate and mechanism. *Clays and Clay Minerals* 45, pp. 54-67.
- Lyons, J., & Snellenburg, J., (1970). Dating faults. *Geological Society of America Bulletin* 82, 1749-1752.
- Kim, J., Dong, H., Seabaugh, J., Newell, S. & Eberl, D., (2004) Role of microbes in the smectite-to-illite transition. *Nature* 303, pp. 830-832.
- Kralik, M., Klima, K., & Riedmueller, G., (1987). Dating fault gouges. *Nature* 327, 315-317.
- Livaccari, R. (1995) Large-magnitude extensional deformation in the South Mountains metamorphic core complex, Arizona; evaluation with paleomagnetism. *Geological Society of America Bulletin* 107, pp. 877-894.

- McGrew, A. & Snee, L. (1994)  $^{40}\text{Ar}/^{39}\text{Ar}$  thermochronologic constraints on the tectonothermal evolution of the northern East Humboldt Range metamorphic core complex, Nevada. *Tectonophysics* 238, pp. 425-450.
- McGrew, A., Peters, M. & Wright, J. (2000) Thermobarometric constraints on the tectonothermal evolution of the East Humboldt Range metamorphic core complex, Nevada. *Geological Society of America Bulletin* 112, pp. 45-60.
- Miller, J. & John, B., (1999). Sedimentation patterns support low-angle normal faulting, southeastern California and western Arizona. *Geological Society of America Bulletin* 111, pp. 1350-1370.
- Miller, E., Dumitru, T., Brown, R., & Gans, P., (1999) Rapid Miocene slip on the Snake Range-Deep Creek fault system, east-central Nevada. *Geological Society of America Bulletin* 111, pp. 886-905.
- Mueller, K., & Snoke, A. (1993) Progressive overprinting of normal fault systems and their role in Tertiary exhumation of the East Humboldt-Woods Hills metamorphic complex, northeast Nevada. *Tectonics* 12, pp. 361-371.
- Peters & Wickham, (1994) Petrology of upper-amphibolite-facies marbles from the East Humboldt Range, Nevada, USA: Evidence for high-temperature retrograde hydrous volatile fluxes at mid-crustal levels. *J. Petrology* 35, pp. 205-238.
- Pytte, A., & Reynolds, R., (1989). The thermal transformation of smectite to illite. *In: Thermal histories of sedimentary basins: Methods and case histories.* Naeser, N., McCulloh, T, eds., New York, Springer-Verlag. P 133-140.
- Reynolds, S., & Lister, G., (1987). Structural aspects of fluid-rock interactions in detachment zones. *Geology* 15, pp. 362-6.
- Reynolds, R. C., Jr. (1993). WILDFIRE - A computer program for the calculation of three-dimensional powder X-ray diffraction patterns for mica polytypes and their disordered variations, Hanover, New Hampshire.
- Reynolds Jr., R., & Reynolds III., R.C., (1996). NEWMOD-for-Windows. The Calculation of One-Dimensional X-ray Diffraction Patterns of Mixed-layered Clay Minerals, Hanover, New Hampshire.
- Rietbrock, A., Tiberi, C., Scherbaum, F. & Lyon-Caen, H. (1996) Seismic slip on a low-angle normal fault in the Gulf of Corinth: Evidence from high-resolution cluster analysis of microearthquakes. *Geophysical Research Letters* 23, pp. 1817-1820.
- Sandler, A. & Saar, H., (2007). R > 1 -type illite-smectite formation at near-surface temperatures. *Clay Minerals* 42, pp. 245-253.
- Scholz, C. (2002). The mechanics of earthquakes and faulting. Cambridge University Press, Cambridge, 471 pp.
- Snoke, A. (1980) Transition from infrastructure to superstructure in the Northern Ruby Mountains, Nevada. in: Crittenden, M. et al., (1980) eds. Cordilleran



metamorphic core complexes *Geological Society of America Memoir* 153, pp. 287-333.

- Snoke, A. & Lush, A. (1984) Polyphase deformation Mesozoic-Cenozoic deformational history of the northern Ruby Mountains-East Humboldt Range, Nevada. In: Western geological excursions, Lintz, J. ed., *Geological Society of America Annual Meeting Guidebook* volume 4, Reno Nevada, Mackay School of Mines, pp. 232-260.
- Snoke, A. & Howard, K. (1984) Geology of the Ruby Mountains-East Humboldt Range, Nevada: A Cordillerian metamorphic core complex. In: Western geological excursions, Lintz, J. ed., *Geological Society of America Annual Meeting Guidebook* volume 4, Reno Nevada, Mackay School of Mines, pp. 260-303.
- Spencer, J., & Chase, C. (1989) Role of crustal flexure in initiation of low-angle normal faults and implications for evolution of the Great Basin *J. Geophysical Research* B 94, pp. 1765-1775.
- Solum, J., van der Pluijm, B. & Peacor, D. (2003) Influence of phyllosilicate mineral assemblages, fabrics and fluids on the behavior of the Punchbowl Fault, southern California. *J. Geophysical Research* B 108, doi:10.1029/2002JBG001858.
- Solum, J., van der Pluijm, B. & Peacor, D. (2005) Neocrystallization, fabrics and age of clay minerals from an exposure of the Moab Fault, Utah. *J. Structural Geology* 27, pp. 1563-1576.
- Solum, J., & van der Pluijm, B. (2007). Reconstructing the Snake River/Hoback Canyon segment of the Wyoming thrust Belt through direct dating of fault rocks. In *Whence the Mountains? Inquiries into the Evolution of Orogenic Systems: A volume in Honor of Ray Price. Geological Society of America Memoir* 433.
- Sroden, J. (1980). Precise identification of illite/smectite interstratifications by X ray powder diffraction. *Clays and Clay Minerals*, 28, 401-411
- Stewart, J., (1983) Extensional tectonics in the Death Valley area, California: Transport of the Panamint Range structural block 80 km northward. *Geology* 11, pp. 153-157.
- Tullis, T. & Weeks, J., (1986), Constitutive behavior and stability of frictional sliding of granite, *Pure and Applied Geophysics.*, 124, 10-42.
- van der Pluijm, B., Hall, C., Vrolijk, P., Pevear, D., & Covey, M., (2001). The dating of shallow faults in the Earth's crust. *Nature* 412, pp. 172-175.
- van der Pluijm, B., Vrolijk, P., Pevear, D., Hall, C., & Solum, J., (2006). Fault dating in the Canadian Rocky Mountains: Evidence for late Cretaceous and early Eocene orogenic pulses. *Geology* 34, pp. 837-840.

- Voll, G., (1976). Recrystallization of quartz, biotite and feldspars from Erstfeld to the Leventina Nappe, Swiss Alps, and its geological significance. *Schweiz. Mineral. Petrogr. Mittl.*, 56: 641-647.
- Wernicke, B. (1995) Low-angle normal faults and seismicity: A review. *J. Geophysical Research B* 100, pp. 20,159-20,174.
- Wernicke, B. & Axen, G. (1988) On the role of isostasy in the evolution of low-angle normal fault systems. *Geology* 16, pp. 848-851.
- Whitney, G., (1990) Role of water in the smectite to illite reaction. *Clays and Clay Minerals* 38, pp. 343-350.
- Wright, J. & Snoke, A. (1993) Tertiary magmatism and mylonization in the Ruby-East Humboldt metamorphic core complex, northeastern Nevada: U-Pb geochronology and Sr, Nd and Pb isotope geochemistry. *Geological Society of America Bulletin* 105, pp. 935-952.
- Yan, Y., van der Pluijm, B., & Peacor, D., (2001). Deformational microfabrics of clay gouge, Lewsi Thrust, Canada: A case for fault weakening from clay transformation. In *The nature and tectonic significance of fault zone weakening* edited by R.E. Holdsworth et al.. *Geological Society Special Publication* 186, pp. 103-112.
- Yin, A. (1989) Origin of regional rooted low-angle normal faults: A mechanical model and its tectonic implications, *Tectonics* 8, pp. 469-482.

## CHAPTER 7: CONCLUSIONS

The research on fault gouge that is described in this dissertation is motivated by the weak behavior of many active faults relative to predictions from rock mechanics (e.g. Kanamori & Anderson, 1975; Lachenbruch & Sass, 1980; Mount & Suppe, 1987; Zoback, 2000; Chéry et al., 2001) and the ability to apply chronologic analysis of gouge to test regional and kinematic hypotheses. The thesis work focuses on transformation of clay minerals and fabrics in brittle fault zones, as clay minerals can be a significant factor in the weakening of faults (e.g. Rutter, 1986; Vrolijk & van der Pluijm, 1999; Rutter et al., 2001; Warr & Cox, 2001).

The dissertation has four objectives that are connected by the focus on clay-rich fault rocks: 1.) Characterize the clay mineralogy and, in particular, clay mineral transformations in natural faults from a variety of geological environments, such as low-angle normal faults (Basin and Range), thrust faults (Spanish Pyrenees) and high-angle normal faults (Rwenzori Mts, East African Rift, Uganda). 2.) Quantify fabric intensities in clay gouges relative to fabrics in other phyllosilicate-rich rocks 3.) To develop the techniques of dating authigenic mineralization in clay gouge, particularly through illite polytype quantification. 4.) Directly date fault gouges to test kinematic and regional hypotheses, such as orogenic wedge evolution and in-sequence thrusting (Spanish Pyrenees) and the dip of low-angle detachments (Ruby Mountains).

The studies in the dissertation have identified patterns of clay mineral transformations and assemblages in fault gouges that are repeated both in space and time. The dissertation developed a robust illite age analysis method of fault dating using illite polytypism, and established that both end-member ages extrapolated from mixtures of illite populations are geologically meaningful. The ages of authigenic clay growth in fault zones were used to test models of regional kinematic evolution in both a compressional environment (Spanish Pyrenees) and in an extensional environment (Ruby Mountains, Nevada).

### **Mineral transformations in clay-rich gouges**

This dissertation describes clay gouges in a variety of geological environments (extensional – Chapters 2, 3, 4, 6, and Appendix A) and compressional (Chapter 5). Most gouges sampled, with the exception of the Rwenzori samples in Appendix A, show evidence of extensive mineral transformations. The presence of mineral transformations in faults of differing ages, tectonic environments and mineralogies indicates that extensive clay mineral transformations in gouges are the norm, rather than the exception. Chapter 2 presents a detailed study of clay mineral transformations in one class of faults, low-angle normal faults, and demonstrates that mineral transformations are ubiquitous. Two main types of mineral transformations are observed: the transformation of detrital chlorite to lower-temperature chlorite-smectite and smectite phases or very low-temperature Mg-rich phases such as sepiolite, palygorskite, lizardite and talc, and the transformation of detrital illite and/or feldspar to the low-temperature  $1M_0$  polytype of illite. These are further developed in Chapter 4 that documents the transformation of  $2M_1$  illite or muscovite to  $1M_0$  illite in gouge from the Sierra Mazatàn

metamorphic core complex; Chapter 5 documents the pervasive transformation of detrital  $2M_1$  illite or muscovite in wall-rock shales and metapelites to authigenic  $1M_d$  illite in fault gouges with illite-rich wallrocks; and Chapter 6 documents the growth of 1-water illite-rich illite-smectite derived from the probable illitization of more smectite-rich illite-smectite in gouge from the Ruby Mountains.

### **Fabric intensities in clay gouges**

Chapter 3 presents fabric intensity data as measured using X-ray texture goniometry (XTG) from most of faults examined mineralogically in Chapter 2. The data demonstrate that clay-rich fault rocks, regardless of tectonic environment, mineralogy or age, have uniformly weak fabrics when compared with fabric intensities of phyllosilicate-rich rocks from other geological environments (such as deep-compaction fabrics in shales and slates; e.g., Day-Stirrat et al., 2007)). Fabric intensity does not vary systematically with either the dominant clay mineral in gouge or tectonic environment, rather giving a fabric intensity of 2-3 MRD (a statistical unit of intensity) for most clay-rich gouges. Fabric intensities from authigenic gouges described in Chapter 2 are very similar to gouges that are detrital in origin (i.e., reworked host rock). The systematic lack of strong fabrics in gouges indicates that, if clay fabric anisotropy is responsible for fault weakening by maintaining a different pressure regime in the gouge zone than in the surrounding wallrock (Rice, 1992), no evidence of such fabric anisotropy is preserved. Thus, either clay-rich gouges do not develop sufficient anisotropy to affect the state of stress in the fault core relative to that of the wall rock, or the development of anisotropy is transient and is not preserved. Fabric intensity data from experimental gouges demonstrate that fabric strength is a function of shear stress and the applied normal stress during shear.

Normal stress without shear produces only very weak fabrics and fabrics do not strengthen with increasing normal stress. The experimental data demonstrate that March strain behavior, which produces fabrics by passive rotation of grains in response to increasing applied normal stress, is unlikely for geological materials with the low porosities and high differential stresses observed in conditions at depths below 1-2 km. Shear strain is required to generate the fabrics observed in fault gouges, but the maximum fabric intensity that can be generated by shear strain is still very low.

### **Methodology for dating illitic gouges**

Two robust approaches for dating illite-rich gouges have been proposed. The first approach, the “illitization of illite-smectite approach”, extrapolates the age of authigenic illite in illite-smectite mixtures by quantitative modeling of XRD patterns and Ar-Ar ages of several size fractions, each containing a different ratio of detrital and authigenic material (van der Pluijm et al., 2001). The second technique, which is developed here, the “polytype quantification approach”, extrapolates the age of the low-temperature  $1M_d$  polytype of illite that is the authigenic phase in fault gouges by quantitative modeling of the relative abundances of the low-temperature  $1M_d$  and high-temperature  $2M_1$  polytypes of illite in several size fractions of a gouge, each with its own ratio of authigenic and detrital illite (Ylagan, 2002; Solum et al., 2005). Both techniques produce reliable ages for the authigenic component of clay gouges, while the ages of the detrital component also give geologically meaningful results. Chapter 4 demonstrates the precision of the polytype quantification approach by quantifying a set of artificial mixtures of  $2M_1$  and  $1M_d$  illite and then applying the approach to a temporally well-constrained fault. The Ar-Ar ages and modeling demonstrate that the gouge is a binary mixture of an authigenic 14.9 Ma component and a detrital 18.9 Ma component. The chapter provides

a rigorous best-fit approach to the quantification methodology and offers validation for the assumption of a binary mixture of detrital and authigenic illite in natural gouges. The chapter also demonstrates that the age of the detrital component is geologically meaningful. Regional use of this is made in Chapter 5, which describes the dating of a suite of thrust faults in the southern Pyrenean fold-and-thrust belt (see below), demonstrating that the detrital component of the gouge, derived from wall rocks in the southern Pyrenean foreland basin, dates from the upper Paleozoic Hercynian orogeny that is exposed in the central portion of the range.

Chapter 6 describes a third approach for dating authigenic illite or illite-smectite in gouges that are so dominated by the authigenic phase that the detrital clay phase is absent, or gouges where authigenic illite is formed by a transformation of a non-clay phase, typically feldspar. The chapter demonstrates that high-speed centrifugation and careful characterization of the resulting material by XRD methods, aided by quantitative modeling of the XRD patterns, produces a size fraction of entirely authigenic material that can be dated by Ar-Ar methods. This approach brings quantitative methods to earlier fault dating attempts (Lyons & Snellenburg, 1970; Kralick et al., 1987), which assumed that a very fine-grained fraction extracted from gouge is exclusively authigenic material. The method presented in Chapter 6 will expand the range of gouges that can potentially be dated by Ar-Ar methods, as illitic gouges that form from the alteration of detrital feldspar can now also be dated reliably.

### **Use of fault gouge ages to test regional hypotheses**

The age of authigenic illite in fault gouge records the time at which the fault gouge formed, and thus, the timing of major fault slip. By establishing the age of several faults

in a region, the relative timing of faulting in an orogen can be established, permitting the direct testing of kinematic hypotheses, such as the critical thrust wedge hypothesis of a continuously internally-deforming mountain belt (Dahlen et al., 1984) and in-sequence foreland faulting (Dahlstrom, xxxx). Chapter 5 dates a suite of thrusts in the south-central and south-eastern Pyrenean fold-and-thrust belt and identifies both in-sequence thrusting and out-of-sequence thrusting, and, in conjunction with previous constraints of the ages of other thrusts, identifies several pulses of orogenic activity: 1.) Late Cretaceous, 2.) Latest Paleocene-Early Eocene, 3.) Middle-Late Eocene and 4.) Oligocene. The Middle-Late Eocene deformation event represents thrusting at many structural levels in the range, both inboard and outboard, and demonstrates that the orogen was behaving as a critical wedge during the Middle and Late Eocene. The ages also demonstrate the presence of young thrusting in the central portion of the range, which was previously inferred to satisfy balanced section constraints (Muñoz, 1992), and explain otherwise puzzling apatite-fission-track ages (Fitzgerald et al., 1999; Gibson et al., 2007). The fault ages indicate that thrusting in the Pyrenees occurred episodically in a series of pulses, where multiple thrusts were active coevally. The critical wedge scenario contrasts with faulting in the eastern segment of the orogen, where in-sequence, foreland progression over a time interval of ~20 Ma is found.

Chapter 6 addresses the kinematics of metamorphic core complexes and in particular whether detachment faults slip at low angles ( $\leq 30^\circ$ ) in the brittle regime. By dating both the main detachment and a high-angle normal fault with a typical listric fault geometry, and establishing that both were active coevally, the geometrical relationship between the two faults requires that the main detachment must have been active at a dip at or below  $30^\circ$ . The chapter adds the Ruby Mountains to a growing list of low-angle normal faults



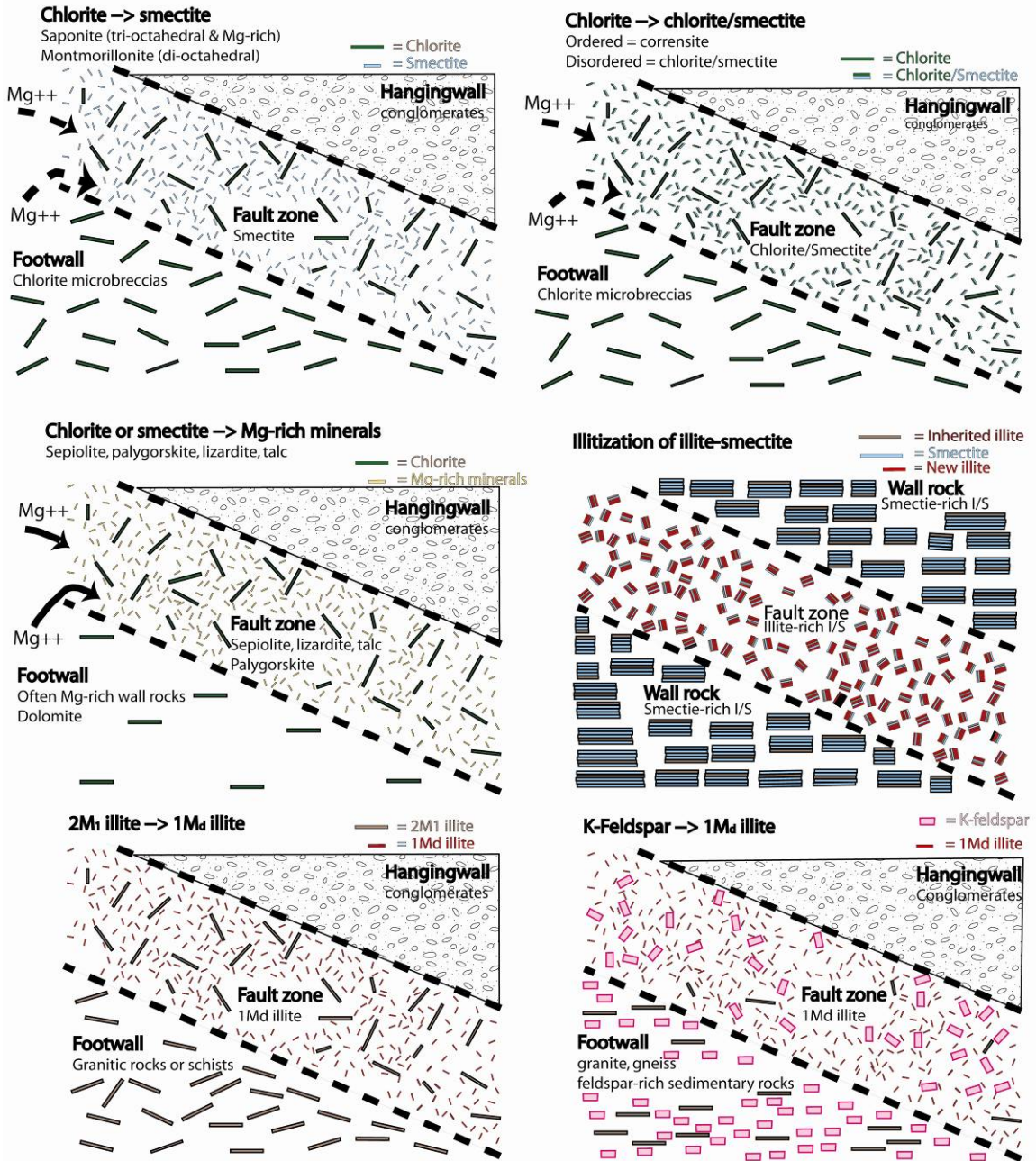
that slip at angles  $<30^\circ$  (e.g. John & Foster, 1993, Livaccarri et al., 1993; Miller & John, 1999), which contrasts with models for fault rotation to explain low-angle faulting.

### **Concluding remarks**

The research in this dissertation emphasizes the key role of clay minerals in brittle faults and contributes to an understanding of clay mineral transformations in brittle fault rocks. Its major contribution is the recognition of near-ubiquitous clay mineral transformations in gouges and uniformly weak fabrics of fault rocks regardless of the tectonic environments. Clay-rich gouges that are detrital in origin (gouges derived from cataclasis of wall rocks without significant transformations) are locally preserved in faults, but they are the exception rather than the norm. Detrital clay gouges require unusual conditions, either in local declivities and cavities in the wallrock, as the result of incomplete transformation of host rock, or gouge formation at very shallow levels of the crust at temperatures too low for authigenic clay growth. Fabric intensities of detrital and authigenic gouges are equally weak, indicating that clay mineral transformations do not significantly affect permeability anisotropy, although they almost certainly act to decrease bulk fault zone permeability.

Two main sets of clay mineral transformations are observed in low-angle normal fault gouges: transformation related to the breakdown of chlorite into lower-temperature tri-octahedral Mg-Fe phyllosilicates, 'retrograde diagenesis' or localized alteration to very Mg-rich assemblages at temperatures  $<150^\circ\text{C}$ , and those that result in the growth of authigenic illite or illite-rich illite-smectite by the breakdown of detrital muscovite or feldspar; see Figure 7-1. These transformations may be thought of as 'chlorite-

breakdown' and 'illite-growth' transformations. At least five clay minerals have been found growing authigenically in the faults sampled in this study:  $1M_d$  illite, illite-rich illite-smectite, smectite (montmorillonite or saponite), corrensite (ordered chlorite-smectite) and disordered chlorite-smectite. Other Mg-rich phases have been found, but are rare relative to these five. Chlorite has not been found as an authigenic mineral, but is common as a detrital phase in gouge. The upper and lower temperature stability limits for these phases place crude constraints on the temperature of formation of clay-rich gouges. Ordered illite-smectite can form at temperatures as low as 45 °C and can persist to temperatures of 140 °C (Freed & Peacor, 1989; Sandler & Sarr, 2007). Discrete smectite can form in soils and can persist to 135 °C (Aplin et al., 2006). Corrensite can form at temperatures between 60-70 °C and 160 °C (Helmold & van der Kamp, 1984; Chang et al., 1986).  $1M_d$  illite can form at 100 +/- 10 °C (Pevear et al., 1997) and the upper limits on the temperature of growth are uncertain, but certainly below 200 °C. (Meunier, 2005). Disordered chlorite-smectite can form in soils and at temperatures below those at which corrensite grows. It is observed as a retrograde alteration product from corrensite and thus forms below the 60 - 160 °C range for corrensite (Nieto et al., 2005). The temperature stability limits are approximate, but all indicate that clay gouges form below 200 °C and probably below 150-175 °C. Their absence in samples from the Rwenzori Mountains (Appendix A) show that a minimal temperature of 50 °C is required, so clay-rich gouges as a class of fault rock form at temperatures between 50 and 175 °C. Previous temperature estimates for the formation of gouges have ranged as high as 230 °C, but did not assess the detrital versus authigenic nature of the components that were interpreted to be in equilibrium (e.g., Damon & Shafiqullah, 2006). The presence of shear-sense indicators and geometry of clay fabrics in most gouges indicate that gouge formation is contemporaneous with deformation, and not the result of post-slip hydrothermal alteration. The presence of



**Figure 7-1:** Schematic figure showing the six mineral transformations found in low-angle normal faults as in this study. Note that only the localized transformation of chlorite or smectite to Mg-rich minerals requires the input of significant  $Mg^{++}$  in solution, whereas the chlorite → chlorite/smectite and chlorite → smectite transitions can result from addition of  $Mg^{++}$ , but do not require it (Hayman, 2006). The illite growth reactions do not require the addition of significant  $K^+$ , except for the illitization of illite-smectite.

water is essential to gouge formation, evidenced by the abundance of hydrous phases relative to wall rocks in most clay-rich gouges. The local preservation of unaltered, relatively anhydrous chlorite-dominated detrital gouge assemblages <300 m along strike from abundantly hydrated gouge assemblages (see Chapter 2), indicates that fluid flow in fault zones is highly anisotropic on a 100's of meters scale. The uniformity of fluid flow along the fault dictates the degree to which clay mineral transformations might occur, but detailed along-fault characterization of the variability of clay mineralogy along exposed faults is required to assess this hypothesis.

#### Summary and wider applications

The results presented in the dissertation demonstrate the widespread occurrence of authigenic clay minerals in clay-rich fault gouges, regardless of tectonic environment. The results highlight the extensive role of mineral transformations in faults in low-temperature environments (<200 °C), commonly thought to be dominated by cataclastic processes. The observed clay mineral transformations in gouges fall into two broad categories, chlorite breakdown transformations, and growth of 1M<sub>d</sub> polytype of illite. Fabric intensities as measured by XTG show that fault gouges have uniformly weak fabrics in comparison with phyllosilicate-rich rocks from other geologic environments. The 1M<sub>d</sub> polytype of illite in gouge can reliably be dated by Ar-Ar methods, recording the age of deformation, while the age of the 2M<sub>1</sub> polytype reflects the age of the provenance area. Direct dating of illitic gouges will become a powerful geochronological technique for structural geologists as it can be brought to bear on a large variety of regional-scale kinematic and tectonic questions.

## References

- Aplin, A., Matenaar, I., McCarty, D. & van der Pluijm, B. (2006). Influence of mechanical compaction and clay mineral diagenesis on the microfabric and pore-scale properties of deep-water Gulf of Mexico mudstones. *Clays and Clay Minerals* 54, No. 4, pp. 500-514.
- Casciello, E., Cesarano, M., & Cosgrove, J., (2004). Shear deformation of pelitic rocks in a large-scale natural fault. *In: Flow processes in faults and shear zones, eds: Alspo, G., Holdsworth, R., McCaffrey, K., & Hand, M., Geological Society of London Special Publications* 224, pp. 113-125.
- Chéry, J., Zoback, M. D., & Hassani, R., (2001). An integrated mechanical model of the San Andreas fault in central and northern California. *J. Geophysical Research, B* 106, pp. 22,051-22,066.
- Chang, H., Mackenzie, F., & Schoonmaker, J., (1986). Comparison between the diagenesis of dioctahedral and tri-octahedral smectite, Brazillian offshore basins. *Clays and Clay Minerals* 34, pp. 407-423.
- Dahlen, F., Suppe, J., & Davis, D. (1984). Mechanics of fold-and-thrust belts and accretionary wedges. *J. Geophysical Research B* 89, pp. 10,087-10,101.
- Dahlstrom, C., (1970). Structural geology of the eastern margin of the Canadian Rocky Mountains. *Bulletin of Canadian Petroleum Geology* 18 p. 332- 406.
- Damon, P. & Shafiqullah, M., (2006). K-Ar ages of fault rocks along the Catalina detachment fault, Tanque Verde Ridge, Rincon Mountains, Arizona. *Arizona Geological Survey Contributed Report* CR-06-A. Arizona Geological Survey, Tuscon, AZ, 18 pp.
- Fitzgerald, P., Muñoz, J., Coney, P., & Baldwin, S., (1999). Asymmetric exhumation across the Pyrenean orogen: implications for the tectonic evolution of a collisional orogen. *Earth and Planetary Sciences Letters* 173, pp. 157-170.
- Freed, R., & Peacor, D., (1989). Variability in temperature of the smectite/illite reactions in Gulf Coast sediments. *Clay Minerals* 24, pp. 171-180.
- Gibson, M., Sinclair, H., Lynn, G. & Stuart, F., (2007). Late-to-post-orogenic exhumation of the Central Pyrenees revealed through combined thermochronological data and modeling. *Basin Research* 19, pp. 323-334.
- Helmold, K., & van der Kamp, P., (1984). Diagenetic mineralogy and controls on albitization and laumontite formation in Paleogene arkoses, Santa Inez Mountains, California. *In: Clastic diagenesis., eds: McDonald, D., Surdham, R., American Association of Petroleum Geologists Memoir* 27 pp. 239-276.

- Kanamori, H. and Anderson, D. L. (1975). Theoretical basis of some empirical relations in seismology. *Bulletin of the Seismological Society of America* 65, pp. 1073-1095.
- Kralik, M., Klima, K., Riedmueller, G., (1987). Dating fault gouges. *Nature* 327, pp. 315-317.
- John, B. & Foster, D., (1993). Structural and thermal constraints on the initiation angle of detachment faulting in the southern Basin and Range: The Chemehuevi Mountains case study. *Geological Society of America Bulletin* 105, pp. 1091-1108.
- Lachenbruch, A. H. and Sass, J. H. (1980). Heat flow and energetics of the San Andreas fault zone. *Journal of Geophysical Research B* 85, pp. 6185-6222.
- Liavaccari, R., Geissman, J. & Reynolds, S., (1993). Paleomagnetic evidence for large-magnitude low-angle normal faulting in a metamorphic core complex. *Nature* 351, pp. pp. 56-59.
- Lyons, J. B., and Snellenburg, J., (1971). Dating faults. *Geological Society of America Bulletin* 82, pp. 1749-1752.
- Meunier, A., (2005). Clays. Springer-Verlag, Berlin, 472 pp.
- Miller, J., & John, B., (1999). Sedimentation patterns support seismogenic low-angle normal faulting, southeastern California and western Arizona. *Geological Society of America Bulletin* 111, pp. 1350-1370.
- Mount, V. and Suppe, J. (1987). State of stress near the San Andreas fault: Implications for wrench tectonics. *Geology* 15, pp. 1143-1146.
- Muñoz, J., (1992) Evolution of a continental collision belt: ECOURS-Pyrenees crustal balanced cross-section. In *Thrust Tectonics*, McClay, K., ed, Chapman and Hall, New York, pp. 235-246.
- Nieto, F., Pilar Mata, M., Baulez, B., Giorgetti, G., Árkai, P., & Peacor, D., (2005). Retrograde diagenesis, a widespread process on a regional scale. *Clay Minerals* 40, pp. 93-104.
- Pevear, D., Vrolijk, P., & Longstaffe, F., (1997). In: Proceedings of Geofluids II '97,(Queens University Belfast) Conference Volume, eds: Hendry, J., Carey, P., Parnell, P., Ruffell, A. & Worden, R. , ISBN 1-897799-83-7. 374-377
- Rice, J. (1992). Fault stress states, pore pressure distributions, and the weakness of the San Andreas Fault. In: *Fault Mechanics and Transport Properties of Rocks; a Festschrift in Honor of W. F. Brace* (edited by Evans, B. and Wong, T.-F.). Academic Press, San Diego, CA, pp. 475-503.
- Rutter, E., Maddock, R., Hall, S., & White, S., (1986). Comparative microstructures of natural and experimentally produced clay-bearing fault gouges. *Tectonophysics* 124, pp. 3-29.

- Rutter, E., Holdsworth, R., & Knipe, R., (2001). The nature and significance of fault-zone weakening, an introduction. *Geological Society of London, Special Publications* 186, pp. 1-11.
- Sandler, A. & Saar, H., (2007). R >1 –type illite-smectite formation at near-surface temperatures. *Clay Minerals* 42, pp. 245-253.
- Schleicher, A., van der Pluijm, B., Solum, J., & Warr, L., (2006). Origin and significance of clay-coated fractures in mudrock fragments of the SAFOD borehole (Parkfield California). *Geophysical Research Letters* 33, L16313, doi:10.1029/2006GL026505, 2006
- Solum, J., van der Pluijm, B. & Peacor, D. (2003) Influence of phyllosilicate mineral assemblages, fabrics and fluids on the behavior of the Punchbowl Fault, southern California. *J. Geophysical Research B* 108, doi: 10.1029/2002JBG001858.
- Solum, J., van der Pluijm, B. & Peacor, D. (2005) Neocrystallization, fabrics and age of clay minerals from an exposure of the Moab Fault, Utah. *J. Structural Geology* 27, pp. 1563-76.
- Solum, J., van der Pluijm, B., (2007). Reconstructing the Snake River/Hoback Canyon segment of the Wyoming thrust Belt through direct dating of fault rocks. In *Whence the Mountains? Inquiries into the Evolution of Orogenic Systems: A volume in honor of Ray Price. Geological Society of America Memoir* 433, pp. 183-196.
- van der Pluijm, B., Hall, C., Vrolijk, P., Pevear, D., Covey, M., 2001. The dating of shallow faults in the Earth's crust. *Nature* 412, pp. 172–175.
- Vrolijk, P. and van der Pluijm, B. (1999) Clay gouge. *J. Structural Geology* 21, 1039-1048.
- Warr, L., & Cox, S., (2001). Clay mineral transformations and weakening mechanisms along the Alpine Fault, New Zealand. In: *The nature and significance of fault zone weakening. Geological Society, London, Special Publications* 186, pp. 85-103.
- Ylagan, R. Kim, C., Pevear, D., Vrolijk, P., 2002. Illite polytype quantification for accurate K-Ar determination. *American Mineralogist* 87, 1536-1545.
- Zoback, M. D., (2000). Strength of the San Andreas fault. *Nature* 405, 31-32.

## **APPENDIX A: CLAY MINERAL ASSEMBLAGES IN FAULT GOUGES FROM THE RWENZORI MOUNTAINS, UGANDA**

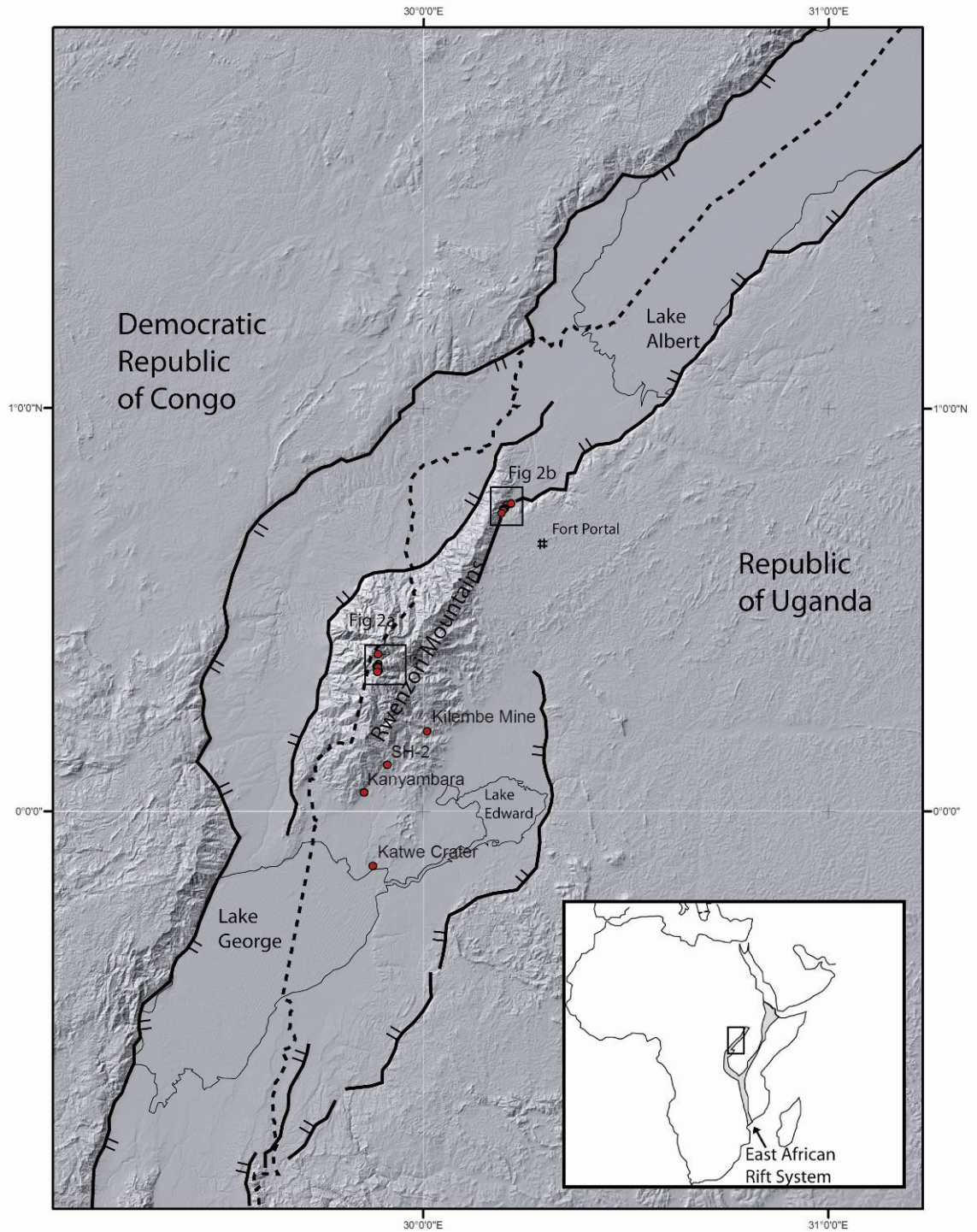
To explore the nature of clay mineral transformations in gouge in high-angle normal faults associated with a major continental rift, the East African Rift System, as opposed to the extensional setting of the western Cordillera, a suite of gouge samples from the Rwenzori Mountains of Uganda was collected and characterized. The gouge samples come from a network of normal and strike-slip faults associated with the exhumation of the Rwenzori rift shoulder block to an unusually high elevation within the East African Rift System. The mechanism by which horst blocks are uplifted to ~5,000 m in an extensional regime is poorly understood (Bahat & Mohr, 1987; Ebinger et al., 1991). An attempt to understand the mechanisms for extreme rift shoulder uplift requires understanding and characterizing the fault networks along which that uplift is accommodated, which was the aim of this study. However, the exposed gouge samples were not yet sufficiently exhumed to allow meaningful dating of the timing of displacement.

### **Regional introduction**

The Rwenzori Mountains are an unusually high, 100 x 50 km, NE-SW trending, fault-bounded block of Precambrian gneiss in the western branch of the East African Rift



Valley in south-western Uganda and the eastern Democratic Republic of Congo. The range can be pictured as a very high 'peninsula' of rift shoulder that is surrounded by rift valley basins on three sides (Figure A-1). The massif rises more than 4 km above the half-graben rift basin floor immediately to the NW and SE, and exhibit ~5 km of total uplift, most of which was accommodated in the last 2.5 Ma (*Rosendahl, 1987, MacPhee et al., 2006, Bauer et al., 2007*). The top of the block is a strongly-dissected, gently SE-dipping paleosurface ranging from 4,500 m to 5,100 m elevation (*Whittow, 1966*). The kinematics of rifting in the East African Rift Valley, and in particular, mechanisms for the extreme uplift (to ~5000 m) of some blocks along the rift margin, are the subject of considerable interest to the structural and geodynamic community. Extension 'should' thin the Earth's crust by reducing elevation in the area being extended, rather than increase it. Although local uplift of rift shoulders due to heating of the crust from below and unloading by faulting is a common and well-described phenomenon (e.g., *Rosendahl, 1987, Jackson & White, 1989*), elevations of rift shoulders are typically only on the order of 1,000 - 2,000 m. above the valley floor (*Erbinger, 1989*). By contrast, the Rwenzoris are uplifted more than 4,000 m above the floor of the rift. Such a magnitude of uplift is impossible to explain by the mechanisms of flexural uplift in response to extensional unroofing, and must require some other process to explain the uplift of hundreds of square kilometers to elevations normally associated with major compressional mountain belts, such as the Andes and the Himalayas. Understanding the mineralogy and the thermal conditions of the fault systems, and eventual timing of major deformation responsible for uplift is therefore a critical step toward understanding the mechanism for the remarkable uplift of the Rwenzoris.

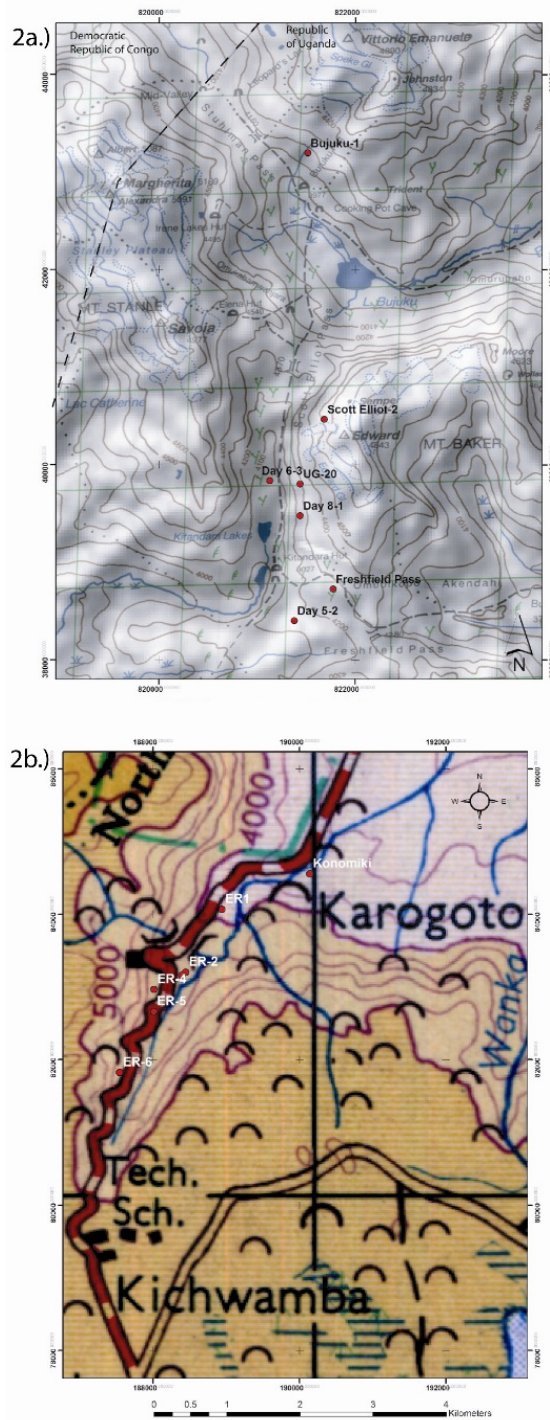


**Figure A-1:** Shaded relief 90 DEM of the Rwenzori Mountains with borders and major rift-flank faults. Red dots indicate locations of faults sampled in this study. Boxes show areas of Figures A-2a and A-2b.

Uplift of the Rwenzori Mountains and the rift flanks of the East African rift valley in general is primarily due to tectonic uplift along range-bounding faults, and not by climate-driven exhumation. Multiple low-temperature thermochronometers from the Rwenzori mountains do not record the thermal effects of post-20 Ma rifting (*MacPhee, et al., 2005, Bauer et al., 2006*). (U-Th)/He ages for zircon (recording the time at which a rock cooled below  $\sim 180$  °C) range from 407 to 238 Ma and apatite fission-track ages (recording the time at which a rock cooled below  $\sim 110$  °C) range from 141 to 89 Ma (*Bauer et al., 2007, unpub*). (U-Th)/He ages for apatite (recording time since a rock cooled below  $\sim 70$  °C) range from 238 Ma to 19 Ma, although most ages are between 30 and 100 Ma (*MacPhee, 2006, Bauer et al 2007*). The old (U/Th)/He ages of apatite, assuming normal geothermal gradients ( $35$  C°/km), imply that no more than 2 km of material has been eroded off of the currently 5 km high Rwenzori Mts during the post 20 Ma uplift associated with the opening of the western branch of the East African Rift. Similarly old apatite fission-track ages are known from rift shoulder rocks further south along the rift margin in Malawi and record regional cooling prior to Neogene rift opening (*van der Beek et al., 1998*).

## **Methods**

23 samples from 19 brittle faults exposed in the Rwenzori Mountains and 3 residual soils were studied by XRD (X-ray diffraction) to identify mineral transformations related to faulting (see Figures A-1 & A-2 for sample locations). The clay-sized fraction ( $<2\mu\text{m}$ ) of the gouges was separated in water using Stokes settling. The clay-sized fraction was then further centrifuged into coarse ( $2\mu\text{m} - 0.2 \text{ m } \mu\text{m}$ ), medium ( $0.2 \mu\text{m} - 0.05 \mu\text{m}$ ) and fine ( $<0.05 \mu\text{m}$ ) size fractions. As clay-forming reactions take place at low temperatures



**Figure A-2:** Small-scale maps of sample locations. 2a.) Map of the high peaks area showing locations of faults sampled. Topographic base map is Rwenzori Mountaineering Services 1:50,000 topographic map superimposed over 90 m DEM. Note that the RMS map does not conform to a standard grid. 2b.) Location of samples collected along the Fort Portal – Bundibugyo road. Base map is 1:250,000 Fort Portal topographic sheet, produced by the Uganda Lands and Surveys Department.

(<200 °C) and are kinetically impeded, authigenic clay minerals are very fine grained, and tend to concentrate in the finest size fraction. Samples were x-rayed both as oriented slurry preparations to accentuate the (00l) peaks and as random patterns to assess polytypism of clay minerals in various size fractions using the same techniques described as in Chapters 2 and 4.

## Results

The Rwenzoris are uplifted along a complex network of faults with mainly normal and dextral strike-slip components. One dominant set of faults strikes parallel to the main flanks of the horst-block and parallel to the main rift faults. These faults are NE-striking, steeply dipping normal faults, with dips around 70° to 80°, and a steeply dipping lineation. A second major set of faults strikes NW, perpendicular to the horst flanks, transects the horst, cutting it into smaller blocks. These NW-striking faults are either steeply dipping strike-slip or normal faults, or a combination of the two (*Koehn et al., in press*). The major range-bounding faults have a clear geomorphic expression, but fault rocks from the range-bounding faults are not exposed, so smaller scale faults with similar structural trends as the main features were sampled. Owing to heavy rainfall and exuberant vegetation, faults are exposed only in roadcuts and quarries at low elevations and in cliff faces at elevations >3800 m in the central portion of the range.

Gouge mineral assemblages from the Rwenzoris are somewhat variable, but gouge mineral assemblages correlate strongly with elevation, and three characteristic mineral assemblages are apparent (see Table A-1). 1.) Gouges sampled at low altitudes contain

| Outcrop              | Sample     |             |               | Clay minerals |          |   |          |      | Non-clay minerals |          |          |          |    |    |    |   |          |   |
|----------------------|------------|-------------|---------------|---------------|----------|---|----------|------|-------------------|----------|----------|----------|----|----|----|---|----------|---|
|                      | Utitude (M | Strike/dip  | Size fraction | C             | V        | I | Polytype | Mica | Sm                | K        | Q        | KF       | PI | Am | Ca | G | Mor      | H |
| Bujuku-1             | 3960       | 040/70E     | < 2.0 µm      | x             | x        |   | 2M1      |      |                   |          | x        | <u>X</u> |    |    |    |   |          |   |
| " "                  | 3960       |             | < 0.4 µm      |               | <u>X</u> |   | 2M1      |      |                   |          | x        | x        |    |    |    |   |          |   |
| Day 63               | 4100       | 080/40S     | < 2.0 µm      | <u>X</u>      |          |   | tr       |      |                   |          |          | x        | x  |    |    |   | x        |   |
| Day 81               | 3990       | 312/28S     | < 2.0 µm      | <u>X</u>      |          |   | x        |      |                   |          |          | x        | x  |    |    |   | x        |   |
| Freshfield Pass      | 4100       | 070/32S     | < 2.0 µm      | x             | x        |   |          |      | <u>X</u>          | x        |          |          |    |    |    |   |          |   |
| " "                  |            |             | 2.0 - 0.4 µm  | x             | x        |   | 2M1      |      |                   | x        |          | x        |    |    |    |   |          |   |
| " "                  |            |             | 0.4 - 0.05 µm | tr            | tr       |   | 2M1      |      | <u>X</u>          | tr       |          | tr       |    |    |    |   |          |   |
| " "                  |            |             | <0.05 µm      |               |          |   |          |      | <u>X</u>          |          |          |          |    |    |    |   |          |   |
| Kitandara - 200 m S  | 3870       | 012/78E     | < 2.0 µm      | x             |          |   |          |      | x                 |          |          |          | x  |    |    |   | <u>X</u> | x |
| Kitandara - residual | 3860       | Resid. soil | < 2.0 µm      | <u>X</u>      |          |   | x        |      | 2M1               | x        |          |          | x  |    |    |   |          |   |
| Scott Elliot         | 4065       | 340/70W     | < 2.0 µm      | x             | x        |   |          |      | <u>X</u>          |          |          |          |    |    |    |   |          |   |
| " "                  |            |             | 2.0 - 0.4 µm  | <u>X</u>      |          |   | x        |      |                   | x        |          |          | x  | x  | x  |   |          |   |
| " "                  |            |             | 0.4 - 0.05 µm | x             | x        |   |          |      | <u>X</u>          | x        |          |          |    |    |    |   |          |   |
| " "                  |            |             | <0.05 µm      |               |          |   |          |      | <u>X</u>          | x        |          |          |    |    |    |   |          |   |
| UG-20                | 4050       | 010/75E     | < 2.0 µm      | <u>X</u>      |          |   |          |      |                   |          |          |          |    |    |    |   |          | x |
| ER-1                 | 1204       | 045/70E     | < 2.0 µm      |               |          |   | x        |      |                   | <u>X</u> | x        |          |    |    |    |   |          |   |
| ER-2                 | 1295       | 026/42W     | < 2.0 µm      |               |          |   | x        |      |                   | <u>X</u> | x        |          |    |    |    |   |          |   |
| ER-3                 | 1290       | 030/80W     | < 2.0 µm      |               |          |   | x        |      |                   | <u>X</u> | x        |          |    |    |    |   |          |   |
| ER-4                 | 1330       | 020/30W     | < 2.0 µm      |               |          |   | x        |      |                   | <u>X</u> | x        |          |    |    |    |   |          |   |
| ER-5                 | 1366       | 070/60N     | < 2.0 µm      |               |          |   | x        |      |                   | <u>X</u> | x        |          |    |    |    |   |          |   |
| ER-6                 | 1416       | 070/28S     | < 2.0 µm      |               |          |   | x        |      |                   | x        | <u>X</u> |          |    |    |    |   |          |   |
| " "                  |            |             | 2.0 - 0.4 µm  |               |          |   | x        |      | 2M1               |          | <u>X</u> |          | x  | x  |    |   |          |   |
| " "                  |            |             | 0.4 - 0.05 µm |               |          |   |          |      |                   |          | <u>X</u> |          |    |    |    |   |          |   |
| " "                  |            |             | <0.05 µm      |               |          |   |          |      |                   |          | <u>X</u> |          |    |    |    |   |          |   |
| Kanyambara           | 1120       | Resid. soil | < 2.0 µm      |               |          |   |          |      |                   | <u>X</u> |          |          |    |    |    |   |          |   |
| " "                  |            |             | 2.0 - 0.4 µm  |               |          |   | x        |      | 2M1               |          | <u>X</u> |          |    |    |    |   |          |   |
| " "                  |            |             | 0.4 - 0.05 µm |               |          |   | tr       |      | 2M1               |          | x        | <u>X</u> |    |    |    |   |          |   |
| " "                  |            |             | <0.05 µm      |               |          |   |          |      |                   |          | x        | <u>X</u> |    |    |    |   |          |   |
| Katwe - ash          | 965        |             | < 2.0 µm      |               |          |   |          | 3T   | phlog             | <u>X</u> | tr       |          |    |    | x  | x |          |   |
| Katwe - disagregati  | 965        | 060/85N     | < 2.0 µm      |               |          |   |          | 3T   | phlog             | <u>X</u> | tr       |          |    |    | x  | x |          |   |
| Kilembe - surface    | 1500       | Resid. soil | < 2.0 µm      |               |          |   | tr       |      |                   | x        | <u>X</u> |          |    |    |    |   |          |   |
| Kilembe-1            | 1450*      | 020/70E     | < 2.0 µm      | x             |          |   |          |      |                   | <u>X</u> |          |          | x  |    |    |   | x        |   |
| Kilembe-3            | 1450*      | 060/70N     | < 2.0 µm      |               |          |   |          |      |                   |          |          |          |    |    |    |   |          |   |
| " "                  |            |             | 2.0 - 0.4 µm  | <u>X</u>      |          |   | tr       |      |                   | x        |          |          |    |    | x  |   |          |   |
| " "                  |            |             | 0.4 - 0.05 µm | x             |          |   |          |      |                   | <u>X</u> |          |          |    |    | x  |   |          |   |
| " "                  |            |             | <0.05 µm      |               |          |   |          |      |                   | <u>X</u> |          |          |    |    | x  |   |          |   |
| Kilembe-4            | 1450*      | 050/80N     | < 2.0 µm      | x             |          |   | tr       |      |                   | <u>X</u> |          |          |    |    |    |   |          |   |
| Konomiki             | 1150       | 020/85W     | < 2.0 µm      |               |          |   | x        |      |                   | <u>X</u> | x        |          |    |    |    |   |          | x |
| " "                  |            |             | 2.0 - 0.4 µm  |               |          |   | x        |      | 2M1               |          | x        |          | x  | x  |    |   |          | x |
| " "                  |            |             | 0.4 - 0.05 µm |               |          |   | tr       |      |                   | <u>X</u> | x        |          |    |    |    |   |          |   |
| " "                  |            |             | <0.05 µm      |               |          |   |          |      |                   | x        | <u>X</u> |          |    |    |    |   |          |   |
| SH-2                 | 1310       | 055/55E     | < 2.0 µm      | x             | x        |   | 2M1      |      |                   | x        | x        | <u>X</u> |    |    |    |   |          |   |
| " "                  |            |             | 2.0 - 0.4 µm  | x             | x        |   | 2M1      |      |                   | x        | x        | <u>X</u> |    |    |    |   |          |   |
| " "                  |            |             | 0.4 - 0.05 µm | tr            | tr       |   |          |      |                   | <u>X</u> |          |          |    |    |    |   |          |   |
| " "                  |            |             | <0.05 µm      |               |          |   |          |      |                   | <u>X</u> |          |          |    |    |    |   |          |   |

**Table 8-1:** Mineralogy of fault gouge samples in the Rwenzoris as determined by XRD. C = chlorite, V = vermiculaite, I = illite, Sm = smectite, K = kaolinite, Q = quartz, KF = K=feldspar, PI = plagioclase, Am = amphibole, Ca = calcite, G = gypsum, Mor = mordenite, Hem = hematite. **Bold** = most abundant phase, tr = trace.

authigenic smectite possibly derived from fault zone transformations, and authigenic kaolinite of probable surficial weathering origin. 2.) High-altitude gouges and protected low-altitude gouges contain authigenic smectite as the only authigenic phase. 3.) Some incohesive fault gouges at both low and high elevations lack evidence of any mineral transformations and consist solely of detrital material derived from the wall rock.

#### Low-altitude surface gouges

Samples collected from surface exposures of faults below 2000 m elevation consistently contain detrital chlorite and muscovite and authigenic dioctahedral smectite and kaolinite (see Figures A-3 and A-4). To assess the effects of tropical weathering on gouge mineralogy, gouge samples were compared with 3 samples of known residual soils that were collected from the eastern Rwenzoris at elevations <2000 m. The residual soil assemblages have very similar clay kaolinite-dominated assemblages to those found in the sampled gouges, indicating that kaolinite-rich gouge samples at low elevations have certainly been heavily affected by surface weathering and may not preserve clay mineral assemblages related to faulting. Both smectite and kaolinite form <130 °C, implying that the clay mineral assemblages have not been deeply exhumed, and could have formed at surficial conditions. The similarity of the low-altitude clay-gouge assemblages to the low-altitude residual-soil assemblages indicates that clay mineral growth found in faults exposed at low-altitude in the Rwenzoris is probably controlled by near-surface weathering and soil-formation processes, and not by fault-related clay growth.

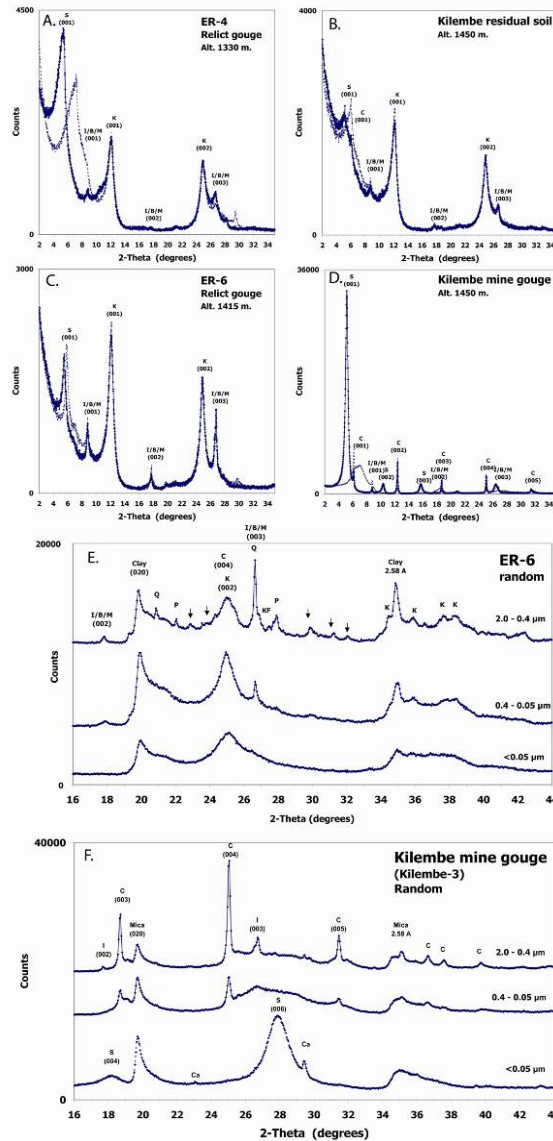
#### Smectite-dominated gouges

Some high-altitude gouge samples (>3000 m) and samples from faults 100 m below the



**Figure A-3:** Outcrop photos of fault exposures along the Fort Portal – Bundibugyo road north of Kichwamba. Upper photo is ER-4, a small brittle fault that formed along the contact of a 20 m thick diabase dike with leucocratic gneiss. The fault strikes 020, dips 30W and has a 20 cm thick gouge zone. Sense of shear is oblique with roughly equal components of normal and sinistral slip. Lower photo is ER-6, a brittle fault with a 10 cm thick clayey gouge that strikes 070 and dips 28S.





**Figure A-4:** XRD patterns of oriented preparations of four samples (<2.0  $\mu\text{m}$  size fraction) from low elevations in the eastern Rwenzoris. A.) ER-4, a low-altitude gouge exposed at the surface. B.) a residual soil exposed near the Kilembe mine. C.) ER-6, a low-altitude gouge exposed at the surface. D.) gouge from Kilembe-3, a fault exposed on the 4500 ft level of the Kilembe mine, 100 m below the surface and protected from surface weathering phenomena. Note the three surface samples all consist predominantly of smectite and kaolinite, while the gouge sampled in the mine lacks kaolinite. Dashed line is air-dried, solid is after glycol salvation. S = smectite, C = chlorite, I/B/M = illite/biotite/muscovite, K = kaolinite. E. & F.) XRD patterns of random preparations of gouges at ER-6 and Kilembe-3. Note the effect of surface weathering on gouges at low elevations. The surface sample (ER-6) contains illite, quartz, chlorite and kaolinite in the 2.0 – 0.4  $\mu\text{m}$  and 0.4 - 0.05  $\mu\text{m}$  size fractions, and almost pure kaolinite in the <0.05  $\mu\text{m}$  size fraction. Arrows indicate  $2M_1$  polytype-specific peaks for  $2M_1$  illite or most probably muscovite. The gouge sampled underground (Kilembe-3) contains illite and chlorite in the 2.0 – 0.4  $\mu\text{m}$  and 0.4 - 0.05  $\mu\text{m}$  size fractions, and smectite in the <0.05  $\mu\text{m}$  size fraction, indicating that smectite is the authigenic clay phase in the gouge when not exposed to surficial processes.

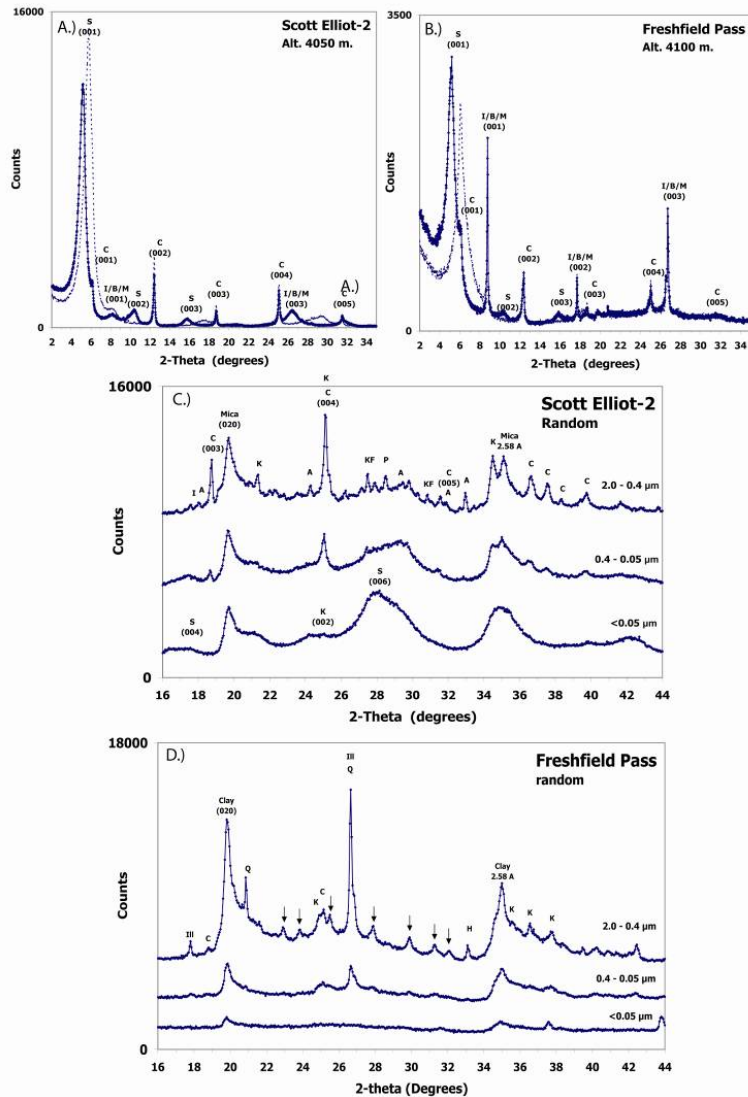
surface inside the Kilembe Mine at 1300 m elevation, contain smectite derived from alteration of detrital chlorite as the authigenic clay phase (see Figures A-4, A-5, & A-6). Unlike the low-altitude gouge surface exposures, the gouges exposed at high altitudes and protected low-altitude gouges mostly lack kaolinite. The high-altitude fault zones at Scott Elliot-2 and Freshfield Pass and the Kilembe Mine samples are not affected by surface weathering, and preserve authigenic smectite related to brittle faulting processes (Figures A-5 & A-6). The presence of dioctahedral smectite and not the 1M<sub>d</sub> polytype of illite (which grows at temperatures >100 °C.) as the authigenic clay phase at Freshfield Pass, where the wall rocks contain muscovite implies that smectite growth occurred at temperatures below 100 °C, the temperature at which 1M<sub>d</sub> illite might be expected to grow. The amount of exhumation of the fault zones that are exposed in the upper reaches of the Rwenzori Mountains is thus probably small, <3 km. The presence of similar smectite-rich assemblages preserved in faults exposed underground at low elevations indicates that most of the authigenic clay related to faulting found throughout the Rwenzoris regardless of modern elevation is smectite, and the brittle faults now exposed experienced gouge formation at temperatures <100 °C.

#### Detrital gouges and disaggregation bands

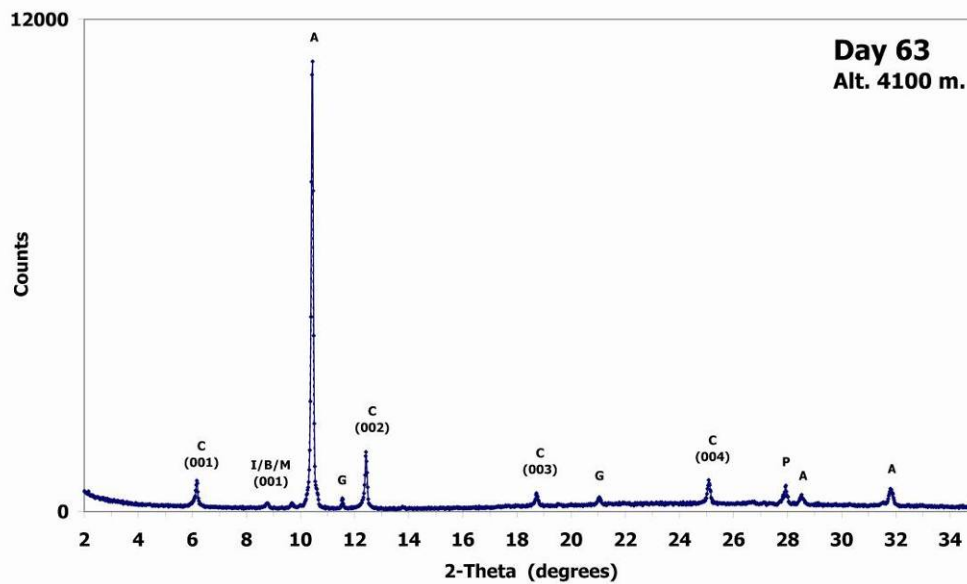
Some fault rocks at both low and high elevations contain solely minerals derived from the wall rocks and do not contain any evidence for clay mineral transformations. Brittle faults that lack authigenic clay growth are found both at high elevation in the central portion of the range (Figure A-7) and in Miocene to Quaternary sedimentary rocks exposed on the rift valley floors both north and south of the range (Figure A-8). These purely detrital fault rocks are evidence for cataclasis and granular flow at very high crustal levels. Two different sorts of clay-free fault rocks are observed, weakly



**Figure A-5:** Field photos of brittle fault exposed on the northwest flank of Mt Baker, east of Scott Elliot Pass, elevation 4065 m. View is towards the southeast. Fault strikes 340 and dips 70 W. Arrow in upper photo indicates outcrop of gouge zone shown in lower photo. Cliff face is 200 m high.



**Figure A-6:** XRD patterns for gouges sampled at high altitudes at Scott Elliot Pass and at Freshfield Pass. A. & B.) Oriented preparations of <2.0  $\mu\text{m}$  size fractions; dashed line is air-dried, solid is glycol-solvated. Note that both gouges consist primarily of smectite, with subsidiary chlorite and illite/muscovite. Extremely sharp and narrow mica and chlorite peaks indicate very large diffracting domain sizes and a metamorphic origin for both minerals. S = smectite, C = chlorite, I/B/M = 10 $\text{\AA}$  mica (illite/biotite/muscovite). C. and D.) Random preparations from gouges at Scott Elliot Pass and at Freshfield Pass. C.) Gouge from Scott Elliot Pass. The 2.0 – 0.4  $\mu\text{m}$  and 0.4 – 0.05  $\mu\text{m}$  size fractions contain a mixture of plagioclase, amphiboles and chlorite, while the <0.05  $\mu\text{m}$  size fraction consists primarily of smectite, with minor kaolinite. D.) Gouge 100 m west of Freshfield Pass. 2.0 – 0.4  $\mu\text{m}$  and 0.4 – 0.05  $\mu\text{m}$  size fractions consist primarily of muscovite, quartz, and minor chlorite derived from the wallrock muscovite schist, along with kaolinite. The <0.05  $\mu\text{m}$  size fraction consists exclusively of a very disordered smectite, evidenced by the absence of a clear (005) peak and instead a gradual downward slope of the powder pattern from the (020) peak at 19.8 $^\circ$  2 $\theta$  to the base of the 2.58  $\text{\AA}$  peak at 34.9 $^\circ$  2 $\theta$ . I = illite/muscovite (arrows indicate 2M<sub>1</sub> polytype-specific peaks), A = amphibole, K = kaolinite, C = chlorite, KF = K-feldspar, P = plagioclase, H = hematite.



**Figure A-7:** Field photographs and XRD pattern of brittle fault exposed on the southeast side of Mt Stanley. Upper left figure shows a 50 cm-thick incohesive breccia highlighted by dashed lines. Footwall and hangingwall are annealed mylonitic amphibolites. Upper right figure is a closeup of the same breccia 100 m downslope. Note ease with which breccia is excavated with a hammer. Lower figure is XRD pattern from outcrop pictured in upper right figure. Note breccia matrix consists of chlorite and amphibole with trace amounts of gypsum and plagioclase. Oriented preparation, dashed line is air-dried, solid line is after glycol salvation. The absence of low-temperature clays such as smectite or vermiculite and the very incohesive texture indicates that the gouge formed at very high levels in the crust, probably in the upper two kilometers of the crust.



**Figure A-8:** Field photographs of normal fault at Katwe Crater. Fault strikes 060 and dips 80° N. View in upper figure is towards the southwest. View of lower figure is vertical in area outline in box shown in upper figure. Wall rocks are weakly cemented fluviually-reworked carbonatite volcanic ashes. Note that fault rock is disaggregated ash with granular flow indicators such as incorporated lenses of coarser- and finer- grained material from wallrock sediments (lower photo) and lack of visible cataclasis or decrease in grain size of fault rock relative to the wall rocks. Uninked euhedral phlogopite flakes to 0.5 cm long are common in the wallrocks and similarly undeformed phlogopite flakes can readily be picked from the deformation bands. Disaggregation bands indicating ductile deformation in the brittle regime (deformation by granular flow without cataclasis) are thought to form only in the upper 1 km of the crust.

consolidated cataclastic breccias in fault zones in crystalline rocks at high elevations and disaggregation bands in weakly cemented sandy sediments at low elevations.

At high elevations, south-dipping mylonite zones are locally reactivated as brittle faults, as at Day 6-3, and Day 8-1 (see Figure A-7). Northeast-striking steeply-dipping brittle normal faults without significant clay growth are also found at UG-20 and Day 5-2. The re-activated mylonite zones contain incohesive clast-supported breccias that range in width from 30 cm to 1 m. The breccias are friable, almost sandy in texture and can be easily extracted with a hammer at outcrop. The breccias consist of variably angular clasts of hangingwall amphibolite from pebble- to boulder-size in a matrix of silt-sized micaceous material. XRD analysis indicates that the matrix consists almost exclusively of chlorite and amphibole. These breccias appear to have formed at very high levels in the crust as the mineral assemblage consists entirely of wallrock minerals and the gouge is friable, indicating very low confining and overburden stresses. The northeast-striking, steeply-dipping brittle faults contain friable clast-supported breccias of angular wall-rock clasts and a sandy-to-silty matrix that consists of wall-rock minerals, gypsum, and occasionally traces of copper minerals such as covalite and chrysocola.

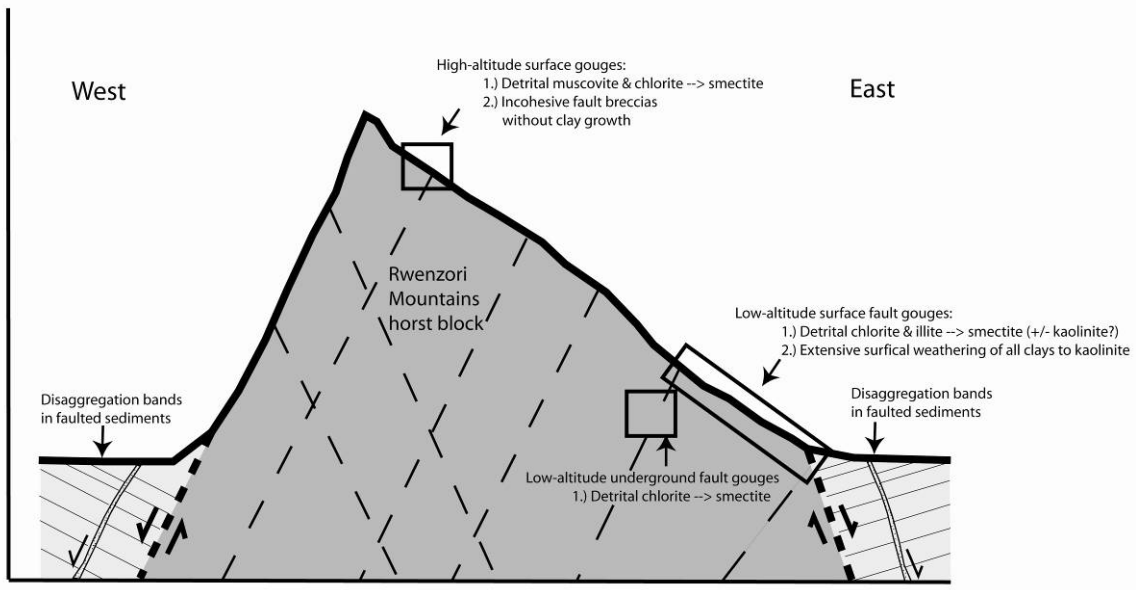
At low elevations in the rift valleys, normal faults are exposed in weakly cemented sandstones and fluvially-reworked tuffs of the rift valley fill sequences. These normal faults have a distinctive field expression in that the fault rocks are disaggregation bands (*Fossen et al., 2007*) and consist of disrupted and rotated grains of wall rock sand and micas without appreciable cataclasis. Centimeter-thick lenses of relatively coarse- and fine-grained sands are preserved in the disaggregation bands at Katwe crater and unkinked fresh detrital phlogopite flakes up to 5 mm in size are found in the coarser lenses (see Figure A-8). The fault rocks formed as a result of distributed granular flow of

wallrock material without appreciable cataclasis. Such ductile granular flow textures are thought to form only in the upper 1 km of the crust (*Antonellini et al., 1994, Fossen et al., 2007*).

## **Discussion and conclusions**

The mineralogy and fabrics of brittle fault rocks are strongly sensitive to the depth of their formation. All of the brittle fault rocks sampled in the Rwenzoris show evidence of formation at very high levels of the crust, mostly at temperatures <100 °C and therefore in the upper 3 km of the crust. All fault rocks, where not heavily overprinted by tropical weather processes at low altitudes, either contain authigenic smectite or lack authigenic clay entirely. The presence of brittle fault rocks at Freshfield Pass that have detrital 2M<sub>1</sub> muscovite and authigenic montmorillonite indicates that the montmorillonite grew below the ~100 °C typically assumed for the growth of illite-rich illite-smectite and the low-temperature 1M<sub>d</sub> polytype of illite (*Hower et al., 1976, Freed & Peacor, 1989*). The brittle fault rocks found at high elevations that lack all authigenic clay also must have formed within 1-2 km of the Earth's surface, evidenced by their lack of compaction or consolidation and detrital mineralogy. A summary sketch illustrating clay mineral assemblages in fault gouges of the Rwenzori Mountains is shown in Figure A-9. The relative and absolute age of the structures remains unclear, owing to the lack of authigenic K-containing phases such as illite. While the smectite-rich gouges may have formed at greater depths than the purely detrital breccias, the long residence time of the Rwenzoris below 100 °C, indicated by 140-89 Ma apatite fission-track ages, indicates that the exposed brittle faults could either have formed at any point since the early Cretaceous or contemporaneously with the major uplift event. This question remains





**Figure A-9:** Summary sketch of Rwenzori massif indicating distribution of various types of fault rocks observed. Relief is not to scale.

unresolved owing to the absence of suitable phases for dating.

The very low-temperature fault rock mineral assemblages are entirely consistent with the proposal that the Rwenzoris are a block rift shoulder that cooled to temperatures  $< 70^{\circ}\text{C}$  during the Paleogene, and then were rapidly uplifted to their current elevation in the last 2-3 million years (*Bauer et al., 2007*). The current high rates of erosion implied by meter-scale annual rainfall and high-altitude glaciation have not been operating for long enough to erode more than 1-2 km off of the top of the range and preserve brittle fault rocks that formed in the uppermost levels of the crust.

### **Acknowledgements**

We are grateful to the RIFTLINK consortium at Mainz and other German Universities for the opportunity to participate in fieldwork in Uganda for two field seasons. We are also grateful to the Uganda Wildlife Authority for permits to samples in Uganda's spectacular parks. We are grateful to the guides and porters of Rwenzori Mountaineering services, without whom fieldwork in the high peaks would have been impossible. We are also grateful to the professors and staff of Mackerere University in Kampala, who's advice and equipment support was invaluable.

## References

- Acocella, V. & Korme, T. (2002) Holocene extension direction along the Main Ethiopian Rift, East Africa *Terra Nova* 14, pp. 191-197
- Antonellini, M., Aydin, A. & Pollard, D., (1994). Microstructure of deformation bands in porous sandstones at Arches National Park, Utah. *J. Structural Geology* 16, pp. 941-959.
- Bahat, D., & Morh, P., (1987). Horst faulting in continental rifts. *Tectonophysics* 141, pp. 61-73.
- Bauer, F., Glasmacher, U., Reiners, P., Nagudy, B., & Bechstaedt, T., (2007). Low-temperature thermochronology, uplift and denudation history of the Rwenzori Mts, Uganda. *Geophysical Research Abstracts* 9, 08781.
- Contreras, J., Anders, M. & Scholz, C. (2000) Growth of a normal fault system: observations from the Lake Malawi basin of the east African rift. *J. Structural Geology*. 22, pp. 159-168
- Ebinger, C. (1989) Tectonic development of the western branch of the East African rift system. *Geological Society of America Bulletin* 101, pp. 885-903.
- Ebinger, C., Karner, G., & Weissel, J., (1991). Mechanical strength of extended continental lithosphere: Constraints from the western rift system, East Africa. *Tectonics* 10, pp. 1239 – 1256.
- Fossen, H., Schultz, R., Shipton, Z., & Mair, K., (2007). Deformation bands in sandstone: a review. *J. Geological Society of London* 164, pp. 755-769.
- Freed, R., & Peacor, D., (1989). Variability in temperature of the smectite/illite reaction in Gulf Coast sediments. *Clay Minerals*, 24, pp. 171 - 180.
- Hower, J., Eslinger, E., Hower, M. & Perry, E., (1976). Mechanism of burial metamorphism of argillaceous sediment: 1. Mineralogical and chemical evidence. *Geological Society of America Bulletin* 87, pp. 725 - 737.
- Kampazu, A., Bonhomme, M. & Kanika, M. (1998) Geochronology of volcanic rocks and evolution of the Cenozoic Western Branch of the East African Rift system. *J. African Earth Science*. 26, pp. 441-461
- MacPhee, D., Bowring, S. & Reiners, P. (2005) Combined (U-Th)/He and U-Pb thermochronology of rift-flank exhumation in east-central Africa *Abstracts Goldschmidt conference 2005* pp. A304.
- MacPhee, D., (2006). Exhumation, rift-flank uplift and the thermal evolution of the Rwenzori Mountains determined by combined U-Pb and (U/Th)/He thermometry. Unpublished M.Sc. thesis, Massachusetts Institute of Technology, 38 pp.

- McConnell, R. (1972) Geological development of the rift system of eastern Africa *Geological Society of America Bulletin* 83, pp. 2549-2572
- Ring, U. (1994) The influence of pre-existing structure on the evolution of the Cenozoic Malawi rift (East African rift system) *Tectonics* 13, pp. 313-326
- Ring, U., Betzler, C. & Delvaux, D. (1992) Normal vs. strike-slip faulting during rift development in East Africa: The Malawi rift *Geology* 20, pp. 1015-1018
- Rein, B. & Kaufmann, H. (2003) Exploration for gold using panchromatic stereoscopic intelligence satellite photographs and Landsat TM data in the Hebei area, China *Int. J. Remote Sensing* 24, pp. 2427-2438
- Rosendahl, B. (1987) Architecture of continental rifts with special reference to east Africa. *Ann. Rev. Earth Planet. Sci.* 15, pp. 445-503
- Strecker, M., Blisnuik, P. & Eisbacher, G. (1990) Rotation of extension direction in the central Kenya Rift *Geology* 18, pp. 299-302.
- Van der Beek, P., Mbede, E., Andreissen, P. & Delvaux, D., (1998) Denudation history of the Malawi and Rukwa Rift flanks (East African Rift System) from apatite fission track thermochronology *J. African Earth Science* 26, pp. 363-385
- Whittow, J. (1966) The landforms of the central Ruwenzori, East Africa. *Geographical Journal* 132, pp. 32-42

## APPENDIX B – FIELD SAMPLE LOCATIONS

| Fault                             | Range                          | Sample         | Latitude    | Longitude    | Notes                         |
|-----------------------------------|--------------------------------|----------------|-------------|--------------|-------------------------------|
|                                   |                                |                | North       | West         |                               |
| Badwater-1                        | Black Mts, CA                  | Bad-1          | 36° 15' 25" | 116° 46' 29" | XRD, XTG & Ar-Ar (in process) |
| Badwater-2                        | Black Mts, CA                  | Bad-2          | 35° 17' 11" | 116° 45' 47" | XRD                           |
| Buckskin-Rawhide                  | Buckskin Mts, AZ               | A-Bomb Canyon  | 34° 10' 8"  | 113° 40' 46" | XRD                           |
| Buckskin-Rawhide                  | Plomosa Mts, AZ                | Plomosa        | 33° 48' 32" | 114° 5' 5"   | XRD                           |
| Bullard                           | Harquahalla Mts, AZ            | Aguila         | 33° 53' 16" | 113° 10' 41" | XRD                           |
| Boundary Canyon                   | Funeral Mts, CA                | Bndy-1         | 36° 44' 29" | 116° 57' 11" | XRD                           |
| Bullard                           | Harcuvar Mts, AZ               | Bull-1         | 34° 3' 33"  | 113° 17' 19" | XRD                           |
| Chemehuevi                        | Chemehuevi Mts, CA             | Lobeck1        | 34° 41' 28" | 114° 37' 4"  | XRD                           |
| Copper Canyon                     | Black Mts, CA                  | Cop-1          | 36° 7' 28"  | 116° 44' 34" | XRD & XTG                     |
| Dante's View                      | Black Mts, CA                  | Dante-1        | 36° 13' 27" | 116° 42' 39" | XRD & XTG                     |
| Exclamation Rock                  | Black Mts, CA                  | ! Rock-1       | 35° 55' 11" | 116° 32' 39" | XRD & XTG                     |
| Mormon-1                          | Black Mts, CA                  | Mor-1          | 36° 2' 45"  | 116° 45' 39" | XRD & Ar-Ar                   |
| Mormon-2                          | Black Mts, CA                  | Mor-2          | 36° 2' 37"  | 116° 44' 12" | XRD & XTG                     |
| Mormon-3                          | Black Mts, CA                  | Mor-3          | 36° 2' 31"  | 116° 44' 20" | XRD & XTG                     |
| Mosaic Canyon                     | Panamint Mts, CA               | Mosaic-1       | 36° 34' 12" | 117° 8' 18"  | XRD & Ar-Ar                   |
| Newberry detachment               | Newberry Mts, NV               | Newberry-1     | 35° 7' 19"  | 114° 38' 33" | XRD                           |
| Panamint range front LANF         | Panamint Mts, CA               | SPark1         | 36° 0' 5"   | 117° 12' 1"  | XRD & Ar-Ar                   |
| Buckskin-Rawhide                  | Rawhide Mts, AZ                | Swan-2         | 34° 10' 8"  | 113° 50' 38" | XRD                           |
| Emigrant Fault                    | Panamint Mts, CA               | Tucki-OC       | 36° 31' 12" | 117° 11' 12" | XRD & Ar-Ar                   |
| Whipple                           | Whipple Mts, CA                | Whip-3         | 34° 21' 55" | 114° 16' 44" | XRD                           |
| Whipple                           | Whipple Mts, CA                | Whip-4         | 34° 22' 2"  | 114° 16' 47" | XRD                           |
| Whipple                           | Whipple Mts, CA                | Whip-5         | 34° 22' 8"  | 114° 17' 11" | XRD & XTG                     |
| Emigrant Fault                    | Panamint Mts, CA               | Wild1          | 36° 34' 12" | 117° 13' 34" | XRD & Ar-Ar                   |
| Central Mojave                    | Waterman Hills, CA             | Waterman Hills | 36° 34' 12" | 113° 40' 46" | XRD & Ar-Ar                   |
| Salton Sea                        | Santa Rosa Mts, CA             | Salton-1       | 36° 34' 12" | 113° 40' 46" | XRD                           |
| Sierra Mazatan                    | Sierra Mazatan, Sonora, Mexico | Maz-1          | 29° 9' 58"  | 110° 13' 58" | XRD & Ar-Ar                   |
| Ruby Mts                          | Ruby Mts, NV                   | Clover-1       | 41° 3' 48"  | 115° 1' 21"  | XRD & Ar-Ar                   |
| Ruby Mts                          | Ruby Mts, NV                   | Clover-1 FW    | 41° 2' 47"  | 115° 0' 39"  | Musc & biot Ar-Ar             |
| Ruby Mts                          | Ruby Mts, NV                   | Secret1        | 40° 52' 12" | 115° 15' 36" | XRD & Ar-Ar                   |
| Ruby Mts                          | Ruby Mts, NV                   | Secret2        | 40° 52' 6"  | 115° 15' 22" | XRD & Ar-Ar                   |
| Ruby Mts                          | Ruby Mts, NV                   | Secret3        | 40° 51' 54" | 115° 15' 16" | XRD                           |
| Ruby Mts                          | Ruby Mts, NV                   | Secret4        | 40° 51' 53" | 115° 15' 15" | XRD & Ar-Ar                   |
| Ruby Mts                          | Ruby Mts, NV                   | FW-1           | 40° 51' 49" | 115° 14' 42" | Musc & biot Ar-Ar             |
| Size 36 Canyon                    | Black Mts, CA                  | Size 36        | 35° 57' 50" | 116° 40' 34" | XRD, XTG & Ar-Ar (in process) |
| Virgin Springs W-1                | Black Mts, CA                  | Virgin-1       | 35° 56' 3"  | 116° 34' 56" | XRD                           |
|                                   |                                |                | North       | East         |                               |
| Abocador                          | Pyrenees                       | Aboc-1         | 42° 9' 5"   | 2° 12' 2"    | XRD & Ar-Ar                   |
| Boixols                           | Pyrenees                       | Boix E-1       | 42° 10' 24" | 1° 10' 52"   | XRD & Ar-Ar                   |
| Cavallera                         | Pyrenees                       | Cav-1          | 42° 16' 10" | 2° 9' 33"    | XRD & Ar-Ar                   |
| Gavernie                          | Pyrenees                       | Gav-1          | 42° 41' 46" | 0° 4' 45"    | XRD & Ar-Ar                   |
| L'Escala                          | Pyrenees                       | Lesc-1         | 42° 8' 44"  | 2° 12' 19"   | XRD & Ar-Ar                   |
| Llavorsi-Senet zone thrust        | Pyrenees                       | Llavorsi-Senet | 42° 31' 26" | 0° 49' 42"   | XRD & Ar-Ar                   |
| Nogueres zone thrust              | Pyrenees                       | Nogueres       | 42° 24' 55" | 0° 45' 21"   | XRD & Ar-Ar                   |
| North limb Ripoll syncline thrust | Pyrenees                       | Arman-1        | 42° 14' 20" | 2° 9' 52"    | XRD & Ar-Ar                   |
| Peramola thrust                   | Pyrenees                       | Peramola-1     | 42° 3' 32"  | 1° 15' 43"   | XRD & XTG                     |
| Vallfogona thrust                 | Pyrenees                       | Vallf-1        | 42° 7' 48"  | 1° 54' 2"    | XRD & Ar-Ar                   |
|                                   |                                | Zone           | North       | East         |                               |
| Bujuku-1                          | Rwenzoris                      |                | 35          | 43197        | 821512 XRD                    |
| Day63                             | Rwenzoris                      |                | 35          | 39838        | 821127 XRD                    |
| Day81                             | Rwenzoris                      |                | 35          | 39479        | 821437 XRD                    |
| Freshfield Pass                   | Rwenzoris                      |                | 35          | 38727        | 821772 XRD                    |
| Kitandara - 200 m S of hut        | Rwenzoris                      |                | 35          | 38403        | 821378 XRD                    |
| Kitandara - resid soil            | Rwenzoris                      |                | 35          |              | XRD                           |
| Scott Elliot                      | Rwenzoris                      |                | 35          | 40467        | 821681 XRD                    |
| UG-20                             | Rwenzoris                      |                | 35          | 39805        | 821435 XRD                    |
| ER-1                              | Rwenzoris                      |                | 36          | 84068        | 188941 XRD                    |
| ER-2                              | Rwenzoris                      |                | 36          | 83204        | 188443 XRD                    |
| ER-3                              | Rwenzoris                      |                | 36          | 83161        | 188394 XRD                    |
| ER-4                              | Rwenzoris                      |                | 36          | 82965        | 188012 XRD                    |
| ER-5                              | Rwenzoris                      |                | 36          | 82661        | 188008 XRD                    |
| ER-6                              | Rwenzoris                      |                | 36          | 81823        | 187542 XRD                    |
| Kanyambara                        | Rwenzoris                      |                | 35          | 5220         | 817731 XRD                    |
| Kilembe Mine                      | Rwenzoris                      |                | 36          | 22029        | 167057 XRD                    |
| Konomiki                          | Rwenzoris                      |                | 36          | 84555        | 190142 XRD                    |
| SH-2                              | Rwenzoris                      |                | 35          | 12742        | 824133 XRD                    |